NOTICE

The quality of this microform is heavily dependent upon the quality of the original thesis submitted for microfilming. Every effort has been made to ensure the highest quality of reproduction possible.

If pages are missing, contact the university which granted the degree.

Some pages may have indistinct print especially if the original pages were typed with a poor typewriter ribbon or if the university sent us an inferior photocopy.

Reproduction in full or in part of this microform is governed by the Canadian Copyright Act, R.S.C. 1970, c. C-30, and subsequent amendments.

AVIS

La qualité de cette microforme dépend grandement de la qualité de la thèse soumise au microfilmage. Nous avons tout fait pour assurer une qualité supérieure de reproduction.

S'il manque des pages, veuillez communiquer avec l'université qui a conféré le grade.

La qualité d'impression de certaines pages peut laisser à désirer, surtout si les pages originales ont été dactylographiées à l'aide d'un ruban usé ou si l'université nous a fait parvenir une photocopie de qualité inférieure.

La reproduction, même partielle, de cette microforme est soumise à la Loi canadienne sur le droit d'auteur, SRC 1970, c. C-30, et ses amendements subséquents.

ISBN 0-315-53830-9

EXPERIMENTS IN ROD BUNDLE SUBCHANNEL FLOWS WITH VARYING ROD-WALL PROXIMITY

by

BARACK HENRY OUMA

A thesis
presented to the University of Ottawa,
February, 1988
in partial fulfillment of the
requirement for the degree of
MASTERS of APPLIED SCIENCE
in
MECHANICAL ENGINEERING

OTTAWA, Ontario, 1988

ABSTRACT

Presented in this study is a detailed experimental investigation of air flow through a model of a five-rod sector of the 37-rod CANDU reactor bundle. Measurements were conducted at 34.2 rod diameters from the duct entrance and at a Reynolds number of 74000. The study was mainly focused on the wall subchannel at various rod-wall proximities.

In the first phase of the research, wall shear stress was measured around the central rod at various rod-wall and rod-rod proximities, including a case of a rod-rod-wall contact and cases of slanting rods. In the second phase, measurements of mean velocities and turbulence parameters were conducted for the design condition, and three off-design conditions, namely, a case of small rod-wall gap, a case with rod-wall contact and a case with rod-rod-wall contact.

The wall shear stress reached minima at rod-wall and rod-rod gaps and maxima at open flow regions. The average and the minimum wall shear stresses decreased dramatically with decreasing gap at small gaps but they changed very little at large gaps. The local friction factor decreased monotonically from the rod-rod and/or rod-wall gaps towards rod surfaces facing the open flow regions. The contours of the mean streamwise velocity, axial turbulence intensity and turbulent kinetic energy bulged towards narrow gaps and corners, and the bulging was more pronounced as the rod-wall gap decreased. The integral length scales and the

Taylor microscale generally increased from the rod surface to a maximum at approximately the mid point towards the subchannel center. Analysis of turbulence parameters showed that turbulence intensities and length scales in rod bundle flows may vary substantially from pipe flow measurements. These parameters depend on the size and shape of the wall subchannel and their magnitudes also depend on the position within the subchannel.

ACKNOWLEDGEMENT

I wish to express my sincere gratitude to Professor Stavros Tavoularis for his continual patience, guidance, encouragement and many instructive discussions which have proved to be the key factors in completing the task in time. His quick editing of the text and providing numerous comments contributed significantly to the quality. I also wish to thank Professors T. Rogers and R. Milane and Dr. S. Sutradhar for reading and commenting on this thesis.

Many thanks are also due to the staff at the departmental workshop for completing the construction of the flow facility in time and to Don Seaman for providing general assistance whenever needed. I also thank my colleagues in the Fluid Mechanics group, with all of whom I shared a warm academic atmosphere.

The financial support provided by the Atomic Energy of Canada Limited is greatly appreciated. Also I highly thank my sponsor, the Kenya Government General Training Fund and the staff of Kenya High Commission, Ottawa, for their quick responses to several requests.

Finally I am extremely indebted to my family for their consistent morale boosting letters all of which contributed towards my success.

NOMENCLATURE

A	cross-section of test-section
A_{FC}	cross-section of flow-cell
d	circular pipe diameter
	Preston tube diameter
D	rod diameter
dA	elementary area of flow cell
D_h	37-rod bundle hydraulic diameter
D_{h_m}	present model hydraulic diameter
d_{h_o}	wall subchannel hydraulic diameter at design condition
d_{h_1}	inner subchannel 1 hydraulic diameter at design condition
d_{h_2}	inner subchannel 2 hydraulic diameter at design condition
dP	pressure drop along duct axis
E_1, E_2	anemometer output voltages
e_1, e_2	fluctuating anemometer output voltages
f	friction factor
f_c	circular pipe friction factor

k	turbulent kinetic energy per unit mass
L	bundle length
$L_{11,1}$, $L_{22,1}$, $L_{33,1}$	streamwise Eulerian integral length scales of the axial, radial and azimuthal fluctuating velocities
P	pitch, static pressure
r	radial distance from the rod surface
R	bundle radius
	rod radius
R_1	radius of inner ring of rods
R_2	radius of middle ring of rods
R_3	radius of outer ring of rods
R_{e_h}	Reynolds number based on hydraulic diameter and bulk velocity
R_t	turbulence Reynolds number
$R_u(\tau)$, $R_{u_r}(\tau)$, $R_{u_\phi}(\tau)$	streamwise autocorrelation coefficients of axial, radial and azimuthal velocity fluctuations
T	time
T_f	fluid temperature
T_w	hot wire operating temperature
U, U_r, U_ϕ	axial, radial, and azimuthal velocity components

u, u_r, u_ϕ axial, radial and azimuthal fluctuating velocity components

U_b bulk velocity

U_o velocity at zero Reynolds shear stress

u_τ friction velocity

u^+ dimensionless velocity

W wall subchannel width

y^+ dimensionless radial distance from the rod surface

$\hat{y}$ radial distance from the rod surface to the line of flow symmetry

GREEK SYMBOLS

Δp pressure difference between Preston tube and static pressure hole

ϵ dissipation rate

ϵ_r radial eddy viscosity

ϵ_ϕ peripheral eddy viscosity

η Kolmogoroff's microscale

λ Taylor microscale

ν dynamic viscosity of air

ρ air density

ϕ peripheral coordinate

θ coordinate transformation angle

τ separation time

τ_w wall shear stress

SUBSCRIPTS AND SUPERSCRIPTS

$()_{av}$ representation of average quantity

$\overline{()}$ representation of time average value

$()'$ representation of root mean square value

TABLE OF CONTENTS

ABSTRACT i
ACKNOWLEDGEMENT iii
NOMENCLATURE iv
List of Tables viii
List of Figures ix

I. INTRODUCTION 1

II. LITERATURE REVIEW 4
2.1 Experiments on Inner Triangular Subchannels 4
2.2 Experiments on Wall Subchannels 6
2.3 Experiments on Inner Square Subchannels 7
2.4 Computational Studies 9

III. DEFINITIONS AND BACKGROUND INFORMATION 11
3.1 Hydraulic Diameter and its Applications 11
3.2 Mean Velocity and Bulk Velocity 13
3.3 Wall Shear Stress and Friction Factor 14
3.4 Velocity Distribution 16
3.4.1 Wall region 16
3.4.2 Core region 17
3.5 Secondary Flows 17
3.6 Turbulence Intensity and Kinetic Energy 18
3.7 Reynolds Stresses 19
3.8 Correlation Coefficients 19
3.9 Length Scales of Turbulence 20
3.9.1 Integral length scale 20
3.9.2 Taylor microscale 21
3.9.3 Dissipation length scale 22

3.10 Turbulence viscosity 22

IV. FLOW FACILITY AND INSTRUMENTATION 24
4.1 Flow Facility 24
4.2 Pressure and Wall Shear Stress Instrumentation 26
4.3 Hot Wire Instrumentation 28
4.4 Signal Conditioning 28
4.5 Signal Discretization and Processing 29

V. EXPERIMENTAL TECHNIQUES AND ACCURACY 31
5.1 Methodology for Pressure Measurements 31
5.2 Methodology for Wall Shear Stress Measurements 33
5.3 Methodology for Turbulence Measurements 35
5.3.1 Working principle of hot wire anemometry 35
5.3.2 Calibration and response of hot wire 36
5.3.3 Determination of the turbulent shear stresses 38
5.3.4 Data acquisition 39
5.3.5 Error analysis for hot wire measurements 40

VI. THE MEASUREMENTS 42
6.1 Preliminary Tests 42
6.2 Mean Static Pressure 43
6.3 Wall Shear Stress 44
6.4 Velocity Profile 46
6.4.1 Mean axial velocity 46
6.4.2 Secondary flows 47
6.4.3 Axial turbulence intensity 48
6.4.4 Radial turbulence intensity 48
6.4.5 Azimuthal turbulence intensity 49
6.5 Correlations 49
6.5.1 Reynolds stress and correlation coefficient 49
6.5.2 Turbulence kinetic energy 50
6.5.3 Autocorrelation coefficient 51
6.6 Scales 52
6.6.1 Integral length scales 52

6.6.2 Taylor microscales *53*

VII. ANALYSIS AND DISCUSSION OF RESULTS 54
7.1 Definition of a Local Characteristic Flow Width 54
7.2 Effect of Wall Subchannel Size on Friction Factor 55
7.3 Effect of wall subchannel size on velocity distribution 56
7.4 Effect of Wall Subchannel Size on rms Velocities 57
7.5 Effect of Wall Subchannel Size on Correlation Coefficient 58
7.6 Effect of Wall Subchannel Size on Scales 59
7.7 Turbulent Kinetic Energy Dissipation Rate 59
7.8 Kolmogoroff's Microscales 60
7.9 Implications about Heat Transfer 61
7.10 Comparison of Flows in the Model and Actual Bundle 61

VIII. CONCLUSIONS 64

BIBLIOGRAPHY 67

LIST OF TABLES

1. Comparison between actual bundle and model 73
2. Measured parameter and instrumentation used 74
3. Friction factors and friction velocity 75
4. Maximum and bulk velocities 76
5. Ratios of Eulerian integral length scales 77

LIST OF FIGURES

1. CANDU nuclear power system 78
2. 37-rod element reactor bundle 79
3. Division of a rod bundle flow channel into subchannels 80
4. Cross-section of triangular subchannel models 81
5. Cross-section of wall and square subchannel models 82
6. Cross-section of a 37-rod CANDU reactor bundle 83
7. Cross-section of the model bundle facility 84
8. Sketch of the flow facility 85
9. Probe traversing mechanism 86
10. Working section assembly showing the static pressure hole locations 87
11. Pitot and Static tubes 88
12. Pitot-static tubes 89
13. Preston tubes 90
14. Positioning of the Preston tube 91
15. Calibration curve of the pressure transducer 92
16. Definition of the angles for a cross wire probe 93
17. Data acquisition circuitry 94
18. Typical calibration of cross-wire probe 95
19. Time-temperature curve 96
20. Velocity distribution along the duct 97
21. Static pressure drop along the bundle axis 98
22. Wall static pressure around rod periphery 99
23. Inflow static pressure 100
24. Differences of wall shear stress readings using two Preston tubes with different diameters 101
25. Distribution of wall shear stress around the central rod for design geometry and with the rod displaced towards the wall 102

26. Distribution of wall shear stress around the central rod for design geometry and with the rod displaced towards the wall 103
27. Variation of maximum, average and minimum wall shear stress with W/D 104
28. Distribution of wall shear stress around the central rod for design geometry and with one end of the rod displaced towards the wall 105
29. Distribution of wall shear stress around the central rod slanting towards the wall 106
30. Variation of maximum, average and minimum wall shear stress on the slanting rod W/D 107
31. Distribution of wall shear stress around the central rod with the rod displaced towards the neighboring one 108
32. Distribution of wall shear stress around the central rod with the rod displaced towards the neighboring one 109
33. Variation of average wall shear stress and wall shear stress on rod surface facing the rod gaps with P/D 110
34. Distribution of wall shear stress around the central rod slanting towards the neighboring one 111
35. Distribution of wall shear stress around the central rod slanting towards the neighboring one 112
36. Variation of average wall shear stress and wall shear stress on slanting rod in the rod gaps with P/D 113
37. Distribution of wall shear stress around central rod at various positions 114
38. Peripheral variation of axial mean velocity at 2 mm from the rod surface (design geometry) 115
39. Velocity distribution at 180^0 116
40. Isovel contours at design condition 117
41. Isovel contours at W/D=1.059 118
42. Isovel contours at rod-wall contact 119
43. Isovel contours at rod-rod-wall contact 120
44. Axial turbulence intensity contours at design condition 121
45. Axial turbulence intensity contours at W/D=1.059 122

46. Axial turbulence intensity contours at rod-wall contact 123
47. Axial turbulence intensity contours at rod-rod-wall contact 124
48. Radial turbulence intensity contours at design condition 125
49. Radial turbulence intensity contours at W/D=1.059 126
50. Radial turbulence intensity contours at rod-wall contact 127
51. Radial turbulence intensity contours at rod-rod-wall contact 128
52. Azimuthal turbulence intensity contours at design condition 129
53. Azimuthal turbulence intensity contours at W/D=1.059 130
54. Azimuthal turbulence intensity contours at rod-wall contact 131
55. Azimuthal turbulence intensity contours at rod-rod-wall contact 132
56. Reynolds shear stress contours at design condition 133
57. Reynolds shear stress contours at rod-wall contact 134
58. Reynolds shear stress contours at rod-rod-wall contact 135
59. Variation of correlation coefficients 136
60. Turbulent kinetic energy contours at design condition 137
61. Turbulent kinetic energy contours at W/D=1.059 138
62. Turbulent kinetic energy contours at rod-wall contact 139
63. Turbulent kinetic energy contours at rod-rod-wall contact 140
64. Autocorrelation coefficients at selected positions for the design conditions 141
65. Autocorrelation coefficients at selected positions for the W/D=1.059 conditions 142
66. Autocorrelation coefficients at selected positions for the rod-wall contact conditions 143
67. Autocorrelation coefficients at selected positions for the rod-rod-wall contact conditions 144
68. Variation of streamwise Eulerian integral length scale of the axial velocity fluctuations 145
69. Variation of streamwise Eulerian integral length scale of the radial velocity fluctuations 146
70. Variation of streamwise Eulerian integral length scale of the azimuthal velocity fluctuations 147
71. Variation of the streamwise Taylor microscale 148
72. Local characteristic flow width at design conditions 149
73. Local characteristic flow width at three different central rod positions ... 150

74. Narrow sector bounded by rod surface and
the locus of maximum velocity 151
75. Distribution of local friction factor in the wall subchannel 152
76a. Variation of velocity distribution with rod-wall gap, δ 153
76b. Variation of velocity distribution with rod-wall gap, δ 154
77. Variation of velocities in the wall subchannel and channel
duct with rod-wall gap, δ 155
78. Velocity distribution in the wall subchannel 156
79. Distribution of the axial rms velocity fluctuation 157
80. Distribution of the radial rms velocity fluctuation 158
81. Distribution of the azimuthal rms velocity fluctuation 159
82. Distribution of correlation coefficient 160
83. Distribution of streamwise Eulerian integral length scale of the
axial velocity fluctuation 161
84. Distribution of streamwise Eulerian integral length scale of the
radial velocity fluctuation 162
85. Distribution of streamwise Eulerian integral length scale of the
azimuthal velocity fluctuation 163
86. Distribution of Taylor microscale 164
87. Distribution of turbulent energy dissipation rate 165
88. Distribution of Kolmogoroff's microscale 166

Chapter 1

INTRODUCTION

The discovery during the first half of this century that nuclear fission of uranium by chain reaction releases large amount of energy led to man's interest in harnessing that energy. Since then, nuclear energy generation has proved to be economically viable and nuclear technology has developed dramatically, especially during the past few decades. Types of reactors in operation include Pressurized Water Reactors (PWRs), Boiling Water Reactors (BWRs), Gas Cooled Reactors (GCRs) and Pressurized Heavy Water Reactors (PHWRs). One of the successful modern designs of PHWRs is the CANadian Deuterium Uranium (CANDU) reactor, designed and developed by the Atomic Energy of Canada Limited (AECL) as a commercial standardized plant.

Shown in figure 1 is a typical 600 MW(e) CANDU Nuclear Power System. In the system, a large, horizontal, cylindrical, stainless steel vessel, called Calandria, contains the cool, low pressure heavy water moderator. About 380 identical pressure tubes, containing the natural uranium fuel bundles and pressurized high temperature heavy water coolant, are also contained in the Calandria. The pressure tubes, presented in figure 2, are about 6 m long, 103.38 mm in diameter and 4 mm in wall thickness. Each pressure tube contains a string of twelve 37-rod fuel bundles stacked end to end. The rods are each 13.08 mm in diameter and ar-

ranged in a compact pattern. As shown in figure 3 this arrangement contains three main types of rod subchannels, namely 'wall' subchannels, 'square' subchannels and 'triangular' subchannels.

Fuel bundle rods are known to vibrate. Vibration or thermal distortion might displace a rod, especially misaligned or bent ones towards another rod or towards the wall. As a result of this displacement the thermalhydraulic performance of the fuel bundle might change, since both the heat transfer from the rod and the diffusion of heat in subchannels in the rod's vicinity would differ from those at the design condition. In order to predict this effect, it is necessary to study the flow and heat transfer characteristics in various rod-rod and rod-wall gaps. The objective of the present research is to collect information on the structure of turbulent flow in wall subchannels and triangular subchannels with varying rod-wall proximities in a geometrically similar, approximately 12.9 upscale model of the 37 rod CANDU reactor fuel bundle. This information which includes the measurement of turbulent characteristics, will lead to predictions of heat transfer from rod surface and heat diffusion in the flow, which is a major concern in rod bundle design. Due to its large size this model permitted the insertion of probes into subchannels without much disturbance to the flow. The model flow Reynolds number (based on the wall subchannel hydraulic diameter and bulk velocity) was 74000, substantially lower than the Reynolds number in the fuel reactor, which was 452000; however, since both Reynolds numbers correspond to fully turbulent subchannel flow, the Reynolds number effect on the turbulent characteristics and heat transfer is expected to be small (Trupp and Azad, 1975). The Mach number in the duct was kept below 0.06 so that the flow could be treated as incompressible, and since the model was designed to be geometrically similar to the actual bundle,

weak dynamic similarity between the model and reactor flows can be reasonably assumed.

The design of the model was such that one rod, centrally located could be moved radially and azimuthally, resulting in changes of the shape and size of the rod-rod and rod-wall subchannels. The central rod could also be slanted both towards the wall and towards another rod.

The experimental work was carried out in two stages. The first stage covers the measurement of wall shear stress, which can be related to the rate of heat transfer from the rod surface, while the second stage involves the measurement of turbulence parameters, which provide a measure of diffusion of heat in various subchannels as the size and shape of the subchannel change. In the wall shear stress measurements the effects of both rod-rod gap and rod-wall gap on the wall shear stress distribution were examined, including a case in which the rod is in contact with both another rod and wall. Mean flow and turbulence parameters were measured at four positions of the central rod, namely the design position, cases with small rod-wall gap, rod-wall contact and rod-rod-wall contact.

The detailed information on the turbulent flow structure in the wall subchannel at the four rod positions could be used to estimate how heat transfer from the rod surface and diffusion of heat in the wall subchannel is affected by the changing of the wall subchannel shape and size. A future extension of this program will provide direct measurements of heat transfer and diffusion by locally heating the rod surface.

Chapter 2

LITERATURE REVIEW

Current fuel bundle designs are based on a heat transfer and subchannel mixing technology derived from a multitude of full-scale and model experiments. These include a few thorough investigations of the turbulent flow structure in rod subchannels. Figure 4 presents division of a rod bundle flow channel into subchannels. Subchannels bounded by at least one wall are called wall subchannels while the ones bounded by rods only are termed inner subchannels. Inner subchannels are characterized by the distance between two adjacent rod centers, called pitch (P), wall subchannels are characterized by the width (W), defined as the diameter (D) of the rod plus the rod-wall gap. The literature review presented in subsequent sections is devoted solely to turbulent structure in rod bundles.

2.1 Experiments on Inner Triangular Subchannels

Eifler and Nijsing [1967] used the triangular array shown in figure 5a to investigate the effects of Reynolds number and rod spacing. They reported that the velocity distribution was compatible with the universal law of the wall and that the main parameter affecting rod bundle subchannel flow was the rod spacing while Reynolds number effect was weak.

Shown in figure 5b is a cross-section of the flow facility used by Kjellstrom

[1974]. He conducted measurements in the central subchannel as indicated in the figure and reported that friction factor in rod subchannels was higher than those predicted for smooth pipes and that the magnitude of secondary flows was about 1% of the average axial velocity. Although Kjellstrom actually detected secondary flows when the pitch to diameter ratio was P/D= 1.217 he could not reach any quantitative conclusions, because of the large scatter of data. He was the first to present Reynolds shear stresses and he also noticed double circulation loops within flow cells using his measured distribution of the wall shear stress combined with a theoretical method proposed by Eifler and Nijsing [1967].

Trupp and Azad [1975] conducted experiments in the rod bundle geometry shown in figure 5c for three tube spacings (P/D=1.20, 1.35, and 1.50) for the Reynolds number range from 12000 to 84000. They reported that the mean axial velocities, the normal stresses and the shear stresses were generally symmetric about the subchannel boundary and subchannel centerline to within a few percent. But for constant distance from the rod surface, correlation coefficients were antisymmetric with respect to these lines in adjoining primary flow cells. This was attributed to the facts that the secondary flow cells were counter-rotating in adjacent primary flow cells and that more than one cell of secondary flow may have existed in each section of the subchannel. Friction factors for all the tests they experimented with were higher than for flow through smooth pipes at the same Reynolds number. They also noticed that local wall shear stresses did not increase monotonically from the position facing rod-rod gap to that facing subchannel centerline as predicted by computational schemes using universal velocity distribution and ignoring secondary flows. This gave a clear indication of the presence and effects of secondary flows, which transport turbulent kinetic energy to

the core region from regions relatively nearer to the wall where turbulent energy levels are higher. The decrease in turbulent kinetic energy from the core region towards the gap would correspond to the inward turning of the secondary currents towards the wall. They then concluded that for homogeneous subchannels, the high mixing rates observed in practice are undoubtedly due in large part to secondary flows, and that enthalpy transfer between subchannels should readily occur due to transfer of thermal energy by the secondary flow cells at the gaps as they flow parallel to each other in thermal communication and are mixed by turbulent diffusion.

Figure 5d is a rod bundle cross-section design due to Rogers and Tahir [1975]. They conducted their experiment with a fixed P/D = 1.40 and Reynolds number ranging from 8100 to 50000. Tahir and Rogers [1979] conducted a more detailed experiment with P/D=1.06 at Reynolds number of 36000. In 1975 they reported that secondary flows, and other macroscopic flow effects, assist turbulent interchange by reducing the mixing distance. In 1979 they reported that the differences between the predictions of the analytical models and those of empirical correlations can be attributed mainly to the effects of secondary flows. Rogers and Tahir [1986] reported that eddy viscosities were highly anisotropic; and in their analysis they stated that secondary flows assist turbulent interchange by reducing the mixing distance as P/D decreases and that the same secondary flows increase the gradients of temperature, velocity and turbulent stresses across the gap.

2.2 Experiments on Wall Subchannels

All known experiments have been conducted on subchannels between a parallel array of rods and a wall. Rehme [1973-1987] conducted several experiments

using a model shown in figure 6a with P/D and W/D varied from 1.07 to 1.40 and 1.045 to 1.252 respectively, and Reynolds number ranging from 60000 to 200000. He defined angular positions from the line joining centerlines of adjacent rods as shown in figure 5a. He reported that the circumferential shear stress was negative for circumferential positions with $\phi < 40^0$, zero at about $\phi = 40^0$, and positive for $\phi > 40^0$; this stress was a maximum at about $\phi = 60^0$ and approached zero again at a position very close to $\phi = 90^0$, confirming the vanishing of the circumferential shear stresses at the symmetry line. Rehme [1987] reported that the eddy viscosity normal to the wall was almost independent of the position of the wall while the one parallel to the wall strongly depended on the position in the cross-section and reached a high value in the gap region. The eddy viscosity values first increased with increasing distance from the wall to a maximum and decreased slightly when approaching the line of maximum velocity. In the same paper he reported that cyclic momentum exchange process by pulsating flow between subchannels as assumed by Rowe et al [1974] is the reason for the increased levels of axial and azimuthal turbulence intensities in the open gap areas of rod bundle flows and for the high levels of Reynolds stress parallel to the walls.

Hooper [1983] conducted experiments in a wall subchannel of rectangular array of 2 by 3 rods and reported that the spatial extent of the high correlation coefficients for both the axial and transverse turbulent velocity components and the auto- and cross-correlation functions computed for the rod gap region support the existence and demonstrate the extent of the periodic intersubchannel momentum exchange process for the wall subchannel test section. He was the first researcher to measure all components of Reynolds stresses, including the correlation between the two transverse velocity fluctuations; his results for P/D=1.107 show that the

later may become significant in the gap region.

2.3 Experiments on Inner Square Subchannels

Tavoularis et al.[1986, 1988] conducted experiments in a square subchannel of 2:1 upscale model of a CANDU reactor shown in figure 6b. They have reported that both mean axial velocity and local wall shear stress exhibited a systematic variation with maxima corresponding to the open flow region and minima near the rod gaps. A similar report is given by Abdelghany and Eichhorn [1986], for the geometry shown in figure 6e. They also noted that the turbulent kinetic energy dissipation rate was typically large at high shear regions and lower near subchannel centers, where production of turbulent kinetic energy by mean shear was small. The eddy viscosity was typically one or two orders of magnitude larger than the kinematic viscosity; and the measured eddy viscosity distribution was compatible with those predicted by Eifler and Nijsing [1967].

Results of experimental work performed by Rowe et al.[1974] using a model facility with a cross-section shown in figure 6c with P/D=1.25 and 1.125 show that the turbulence intensity in the axial direction had a relative maximum on the center line between subchannel centers and the rod gap at about 15^0 to 20^0 from the gap. This relative maximum was found to be high at low P/D. They also reported that autocorrelation functions had in general exponential decay with little or no evidence of dominant periodic behaviour; however, some of the autocorrelation functions obtained in certain regions of the flow channel at the smaller rod gap spacing did show definite periodic behaviour. According to their measurements this periodic behaviour was limited to the region between the subchannel center and rod gap where there was also evidence of secondary flows. Similar periodic

behaviour of autocorrelation was also reported by Tavoularis et al. [1986] and Hooper [1983]. From their results it can be concluded that the reduction of rod gap spacing might lead to measurable periodic flow pulsations in the regions adjacent to the rod gap. This together with secondary flows, increased turbulence intensity and increased integral length scale indicate an enhancement of cross-flow mixing to help compensate for a decrease in rod gap spacing. Their data suggest that the lateral freedom of the open array allows rather large turbulence structures to move through the gap with relative ease. Their data also indicate that the eddy diffusivity estimates cannot be based on pipe data alone, because diffusion in bundles is augmented by macroscopic flow processes. These additional macroscopic pulsations aid the mixing process in the same manner as do the secondary flow effects and may be thought of as also serving to reduce the mixing distance at low P/D.

Creer et al. [1979] conducted their research in a square subchannel shown in figure 6d at Reynolds number of 58000 with blockages which created area reduction in flow area of 70 and 90%. They reported that their results indicated that extensive flow disturbances existed downstream from the blockage clusters but only minor ones upstream of the blockages. They also reported that recirculation zones for both 70 and 90% blockages were detected downstream from the blockage clusters and persisted for approximately three to five hydraulic diameters.

2.4 Computational Studies

Eifler and Nijsing [1967] have developed a computer code, called VELASCO, which has been used to predict turbulence structure in rod bundles. Another code, called COBRA, has been used by Rowe et al. [1974]. These codes neglect the effect

of secondary flows although such effects on turbulence structure as well as on the distribution of mean velocity and wall shear stress can be significant.

Carajilescov and Todreas [1976] used a one-equation model in the prediction of turbulence kinetic energy, fluctuating rms velocities and mean local velocity. They compared their predictions with their experimental data obtained with the use of Laser Doppler Anemometry and other data from previous experimental studies. The predicted velocity distribution was in close agreement with the experimental data while there were discrepancies in the wall shear stress distribution. According to them those discrepancies were due to the presence of secondary flows which, according to them was weak near the gaps and strong in the open flow areas, and tended to homogenize the wall shear stress distribution in the open flow area.

Kaisser and Zeggel [1987] developed a computer model based on anisotropic eddy viscosities. This model, in contrast to the one-equation model, needed neither iteration nor the solution of additional differential equations. Their results compared very well with those of VELASCO. They also suggested that, instead of using their empirical turbulence model, it would be possible to apply more complex models like one or two equation models, for an improved prediction of the turbulence structure.

Chapter 3

DEFINITIONS

AND

BACKGROUND INFORMATION

3.1 Hydraulic Diameter and Its Applications

A great deal of experimental and theoretical research concerning turbulent flow and heat transfer in channels has been performed on circular pipe flows, where the obvious characteristic length is the diameter of the pipe. As a result, a significant amount of information is known about both the velocity and temperature fields in circular pipe flows. A common simplification in studies of fluid flows and heat transfer through channels of non-circular cross-sectional areas is to consider a circular pipe flow with comparable flow characteristics. The diameter of such a pipe is called hydraulic diameter, and is normally defined as four times the channel cross-sectional area divided by its wetted perimeter.

Experiments in laminar and turbulent flows have shown that the use of the hydraulic diameter in evaluating non-dimensional numbers like Reynolds and Nusselt numbers results in a good approximate correlation between the gross flow characteristics in channels of various cross-sectional shapes and in circular ones. Ob-

viously this approach can not describe peripheral variation of various parameters like wall shear stress and friction factor, as it can only provide a rough estimate of the average variation of such parameters along the channel. However, such a description may be useful as a reference for comparisons with measurements in the actual geometry.

It has been established that the velocity distribution in the vicinity of the channel wall is essentially independent of the shape of the channel cross-section. In rod bundle flows, the flow through individual subchannels depends primarily on the local flow conditions. Thus, by using a hydraulic diameter for each subchannel and local flow conditions, one could evaluate the friction factor, Reynolds number, Nusselt number and intensities and scales for each subchannel based on relations developed for circular pipe flows.

For the 37-element rod bundle, shown in figure 3, the hydraulic diameter is given by

$$D_h = \frac{\pi(4R^2 - 37D^2)}{2\pi R + 37\pi D} \qquad (3-1)$$

where R is the radius of the pressure tube and D is the diameter of the rods. The hydraulic diameter of the present model (figure 7) which includes only a cluster of 5 rods and has additional flat walls is

$$D_{h_m} = \frac{4(\frac{\pi}{6}R^2 - \frac{1}{2}(R_1 + D)^2 \cos\frac{\pi}{6} - \frac{5\pi D^2}{4} - (\frac{2\pi R_3 - 18D}{18})(R - (R_1 + D)))}{\frac{\pi}{6}R - 2(\frac{2\pi R_3 - 18D}{18}) + (R_2 - D) + 2(R - (R_2 - D)) + 5\pi D} \qquad (3-2)$$

The hydraulic diameter of the subchannels between two outer rods and the pressure tube wall for the design conditions is

$$d_{h_o} = \frac{4(\frac{\pi}{18}R^2 - \frac{\pi}{18}R_3^2 - \frac{97\pi}{720}D^2)}{\frac{\pi R}{9} + \frac{97\pi D}{180}} \qquad (3-3)$$

where R_1 , R_2 and R_3 are the corresponding radii at the centers of the inner, middle and outer bundle rods. Finally the hydraulic diameter of the two inner,

triangular subchannels (Figure 7) are

$$d_{h_1} = \frac{0.51(2R_2 sin\frac{\pi}{12})(2R_3 sin\frac{\pi}{18})}{\pi D} \qquad (3-4)$$

$$d_{h_2} = \frac{0.69(2R_2 sin\frac{\pi}{12})^2}{\pi D} \qquad (3-5)$$

The subchannel hydraulic diameters obviously change when a rod is displaced from its design position. The nominal values for the present experiments are

$D_h = 95.4\text{mm}$

$D_{h_m} = 55.6\text{mm}$

$d_{h_o} = 88.5\text{mm}$

$d_{h_1} = 35.6\text{mm}$

$d_{h_2} = 48.8\text{mm}$

3.2 Mean Velocity and Bulk Velocity

For stationary turbulent flows, such as the present one, it is possible to define the statistical mean velocity $\overline{U}$ at any point in the flow as a time average

$$\overline{U} = \frac{1}{T}\int_0^T U dt \qquad (3-6)$$

where U is the instantaneous velocity at the point and T is the integral time large enough for the integral to converge.

The bulk velocity for incompressible flow perpendicular to an area A is defined as

$$U_b = \frac{1}{A}\int_A \overline{U} dA \qquad (3-7)$$

where dA is an element of area and A is the entire area of flow. The Reynolds

number for a non-circular channel flow can be defined as

$$Re_h = \frac{U_b D_h}{\nu} \qquad (3-8)$$

where ν is the kinematic viscosity of the fluid. According to this definition, Re_h might vary for different flow subchannels.

3.3 Wall Shear Stress and Friction Factor

Wall shear stress is the tangential force per unit area acting on an immersed surface in a direction opposite to the flow direction. For Newtonian fluids, the wall shear stress is related to the velocity gradient at the wall as

$$\tau_w = -\mu \frac{\partial \overline{U}}{\partial y}|_{y=0} \qquad (3-9)$$

where μ is the absolute (dynamic) viscosity of the fluid, and all quantities are considered to be local averages for turbulent flows. A related quantity is the local friction velocity, defined as

$$u_\tau = \sqrt{\frac{\tau_w}{\rho}} \qquad (3-10)$$

where ρ is the fluid density.

In fully developed, circular pipe flows, the pressure drop is related to the wall shear stress, which is constant around the pipe perimeter, as

$$\tau_w = -\frac{d}{4}\frac{dP}{dx} \qquad (3-11)$$

where d is the pipe diameter and x is the axial direction. In non-circular channel flows, the wall shear stress generally varies around the perimeter. As a result, the use of a hydraulic diameter in the above expression might lead to inaccurate predictions of the local wall shear stress. The wall shear stress can be presented

in dimensionless form as a friction factor (using Farning definition of the friction factor)

$$f = \frac{2\tau_w}{\rho U_b^2} \qquad (3-12)$$

For circular pipes the friction factor can be expressed in terms of the pressure gradient as

$$f_c = \frac{d}{2}\frac{\frac{-dP}{dx}}{\rho U_b^2} \qquad (3-13)$$

Ibragimov et al. [1967] has postulated that the friction factor for rod subchannels can be estimated from the one for circular pipes at the same Reynolds number as

$$\frac{f}{f_c} = (0.58 + 0.42e^{0.021g^3})(1.0 + 0.1(\beta+1)^{\frac{4}{3}}) \qquad (3-14)$$

where g is a geometrical factor calculated as

$$g = \frac{\hat{y}_{max} - \hat{y}_{min}}{\hat{y}_{av.}}\left(\frac{A_{FC}}{\hat{y}_{av.}^2}\right)^{0.25} \qquad (3-15)$$

and

$$\beta = \pm\frac{2\hat{y}_{av.}}{D} \qquad (3-16)$$

(+ for a convex surface, - for a concave surface).

Here, $\hat{y}$ is the distance from the wall to the section of maximum velocity, A_{FC} is the flow cell area, D is the rod diameter, and a flow cell is defined as a geometric subdivision of a subchannel.

As was noticed by Eifler and Nijsing [1967], the local friction factor cannot be easily determined from the local shear stress in rod bundle subchannel flows, because it involves the unknown local bulk velocity in an elementary area bounded by the wall element in question. Trupp and Azad [1975] suggested the use of an empirical expression, applicable to triangular subchannels, as

$$f = CRe^{-n} \qquad (3-17)$$

with the constants C and n depending on the subchannel shape as

$$C = 0.287(\frac{d_h}{D} - 0.30)^{-\frac{1}{2}} \qquad (3-18)$$

and

$$n = 0.368(P/D)^{-1.358} \qquad (3-19)$$

where P is the pitch, D is the rod diameter and d_h is the subchannel hydraulic diameter. These values were a result of least-square-fit to data in the range $10^4 \leq Re \leq 10^5$, $1.2 \leq P/D \leq 1.5$.

3.4 Velocity Distribution

Turbulent channel flows are customarily divided into two main regions, the wall region and the core region.

3.4.1 Wall region

In this region the local mean velocity depends only on local conditions. Its distribution can be expressed in dimensionless form as

$$u^+ = f(y^+) \qquad (3-20)$$

where

$$u^+ = \frac{\overline{U}}{u_\tau} \qquad (3-21)$$

and

$$y^+ = \frac{u_\tau y}{\nu} \qquad (3-22)$$

Equation (3-20) is known as the law of the wall and has been confirmed by many independent experiments. This wall region can be further subdivided into three subregions; the laminar, the buffer and the inertial sublayers.

The laminar sublayer is dominated by viscous shear stresses and it extends upto about $y^+ = 4$. In this region u^+ varies linearly with y^+, that is

$$u^+ = y^+, \quad 0 \leq y^+ < 4 \tag{3-23}$$

In the buffer sublayer the viscous shear stresses are of the same magnitude as the Reynolds stresses. This layer extends to $y^+ \approx 30 - 40$. McDGalbraith et al. [1977] postulated that the velocity profile in this region can be approximated by the relation

$$u^+ = 4.2 - 5.7 \ln y^+ + \frac{5.1}{(\ln y^+)^2} - 0.7(\ln y^+)^3, \quad 4 \leq y^+ < 30 \tag{3-24}$$

In the inertial sublayer, the flow is fully dominated by the Reynolds stresses. The velocity distribution is logarithmic, that is,

$$u^+ = A \log_{10} y^+ + B \tag{3-25}$$

Typical values of the constants A and B (Patel, 1965) are 5.45 and 5.5 respectively.

3.4.2 Core region

In this region, the velocity distribution depends on the channel cross-sectional shape. The region is sometimes called the velocity defect region or the wake region.

3.5 Secondary Flows

When a turbulent fluid flows within a straight non-circular duct, a transverse mean flow exists even when the flow is fully developed. This transverse flow, commonly known as the secondary flow, generates vortical motions superimposed upon the axial mean flow. Thus turbulent flow in a non-circular duct is of a

three dimensional nature even for the mean velocity field. This secondary flow consists of a motion of the core fluid to flow toward corner regions along the corner bisectors, then parallel to the walls and finally back into the core through the wider regions. Although the magnitude of the secondary flow is generally small (typically 1% of the bulk velocity), its presence displaces the mean isovels considerably toward the narrow regions, yielding a comparatively high velocity field there. The first explanation of this phenomenon was given by Prandtl in 1925, who suggested that the anisotropy of the cross planar (transverse) normal stresses is responsible for secondary flow generation. Prandtl postulated that the velocity fluctuations tangential to an isovel exceed those perpendicular to it so that a centrifugal acceleration is induced in the region of isovel curvature, driving the fluid radially outwards. A thorough description of the phenomenon was first given by Brundrett and Baines [1964] through hot wire measurements of all six Reynolds stress components in a square duct. Their results showed that the gradients in the cross planar Reynolds stress generate the streamwise vorticity and are fully responsible for secondary motion.

3.6 Turbulence Intensity and Kinetic Energy

Turbulence is a rotational and three dimensional time dependent random motion encountered in fluid flows. It always occur at large Reynolds number and it enhances mixing and kinetic energy dissipation. Due to its random nature, turbulence can only be described by statistical means.

Using Reynolds decomposition procedure (Reynolds, 1894) in a cylindrical coordinate system, the instantaneous axial, radial and azimuthal velocity compo-

nents U, U_r, U_ϕ can be decomposed into means and fluctuations as

$$U = \overline{U} + u, \quad U_r = \overline{U_r} + u_r, \quad U_\phi = \overline{U_\phi} + u_\phi \qquad (3-26)$$

where overbars denote averages and, by definition, $\overline{u} = \overline{u_r} = \overline{u_\phi} = 0$. The root mean square values of the velocity fluctuations are defined as

$$u' = \sqrt{\overline{u^2}}, \quad u'_r = \sqrt{\overline{u_r^2}}, \quad u'_\phi = \sqrt{\overline{u_\phi^2}} \qquad (3-27)$$

In flows with dominant axial velocity $\overline{U}$, the local intensity of turbulence is characterized by the ratios $u'/\overline{U}$, $u'_r/\overline{U}$ and $u'_\phi/\overline{U}$.

Finally the turbulence kinetic energy per unit mass is defined as

$$k = \frac{1}{2}(u'^2 + u'^2_r + u'^2_\phi) \qquad (3-28)$$

3.7 Reynolds Stresses

The Reynolds stress tensor, defined as $\begin{pmatrix} -\rho\overline{u^2} & -\rho\overline{uu_r} & -\rho\overline{uu_\phi} \\ -\rho\overline{u_r u} & -\rho\overline{u_r^2} & -\rho\overline{u_r u_\phi} \\ -\rho\overline{u_\phi u} & -\rho\overline{u_\phi u_r} & -\rho\overline{u_\phi^2} \end{pmatrix}$, can be interpreted as a set of additional stresses in the fluid due to a fluctuating velocity field. The Reynolds stress tensor is symmetric. The diagonal components $-\rho\overline{u^2}$, $-\rho\overline{u_r^2}$, $-\rho\overline{u_\phi^2}$ are called normal stresses and contribute little to the transport of mean momentum. The off-diagonal components are called shear stresses; they play a dominant role in the theory of mean momentum transfer by turbulent motion.

3.8 Correlation Coefficients

The correlation coefficient $R_{ij}(\tau)$ between the velocity fluctuations u_i and u_j

in the cartesian coordinate system (x_1, x_2, x_3) is defined as

$$R_{ij}(\tau) = \frac{\overline{u_i(t)u_j(t+\tau)}}{u_i' u_j'} \qquad (3-29)$$

where τ is the time delay. When $i = j$, $R_{ii}(\tau)$ is called the autocorrelation coefficient; when $i \neq j$, $R_{ij}(\tau)$ is called the cross-correlation coefficient. A similar definition would apply if the components u, u_r, and u_ϕ are used instead of u_i, $i = 1, 2, 3$.

3.9 Length Scales of Turbulence

Turbulent flow of fluids at high Reynolds numbers is characterized by several length scales, which assume specific roles in the description and analysis of the flow. These scales are bounded from above by the dimensions of the flow field and from below by the scales related to the dissipative activity of molecular motions.

3.9.1 Integral length scales

The characteristic size of the most energetic turbulent eddies is commonly measured by the Eulerian integral length scales, defined as the integrals of corresponding two-point, spatial correlation coefficients. In flows with a strong axial mean velocity and relatively low turbulent intensity, it is convenient to define the streamwise Eulerian integral time scales as

$$T_{ij} = \int_0^\infty R_{ij}(\tau) d\tau \qquad (3-30)$$

and, then, by employing the so called Taylor's 'frozen flow' approximation, to determine the streamwise Eulerian integral length scales as

$$L_{ij} = \overline{U} T_{ij} \qquad (3-31)$$

In practice, integration in equation (3-30) is carried up to the first zero of $R_{ij}(\tau)$ or to a point where $R_{ij}(\tau)$ is negligible.

3.9.2 Taylor microscales

The Taylor microscale is associated with the size of the eddies which are transferring energy to the smallest eddies which are mainly responsible for viscous dissipation. Its formal definition is in terms of the initial part of the isotropic two-point correlation function (e.g. Hinze, 1975). However, this scale can be also estimated from the variances of the velocity field and its spatial derivative as

$$\lambda_u = [\frac{\overline{u^2}}{\overline{(\frac{\partial u}{\partial x})^2}}]^{\frac{1}{2}} \qquad (3-32)$$

By Taylor approximation, the streamwise spatial derivative can be expressed in terms of the time derivative as

$$\frac{\partial u}{\partial x} = \frac{1}{\overline{U}} \frac{\partial u}{\partial t} \qquad (3-33)$$

Consequently, the Taylor microscale can be estimated as

$$\lambda_u = \overline{U}[\frac{\overline{u^2}}{\overline{(\frac{\partial u}{\partial t})^2}}]^{\frac{1}{2}} \qquad (3-34)$$

Taylor's microscales are larger than the scales relevant to dissipation of kinetic energy into heat, however, they are useful among others, in the estimation of the turbulent kinetic energy dissipation rate, ϵ, since in isotropic turbulence

$$\epsilon = 15\nu(\overline{\frac{\partial u}{\partial x}})^2 = 15\nu(\frac{\overline{u^2}}{\lambda_u^2}) \qquad (3-35)$$

Equation (3-35) is known to provide reasonable estimates of ϵ even in some non-isotropic flows (see, for example, Tavoularis and Corrsin, 1981) and will be used for estimating ϵ in the rod bundle flow.

3.9.3 Dissipation length scale

According to the Kolmogoroff's [1941] hypothesis, the characteristic size η of the smallest eddies of relevance to turbulence dynamics associated with viscous dissipation depends only on the dissipation rate of kinetic energy per unit mass, ϵ, and the kinematic viscosity, ν. By dimensional analysis, it is possible to define the 'Kolmogoroff' microscale as

$$\eta = (\frac{\nu^3}{\epsilon})^{\frac{1}{4}} \qquad (3-36)$$

As the Reynolds number of the turbulence increases, the energy-containing and the energy dissipating eddies are more widely separated and the smaller eddies come into a state of statistical equilibrium. As the energy is passed on, information is being lost so that eventually, at large Reynolds number values, the small-scale structure tends to be independent of the initial conditions and the source of the turbulence energy. At length scales much smaller than the size of the energy containing eddies but also much larger than η the turbulence tends to be isotropic and there is a balance between the energy fed in from the larger eddies and that taken out to the smallest eddies. This is called the inertial subrange of the turbulent energy spectrum.

3.10 Turbulence Viscosity

The statistical formulation of turbulent flows leads to an open hierarchy of equations, namely a set of equations with more unknowns than the number of independent equations. At the lowest level, this involves the equations for the

mean velocity, which also include the Reynolds stresses. One of the most widely used 'closure' approximations is to relate the Reynolds stresses to the mean field gradients by so called gradient transport relationship. This implies an analogy between the Reynolds stresses in the equations of motion and the viscous stresses due to molecular motions by assuming that the Reynolds stresses, like the viscous stresses, are directly proportional to the velocity gradient. This assumption was first made by Boussinesq (1877), who introduced the concept of an 'apparent' or 'turbulence' or 'eddy' viscosity ϵ_m. A more complete formulation should relate the second-order turbulence stress tensor to the second-order rate of deformation tensor through a fourth-order eddy viscosity tensor. Instead of dealing with the extremely complex, tensor forms of the above parameters, it is customary to consider only the components of interest, namely those corresponding to dominant velocity gradients. With respect to a cylindrical coordinate system, centered on a rod axis in a fully developed rod-bundle flow, with u, u_r and u_ϕ representing axial, radial and azimuthal velocity fluctuations, one would be interested in two turbulent viscosities, namely the radial and the azimuthal ones, defined as

$$\epsilon_r = -\overline{uu_r}/(\frac{\partial \overline{U}}{\partial r}) \qquad (3-37)$$

and

$$\epsilon_\phi = -\overline{uu_\phi}/(\frac{1}{r}(\frac{\partial \overline{U}}{\partial \phi})) \qquad (3-38)$$

Chapter 4

FLOW FACILITY

AND

INSTRUMENTATION

4.1 Flow Facility

The flow facility was a model of an outer segment of the 37-rod fuel bundle of the CANDU reactor, nominally 12.9 times larger than the actual one. It consisted of five circular pipes, arranged in a quasi-trapezoidal duct with a circular arc top, as shown in figure 7. The duct was made of aluminium sheets except at the working section near the exit, in which the top cover was made of lexan to enable visibility of the probes from the outside. The duct was 6.10 m long, 390 mm high at the center, with a trapezoidal base length of 297 mm, a trapezoidal side length of 360 mm and an arc length of 687 mm. Five aluminium pipes with a nominal diameter of 168 mm and thickness of 3 mm were installed in the duct as shown in figure 8. The four pipes were held fixed on the duct walls, while the fifth was suspended at both ends in such a way that it could be traversed within the duct. The pipes were fitted with paraboloid wooden blocks at the inlet end in order to facilitate smooth flow transition from the plenum chamber into the duct. Circular rings were attached to each block in order to act as boundary layer trips and thus

to enhance the full-development of flow in the subchannels.

The duct was set up as an open-discharge wind tunnel, shown in figure 8. The flow intake box was equipped with baffles and lined with convoluted foam, which reduced the acoustic noise considerably. The intake was also equipped with fiberglass air filters for dust removal as required for hot wire operation. The flow was produced by a centrifugal fan, positioned after the intake box and driven by an electric motor, rated at 5HP, 3440 rpm. To achieve even distribution of air flow, a pressure box was installed between the fan outlet and the duct inlet. The contraction ratio (namely the ratio of the pressure box cross-sectional to the duct open area) was 5.6.

The movable rod could be traversed horizontally and vertically with an accuracy of 1 mm as well as rotated by 360^0 about its axis. At the design condition the clearance between the outer rods was nominally 25.0 mm while that between the outer rods and the wall was nominally 25.4 mm. With these clearances it was possible to insert miniature probes into the flow without appreciable disturbance to the flow field.

The flow facility was designed such that the length to diameter ratio, L/D for the model was about the same as that of the actual reactor tube. The scale ratio of 12.9 was based on the ratio of the available aluminium pipe diameter to bundle rod diameter. Due to eccentricity and imperfection of construction, the rod-wall gap varied between 25.0 mm and 25.4 mm and the rod-rod gap varied between 24.2 mm and 24.8 mm. These measurements scaled down to the actual bundle size would give a rod-wall gap range of 1.98 mm to 2.01 mm instead of 2.01 mm and rod-rod gap range of 1.88 mm to 1.93 mm instead of 1.98 mm.

All measurements were taken at a position 65 hydraulic diameters downstream from the flow entry. The probes were inserted into the flow from the exit end of the duct. Probe mounting and traversing systems were designed and constructed locally in the departmental workshop. They permitted accurate traversing of pressure tubes and hot wire probes within the subchannels surrounding the central rod with an accuracy of 0.5 mm. The traversing system with the probe mounting, shown in figure 9, could be traversed manually azimuthally. Probes (pressure tubes and hot wires) held by the mount were traversed radially in the entire test section.The design of the mount ensured proper alignment of the probe axis with the flow direction and also a smooth traversing.

4.2 Pressure and Wall Shear Stress Instrumentation

Wall static pressure can be measured by using infinitesimally small, clean, burr-free, square-edged surface holes with their axes perpendicular to the surface. Because it is difficult to machine such holes and because their response to pressure changes is very slow, a somewhat different approach was followed in the present research. Thin hollow tubes of 0.406 mm internal diameter and 0.711 mm external diameter were each glued inside holes of 0.764 mm diameter drilled perpendicularly to the rod surface. The tube protrusions were filed with fine sand paper such that there were no protrusions or depressions near the holes.

Static pressure measurements were carried out at the working section utilizing both pressure holes on the rod surface and static pressure tubes inserted in the flow. Eight identical surface pressure holes were positioned along the circumference of the central rod as shown in figure 10. The static pressure tube (shown together with a total pressure tube in figure 11) had an outer diameter of 1.3 mm and 2

equidistant hole-pairs with 0.572 mm diameter. The miniature pitot-static tube (figure 12) used for the measurement of the flow velocity had an outer diameter of 2mm, 4 equidistant static holes of 0.343 mm diameter and a pitot hole diameter of 0.45 mm.

Measurements of wall shear stress were conducted with the use of the Preston tube technique (Preston, 1954), by applying the analysis due to Patel [1965], which accounts for possible errors due to flow displacement. Two Preston tubes of inner diameters 0.41 and 0.91 mm, and inner to outer diameter ratios of 0.57 and 0.61 respectively (figure 13) were separately used in conjunction with the surface pressure holes as shown in figure 14. Statistical analysis of the difference in wall shear stress readings obtained by the two Preston tubes gave nearly zero mean difference with standard deviation ranging between 4 and 9% of the average wall shear stress. This indicated that the difference was most likely non-systematic and that the two tubes had comparable accuracies for the wall shear stress measurement. Therefore the reported measurements of the wall shear stress were conducted using the larger Preston tube, which had a shorter settling time. The wall shear stress at circumferential positions between consecutive holes was measured by rotating the central rod up to 15^0. A Validyne DP 108 variable reluctance, diaphragm type, pressure transducer was used for the measurement of all pressures. It was connected to a TSI 1076 integrating voltmeter with a time constant selectable at 0.1, 1.0, 10, or 100 seconds. The voltmeter readings were taken with an accuracy of 1 mV. Figure 15 shows a calibration curve of the pressure transducer against a liquid manometer of known manometric fluid.

4.3 Hot Wire Instrumentation

Both single and cross-wire probes were available for the measurement of mean velocity and turbulent parameters. Although the single wire (TSI model 1264 BJW) was used for preliminary measurements, most of the results reported here were obtained with the cross-wire probe (TSI model 1248BJ - T 1.5) shown in figure 16, which is capable of resolving simultaneously two orthogonal velocity components. Each probe consisted of two thin cylindrical sensors, 1 mm long, 0.5 mm apart and 5 μm in diameter which were at right angles to each other and at 45^0 with the probe axis.

The hot wires were operated by two TSI 1050 constant temperature anemometer modules powered by a TSI 1050 2D monitor and power supply.

4.4 Signal Conditioning

The anemometer output signals were monitored in the D - 13 CRT display unit of a Tektronix 5113 dual beam storage oscilloscope. Two 5A22N differential amplifiers in the oscilloscope were used for amplifying and conditioning the signals. The amplifiers were equipped with low-pass filters having a selectable cut-off frequency between 0.1 kHz and 1 MHz in a 7 step, 1-3-10 sequence and with high-pass filters with selectable cut-off frequency between DC and 10 kHz in a 7 step 1-10-100 sequence, both with slopes of 3db per octave. The available amplifier gains ranged from 0.1 to 50000 in an 18 step, 1-2-5 sequence. The DC offset range could be set to $\pm$ 0.5 V or $\pm$ 50 V depending on the gains used. The 5B10N time

base of the amplifier, used to change the width of the display, had sweep rates from 1μs/div to 5s/div in a 21 step, 1-2-5 sequence.

Two identical home-made, fourth-order Butterworth type, low-pass filters with cut-off frequencies of 1, 3, and 10 kHz, gain of 0.5, 1, 2, 5, 10 and 50, and DC offset of upto $\pm$7 volts were also available. The filters were powered by a 15 volt DC supply unit. The signal outputs from the anemometer were fed into the filters and then into the analog to digital (A/D) converter as shown in figure 17.

4.5 Signal Discretization and Processing

The amplified, conditioned signals were discretized and processed using a 2828 model of DT2821 series analog to digital (A/D) converter designed for low level inputs. The DT2821 series boards contain an on-board programmable pacer clock which can be used to provide clock pulses to control the rate of conversions for the board A/D subsystem. The pacer clock operates under the program control, and provides a usable range of 7.5μs (129 kHz) to 2 seconds (0.5Hz). Alternatively, an external clock selected to A/D conversion event. The DT2821 boards are high speed analog and digital I/O boards designed to be used with the IBM personal computer AT (PCAT) or compatible computer systems. The 2828 model used here had resolution of 12 bits, throughput rate of 100 kHz, maximum gain of 1 and 4 channels with an accuracy of 0.03%. A/D selection on the DT2821 series is accomplished using a unique RAM channel-gain list. The RAM channel gain list is 16-location memory space which allows any of the channels at any gain to be sampled in any sequence at the full throughput rate. It also permits the same channel to be sampled at different gains.

The package used in acquiring data is ATLAB which is a real-time software package for data translations IBM PCAT compatible DT2821 series of analog to digital I/O boards. The package contains libraries of routines designed to be called from Microsoft's Fortran, C, and Pascal, and operated under the personal computer disk operation system (PC DOS). The ATLAB allows the control of all the analog and digital I/O capabilities of the interface boards through operation-specific routines which greatly simplify the programing of the hardware interfaces. An error processing system checks for segment errors and generates an error report if any are detected. The A/D converter was used in conjunction with an IBM PCAT, which had high capacity 1.2 MB floppy disk drive, 20 MB hard disk capacity, combination hard disk drive and floppy disk drive control card. It is also equiped with 84-key adjustable keyboard, setup software socket for 8028S7 math coprocessor. The PCAT was accompanied with a monitor, printer and keyboard.

Chapter 5

EXPERIMENTAL TECHNIQUES

AND

ACCURACY

5.1 Methodology for Pressure Measurements

A miniature pitot-static tube was used in obtaining the dynamic pressure for the evaluation of mean velocity fields. Measurements were conducted in the entire working section by traversing the probe circumferentially at 10^0 intervals and radially at 2 to 4 mm intervals. The velocity at any point was evaluated according to Bernoulli's equation as

$$U = \sqrt{\frac{2(P_o - P)}{\rho}} \qquad (5-1)$$

where P_o is the total pressure, P is the static pressure and ρ is the flow density.

Inaccuracies of the pressure measurement can be caused by misalignment of the probe with the mean velocity direction, probe vibrations, fluid compressibility, shape of the tube nose, turbulence and wall proximity.

The effects of misalignment of the probe axis with the flow direction is more severe on static tubes than on total tubes. This error is expected to be less than 0.7% of the actual static pressure (Ower and Pankhurst. 1977). The downstream

body of the pitot-static tube was stiffened by insertion into a thicker, hollow tube in order to reduce bending due to its own weight and to minimize probe vibrations.

According to Macmillan [1957], interference of the tube with the flow becomes significant when the tube axis is closer to the wall than about three external diameters (or tube heights for flat tubes). The net effect is that the indicated velocity is higher than the actual one in the absence of the tube. Eifler and Nijsing [1967] modified Macmillan's [1957] numerical results for dual wall effect in bundle flows and found a maximum error of 7.5% of mean axial velocity for impact tube measurements in their minimum rod gaps which were about two times the tube diameter. In this experiment the rod gaps were at least ten tube diameters at the design conditions, hence dual effect was not expected to be significant except in the rod-rod or rod-wall contact cases. Errors for readings close to the wall were estimated to be approximately 2.2% of mean axial velocity at a distance of 2.5 mm, equal to two tube diameters.

Up to the present time, the understanding of turbulence effect on pressure tube readings is incomplete. Coupled with shear effects and other effects already mentioned, turbulence intensity effects are non-linear. Tavoularis [1986] reported that as a guide for the order-of-magnitude estimation of turbulence errors in the mean velocity measurement by pitot-static tubes, one can use the expression;

$$U = U_{ind}(1 + \frac{ck}{U^2})^{-\frac{1}{2}} \qquad (5-2)$$

where k is the mean square turbulent kinetic energy and the empirical coefficient c is between 0.3 (for very small turbulence scale compared to the tube diameter) and 2 (for very large turbulence scale). Following Goldstein [1936], the static pressure tube reads a pressure that is higher than the actual static pressure by

$\frac{1}{2}\rho[\frac{1}{2}(\overline{u_r^2} + \overline{u_\phi^2})]$; and the total pressure tube would read high by an amount equal to $\frac{1}{2}\rho(\overline{u^2} + \overline{u_r^2} + \overline{u_\phi^2})$. In this research the axial turbulence intensity was upto 10% of the local velocity, so the maximum error in static pressure tube reading would be 0.25% while that of the total pressure tube would be 1%. Although the measurements can be corrected by deploying equation (5-2), corrections will not be applied in view of the small error magnitudes and the uncertainty in the value of c.

5.2 Methodology for Wall Shear Stress Measurement

Reviews of the different methods available on the measurement of wall shear stress have been compiled by Winter [1977] and Hanratty and Campbell [1983]. In the present study, the Preston tube method, devised by Preston [1954], was utilized. In his method, the static pressure is measured by a surface pressure tap and the total pressure is measured by a thin, open tube resting on the surface close to the position of the surface pressure measurement. This total pressure tube is referred to as the Preston tube. Preston [1954] postulated that the difference in pressure, Δp, between the total pressure and static pressure is related to the wall shear stress, τ_w, the fluid properties and the diameter, d, of the tube, as

$$\frac{\Delta p d^2}{4\rho\nu^2} = F(\frac{\tau_w d^2}{4\rho\nu^2}) \qquad (5-3)$$

where the function F can be obtained by calibration in a circular pipe where the skin friction can be calculated from the pressure drop. Based on this calibration procedure, Preston [1954] proposed the following relationship

$$\log\frac{\tau_w d^2}{4\rho\nu^2} = -1.396 + \frac{7}{8}\log\frac{\Delta p d^2}{4\rho\nu^2} \qquad (5-4)$$

Although several authors questioned the accuracy of this technique, Head and

Rechenberg [1962] tested the method in both developed turbulent pipe flow and developing boundary layer flows and found it accurate. An improved procedure was developed by Patel [1965] who conducted experiments with 14 different size tubes with varying internal to external diameter ratios. Patel defined two parameters as

$$x^* = \log(\frac{\Delta p d^2}{4\rho\nu^2}) \qquad (5-5)$$

and

$$y^* = \log(\frac{\tau_w d^2}{4\rho\nu^2}) \qquad (5-6)$$

and proposed the universal relationship

$$y^* = \frac{1}{2}x^* + 0.037; \quad y^* < 1.5, \quad x^* < 2.926 \qquad (5-7)$$

$$y^* = 0.8287 - 0.1381x^* + 0.1437x^{*2} - 0.0060x^{*3}; \quad 1.5 < y^* < 3.5 \qquad (5-9)$$

$$x^* = y^* \log(1.95y^* + 4.10); \quad 3.5 < y^* < 5.3 \qquad (5-10)$$

In conclusion, the Preston tube technique appears to be reliable and well documented. Patel's [1965] procedure was used in the present analysis, since it is generally accepted as more accurate than other calibrations. An estimate of the error due to the static pressure taps can be made following the technique of Franklin and Wallace [1970]. For the maximum friction Reynolds number, $Re^* = u_\tau d_{hole}/\nu \approx 21.6$, this error was about 0.04% u_τ and therefore, was neglected. The Preston tubes were not positioned at exactly the same position as the surface pressure holes, in order to reduce flow distortions. Readings with the Preston tube at various positions within a distance of 6 mm from the surface pressure hole were scattered around a value with a standard deviation of 0.86% of the mean, which was considered negligible.

The readings of Preston tubes can also be affected by the vicinity of other walls due to possible deviations of the velocity distribution from the law of the wall, which is the basis for the wall shear stress calibration equations. Though Tahir and Rogers [1986] have reported that the law of the wall applies to rod gaps at least for $y^+ > 100$, deviation from the law of the wall is inevitable as the gap diminishes. In this present investigation the ratio of Preston tube diameter to gap at design conditions was 0.0625. Wall shear stress measurements are reported for positions where this ratio was less than 0.3, while the wall shear stress at rod contact positions was assumed to be zero.

5.3 Methodology for Turbulence Measurement

5.3.1 Working principle of hot wire anemometry

There are two types of hot wire anemometry: constant current anemometry (CCA) and constant temperature anemometry (CTA). In this research, CTA was used. CTA has a high frequency response due to the use of a high gain amplifier in a feedback circuit.

When a current is passed through a wire, heat is generated. In equilibrium this is balanced by heat losses (primarily convective) to the surroundings. For a wire immersed in a fluid flow, this convective heat transfer will change with a change in velocity. As a result of this, the wire temperature will change and eventually reach a new equilibrium, if the power input remains constant.

The electrical power dissipated on the wire is

$$E_w = I^2 R_w \qquad (5-11)$$

where I is the current through the wire and R_w is the wire resistance. For heat balance through the wire

$$\frac{dW}{dt} = E_w - H \qquad (5-12)$$

where W is thermal energy stored in the wire, that is $W = C_w T_w$ (C_w is the heat capacity of wire) and H is the rate of heat transfered to the surroundings. If the temperature of the wire is maintained constant by the feedback circuit, $\frac{dW}{dt} = 0$, so that

$$E_w = H \qquad (5-13)$$

Thus the heat transfer equation becomes

$$I^2 R_w = h A_w (T_w - T_f) \qquad (5-14)$$

where h is the heat transfer coefficient from the wire to the flow, A_w is the heat transfer area and T_f is the flow temperature. The anemometer provides an output voltage, E, equal to

$$E = I(R_w + R_{cable} + R_{lead}) \qquad (5-15)$$

where R_{cable} and R_{lead} are additional resistances. For constant T_w, R_w is also a constant. Then one can write equation (5-14) in the form

$$\frac{E^2}{(T_w - T_f)} = A' + B' U^n \qquad (5-16)$$

where A', B' and n are calibration constants. Further considering cases with T_f constant, equation (5-16) can further simplify to

$$E^2 = A + B U^n \qquad (5-17)$$

Equation (5-17) is known as the modified King's law between the output voltage of a single sensor and the velocity of the surrounding fluid. The constants A, B

and n are to be determined by calibration in a flow with constant temperature T_f, equal to that during measurement.

5.3.2 Calibration and response of cross wire

To measure turbulence characteristics with hot wire anemometry, the cold resistance of the wire was measured at the ambient temperature. Then the resistance of the wire was adjusted to that of the operating temperature, using an overheat ratio of 1.7. The wire frequency response was optimized using the standard square wave test under typical flow conditions. As the velocity of the flow changes, a feedback servosystem senses any imbalance of the bridge in the anemometer, caused by the change in velocity and keeps the resistance of the wire constant by continuously adjusting the current through the wire. The output of the anemometer is a voltage proportional to this current.

Each sensor was calibrated separately against a pitot-static tube in a uniform flow produced by a calibration jet. Both the wire and pitot-static tube were placed at the exit of the jet, and the temperature of the jet was noted. Calibration constants A and B of equation (5-17) were adjusted to that of the flow temperature.

For the turbulence levels encountered in this flow, the effective yaw of the probe was always less than 10^0; hence the angular sensitivities of each wire were practically constant and approximately equal. The conversion of the voltages to velocity for the cross wire probe, with two mutually perpendicular sensors set at $\pm 45^0$ to the main flow (figure 16) was based on the following analysis.

Neglecting convection parallel to the sensors, the effective cooling velocities, that is, the equivalent velocities normal to the two sensors that would produce the

same cooling, can be written as

$$U_{eff1} = (U + U_r)cos45^0 \qquad (5-18)$$

$$U_{eff2} = (U - U_r)cos45^0 \qquad (5-19)$$

where U is the instantaneous velocity component in the streamwise direction and U_r is the instantaneous transverse velocity component. The effective cooling velocities were computed from the voltages E_1 and E_2 as

$$U_{eff1} = (\frac{E_1^2 - A_1}{B_1})^{\frac{1}{n_1}} \qquad (5-20)$$

and

$$U_{eff2} = (\frac{E_2^2 - A_2}{B_2})^{\frac{1}{n_2}} \qquad (5-21)$$

Typical calibration curves are shown in figure 18 together with the calibration constants. Then, the actual instantaneous velocity components U and U_r were calculated for each measurement by solving the linear system of equations (5-18) and (5-19).

5.3.3 Determination of the turbulent shear stresses

Two of the three turbulent shear stresses, namely, $-\rho\overline{uu_r}$ in the radial plane parallel to the duct axis and $-\rho\overline{uu_\phi}$ in the circumferential plane parallel to the duct axis can be measured directly. The remaining Reynolds stress $-\rho\overline{u_r u_\phi}$ can be determined by measuring the Reynolds stresses in a plane inclined at an angle θ to the plane parallel to the duct axis. By rotating the system of coordinates about the duct axis the Reynolds stress tensor can be transformed according to the following law,

$$\overline{u_i u_j} = \overline{u_k u_l} e_{ik} e_{jl} \qquad (5-22)$$

where $\overline{u_i u_j}$ and $\overline{u_k u_l}$ are the components of the tensor in the old and the new coordinate system respectively, and e_{ik} is the cosine of the angle between the i^{th} axis of the old coordinate system and the k^{th} axis of the new coordinate system. For the selected coordinate system e_{ij} can be written in matrix form as

$$e_{ij} = \begin{pmatrix} 1 & 0 & 0 \\ 0 & cos\theta & -sin\theta \\ 0 & sin\theta & cos\theta \end{pmatrix} \qquad (5-23)$$

Thus the analysis of equation (5-23) gives

$$\overline{u^2} = \overline{u_\theta^2} \qquad (5-24)$$

$$\overline{uu_r} = \overline{u_\theta u_{r_\theta}} cos\theta - \overline{u_\theta u_{\phi_\theta}} sin\theta \qquad (5-25)$$

$$\overline{uu_\phi} = \overline{u_\theta u_{\phi_\theta}} sin\theta + \overline{u_\theta u_{\phi_\theta}} cos\theta \qquad (5-26)$$

Further tensor analysis gives the lateral turbulence intensity and other components of the stress tensor as

$$\overline{u_r^2} = \overline{u_{r_\theta}^2} cos^2\theta + \overline{u_{\phi_\theta}^2} sin^2\theta - 2\overline{u_{r_\theta} u_{\phi_\theta}} sin\theta cos\theta \qquad (5-27)$$

$$\overline{u_\phi^2} = \overline{u_{r_\theta}^2} sin^2\theta + 2\overline{u_{r_\theta} u_{\phi_\theta}} cos\theta sin\theta + \overline{u_{\phi_\theta}^2} cos^2\theta \qquad (5-28)$$

$$\overline{u_r u_\phi} = \overline{u_{r_\theta}^2} cos\theta sin\theta \overline{u_{r_\theta} u_{\phi_\theta}} cos^2\theta - \overline{u_{r_\theta} u_{\phi_\theta}} sin^2\theta - \overline{u_{\phi_\theta}^2} sin\theta cos\theta \qquad (5-29)$$

From these three equations the third Reynolds shear stress $-\rho\overline{u_r u_\phi}$ was evaluated from the measurements.

5.3.4 Data acquisition

In this research the filter cut-off frequency was set at 10 kHz. Since the anemometer readings were between 2.8 and 4.2 volts, the DC offset was set at -3.5 volts and the gain used in the signal amplification was set at 10; this gave

a high resolution for the A/D converter which had a range of ±10 volts. In this particular research the ATLAB program used for data acquisition was ATLEX03 FORTRAN, modified to take 28000 points per buffer. The number of buffers used per record was 3 and the data was acquired at 36 kHz for two channels, that is, 18 kHz per channel. The ATLEX03 FORTRAN stored the data in the memory. These data were then copied to 1.2 MB floppy diskettes for analysis at a later time.

5.3.5 Error analysis for hot wire measurements

Temporal resolution

The temporal resolution of the measuring system can be determined by comparing the characteristic times of the hot wire and A/D conversion system with the characteristic times of the flow. A typical convection time (Corrsin, 1963) of the smallest relative motions (corresponding to viscous dissipation phenomena) in the current flow field was

$$(\frac{1}{\overline{U}})(\frac{\nu^3}{\epsilon})^{\frac{1}{4}} \approx 8.3\mu s$$

in both rod-wall gap and wall subchannel at design condition. The convective time in the wall subchannel at both rod-wall and rod-rod-wall contacts were respectively 10.4μs and 15.5μs. The typical convective time of the energy containing eddies, T_u was 2.5 ms near the rod surface and 3.7 ms in the open flow in all conditions tested except in the wall subchannel at the rod-rod-wall contact in which they were 2.0 ms and 3.0 ms respectively. Characteristic time for hot wire was

$$\frac{d_{sensor}}{U_b} = 0.36\mu s$$

while that for the data acquisition system (sampling time) was 55μs. Therefore,

phenomena associated with energy production and transfer within the inertial subrange of the energy spectrum would be detected, while the fastest, dissipative actions might be unresolved.

Spatial resolution

For a cylindrical hot wire, the spartial resolution is limited by the length of the wires and the distance between the sensors in the case of cross wire probe. The length and spacing of the sensors can be compared with the characteristic length scales of the flow. In the present study, the Eulerian integral length scales, $L_{11,1}$, $L_{22,1}$ and $L_{33,1}$ were between 10.0 mm and 80.0 mm, the Taylor microscale, λ_u, was between 1.4 mm and 3.6 mm while the Kolmogoroff microscale, η, was between 0.076 mm and 0.127 mm. In this study the sensors length, l_s, was approximately 1 mm and spacing, δ_s, was approximately 0.5 mm, so

$l_s/L_{11,1} = 0.0125$ to 0.1; $l_s/\lambda_u = 0.278$ to 0.714; $l_s/\eta = 7.87$ to 13.16; $\delta_s/L_{11,1} =$ 0.006 to 0.05; $\delta_s/\lambda_u = 0.139$ to 0.357; $\delta_s/\eta = 3.935$ to 6.58

The resulting errors in turbulence characteristics can be estimated from the above ratios assuming a likely turbulence structure. For example, the measurement error in $\overline{u^2}$ can be estimated as (Corrsin, 1963) $(\overline{u^2} - \overline{u^2_{measured}})/\overline{u^2} \approx l_s/(24\lambda_u^2) \approx$ 0.003 to 0.02. Thus the measurement error of the fluctuating velocity component in the streamwise direction was expected to be between 0.3% and 2% of the actual value.

Chapter 6

THE MEASUREMENTS

6.1 Preliminary Tests

A number of preliminary test measurements were carried out at approximately 34 rod diameters downstream from the duct entrance, using pitot, static and pitot-static tubes and a single hot wire probe. The temperature of the air was monitored with a thermometer during the experiment. Figure 19 shows a plot of temperature against time and it indicates that after about 60 minutes of operation, the duct flow temperature would stabilize. Thus all the readings were taken after the tunnel had run for at least 90 minutes. The flow rate through the duct was also found to be constant with time. This was verified with the use of a reference pressure tube inserted in the flow near the flat wall, which showed a constant reading throughout the experiment.

A major concern in the present experiments was whether the flow was fully developed at the measuring location. A series of velocity measurements were conducted at 4 downstream locations, that is, at x/D = 18.6, 23.2, 27.7 and 32.2 using a pitot-static tube inserted through the side wall. Measurements at x/D = 27.7 and 32.2 are nearly identical to that at the measuring location as shown in figure 20, indicating that the velocity field was developed at least for $x/D \geq 27.7$. The measured wall static and inflow static pressures presented in the

following sections also confirmed that the flow was fully developed.

6.2 Mean Static Pressure

Shown in figure 21 is the mean static pressure, averaged across different transverse planes for the design geometry. The pressure dropped along the duct continuously until it reached the atmospheric value at the duct exit. The pressure gradient, dP/dx, was practically constant in the downstream half of the duct and equal to about -5.63 Pa/m.

Shown in figure 22 is the variation of wall static pressure around the periphery of the central rod at x/D =34.24 for the design geometry. The pressure coefficient, C_{p_ϕ}, was defined as

$$C_{p_\phi} = \frac{\overline{P(\phi)} - \overline{P(0)}}{\frac{1}{2}\rho U_b^2} \qquad (6-1)$$

where $\overline{p(0)}$ is a reference pressure measured at $\phi = 0^0$. The static pressure around the periphery showed no significant variation.

Figure 23 presents the distribution of mean inflow static pressure along radial lines in the wall and inner subchannels as well as in the rod-wall and rod-rod gaps. The pressure coefficient in this case was defined as

$$C_{p_r} = \frac{\overline{P(r)} - \overline{P(0)}}{\frac{1}{2}\rho U_b^2} \qquad (6-2)$$

In all cases the pressure variation was very small, indicating that the pressure was nearly constant in the entire cross-section.

6.3 Wall Shear Stress

Detailed measurements of the wall shear stress around the periphery of the central rod were conducted for the design geometry as well as for several other cases with varying rod-wall and/or rod-rod proximities. As shown in figure 24 the difference between the values measured by the two different Preston tubes had a near zero mean and a non-systematic variation; therefore all reported measurements were conducted with the larger tube which had a faster response.

The measurements were normalised with the corresponding average wall shear stress, $\tau_{w_{av}}$, defined as

$$\tau_{w_{av}} = \frac{1}{2\pi}\int_0^{2\pi} \tau_w(\phi)d\phi \qquad (6-3)$$

The distributions of wall shear stress for different radial displacements of the central rod are shown in figures 25 (cartesian plot) and 26 (polar plot). These distributions have minima near narrow gaps and maxima in open flow regions. A reduction in W/D results in a decrease of τ_w in the rod-wall gap and an increase of τ_w in the open parts of the subchannels. Also the wall shear stress was found not to increase monotonically from the rod-wall gap towards the open flow regions. This trend has already been reported by Kjellstrom [1974], Trupp and Azad [1975] and Rehme [1978, 1980, 1982]. According to Trupp and Azad, this variation of wall shear stress is due to the influence of secondary flows, which are expected to be stronger at low W/D.

Presented in figure 27 are the variations of the maximum, average and minimum wall shear stress with W/D. These quantities change appreciably at values of

W/D close to 1 but relatively little at large W/D. As shown in figures 28, 29 and 30, the wall shear stress distributions for cases with the downstream end of the rod slanting towards the wall were similar but with milder variations, compared to corresponding cases of parallel rod displacement with the same W/D at the measuring station.

The distributions of wall shear stress with the central rod displaced towards a neighboring rod are presented in figures 31, 32 and 33, and those with the rod slanting towards a neighboring one are presented in figures 34, 35 and 36. As the rod-rod gap was narrowed, the wall shear stress decreased faster than when the rod-wall gap was narrowed. At both rod-rod and rod-wall contacts the stresses were zero at the points of contacts, but at wider gaps the stresses at rod-rod gap were greater than those at rod-wall gap, hence indicating a more dramatic increase in stresses at the rod-rod gap as compared to those in the rod-wall gap. The side of the rod that is exposed to the large open flow region is subjected to an increase in wall shear stress as the rod-rod gap is narrowed, though the increase is gradual tending to an asymptotic value. The surface of the rod facing inner subchannels does not experience much change in wall shear stress. The values in this subchannel when normalised with the average wall shear stress collapse. Thus it is possible to predict the wall shear stress distribution in this subchannel once the average wall shear stress is known. Again the plots of slanting cases give similar trends as the narrowing of the rod-rod gap and the average shear stress did not change much with varying rod-rod gap.

A case in which the central rod was in contact with both the wall and a neighboring rod was also investigated. As shown in figure 37 the distribution of wall shear stress in this case was similar to that of rod-wall contact from $\phi = 0^0$

to 60^0 and similar to that of rod-rod contact for the remainder of the rod surface. The rod-rod-wall contact had the minimum average wall shear stress. All the shear stresses presented in figure 37 were normalised by the average shear stress at the design condition.

6.4 Velocity Measurements

6.4.1 Mean axial velocity

Mean axial velocity distribution around rod periphery at 2 mm from the rod surface is shown in figure 38 while the distribution of the mean axial velocity in the radial direction is shown in figure 39. From figure 38 it is evident that higher velocity gradients near the rod surface occur at the position facing large open flow regions and lower velocity gradients occur at the gaps. This is consistent with the presence of high wall shear stresses at the open flow regions. Figure 39 indicates that the hot wire velocity measurements were conducted at $y^+ > 100$ and that the inner part of the wall layer was inaccessible with the present probes. Computation of the constants A and B using the universal law of the wall, equation (3-25) gave 5.19 and 4.5 respectively, which are close to Patel's respective values of 5.45 and 5.5.

Isovel contours for different positions of the central rod are shown in figures 40, 41, 42, and 43. In all cases, the local mean velocity was normalised with the maximum velocity indicated as $\overline{U_{max}}$ and occurring in the inner subchannel. Figure 40, corresponding to the design geometry, shows that the flow in the duct was symmetric and that the wall subchannel's maximum velocity was $87\%\overline{U_{max}}$. The contours bulge towards the narrow regions, a phenomenon which has also

been reported by Kjellstrom [1974], Trupp and Azad [1975], Rehme [1983] and Tahir and Rogers [1986].

As W/D decreased, the maximum velocity in the open channel decreased but the flow area having large velocity increased so that the flow rate through the test section did not change appreciably. The maximum velocity at the wall subchannel was 82%$\overline{U_{max}}$ at W/D=1.059, 80%$\overline{U_{max}}$ at rod-wall contact and 60%$\overline{U_{max}}$ at rod-rod-wall contact. Since both $\overline{U_{max}}$ and the relative maximum at the wall subchannel decreased as the size of the wall subchannel decreased the flow rate through the wall subchannel became lower as well. Graphical integration of the velocity readings at both design condition and rod-wall contact gave nearly the same discharge, thus indicating that the flow rate was nearly constant.

6.4.2 Secondary flows

Measurements of mean transverse velocity in this duct are not presented here because of the relatively large errors involved. However, such measurements indicate clearly that secondary flows exist and that their magnitude is up to 1% of the bulk velocity, which is comparable to values reported by Kjellstrom [1974] and Trupp and Azad[1975]. The magnitude of the secondary flows is higher in the wall subchannel for the cases of rod-wall and rod-rod-wall contacts. Secondary flows transport fluid towards the narrow regions and corners along bisectors of corner regions and then away from the corners and narrow gaps towards the main stream. By this movement, fluid with large mean axial velocity is transported towards the narrow regions and corners, causing the bulging of the mean axial velocity contours and non-monotonic variation of wall shear stress near the gaps and corners. Thus the presence of secondary flows in rod bundles enhances momentum and heat

transfer within the subchannel.

6.4.3 Axial turbulence intensity

Figures 44, 45, 46 and 47 presents contours of constant axial turbulence intensity, $u'/\overline{U}$, for four different central rod positions. In all cases the intensity was 6-7% near the centers of the subchannels and increased towards the rod and wall surfaces. It is noted that the turbulence intensity in the subchannel cores was higher than that of a fully developed pipe flow, which is 3.6% (Laufer, 1954). Comparable turbulence intensities in rod subchannels have been reported by Rehme[1982] and Tavoularis et al. [1988]. At design condition the contours are symmetric about the model axis. The minimum turbulence intensity in the wall subchannel does not change very much with the change in size of the subchannel. Like the mean isovels, the constant turbulent intensity contours bulge towards narrow regions and corners, a phenomenon attributed to the influence of secondary flows.

6.4.4 Radial turbulence intensity

Contour plots of radial turbulence intensity, $u_r'/\overline{U}$, for all four cases are in figures 48, 49, 50 and 51. The magnitude of the radial intensity is roughly half that of the axial intensity, reaching minima of 2.5 to 4% in the subchannel cores. The contours bulge towards the narrow gaps and corners just like the axial intensity ones. Changes in size of the wall subchannel have little effect on the radial intensity.

6.4.5 Azimuthal turbulence intensity

Contour plots for the azimuthal turbulence intensity, $u'_\phi/\overline{U}$, are presented in figures 52, 53, 54, and 55. Similarly to the other two intensities, minimum azimuthal intensity is observed in the subchannel centers where it is nearly identical to the radial one. There is a slight reduction in the intensity with decreasing wall subchannel size. This is due to the fact that the region for the circumferential motion is reduced.

6.5 Correlations

6.5.1 Reynolds stress and correlation coefficients

Figures 56, 57 and 58 present contour plots of the Reynolds shear stress $-\rho\overline{u_\phi u_r}$ at design, rod-wall contact and rod-rod-wall contact conditions. This shear stress is positive near the rod surface, it decreases to zero near the point of maximum velocity and then it becomes negative. Very close to the rod, the Reynolds shear stress is negligible compared to the viscous stress.

Another measured Reynolds shear stress, $-\rho\overline{u_\phi u_\phi}$, was generally of lower magnitude compared to $-\rho\overline{u_\phi u_r}$, except near the corners. At rod-rod-wall contact condition, $-\rho\overline{u_\phi u_r}$ was 0.2155 N/m^2 and $-\rho\overline{u_\phi u_\phi}$ was 0.0922 N/m^2 at r/R=0.048 and $\phi = 70^0$, while at the same radial position and $\phi = 90^0$, which is rod-rod corner, they were respectively $0.1654 N/m^2$ and 0.1764 N/m^2, though at rod-wall corner they were 0.124 N/m^2 and 0.037 N/m^2 respectively.

The third Reynolds shear stress, $-\rho\overline{u_r u_\phi}$, was estimated by first measuring turbulence parameters in an inclined plane as explaincd in section 5.3.3 and using equations (5-27), (5-28) and (5-29). It was found that this stress was significant with higher values near the rod surface and lower values at the subchannel center at both rod-wall and rod-rod-wall contacts condition, while at design condition the value was nearly constant. This shear stress, like $-\rho\overline{uu_\phi}$, had no systematic variation.

By normalizing Reynolds shear stress by the product of local rms velocities, the Reynolds shear stress can be presented as a correlation coefficient. The correlation coefficient, $\overline{uu_r}/u'u'_r$ had maximum value of about 0.4 to 0.5 which is comparable to the typical value of 0.4 in fully developed pipe flow and other shear flows. As can be seen in figure 59, this correlation coefficient decreased as the size of wall subchannel reduced. The correlation coefficient, $\overline{uu_\phi}/u'u'_\phi$, was lower than $\overline{uu_r}/u'u'_r$ except near the corners where u'_ϕ was minimal.

6.5.2 Turbulent kinetic energy

Presented in figures 60, 61, 62, and 63 are contours of the turbulent kinetic energy per unit mass evaluated using equation (3-28). In all cases the kinetic energy of turbulence decreased from high values near the rod surfaces to minima at the subchannel centers. The contour plots are nearly similar to those of the axial turbulence intensity. The turbulence kinetic energy levels at the wall subchannel decreased with the reduction in size of the wall subchannel. The minimum level at design was 1.0 m^2/s^2, at rod-wall contact was 0.6 m^2/s^2 and at rod-rod-wall contact was 0.2 m^2/s^2. At the same time the minimum value in the inner subchannel decreased from 1.0 m^2/s^2 at design condition to 0.8 m^2/s^2 at rod-wall and

rod-rod-wall contacts. Near the rod surface, the kinetic energy remained roughly constant except on the surface facing the wall subchannel where the kinetic energy decreased with decreasing size of the wall subchannel. Like the isovels, the kinetic energy contours bulge towards the narrow gaps and corners. This bulging might be due to the presence of secondary flows which convey high energy particles towards the gaps and corners (Trupp and Azad, 1975).

6.5.3 Autocorrelation coefficients

Autocorrelation coefficients $R_u(\tau)$, $R_{u_r}(\tau)$ and $R_{u_\phi}(\tau)$ at selected positions in the duct are presented in figures 64, 65, 66 and 67. In all cases the autocorrelation coefficients satisfied the relationship $R_u(\tau) > R_{u_r}(\tau)$, except perhaps at large separations where both curves had small amplitudes.

At design and W/D=1.059 conditions, $R_{u_\phi}(\tau) > R_u(\tau)$ at rod-wall gaps. In this position the movement of the azimuthal fluctuating velocity component, u_ϕ, was unobstructed hence it permits large scale motions to be correlated across the gap. The autocorrelation coefficients at other positions presented in the design and W/D=1.059 conditions approximate closely those which had been reported in two-dimensional duct flows (Comte-Bellot, 1965), pipe flows at half radius (Sabot et al., 1973) and uniformly sheared flows (Tavoularis and Corrsin, 1981).

At rod-wall contact condition, the autocorrelation coefficients at the rod-wall corner had a nearly exponential decay while those at wall subchannel near rod surface and rod-rod gap were close to those already reported in other flows mentioned above, however, those at the wall subchannel core depict behavior similar to those in rod-wall gap.

At rod-rod-wall contact the autocorrelation coefficients at rod-wall corner approximated those that had been reported as mentioned above while those at wall subchannel and rod-rod corner had an exponential decay.

6.6 Scales

6.6.1 Integral length scales

Figures 68, 69, and 70 present the distribution of integral length scales with distance from the rod surface normalised with the rod radius.

The streamwise Eulerian integral length scale of the axial velocity fluctuation decreased with the reduction in size of the wall subchannel. The magnitude of this length scale is minimum at the rod surface and increased to higher values towards the subchannel center.

The streamwise Eulerian integral length scales of the radial velocity also decreased in magnitude with reduction in wall subchannel size. Near the rod surface the magnitude of this scale is lower than that of the axial velocity fluctuation, however, towards the subchannel center the two magnitudes are nearly identical.

Another important length scale of interest in rod-bundle flows is the streamwise Eulerian integral length scale of the azimuthal velocity fluctuation since this can be related to intersubchannel mixing. Very close to the rod, the scales in the rod-rod and rod-wall gaps are identical but far away from the rod surface, scales at rod-wall gap are higher than those at the rod-rod gap. In the wall subchannel, the scales are higher than those in both the rod-rod and the rod-wall gaps.

At rod-rod-wall contact, the three length scales are of the same magnitude

in the wall subchannels. In all other conditions, the radial scale is small at the rod surface and is of the same magnitude as the azimuthal one in the subchannel center; both are smaller than the axial one, though near the rod surface, the axial scale is of the same magnitude as the azimuthal one.

6.6.2 Microscales

Figure 71 presents the distribution of Taylor microscale in the rod-wall gap, rod-rod gap and wall subchannels.

The distribution of the microscale in both gaps is identical. For the distribution in the wall subchannel, the microscale distribution is such that the magnitude increased with increasing distance up to a maximum and then decreased. Also the microscale decreased with reduction in subchannel size.

Chapter 7

ANALYSIS AND DISCUSSION OF RESULTS

7.1 Definition of a Local Characteristic Flow Width

The geometrical complexity and the diversity of shapes of rod subchannels makes comparison of flow characteristics under different conditions very difficult. It was decided to discuss the measurements using as reference data in pipe flows, which have been well documented. In doing so, it is necessary to use a length that would be equivalent to the pipe radius. The hydraulic radius is probably a suitable parameter for describing bulk properties but not local conditions. Therefore, a local characteristic width must be introduced. Among the various other choices, most appropriate appears to be the radial distance between the rod surface and the line of maximum axial velocity, which is analogous to the cross-section center in pipe flows. Figure 72 presents the variation of the so defined local characteristic flow width, $\hat{y}$, around the periphery of the central rod at design condition. It can be seen that the line of maximum velocity nearly coincided with the line of zero shear stress $-\rho\overline{uu_r}$. Figure 73 shows plots of $\hat{y}$ in the wall subchannel for three central rod positions. As can be seen in figure 73, the magnitude of $\hat{y}$ decreased

with reduction in size of the wall subchannel.

7.2 Effect of Wall Subchannel Size on Friction Factor

The local friction factor $f(\phi)$, defined by equation (3-12), requires the determination of a local bulk velocity which is variable in non-circular channel flows. For this flow, it was decided to define the local bulk velocity as the average velocity through a narrow sector bounded by the rod surface and the locus of maximum velocity, as shown in figure 74. Figure 75 presents the variation of the local friction factor on the rod surface facing the wall subchannel for the four rod positions investigated.

The average friction factor, f_{av}, around the central rod, defined as

$$f_{av} = \frac{\tau_{w_{av}}}{\frac{1}{2}\rho U_b^2} \qquad (7-1)$$

decreased as the size of the wall subchannel decreased. However, the local friction factor on the rod surface in the wall subchannel increased as the wall subchannel decreased in size. In all cases the magnitude of the local friction factor was higher than that of the respective average friction factor. The ratio of the local friction factor to the respective average friction factor increased as the wall subchannel decreased. This ratio varied between 1.00 and 1.12 at design position to between 2.02 and 3.03 at rod-rod-wall contact. Normalised by the friction factor for pipe flow at the same Reynolds number, the average friction factors at design position, W/D=1.059, rod-wall and rod-rod-wall contacts were respectively 1.16, 1.12, 0.98 and 0.80. The ratio of the local friction factor $f(\phi)$ and the pipe friction factor at the same Reynolds number varied between 1.14 to1.31 at design position, between 1.90 and 3.03 at rod-wall contact and between 1.82 and 2.45 at rod-rod-wall

contact.

The local friction factor had maxima at the rod-wall gap and rod-rod gap and a minimum at positions on the rod surface facing the open flow.

7.3 Effect of Wall Subchannel Size on the Mean Velocity Distribution

Presented in figures 76a and 76b are the thicknesses of the viscous ($y^+ = 4$) and buffer ($y^+ = 30$) sublayers in the rod-wall gap for various values of the rod-wall gap, δ, evaluated using equation (3-22). Both layers increased gradually with decreasing δ. When normalised with δ, the boundary layer thickness increased drastically at small δ, it remained however a small percent for $\delta/D > 3\%$. Therefore, it may be concluded that relaminarization of flow in the gap is very unlikely.

Figure 77 shows the variations of wall subchannel bulk velocity and of the maximum velocities in the wall subchannel and in the entire duct with δ/D. The subchannel bulk velocity dropped dramatically at low δ/D. This implies that at low δ/D the fluid in the wall subchannel will be subjected to higher temperatures than at the design condition.

Figure 78 presents mean velocity radial profiles in the wall subchannel at various subchannel sizes; data in pipe flows are also presented for comparison. In general, the velocity distribution in the wall subchannel was 'flatter' than that of the pipe flow away from the gaps and less flat than that of pipe flow in the gaps. Radial lines with respect to central rod coincide with the velocity gradient lines near the rod surface only. Therefore, the analogy between the maximum velocity

line in rod subchannels and centerline in pipe flows is rather weak.

7.4 Effects of Wall Subchannel Size on rms Velocities

Figure 79 shows the variation of axial rms velocity with distance from the wall. Near the wall (where the axial velocity gradient is large) the rms velocity is high, but in the subchannel core it is reduced to a minimum. The data for wall subchannel at the design conditions approximate pipe flow data except very close to the rod surface. The values at the rod-wall and rod-rod gaps and wall subchannel at rod-wall contact were higher than pipe flow data while those in the wall subchannel at rod-rod-wall contact were lower than pipe flow data.

The radial rms velocity is presented in figure 80. In all cases examined, this parameter was smaller than pipe flow data. The values at rod-wall and rod-rod gaps and wall subchannel at rod-wall contact collapsed and were higher than those in the wall subchannels at design and rod-rod-wall contact. The radial rms velocity was also minimum at the subchannel center.

Presented in figure 81 is the azimuthal rms velocity distribution. Like the axial component, it is high near the rod surface and decreases to a minimum at the position of maximum streamwise velocity. Unlike the axial and radial components, the azimuthal component reduced in the wall subchannel as the size of the wall subchannel decreased. The values in the rod-wall gap and rod-rod gap at design are higher than pipe flow data while all the values in the wall subchannels at three central rod positions are lower than pipe flow data except at points very close to the rod surface. At the subchannel center the azimuthal rms velocity is of the

same magnitude as the radial one.

7.5 Effect of Wall Subchannel Size on Correlation Coefficients

Presented in figure 82 is the distribution of correlation coefficient, $\overline{uu_r}/u'u'_r$, in the wall subchannel at three different central rod positions. The correlation coefficient of the wall subchannel at the design condition is higher than those of the wall subchannel at the rod-wall and rod-rod-wall contacts. The values in the rod-rod and rod-wall gaps lie between the values in the wall subchannel at design condition and in the wall subchannel at rod-wall contact. The values in the wall subchannel at rod-rod-wall contact are close to pipe flow data. In general this correlation coefficient decreased with reduction in wall subchannel size.

7.6 Effects of Wall Subchannel Size on Scales

Figures 83, 84, 85 and 86 respectively present the distributions of the streamwise Eulerian integral length scales of axial, radial and azimuthal velocity fluctuations normalized with $\hat{y}$ and of the Taylor microscale. The length scales in the wall subchannel decreased in size with reduction in subchannel size and their values were higher in the rod-rod and rod-wall gaps.

The scales of axial velocity fluctuation in wall subchannel at design and rod-wall contact collapsed with pipe flow data near the rod surface and these scales are higher than pipe flow data in the subchannel center; while those at rod-rod-wall contact are lower than pipe flow data near the rod surface and collapsed with the pipe flow data at subchannel center. The scales of the radial velocity fluctuation in the wall subchannel at design condition and rod-wall contact collapsed and both are higher than the values at rod-rod-wall contact; and all these scales are higher than pipe flow data.

The Taylor microscale in the wall subchannel also decreased in size with reduction in wall subchannel size and the values in rod-wall and rod-rod gaps collapsed. These values in the rod-wall and rod-rod gaps happen to fall between those in the wall subchannels at rod-wall contact and rod-rod-wall contact.

7.7 Turbulent Kinetic Energy Dissipation Rate

Presented in figure 87 is the distribution of turbulent kinetic energy dissipation rate in the wall subchannel at three central rod positions. Turbulent kinetic energy

dissipation rate was evaluated using equation (3-35). In all cases tested the dissipation rate had a maximum near the rod surface and decreased with increasing distance from the rod to a minimum at the subchannel center. This is consistent with the fact that production of turbulent kinetic energy by the mean shear is small near the subchannel center, where turbulence is maintained by transport from high shear regions. At both rod-rod and rod-wall gaps, the dissipation rate does not have the dramatic decrease to a minimum that is observed in the open region of the wall subchannel. In all three wall subchannels tested the highest dissipation rate was seen to be at rod-wall contact and the dissipation rates at the subchannel center were the same in all cases. The minimum dissipation rate at the gaps was higher than that at the subchannel center. Near the rod surface the turbulent kinetic energy dissipation rate is of comparable magnitude to the production term, $\overline{uu_r}\partial\overline{U}/\partial r$, but towards the subchannel center, the dissipation rate is higher than the production term.

7.8 Kolmogoroff's Microscales

Figure 88 shows the variation of the Kolmogoroff's microscales in the wall subchannel at three positions of the central rod. These scales were computed from the turbulent kinetic energy dissipation rate, ϵ, and the kinematic viscosity, ν, using equation (3-36). The scales are minimum near the rod surface where shear rates are high and large at the subchannel center where there are low shear rates. Like in the case of the kinetic energy dissipation rate, the values of the scales at rod-rod and rod-wall gaps collapsed. For the wall subchannels, the scales in the case of rod-wall contact were minimal. At the subchannel center, the scale at rod-rod-wall contact was larger than the other two cases which were of the same

magnitude.

7.9 Implications about Heat Transfer

In section 7.2 it was found that the friction factor, based on a "local" bulk velocity was higher in the gaps than in the open subchannel regions. However, as it is most likely to happen in design practice, the friction factor and the heat transfer coefficient are defined based on the overall bulk velocity in the bundle. In this case the friction factor has the same variation as the wall shear stress, namely it changes from lower values in the gaps to larger values in the open subchannel regions. If one uses the Reynolds analogy for pipe flow, the Stanton number and, therefore, the heat transfer coefficient would be expected to show a similar variation. One may notice, however, that significant drop in the gap wall shear stress occurred only for very small gaps, namely for $\delta/D < 2.5\%$; in the CANDU bundle, this corresponds to rod-wall gaps less than 0.3 mm.

7.10 Comparison of Flows in the Model and Actual Bundle

The present model is geometrically similar to the CANDU bundle. If one assumes incompressible single phase flow and neglects gravitational forces, dynamic similarity of the two flows would be achieved by matching the Reynolds numbers in the two situations. Since the model Reynolds number was lower than the one in the actual bundle, it seems necessary to address the possible consequences of this difference. In general, the higher the Reynolds number is in a channel flow, the thinner the wall layer would be. Therefore, it is expected that any implication of the present study concerning heat transfer in the model flow would only have to

be corrected favorably for the actual bundle, and that any speculations concerning reactor safety based on the present work would tend to be somewhat conservative when applied to the actual bundle. An estimate of differences in the wall layers for the two flows is presented below.

Since both the model and the actual Reynolds numbers are in the fully turbulent regime for channel flow, one may assume that the friction factor in the model is the same as that in the actual bundle and that the local bulk velocity in each case is directly proportional to the respective bulk velocity. Then, the friction velocity, u_τ, for the actual bundle could be estimated using equations (3-12) and (3-10) and flow properties at the actual flow temperature. From the values of u_τ obtained, the thicknesses of the viscous sublayer and the buffer sublayer for both model and actual bundle were determined using equation (3-22). In general, these thicknesses, normalised by the respective rod diameter, had an approximate ratio of 3.6 with the model thicknesses being the larger ones. The viscous sublayer thickness in the actual bundle at design condition was found to vary between 0.013%D and 0.015%D and at rod-rod-wall contact this variation was between 0.018%D and 0.024%D.

The ratio of the normalised buffer sublayer thickness in the model to that in the actual bundle was the same as that of the viscous sublayer. The buffer sublayer thickness in the actual bundle varied between 0.096%D and 0.12%D at design condition and between 0.13%D and 0.18%D at rod-rod-wall contact. Thus at rod-wall and rod-rod-wall contacts and very narrow gaps of less than 0.048%D, the flow through the gaps and in the vicinity of the contacts is in the viscous layer. However, the extent of 'relaminarized' flow region is extremely small and it is not expected to have a significant effect on the overall parameters. In any case, heat

transfer coefficients would tend to be larger in the actual than in the model.

Chapter 8

CONCLUSIONS

The main conclusions drawn from measurements in a 12.9 upscale model of a 37-rod bundle of the CANDU reactor are listed below.

1. The wall shear stress varied from minima in the gaps to maxima in the open flow regions; its variation was not monotonic, but it reflected the effects of secondary flows.

2. The wall shear stress at the wall subchannel depended on the shape and size of the subchannel and could not be easily predicted from pipe flow data especially near narrow gaps.

3. At small rod-wall proximities (i.e. for gaps less than 2.5% of the rod diameter) both the average wall shear stress and the local wall shear stress in the gap were low. This implies that heat transfer from the rod surface would also be low under such conditions.

4. As the wall subchannel decreases in size, the flow rate in this subchannel decreased. Thus the fluid in the subchannel will experience higher temperature at small rod-wall proximity than at design condition.

5. The velocity contours bulge towards the gaps and the bulging became more

pronounced as the gaps narrowed. This phenomenon is attributed to secondary flows.

6. The turbulence intensities were generally higher than those in fully developed pipe flow. A change in size of the wall subchannel had a negligible effect on the axial and radial intensities, while the azimuthal intensity decreased with reduction in size of the wall subchannel. These intensities also bulged towards the corners and narrow gaps.

7. The Reynolds stress in the plane parallel to the rod axis had a large value near the rod surface, decreased to zero near the locus of maximum mean velocity and then it reversed sign. The maximum magnitude of the correlation coefficient was about 0.4-0.5.

8. Like the mean axial velocity, the turbulence kinetic energy bulged towards the narrow gaps and corners. The kinetic energy had maximum values at positions near the rod and wall surfaces and minimum values at the subchannel centers.

9. The autocorrelation function shapes at positions in the wall subchannel near the rod surface were comparable to those in uniformly shear flows and flows in two dimensional ducts. However, the autocorrelations in the rod-wall gap had a peculiar ordering, reflecting positive mixing between flows in the subchannels separated by the gaps.

10. The friction factor based on a "local" bulk velocity increased with a decrease in wall subchannel size; it also decreased monotonically from a maximum at the rod-wall gap to a minimum at the position facing the open flow region and then it increased monotonically to a maximum at the rod-rod gap.

11. At very close rod-wall proximity and at rod-wall contacts, the flow through the gap or in the vicinity of the contacts was dominated by viscous stresses.

12. The turbulent kinetic energy dissipation rate was higher near the wall and lower at subchannel centers where the shear is also low.

13. The rms velocities in the radial and azimuthal directions were lower than those of pipe flows while the axial rms velocity in the wall subchannel at design condition was comparable to pipe flow data.

BIBLIOGRAPHY

Abdelghany, M.and Eichhorn, R. (1986), Measurements of wall shear stress in axial flow in a square lattice rectangular rod bundle. Journal of Fluids Engineering, volume 108, pages 166-173.

Batchelor, G. K. (1953) The Theory of Homogeneous Turbulence. Cambridge University Press.

Brundrett, E. and Baines, W. D. (1964), The production and diffusion of vorticity in duct flow. Journal of Fluid Mechanics, volume 15, pages 375-394.

Budwig, R., Tavoularis, S. and Corrsin, S. (1985), Temperature fluctuations and heat transfer flux in grid-generated isotropic turbulence with steamwise and transverse mean temperature gradients. Journal of Fluid Mechanics, volume 153, pages 441-460.

Carajilescov, P. and Todreas, N. E. (1975), Experimental and analytical study of axial turbulent flows in an interior subchannel of a bare rod bundle. Journal of Heat Transfer volume 98, pages 262-268.

Comte-Bellot G. (1965), Ecoulement turbulent entre deux parois paralleles. Publications Scientifiques du Ministere de l'Air, No. 419, Paris France.

Corrsin S. (1963), Turbulent flow, Experimental methods in Handbuch der Physik, volume 8, pages 524-590. (ed. S. Flugge and C. Truesdell), Berlin: Springer-verlag.

Creer J. M., Bates J. M. Sutey A. M. and Rowe D. S. (1979), Turbulent flow in a model nuclear fuel bundle containing partial flow blockages. Engineering and Design, volume 52, pages 22-42.

Eifler, W. and Nijsing R. (1967), Experimental investigation of velocity distribution and flow resistance in a triangular array of parallel rods. Nuclear Engineering and Design, volume 5, pages 22-42.

Escudier, M. P. and Achary M. (1987), Critique of the computational Preston tube method. Experiments in Fluids, volume 5, pages 59-65.

Franklin, R. E. and Wallace, J. M. (1970), Absolute measurements of static hole error using flush transducers. Journal of Fluid Mechanics, volume 42, pages 83-92.

Goldstein, S. (1936), A note on the measurement of total head and static pressure in a turbulent stream , Proceedings of the Royal Society London, series A, volume 150, pages 570-572.

Hanratty, T. J. and Campbell, J. A. (1983), Measurement of wall shear stress, Fluid Mechanics Measurements, pages 559-615 (ed. by R. J. Goldstein), Hemisphere Publishing Corp., Reading, U.S.A.

Head, M. R. and Rechenberg, I (1962), The Preston tube as a means of measuring skin friction. Journal of Fluid Mechanics, volume 14, pages 1-17.

Hinze, J. O. (1975), Turbulence. Second Edition. McGraw-Hill New York.

Hollingshead, A. B. and Rajaratnam N. (1980), Calibration chart for the Preston tube. Journal of Hydraulics Research, volume 18, pages 313-326.

Hooper, J. D. (1983), The development of large scale structure in the rod gap region for in-line flow through closely spaced rod arrays. Proceedings of the Fourth Symposium on Turbulent Shear Flows, Karlsruhe, F. R. Germany, pages 1.23-1.27.

Hwang Li-San and Emmet M. L. (1963), Shear measurement technique for rough surfaces. Journal of Hydraulics Engineering, volume 89, pages 19-37.

Ibragimov, M. Kh., Isupov, I. A., Kobzar, L. L. and Sabbotin, V. I. (1966), Calculation of the tangential stresses at the wall of a channel and the velocity distribution in a turbulent flow of liquid. Soviet Atomic Energy, volume 21, pages 731-739.

Ibragimov, M. Kh., Isupov, I. A., Kobzar, L. L. and Sabbotin, V. I. (1967), Calculation of hydraulic resistivity coefficients for turbulent fluid flow in channels of non-circular cross-section. Soviet Atomic Energy, volume 23, pages 1042-1063.

Kaisser, H. G. and Zeggel, W. (1987), Turbulent flows in complex rod bundle geometries numerically predicted by the use of FEM and a basic turbulence model. Nuclear Engineering and Design, volume 99, pages 351-363.

Karnik, U. and Tavoularis, S. (1987), Generation and manipulation of uniform shear with the use of screens. Experiments in Fluids, volume 5, pages 247-254.

Kjellstrom B. (1974), Studies of Turbulent Flow Parallel to a Rod Bundle of Triangular Array. Report AE-487 AB Atomenergi, Sweden.

Laufer, J. (1954), The Structure of Turbulence in Fully Developed Pipe Flow. National Advisory Committee for Aeronautics, Report 1174.

Launder, B. E. and Ying W. M. (1972), Secondary flows in ducts of square cross-section. Journal of Fluid Mechanics, volume 54, pages 289-295.

McDGalbraith, R. A., Sjolander, S. and Head, M. R. (1977), Mixing length in the wall region of turbulent boundary layer. Aeronautical Quarterly, May 1977, pages 97-110.

MacMillan, F. A. (1957), Experiments on pitot tubes in shear flow. Research and Memoranda, No. 3028, Aeronautical Research council, London, U.K.

Monin, A. S. and Yaglom, A. M. (1975), Statistical Fluid Mechanics: Mechanics of Turbulence, volume 1 & 2, The MIT Press.

Nakayama, A. and Chow, W. L. (1986), Turbulent flows within straight ducts. Encyclopedia of Fluid Mechanics, Gulf Publishing Company, volume 1, chapter 21, pages 639-674.

Onsrud, G., Persen, L. N. and Saetran, L. R. (1987), On the measurement of wall shear stress. Experiments in Fluids, volume 5, pages 59-65.

Ower, E. and Pankhurst, R. C. (1977), The Measurement of Air Flow, Fifth Edition, Pergamon Press , Oxford.

Patel, V. C. (1965), Calibration of the Preston tube and limitations in its use in pressure gradients. Journal of Fluid Mechanics, volume 23, pages 185-208.

Preston, J. H. (1954), The determination of turbulent skin friction by means of pitot tubes. Journal of the Royal Aeronautical Society, volume 58, pages 109-121.

Prinos, P., Townsend, R. and Tavoularis, S (1985), Structure of turbulence in compound channel flow. Journal of Hydraulic Engineering, volume 111, pages 1246-1261.

Prinos, P., Tavoularis, S and Townsend, R. (1988), Turbulence measurements in smooth and rough-walled trapezoidal ducts. Journal of Hydraulic Engineering, volume 114, pages 43-53.

Rehme, K. (1973), Simple methods of predicting friction factors of turbulent flow in non-circular channels. International Journal of Heat and Mass Transfer, volume 16, pages 933-950.

Rehme, K (1978), The structure of turbulent flow through a wall subchannel of a rod bundle. Nuclear Engineering and Design, volume 45, pages 311-323.

Rehme, K. (1980), Turbulent momentum transport in rod bundles. Nuclear Engineering and Design, volume 62, pages 137-146.

Rehme, K. (1982), Distributions of velocity and turbulence in parallel flow along an asymmetric rod bundle. Nuclear Technology, volume 59, pages 148-159.

Rehme, K. (1987), On the development of Turbulent flow in wall subchannel of rod bundle. Nuclear Technology, volume 77, pages 331-342.

Rehme, K. (1987), The structure of turbulent flow through rod bundles. Nuclear Engineering and Design, volume 99, pages 141-154.

Rodi, W. (1982), Examples of turbulence models for incompressible flows. American Institute of Aeronautics and Astronautics Journal, volume 20, pages 872-879.

Rogers, J. T. and Tahir, A. E. E. (1975), Turbulent interchange mixing in rod bundles and the role of secondary flows. AIChE-ASME Heat Transfer Conference, San Francisco, California.

Rowe, D. S., Johnson, B. M. and Knudsen, J. G. (1974), Implications concerning rod bundle cross flow mixing based on measurements of turbulent flow structure. International Journal of Heat and Mass Transfer, volume 17, pages 407-419.

Sabot, J., Renault, J. and Comte-Bellot, G. (1973), Space-time correlations of the transverse velocity fluctuations in pipe flow. The Physics of Fluids, volume 16, pages 1403-1405.

Sabot, J., Saleh, I. and Comte-Bellot, G. (1977), Effects of roughness on the intermittent maintenance of Reynolds shear stress in pipe flow. The Physics of Fluids, volume 21, pages S150-S155.

Samet, M. and Einav, S. (1985), Directional sensitivity of unplated normal wire probes. Review of Scientific Instruments, volume 56, number 12, pages 2299-2305.

Tahir, A. E. E. and Rogers, J. T. (1979), The mechanism of secondary flows in turbulent interchange in rod bundles. Proceedings of the Seventh Canadian Congress of Applied Mechanics; Sherbrooke, Canada, pages 773-774.

Tahir, A. E. E. and Rogers, J. T. (1986), Turbulent flow structure in a closely packed triangular array rod bundle. Presented at the Eighth International Heat Transfer Conference, San Francisco.

Tavoularis, S. and Corrsin, S. (1981), Experiments in nearly homogeneous turbulent shear flow with a uniform mean temperature gradient; part 1. Journal of Fluid Mechanics volume 104, pages 311-347.

Tavoularis, S. (1983), Simple corrections for the temperature sensitivity of hot wires. Review Scientific Instruments, volume 54, pages 741-743.

Tavoularis, S. and Corrsin S. (1985), Effects of shear on the turbulent diffusivity tensor. International Journal of Heat and Mass Transfer, volume 28, pages 265-276.

Tavoularis, S. (1985), Asymptotic laws for transversely homogeneous turbulent shear flows. Physics of Fluids volume 28 pages 999-1001.

Tavoularis, S., Prinos, P. and Sitaraman S. (1986), Subchannel Flows Measurement in a Model of the 37-rod CANDU Reactor Fuel Bundle. Technical Report UOME-BF-8602. University of Ottawa, Canada.

Tavoularis, S. (1986), Techniques for turbulence measurements. Encyclopedia of Fluid Mechanics, Gulf Publishing Company, volume 1, pages 1207-1255.

Tavoularis, S., Sitaraman, S. and Prinos, P. (1988), Measurements of turbulent flows in rod bundle subchannels. International Journal of Engineering Fluid Mechanics (in press).

Tennekes, H and Lumley, J. L. (1981), A First Course in Turbulence. The MIT press.

Townsend A. A. (1976), The Structure of Turbulent Shear Flow. Second edition. Cambridge University Press.

Trupp, A. C. and Azad, R. S. (1975), The structure of turbulent flow in triangular array rod bundles. Nuclear Engineering and Design, volume 32, pages 47-84.

Winter, K. (1977), An outline of the techniques available for the measurement of skin friction in turbulent boundary layers. Progress in Aerospace Science volume 18, pages 1-57.

White F. M. (1974), Viscous Flow Theory. McGraw Hill.

PARAMETER	UNITS	REACTOR BUNDLE	MODEL
Operating fluid	-	Heavy water	Air
Fluid temperature	^{0}C	220-240	25-28
Fluid pressure	MPa	13.79	Atmospheric
Bundle length	m	0.50	6.10
Rod diameter	mm	13.08	168.27
Pitch to diameter ratio, P/D	-	1.14	1.14 at design
Bundle hydraulic diameter	mm	7.85	88.48, wall subchannel
			55.58, cross-section
Subchannel equivalent pipe Reynolds number	-	452000	74000

Table 1. Comparison between actual bundle and model

MEASURED PARAMETERS	INSTRUMENTATION USED
Wall shear stress	Preston tubes
Local mean velocity	Pitot-static tubes Hot wire anemometry
Turbulence intensity	Hot wire anemometry
Turbulent kinetic energy	Hot wire anemometry
Reynolds stresses	Hot wire anemometry
Autocorrelation coefficients	Hot wire anemometry
Length scales	Hot wire anemometry

Table 2. Measured parameters and instrumentation used

ϕ	Friction factors		Friction velocity			
	Design	W/D=1.059	Design		W/D=1.059	
			model	actual	model	actual
0	0.0064	0.00866	0.6831	0.3001	0.6071	0.2668
30	0.0062	0.00713	0.7104	0.3119	0.6482	0.2849
60	0.0056	0.00595	0.7051	0.3092	0.6765	0.2973
90	0.0060	0.00623	0.7235	0.3176	0.7154	0.3143
120	0.0057	0.00618	0.7825	0.3425	0.7738	0.3401

ϕ	Friction factors		Friction velocity			
	Rod-wall contact	Rod-rod-wall contact	Rod-wall contact		Rod-rod-wall contact	
			model	actual	model	actual
40	0.00968	0.00933	0.6043	0.2564	0.4227	0.1858
75	0.00743	0.0095	0.6795	0.2988	0.5518	0.2429
90	0.00886	0.0196	0.7188	0.3160	0.4523	0.1988
110	0.0098	-	0.7820	0.3437	-	-
130	0.0081	-	0.7825	0.3551	-	-

Table 3. Friction factors and friction velocities

CENTRAL ROD POSITION	$\overline{U_{max}}$	U_b		
		wall subchannel	inner subchannel 1	inner subchannel 2
Design	16.80	12.634	13.104	13.948
W/D=1.059	16.66	12.259	13.182	13.990
Rod-wall contact	15.24	8.852	12.215	12.471
Rod-rod-wall contact	14.28	5.75	8.687	11.654

Table 4. Maximum and bulk velocities

$r/\hat{y}$	Design condition						Rod-wall contact		Rod-rod-wall contact		Shear flows		Isotropic flows	
	rod-wall gap		wall subchannel		rod-rod gap		wall subchannel		wall subchannel		Tavoularis and Corrsin			
	$\frac{L_{22,1}}{L_{11,1}}$	$\frac{L_{33,1}}{L_{11,1}}$	$\frac{L_{22,1}}{L_{11,1}}$	$\frac{L_{33,1}}{L_{11,1}}$	$\frac{L_{22,1}}{L_{11,1}}$	$\frac{L_{33,1}}{L_{11,1}}$	$\frac{L_{22,1}}{L_{11,1}}$	$\frac{L_{33,1}}{L_{11,1}}$	$\frac{L_{22,1}}{L_{11,1}}$	$\frac{L_{33,1}}{L_{11,1}}$	$\frac{L_{22,1}}{L_{11,1}}$	$\frac{L_{33,1}}{L_{11,1}}$	$\frac{L_{22,1}}{L_{11,1}}$	$\frac{L_{33,1}}{L_{11,1}}$
0.30	0.535	0.622	0.597	0.683	0.618	0.709	0.606	1.482	0.683	0.991				
0.50	0.684	0.858	0.812	0.617	0.608	0.810	0.943	1.521	0.695	0.979	0.23	0.34	0.5	0.5
0.80	0.935	0.765	0.910	0.830	0.805	0.581	0.918	1.215	0.663	0.853				

Table 5. Ratios of Eulerian integral length scales

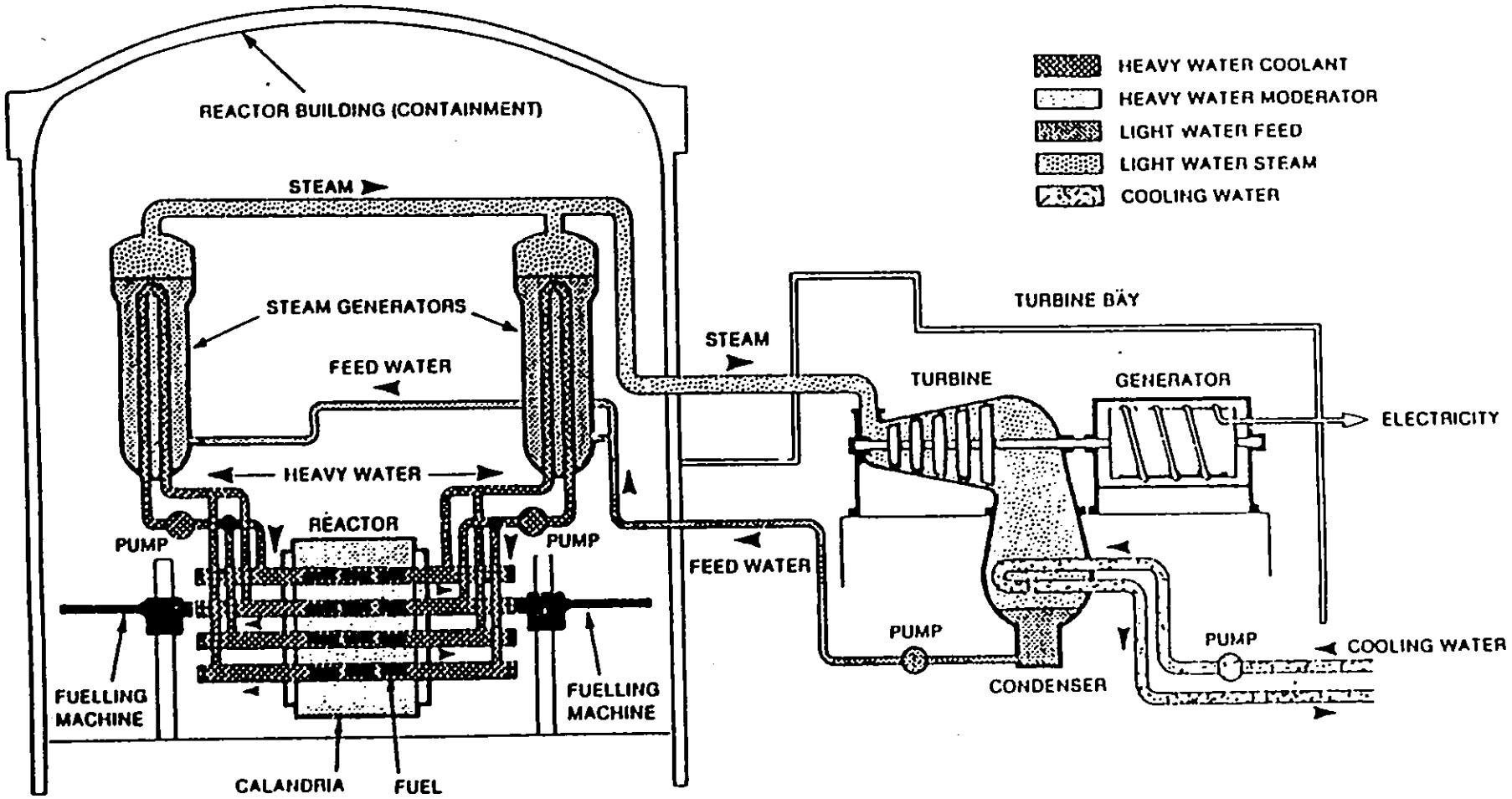

Figure 1. CANDU nuclear power system

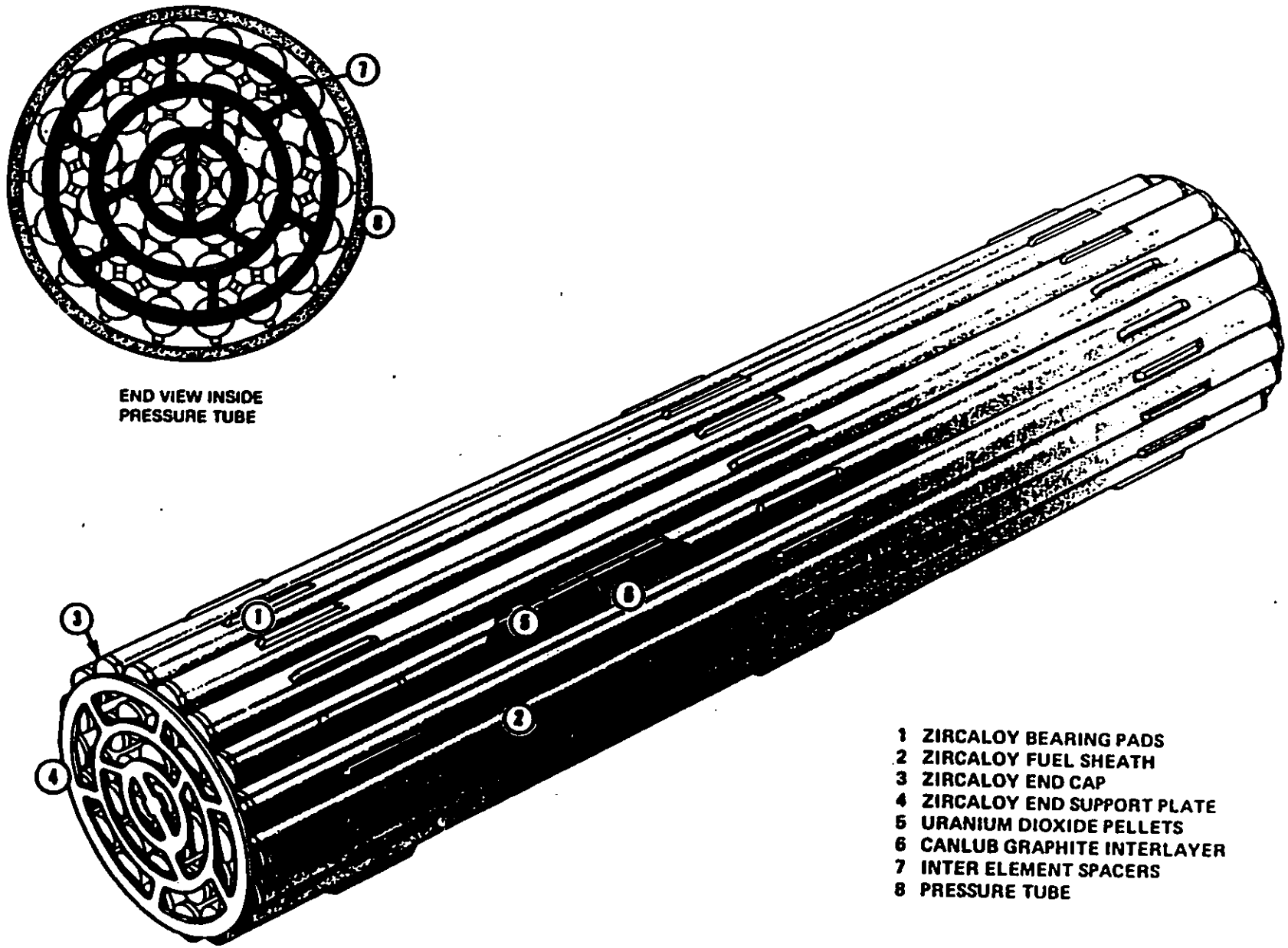

Figure 2. 37-rod element reactor bundle

RING	RADIUS(mm)	NO. OF RODS
1	14.88	6
2	28.75	12
3	43.14	18

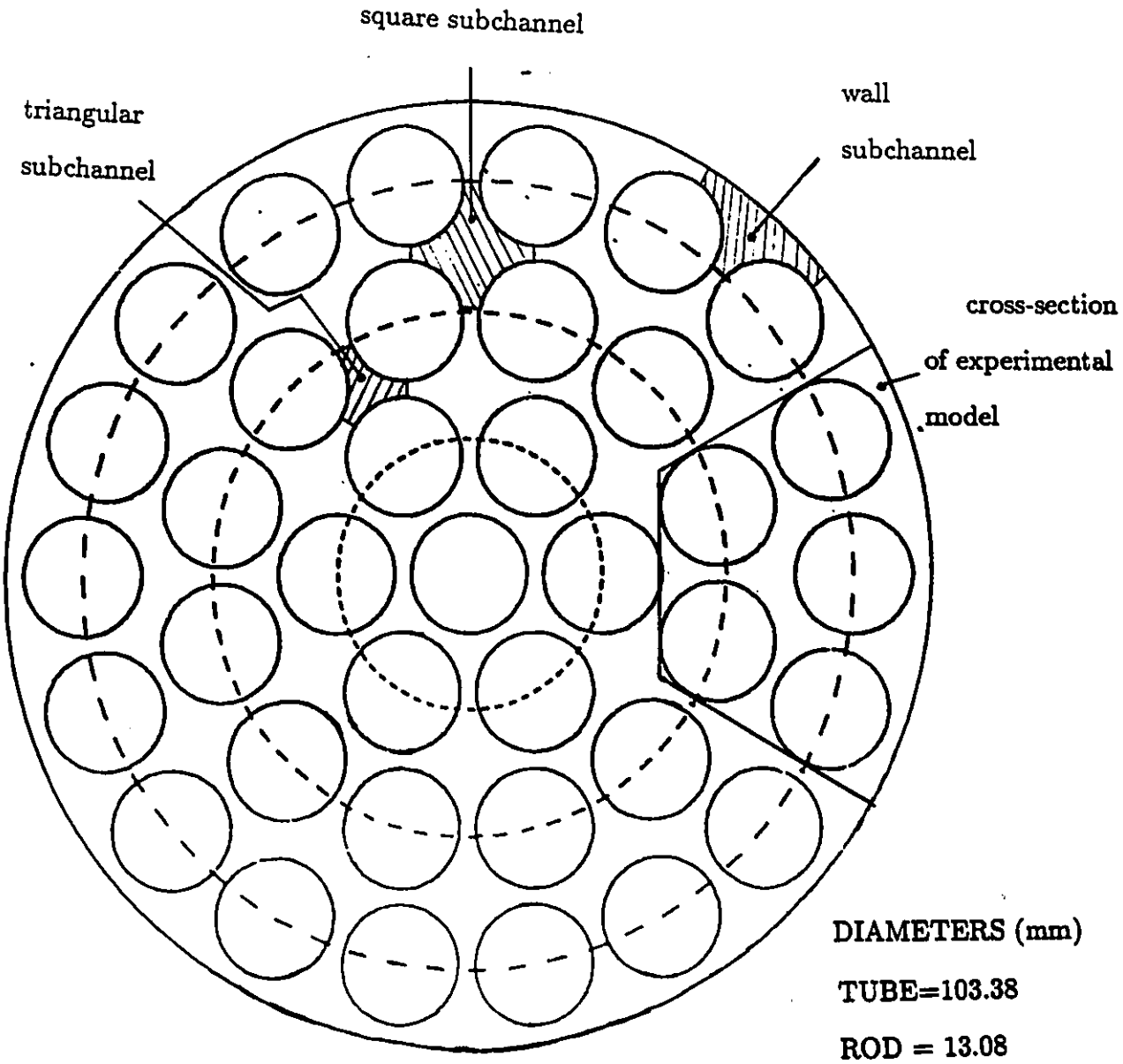

Figure 3. Cross-section of a 37-rod CANDU reactor bundle

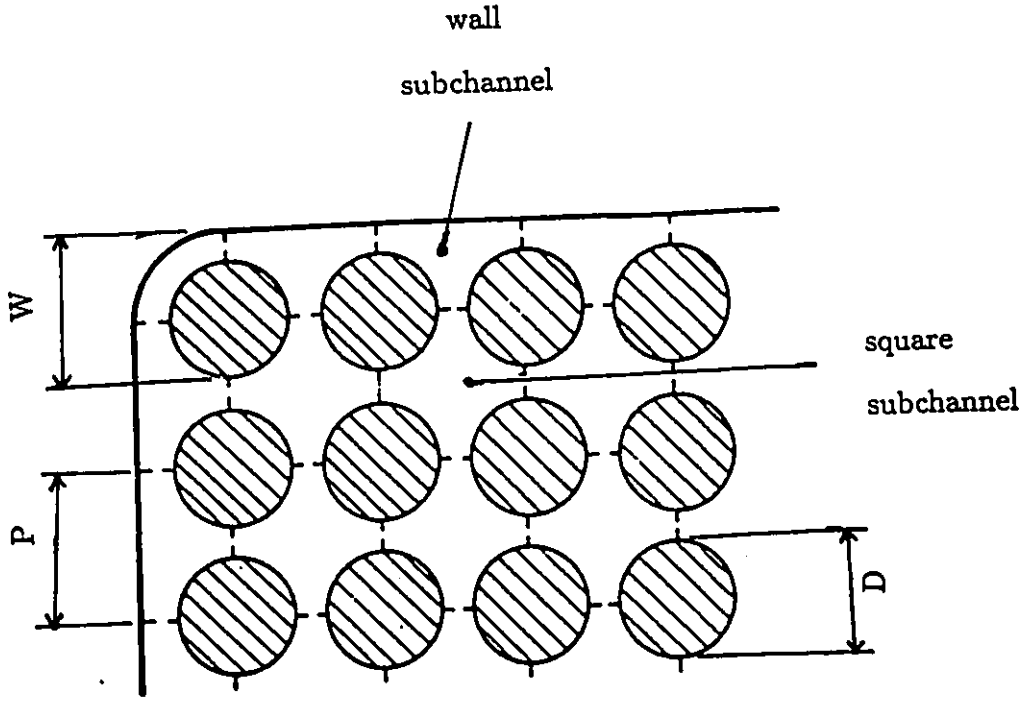

a. Rod bundle of square array

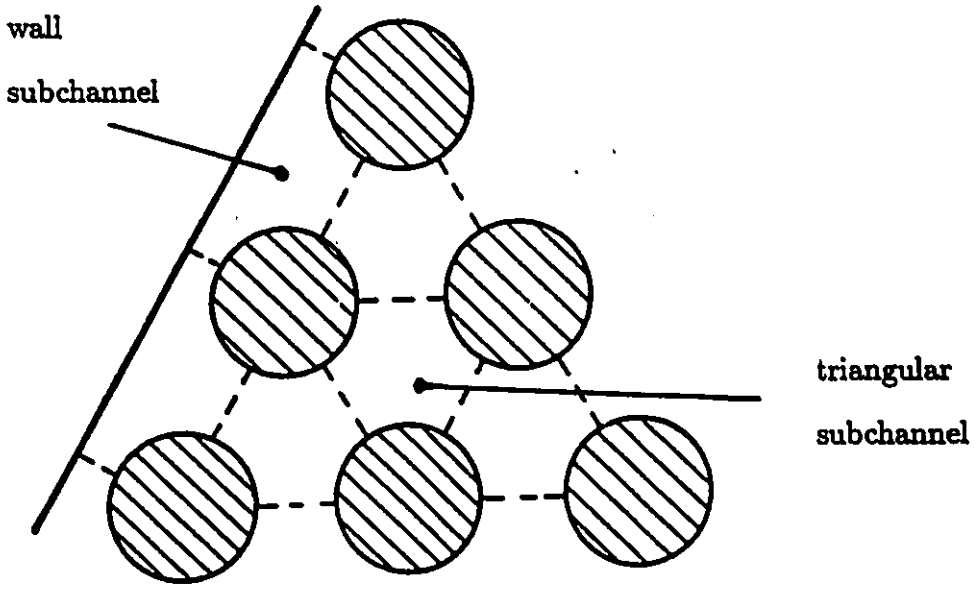

b. Rod bundle of triangular array

Figure 4. Division of a rod bundle flow channel into subchannels

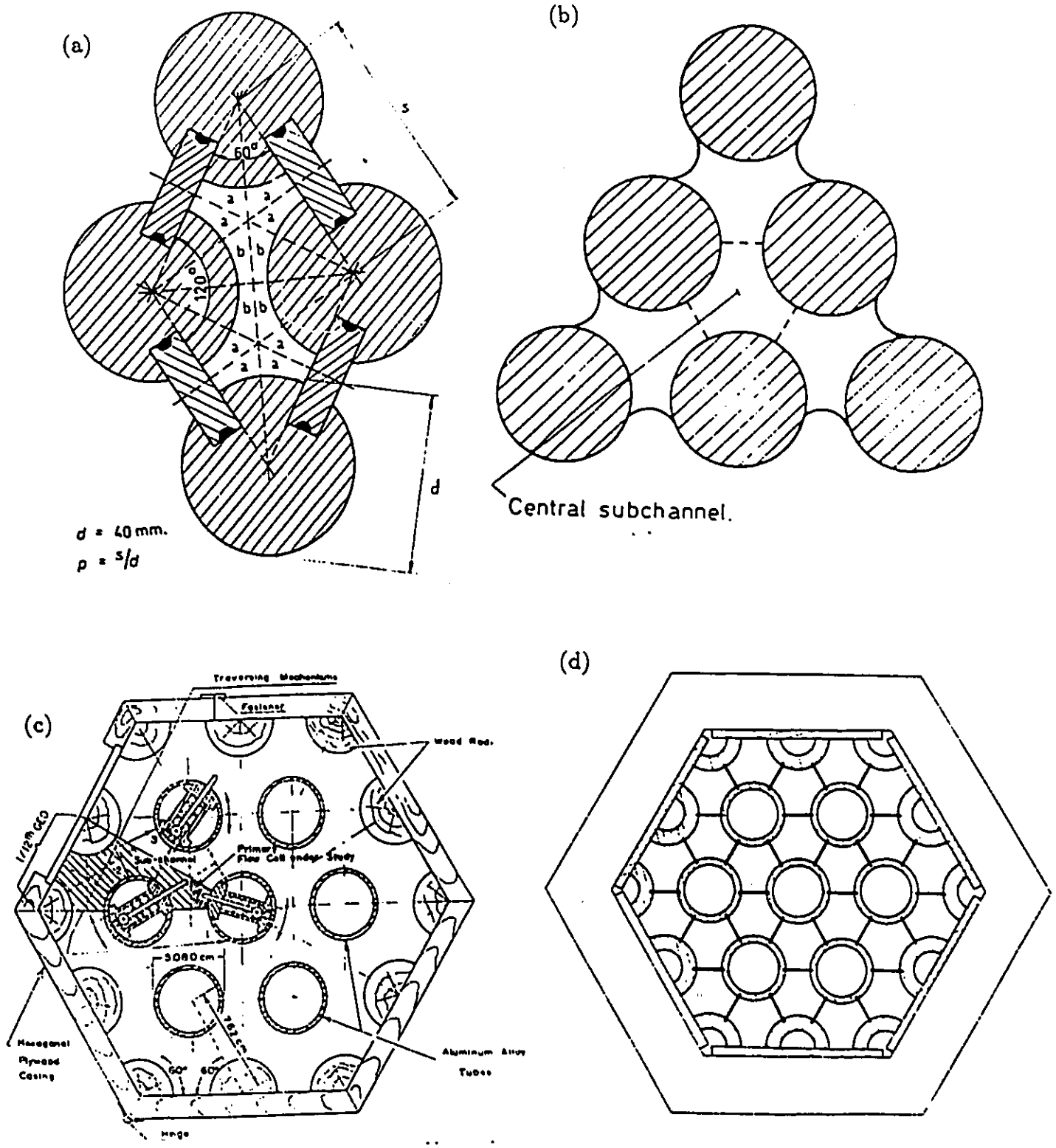

Figure 5. Cross-sections of triangular subchannel models (a) Eifler and Nijsing(1967), (b) Kjellstrom(1974), Trupp and Azad(1975), (d) Rogers and Tahir(1975, 1979)

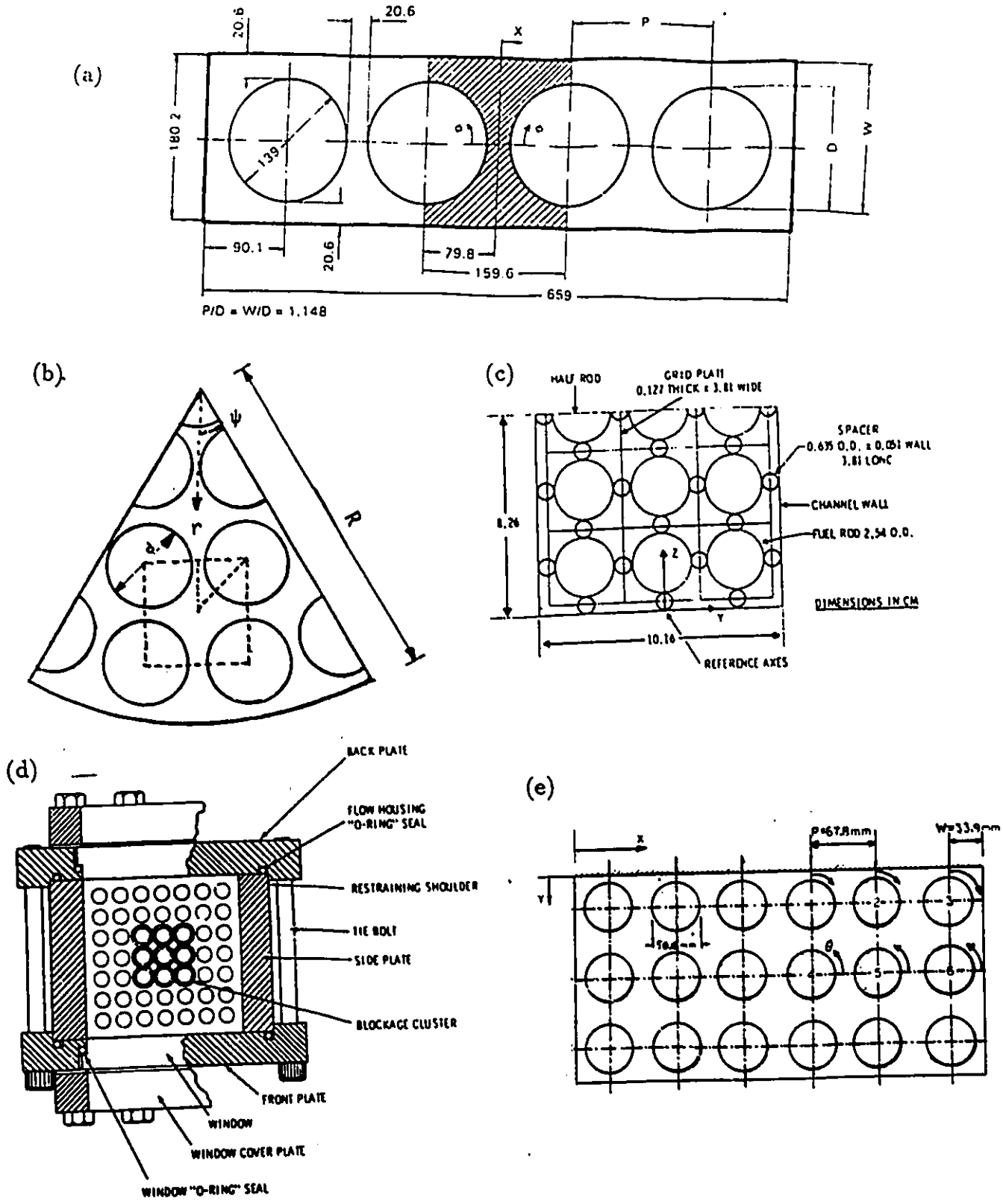

Figure 6. Cross-sections of wall and square subchannel models (a) Rehme(1973-1987), (b) Tavoularis et al.(1986-1988), (c) Rowe et al.(1974), (d) Creer et al.(1979), (e) Abdelghany and Eichhorn(1986)

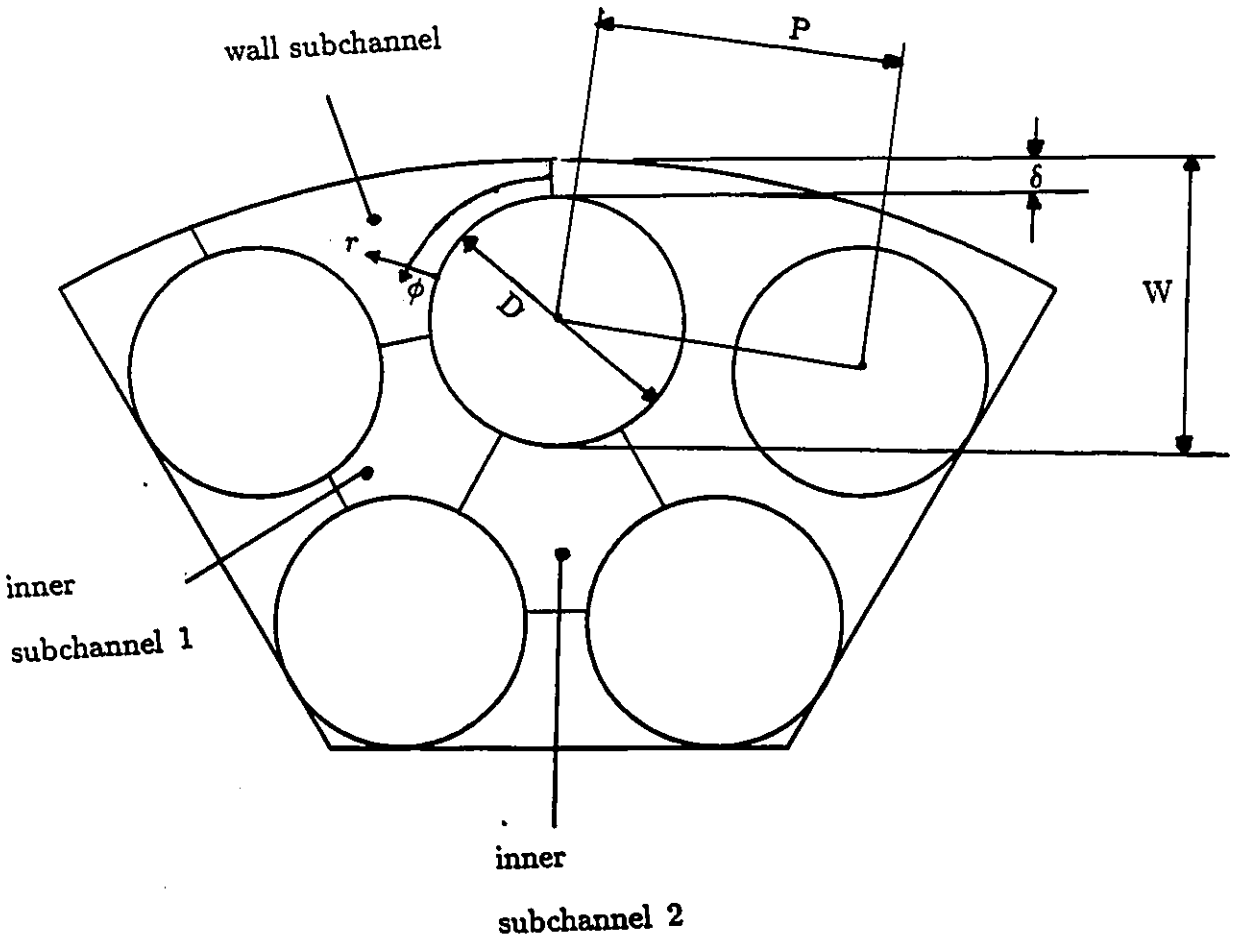

Figure 7. Cross-section of the model bundle facility (x-axis outwards)

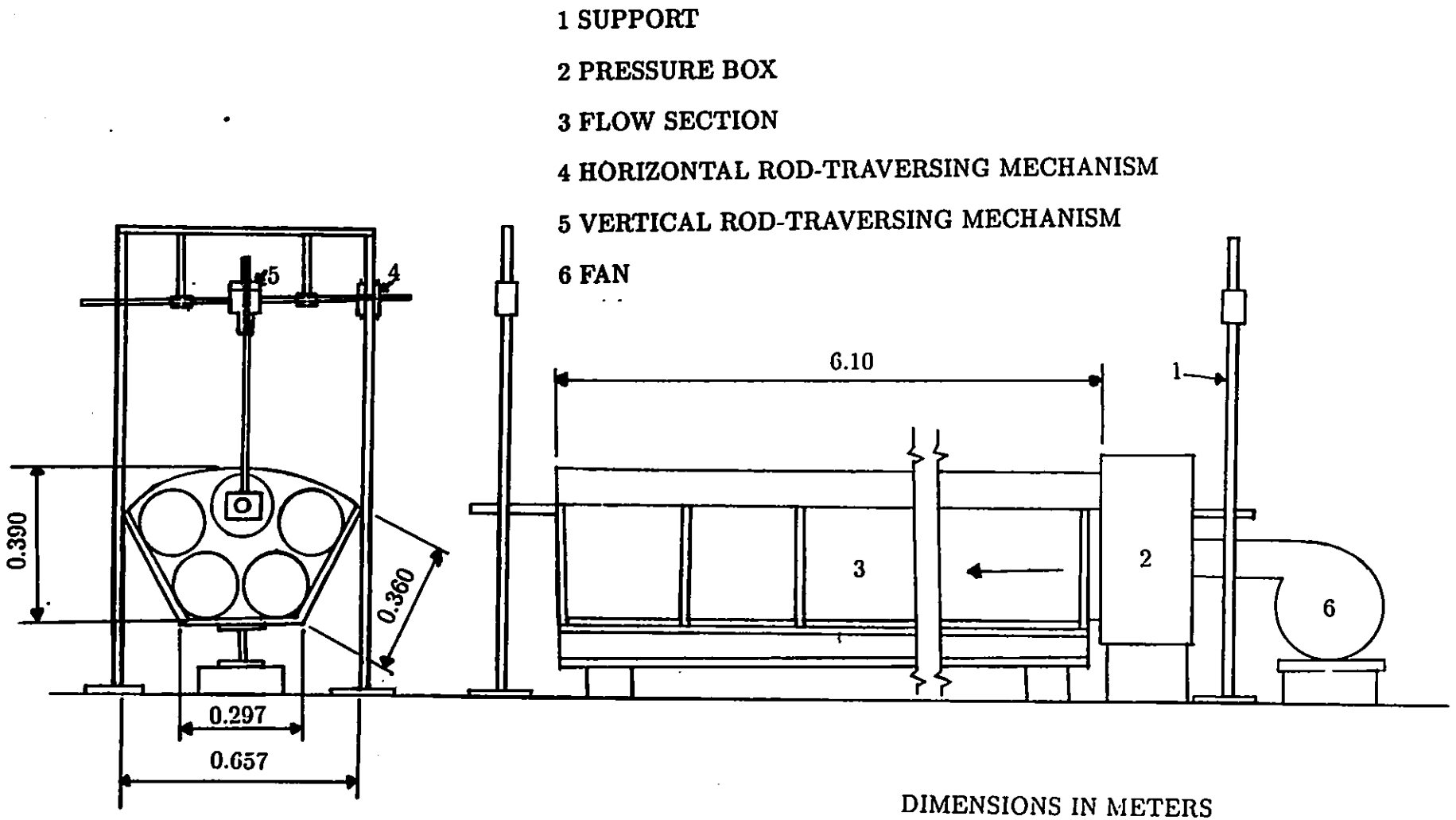

Figure 8. Sketch of the flow facility

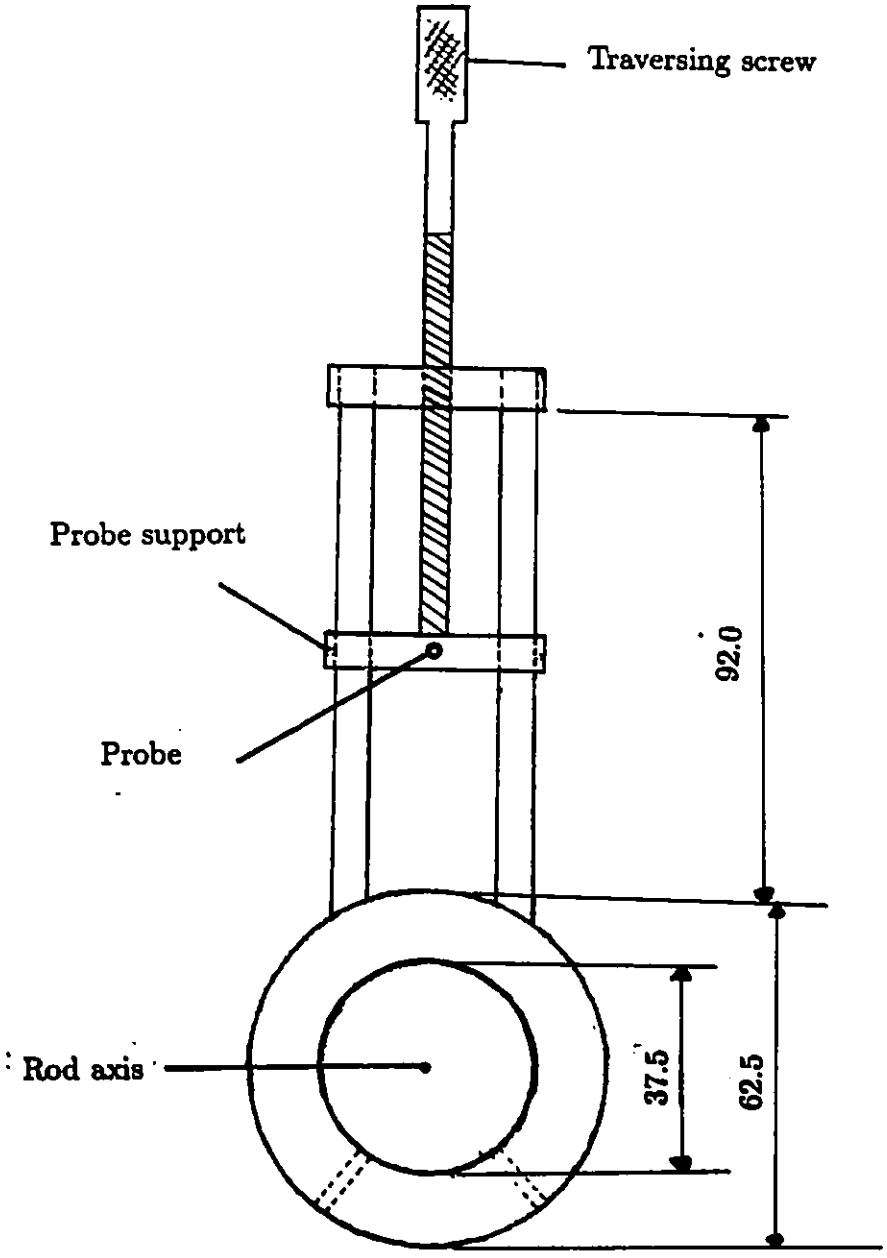

DIMENSIONS IN MM

Figure 9. Probe traversing mechanism

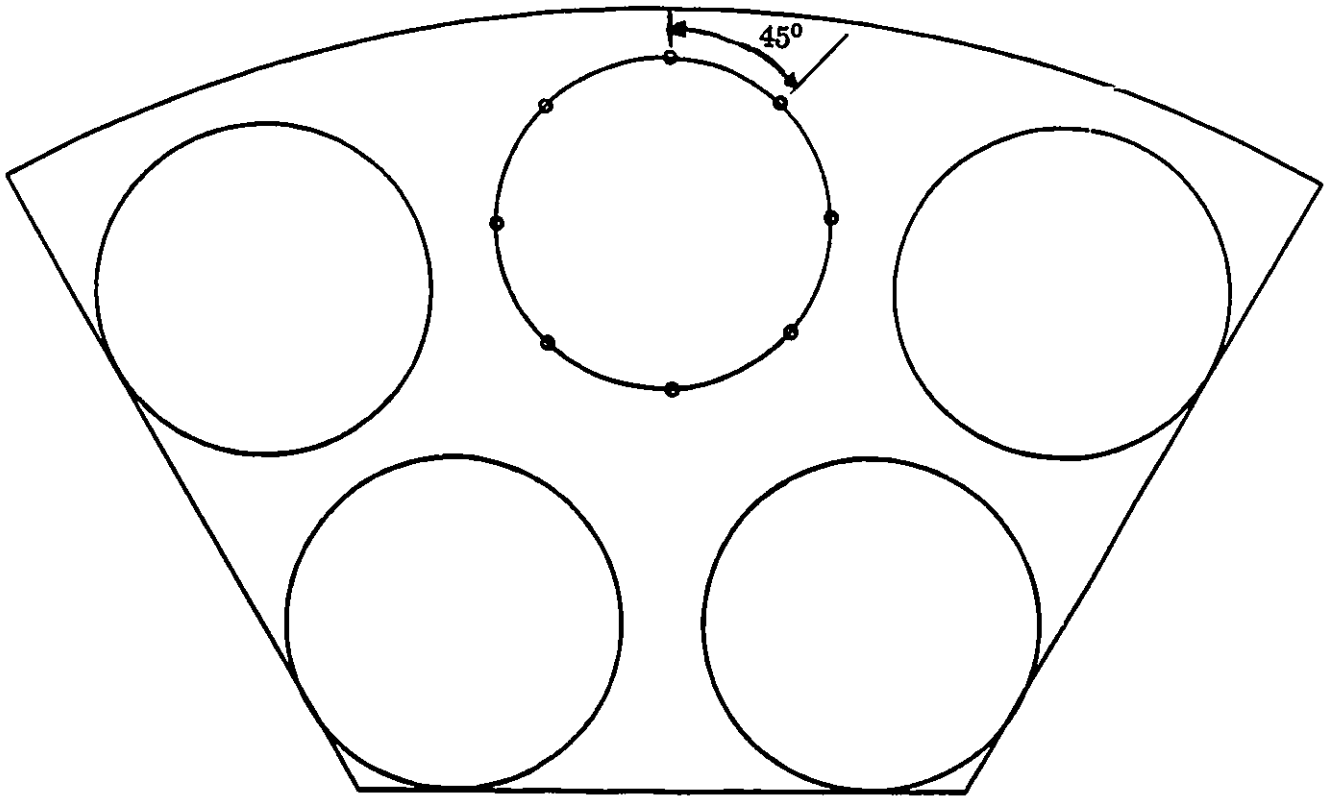

Figure 10. Working section assembly showing the static pressure hole locations

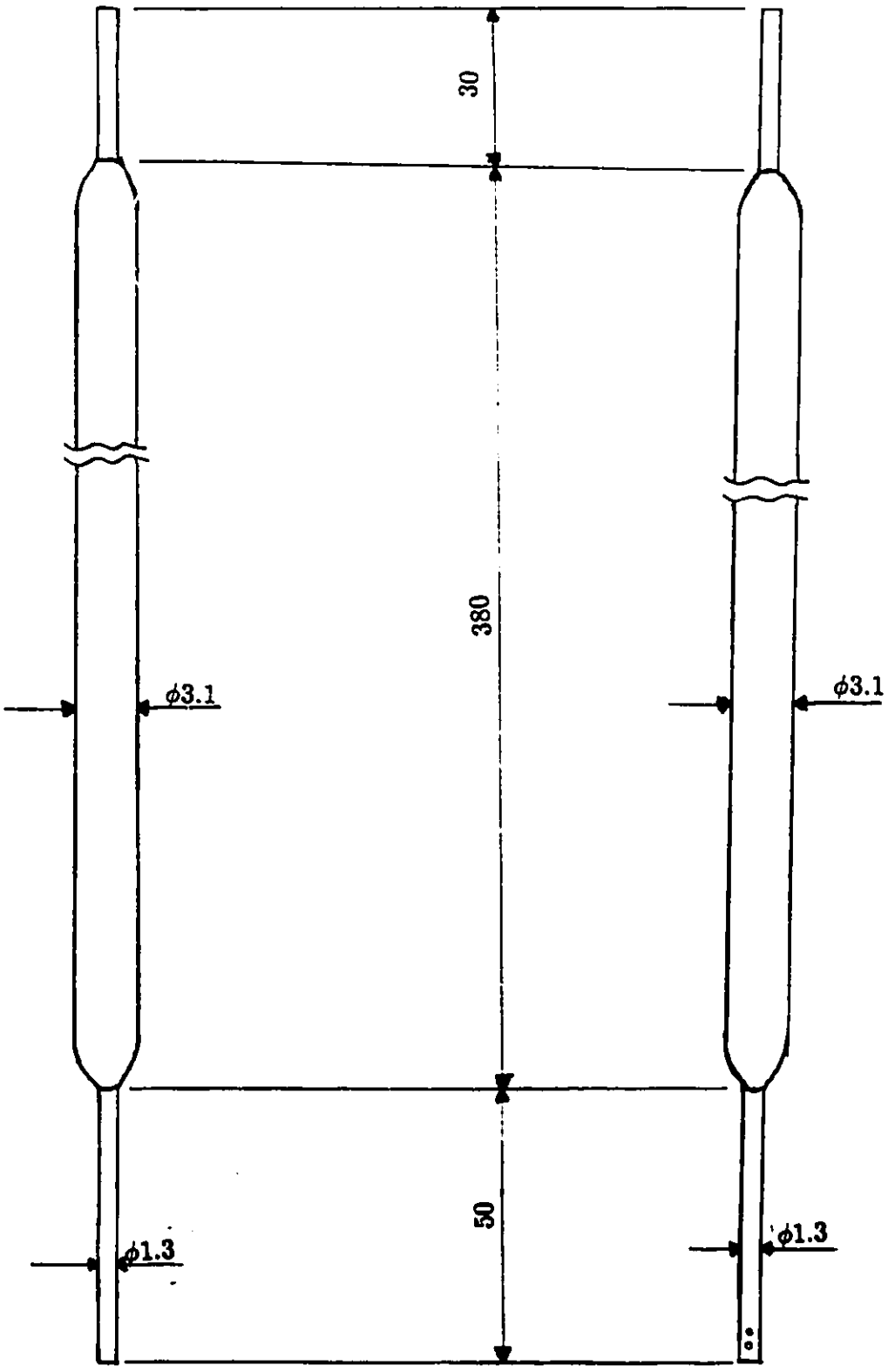

Figure 11. Pitot and Static tubes

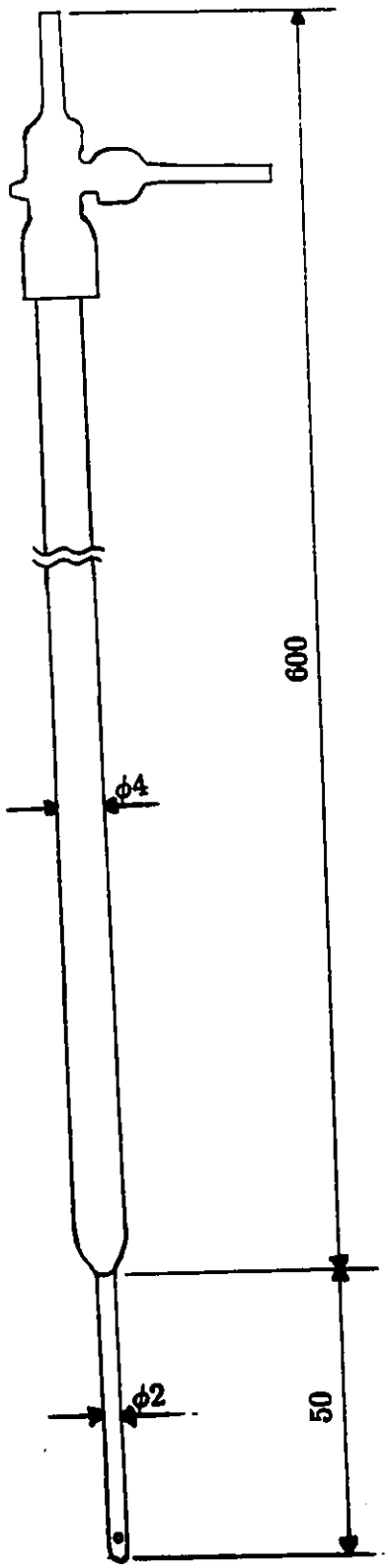

Figure 12. Pitot-static tube

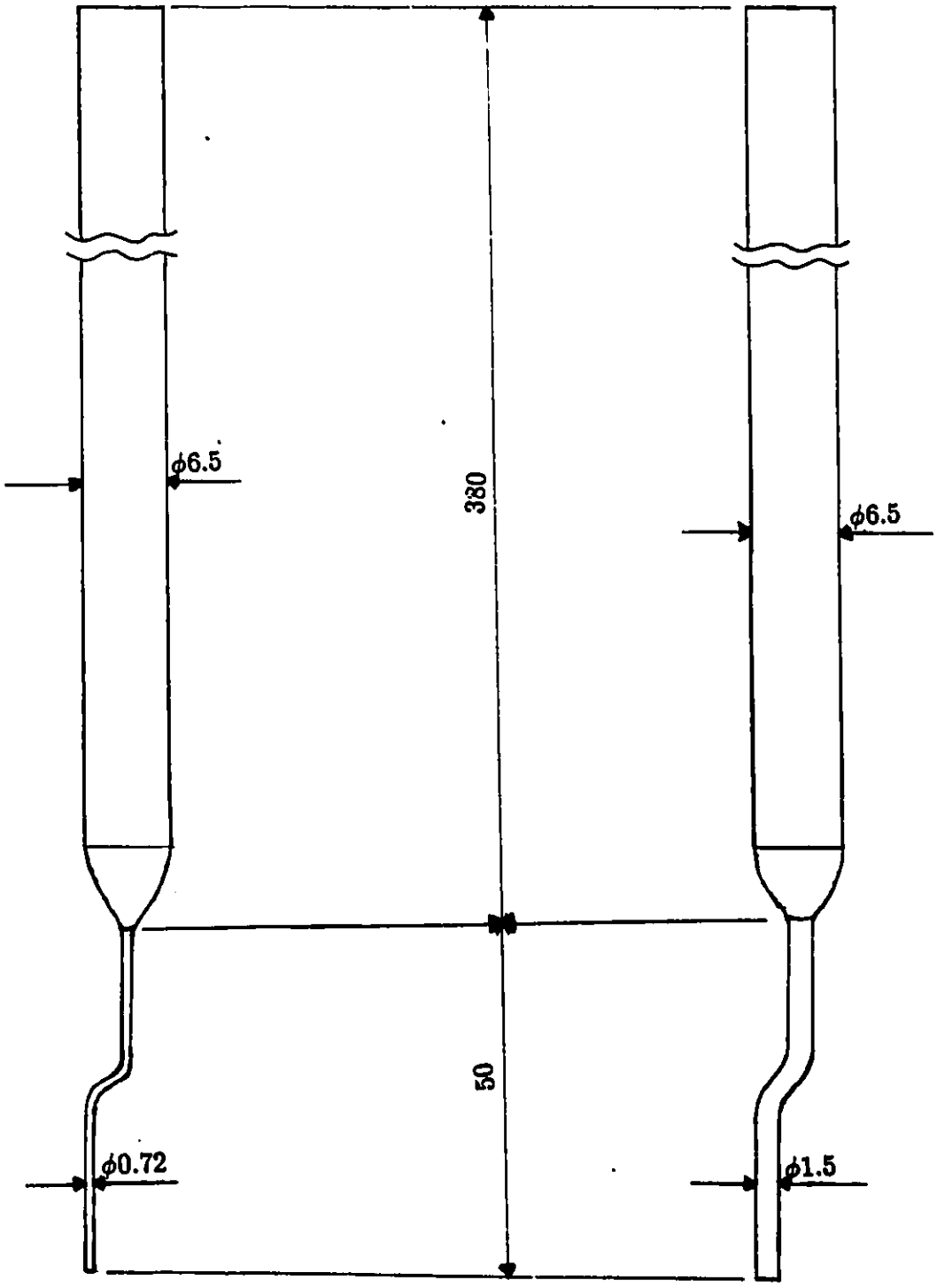

Figure 13. Preston tubes

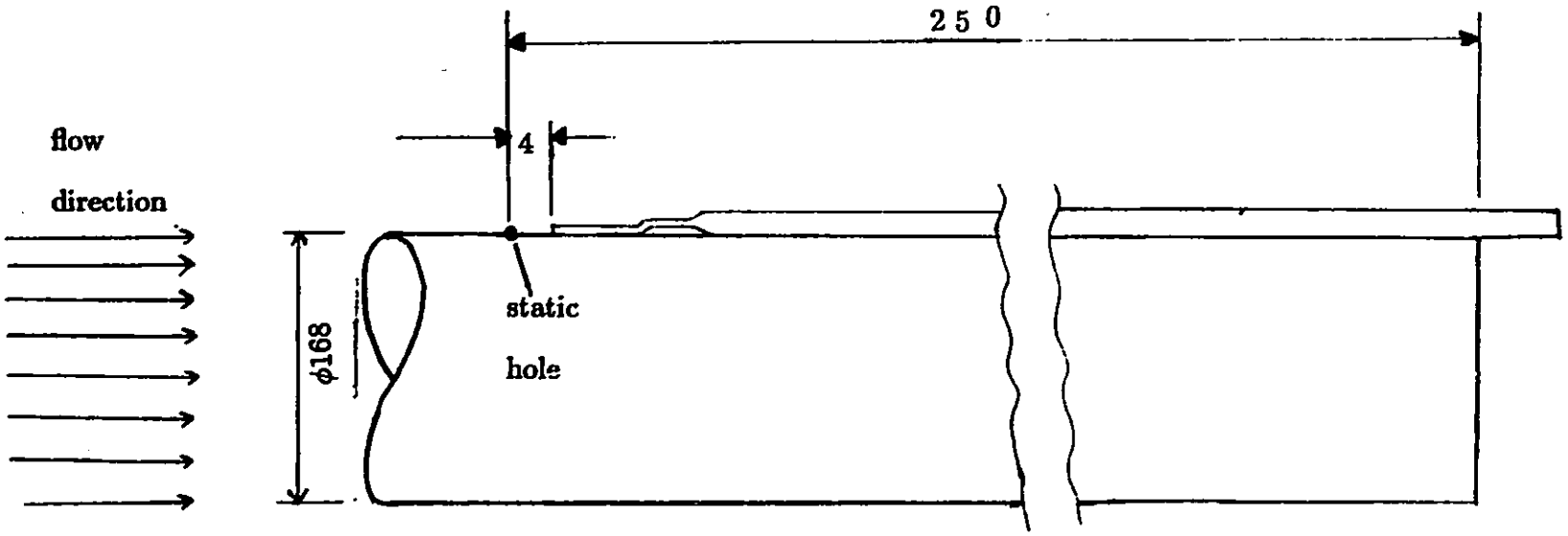

Figure 14. Positioning of the Preston tube

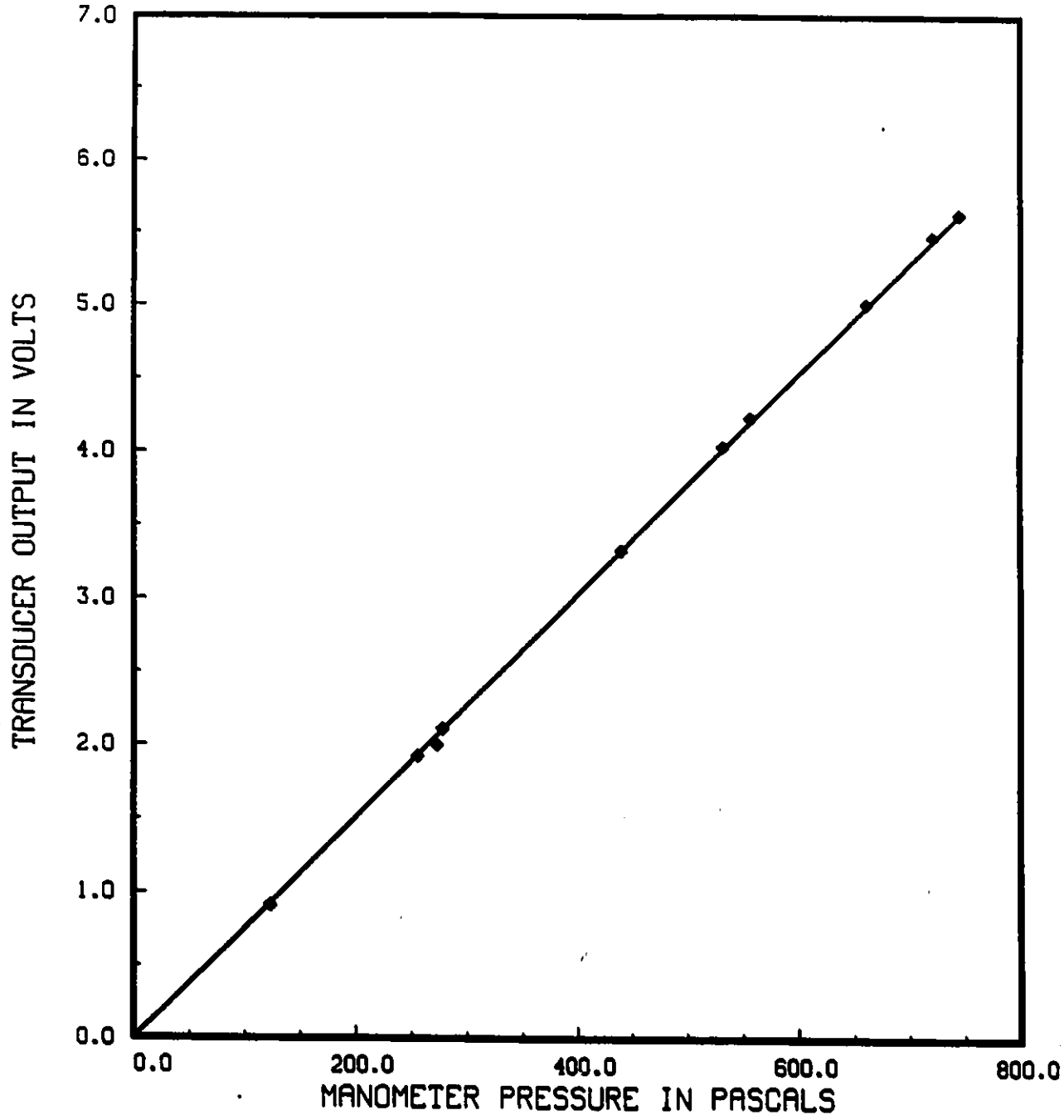

Figure 15. Calibration curve of pressure transducer

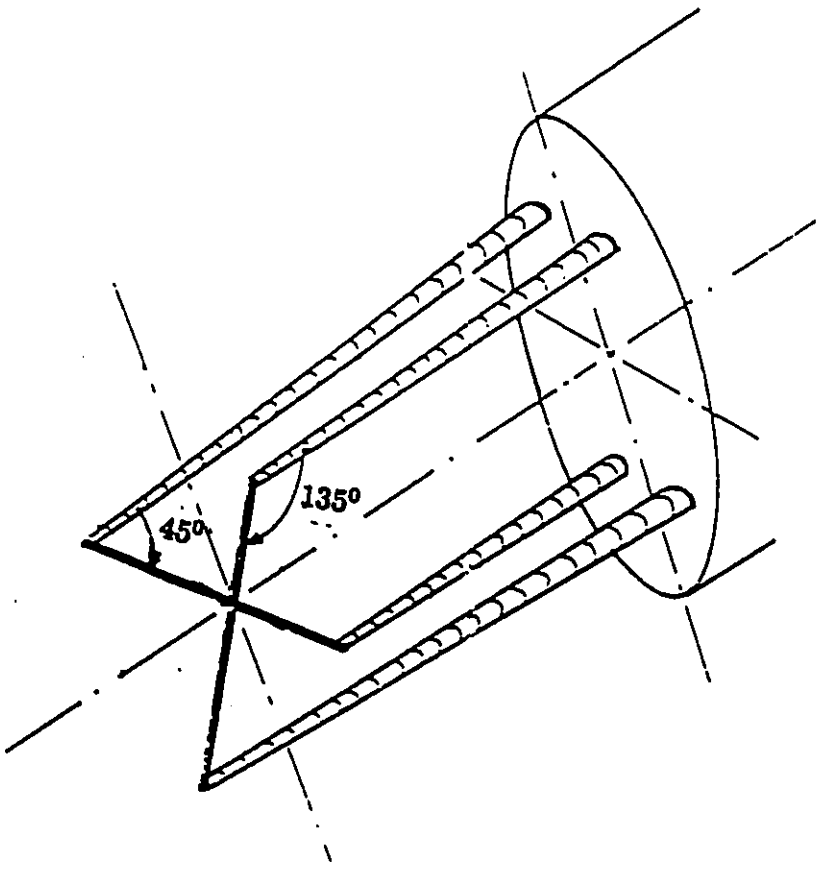

Figure 16. Sketch of the cross-wire probe

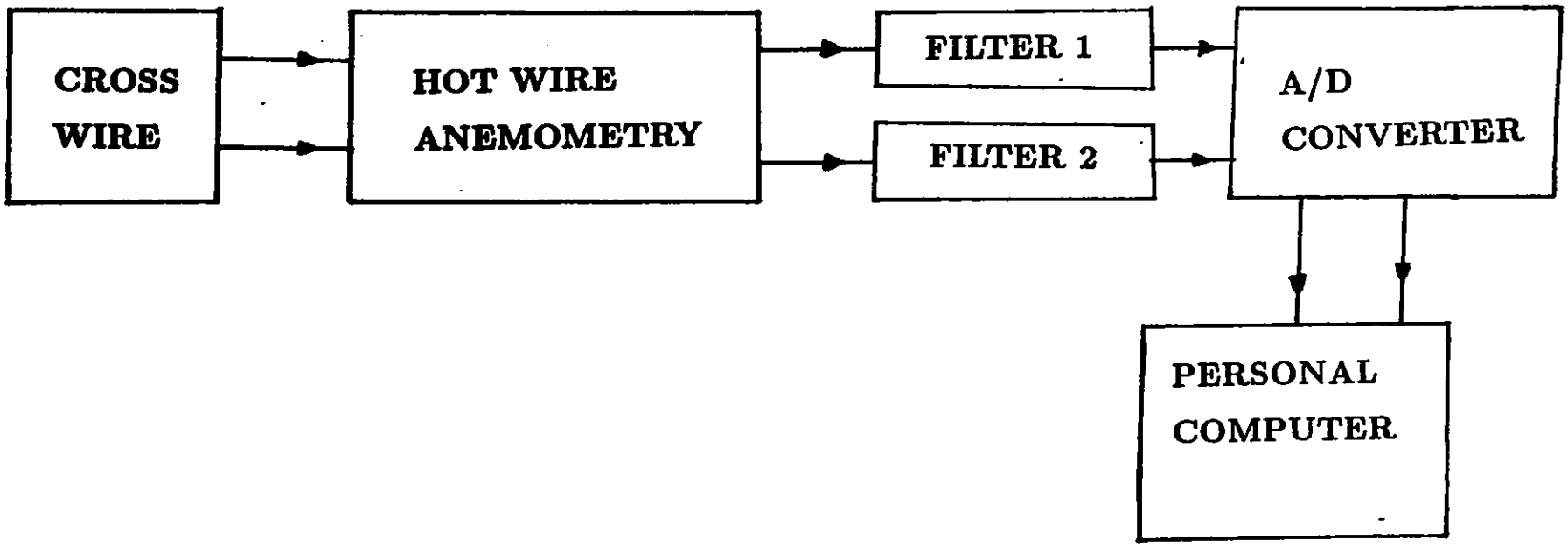

Figure 17. Data acquisition circuitry

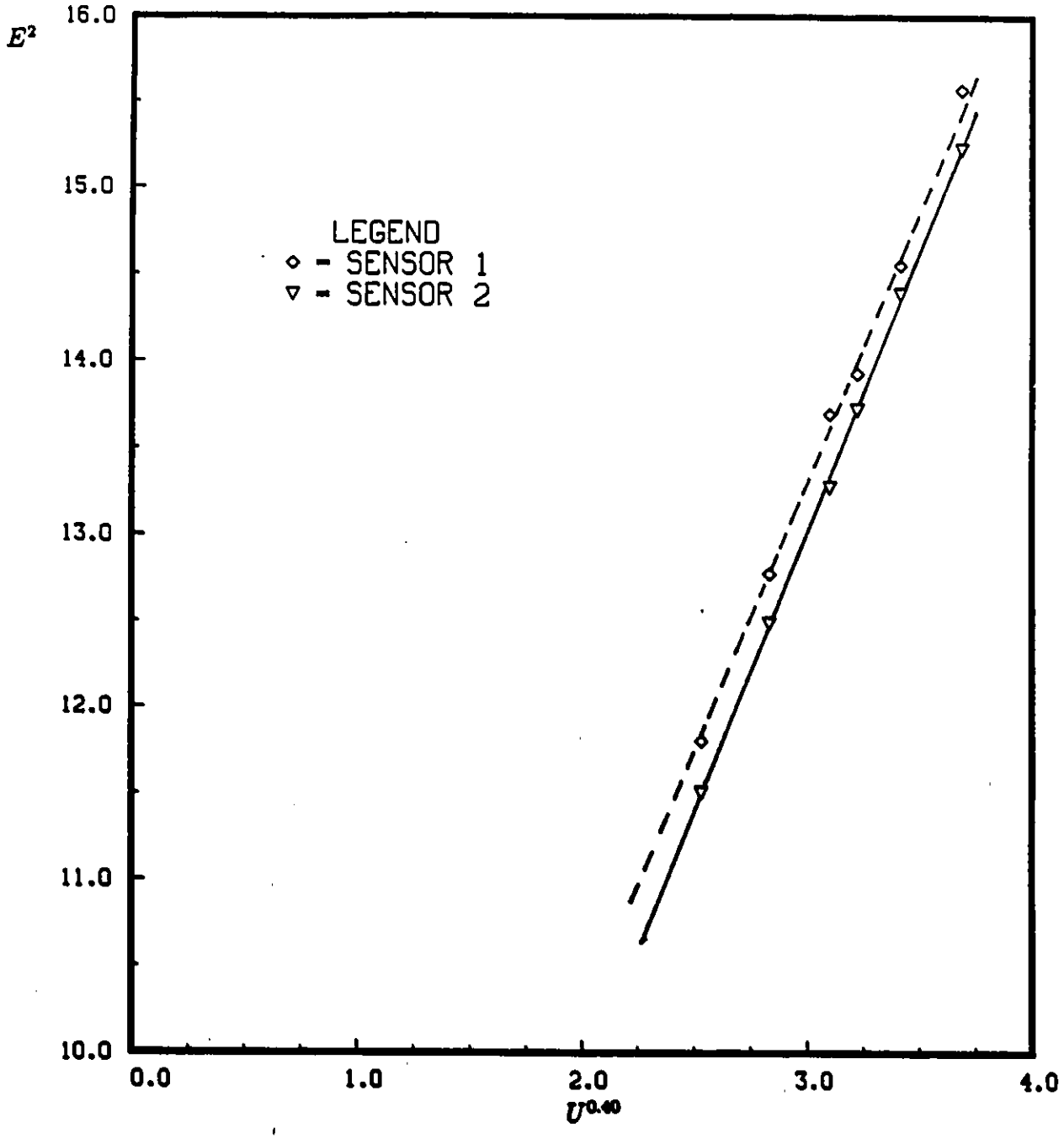

Figure 18. Typical calibration of cross wire probe Equations (5-22) and (5-23), $A_1 = 3.75507$, $B_1 = 3.26534$, $n_1 = 0.4$, $A_2 = 3.3882$, $B_2 = 3.28834$, $n_2 = 0.4$

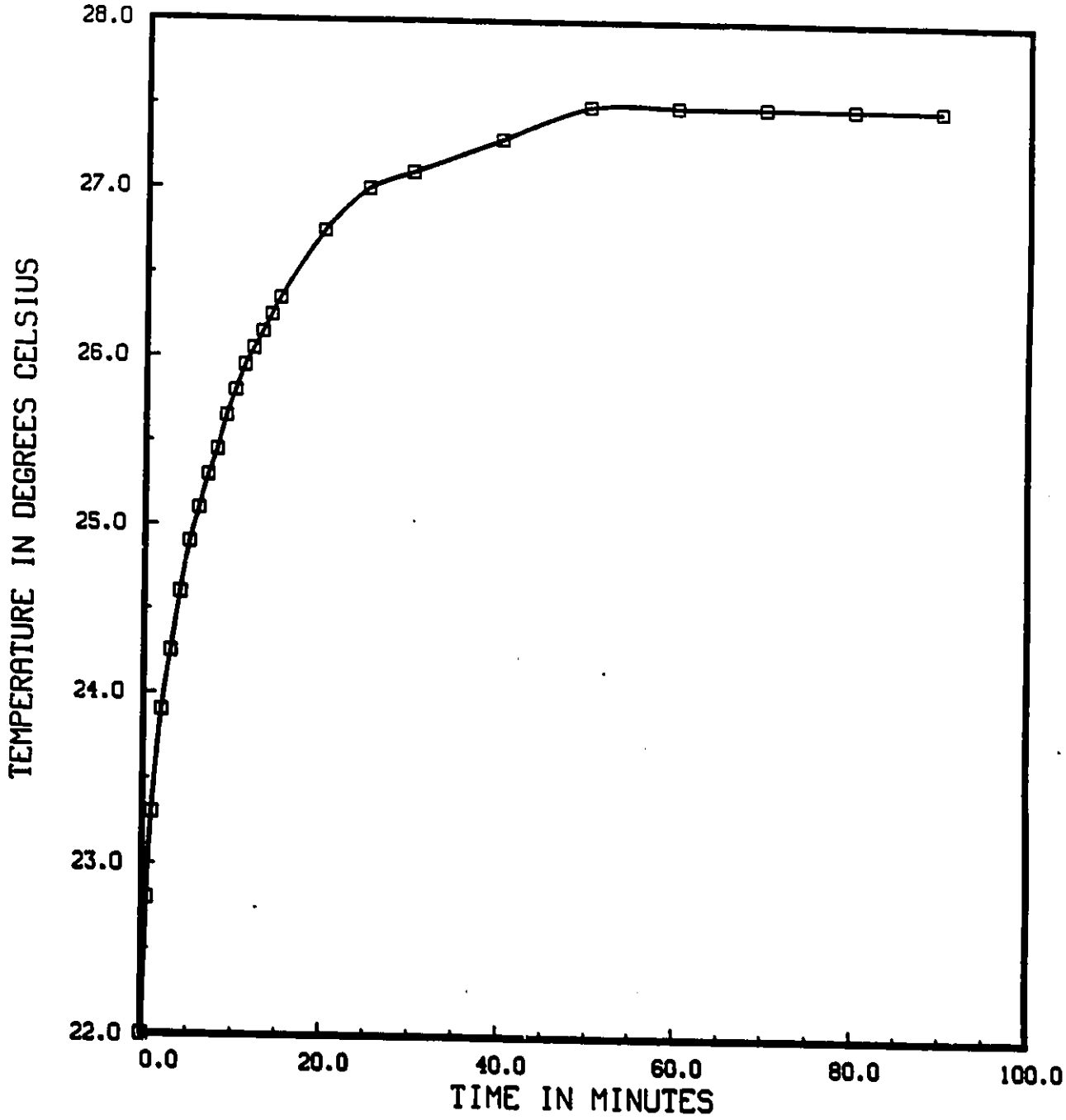

Figure 19. Flow temperature as a function of duct operating time

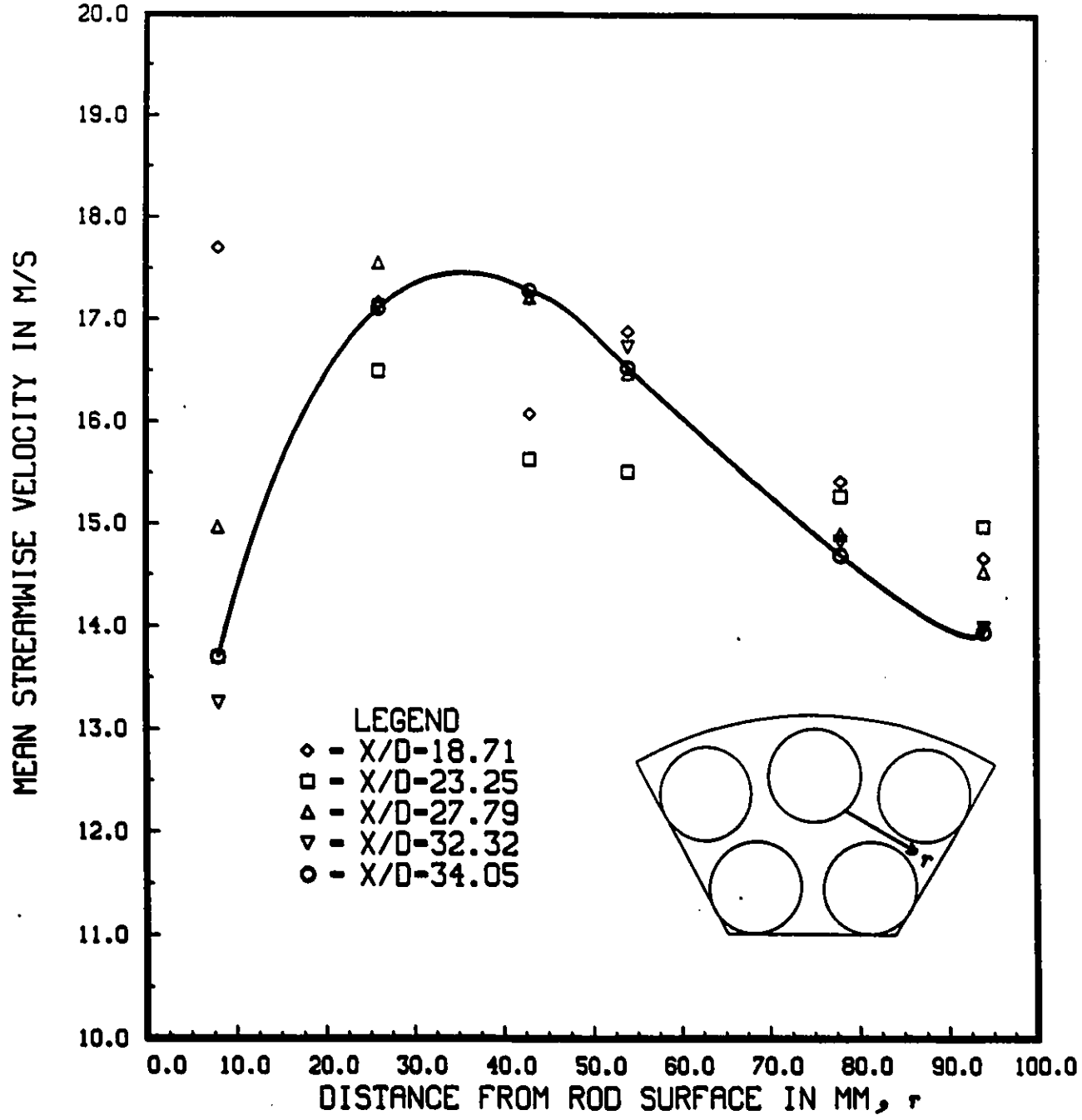

Figure 20. Velocity profiles at different downstream locations

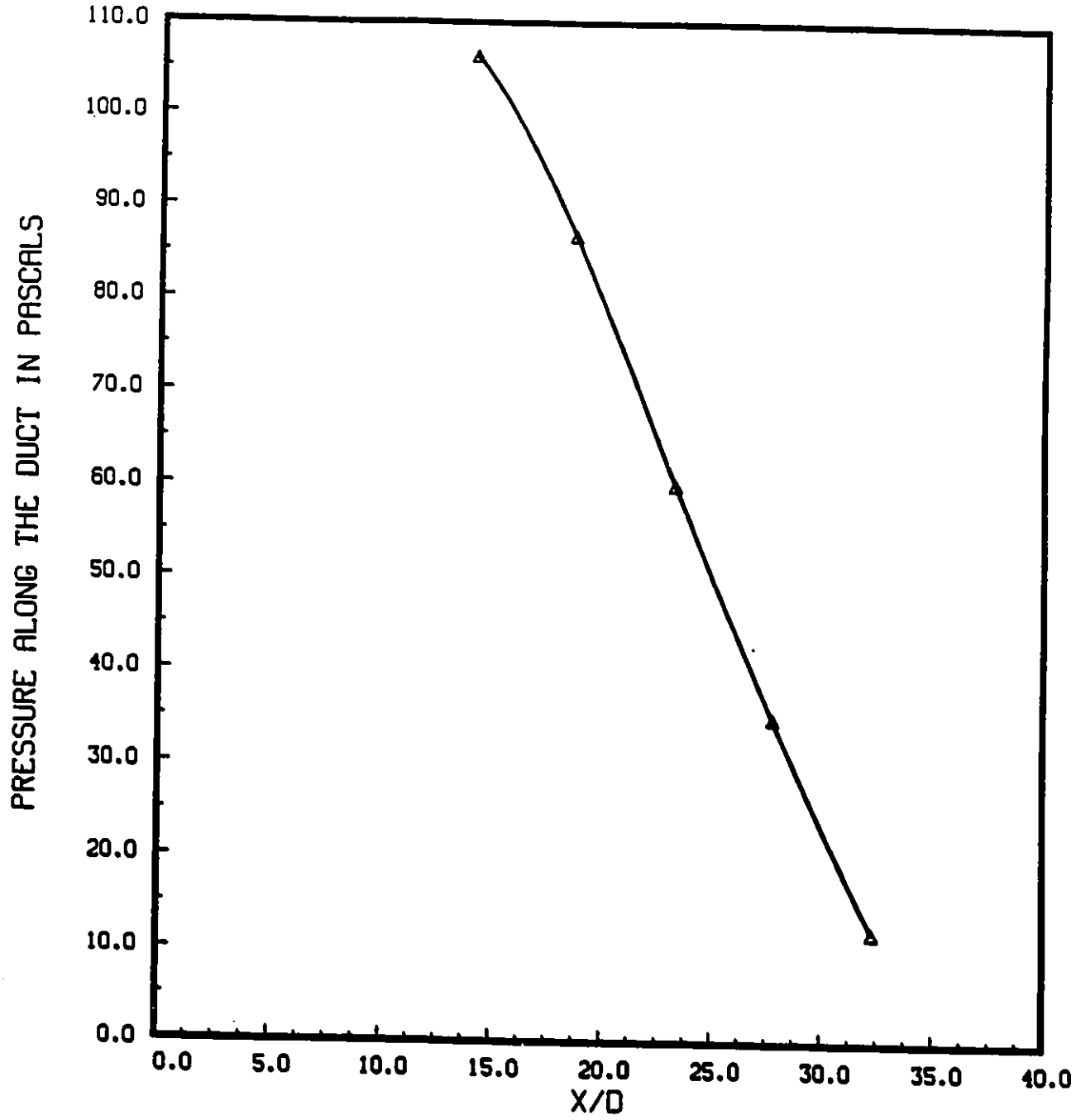

Figure 21. Mean static pressure drop along the duct for the design geometry

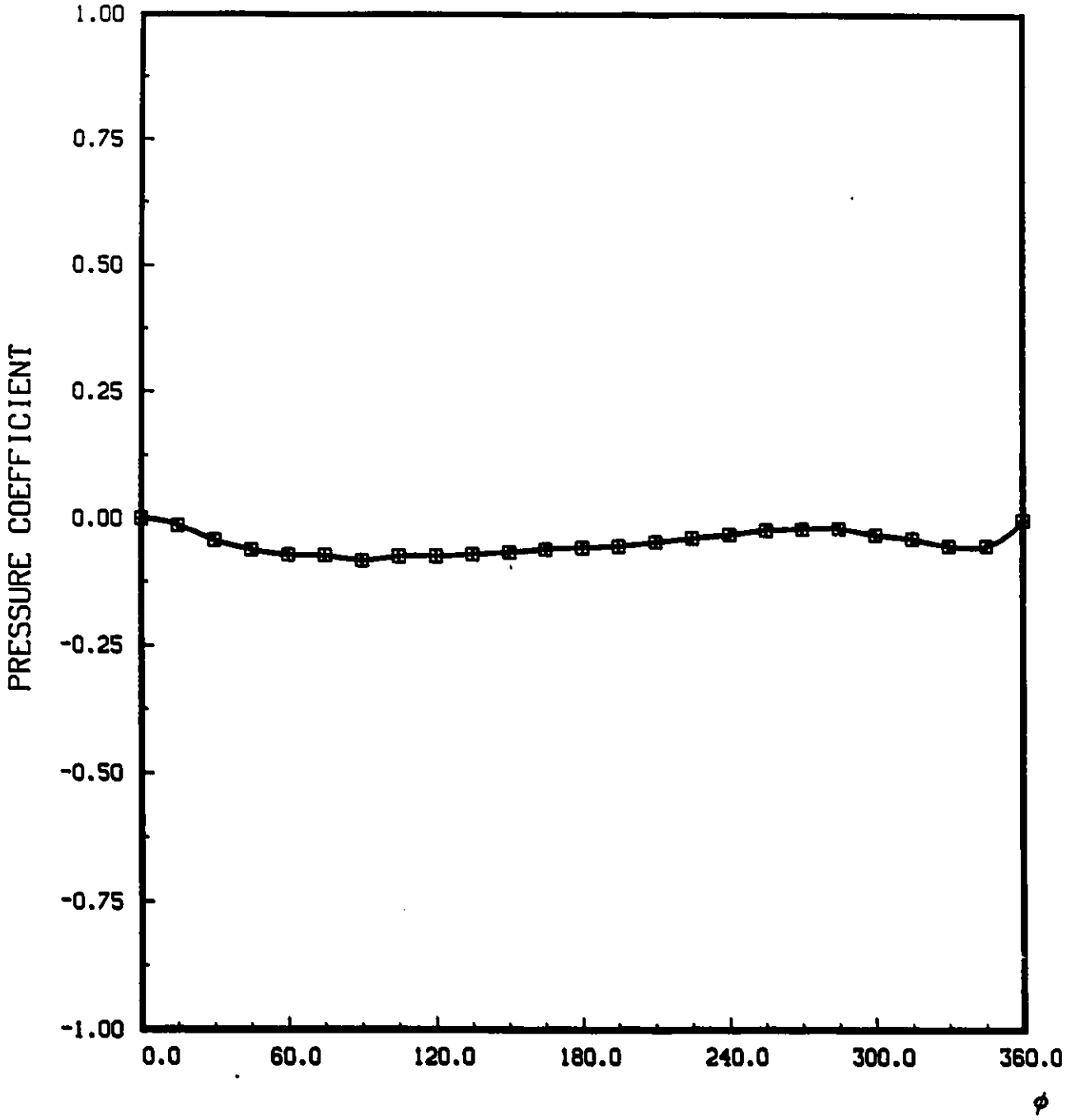

Figure 22. Wall static pressure variation around rod periphery

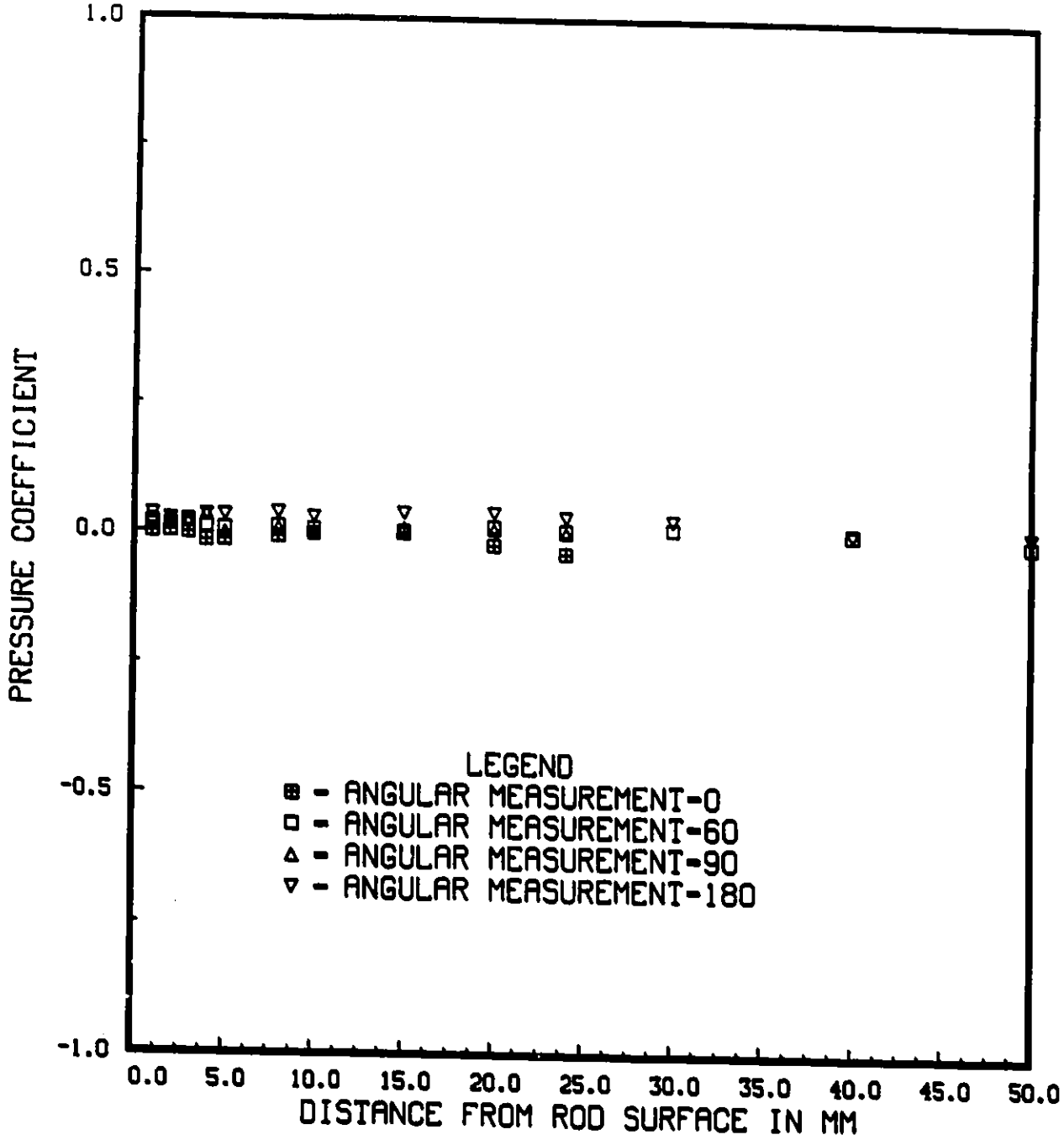

Figure 23. Inflow mean static pressure variation

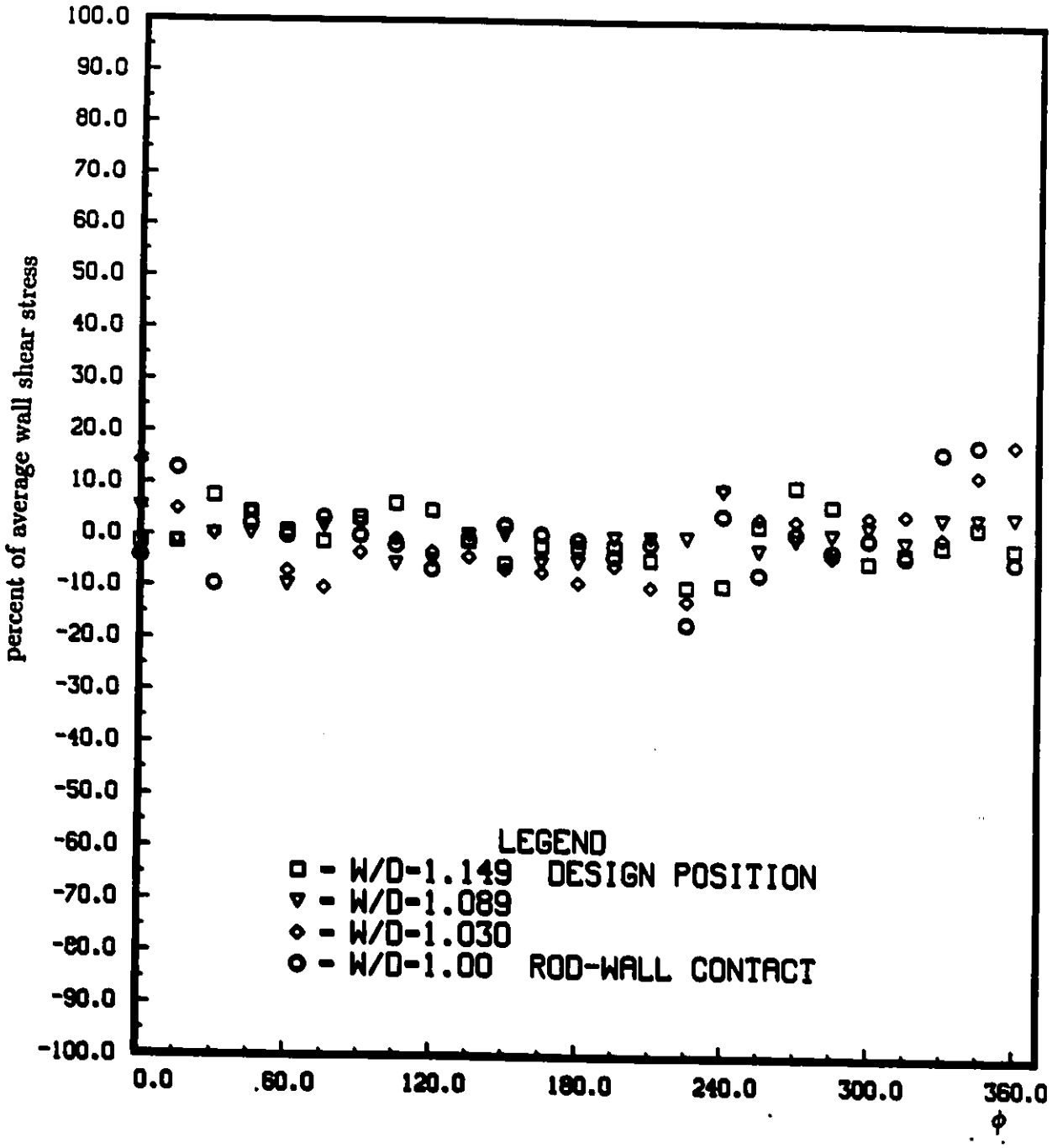

Figure 24. Differences of wall shear stress readings using two Preston tubes with different diameters

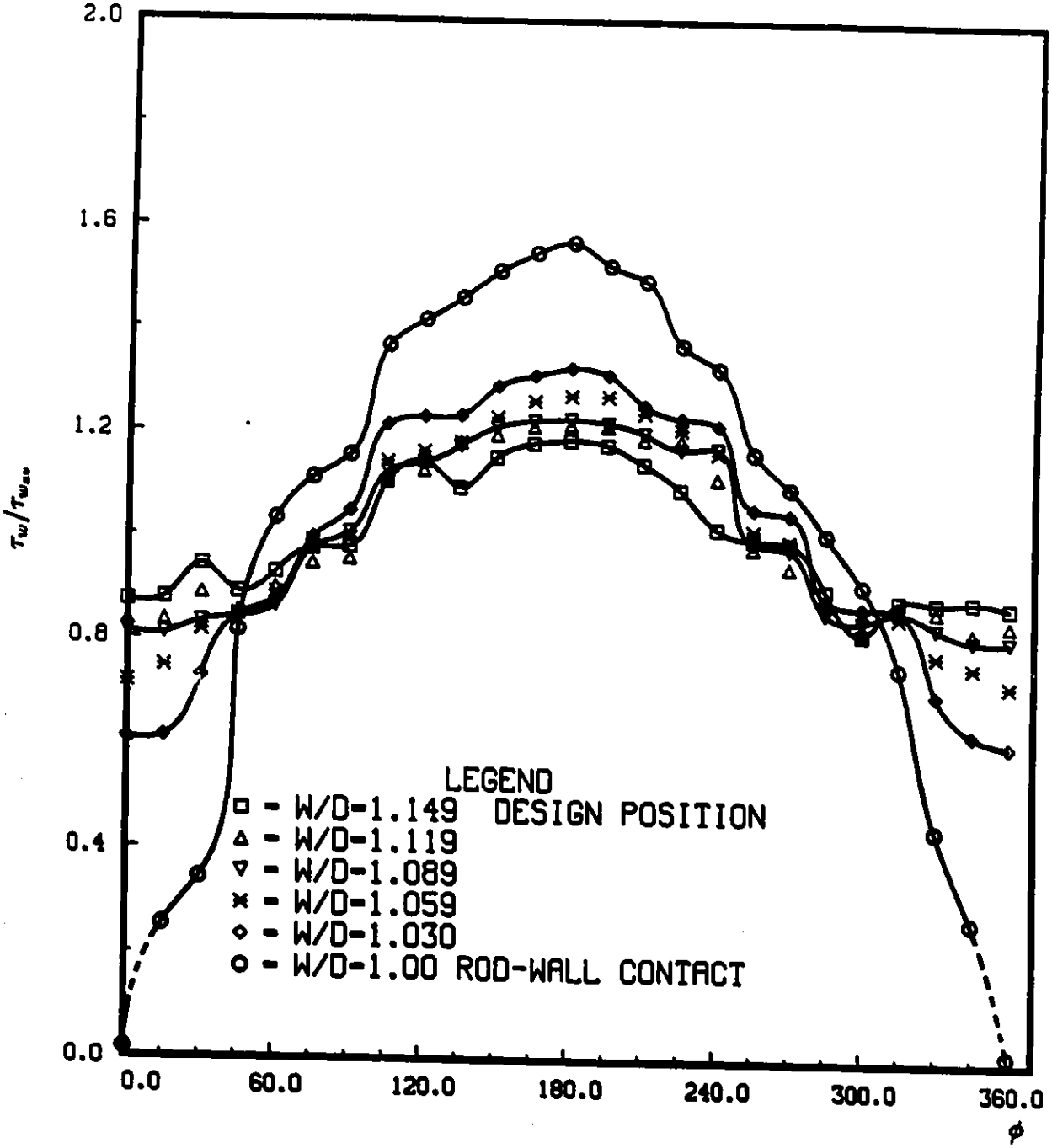

Figure 25. Distribution of wall shear stress around the central rod for the design geometry and with the rod displaced towards the wall

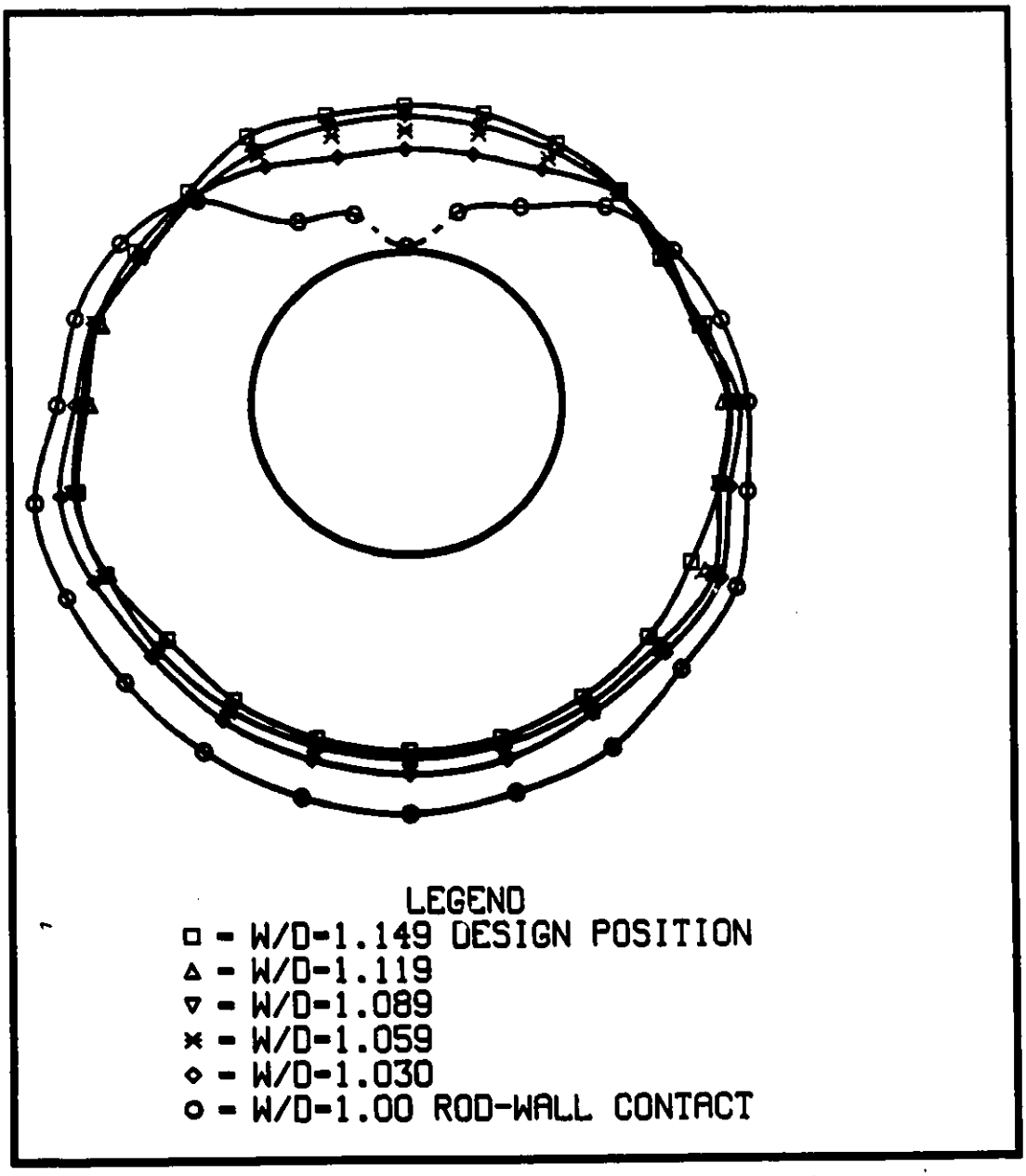

Figure 26. Distribution of wall shear stress around the central rod for the design geometry and with the rod displaced towards the wall

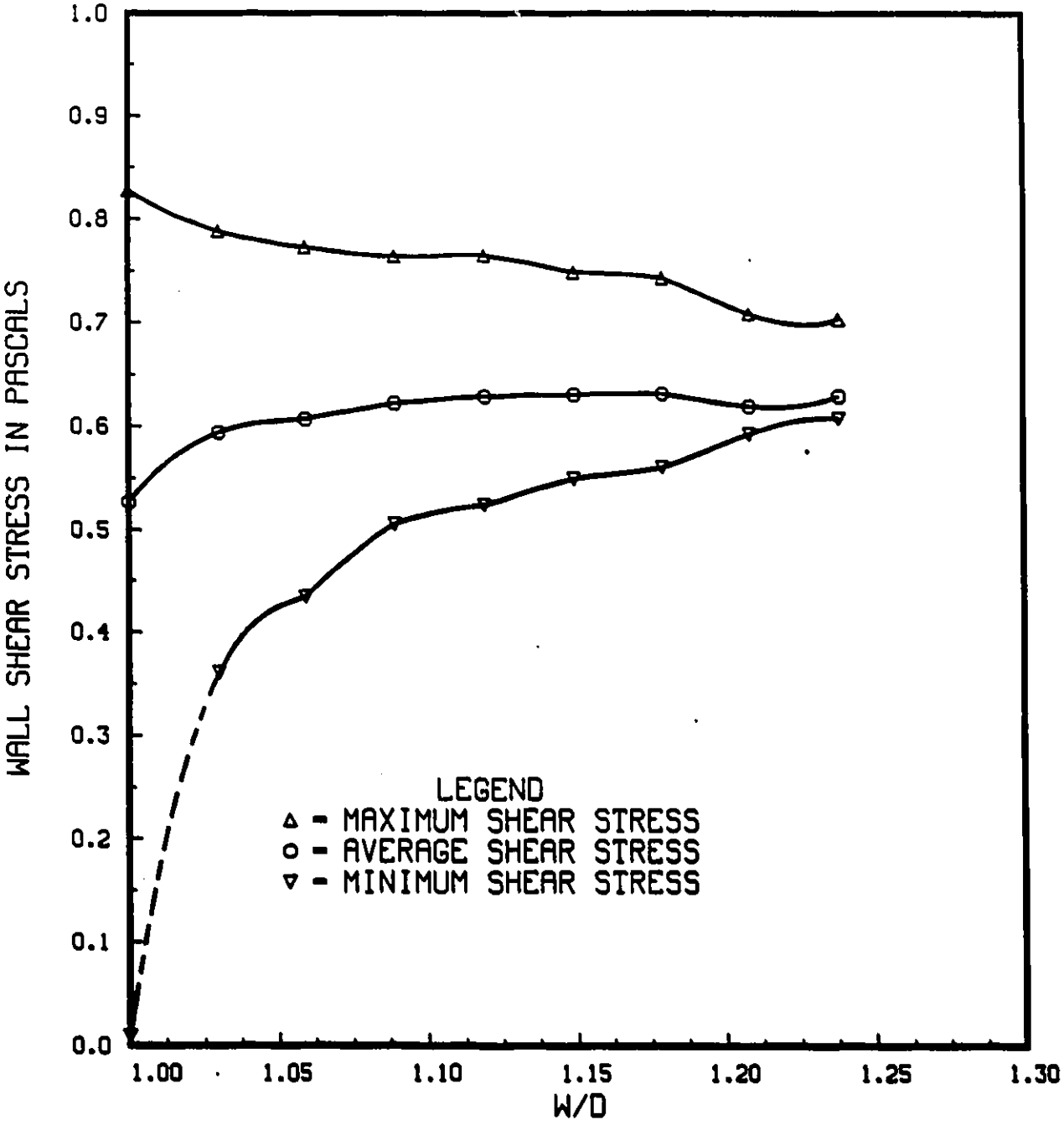

Figure 27. Variation of maximum, average and minimum wall shear stress with W/D

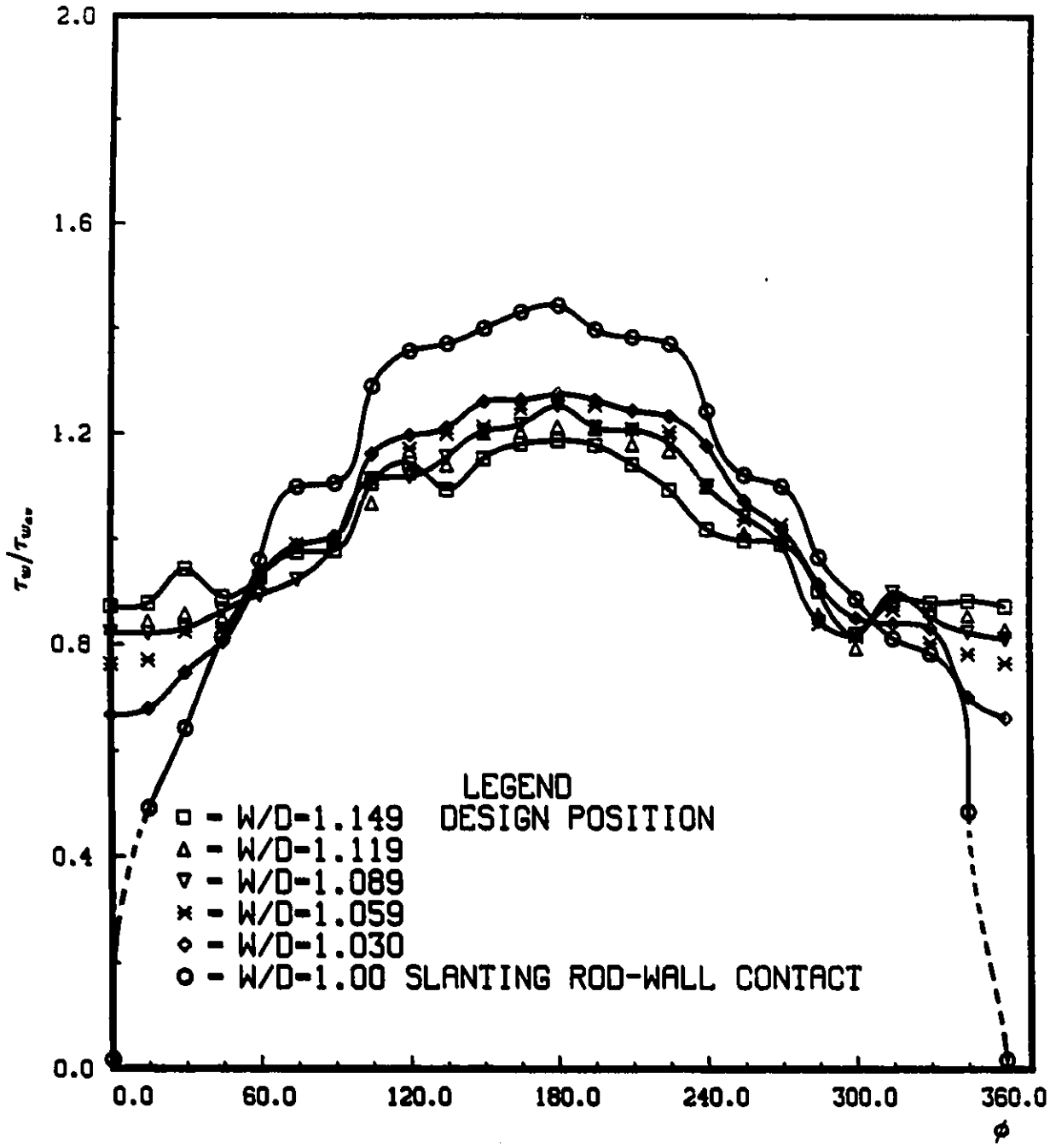

Figure 28. Distribution of wall shear stress around the central rod for the design geometry and with one end of the rod displaced towards the wall

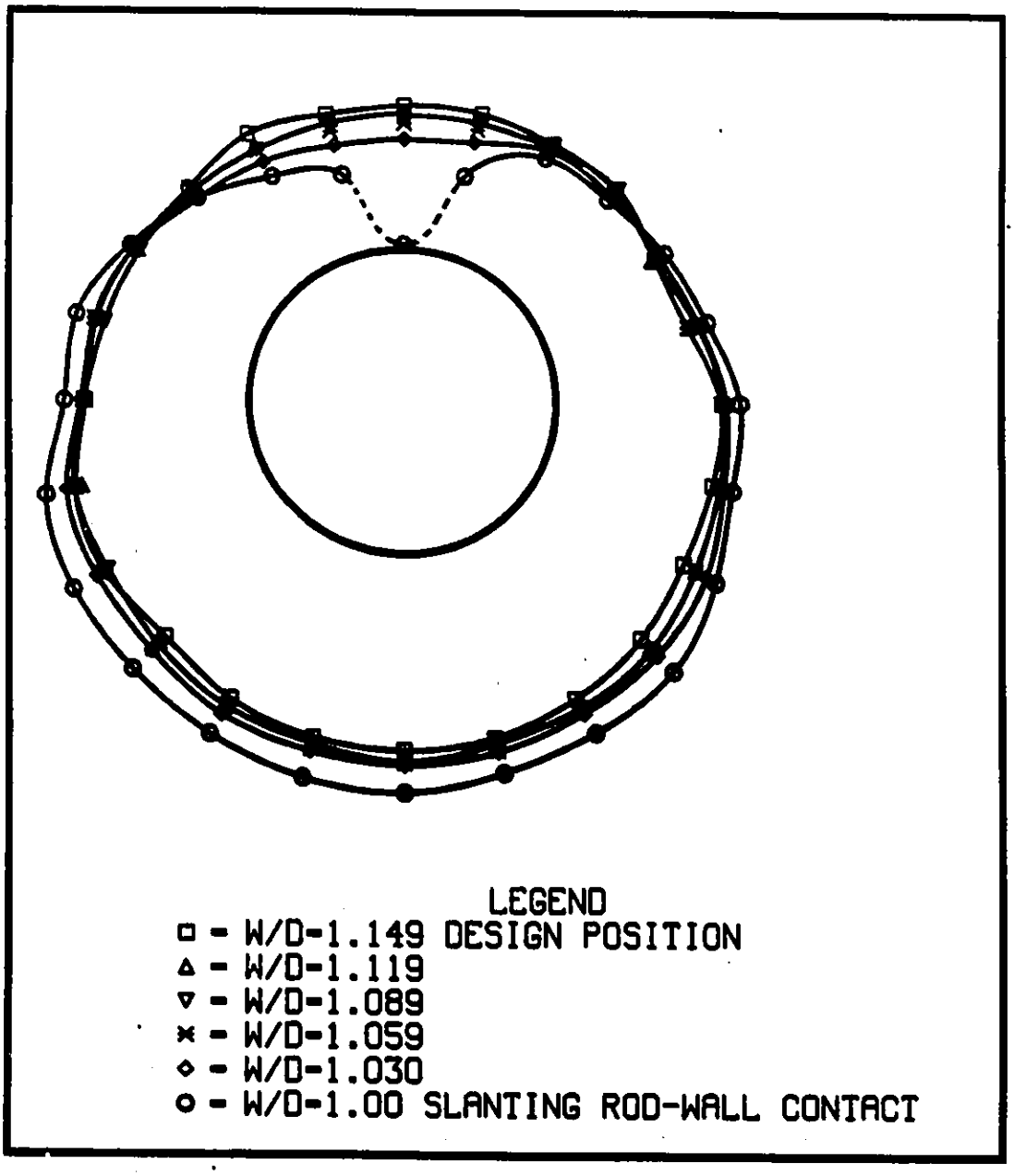

Figure 29. Distribution of wall shear stress around the central rod slanting towards the wall

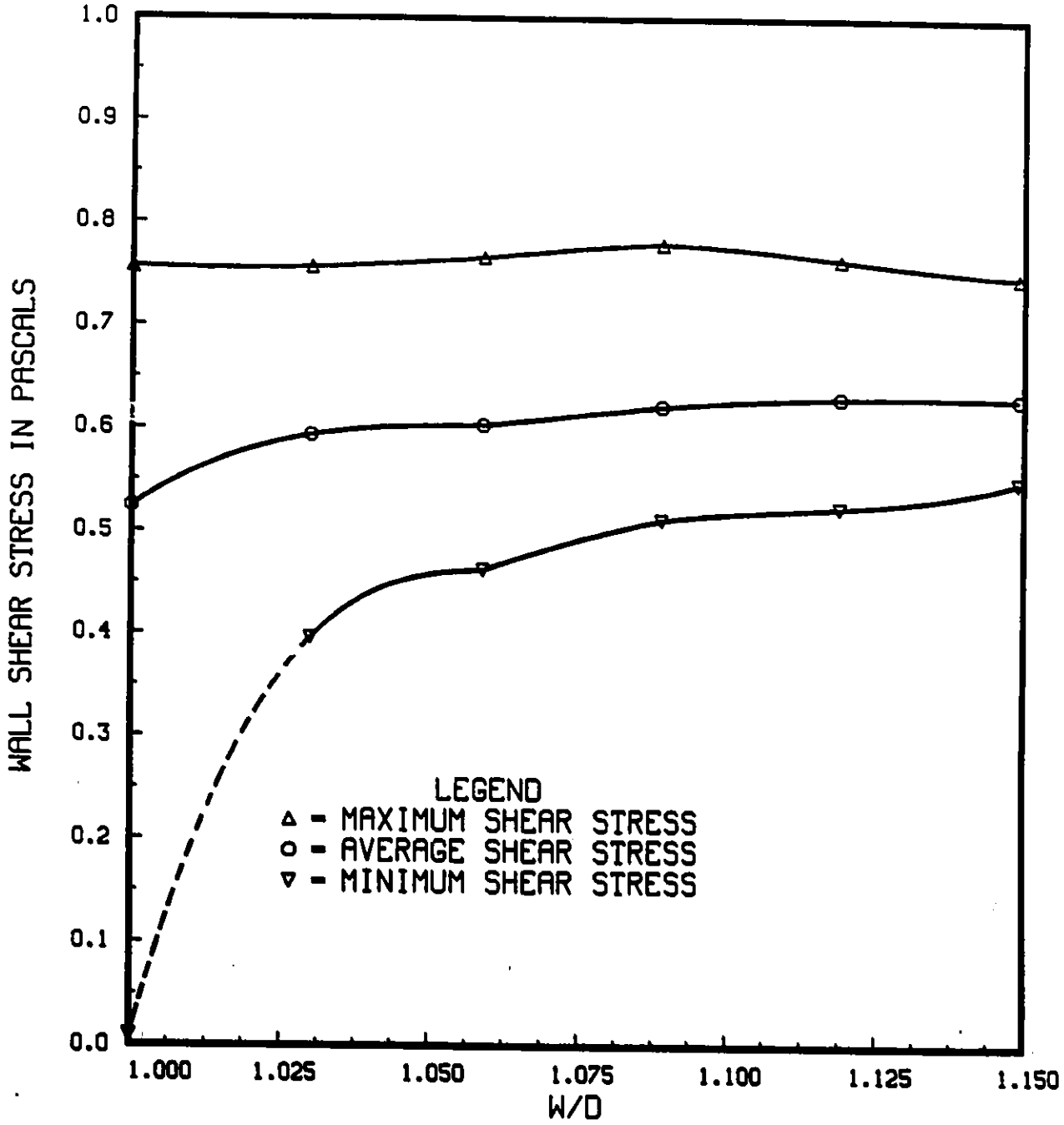

Figure 30. Variation of maximum, average and minimum wall shear stress on the slanting rod with W/D

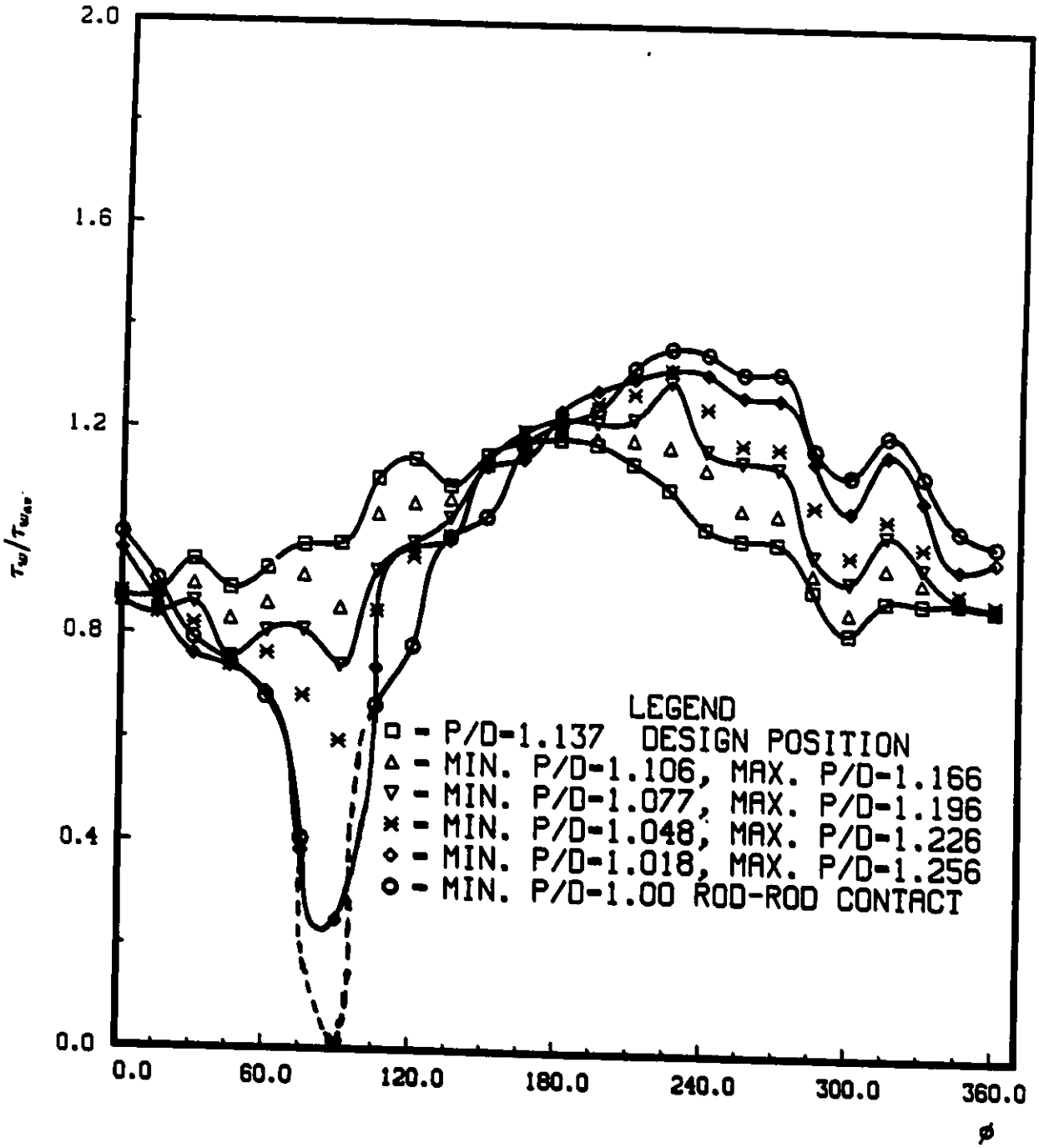

Figure 31. Distribution of wall shear stress around the central rod with the rod displaced towards a neighboring one

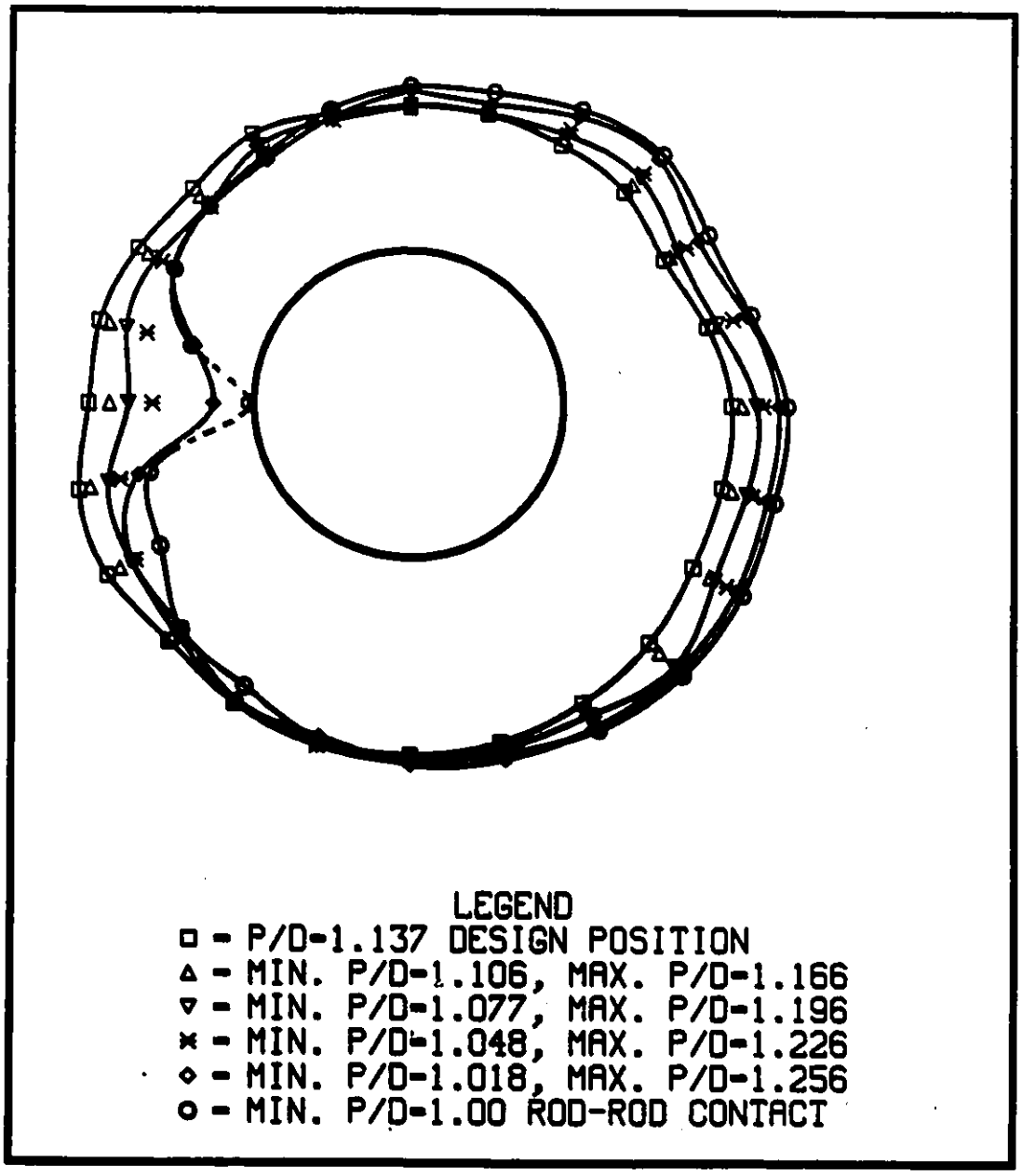

Figure 32. Distribution of wall shear stress around the central rod with the rod displaced towards a neighboring one

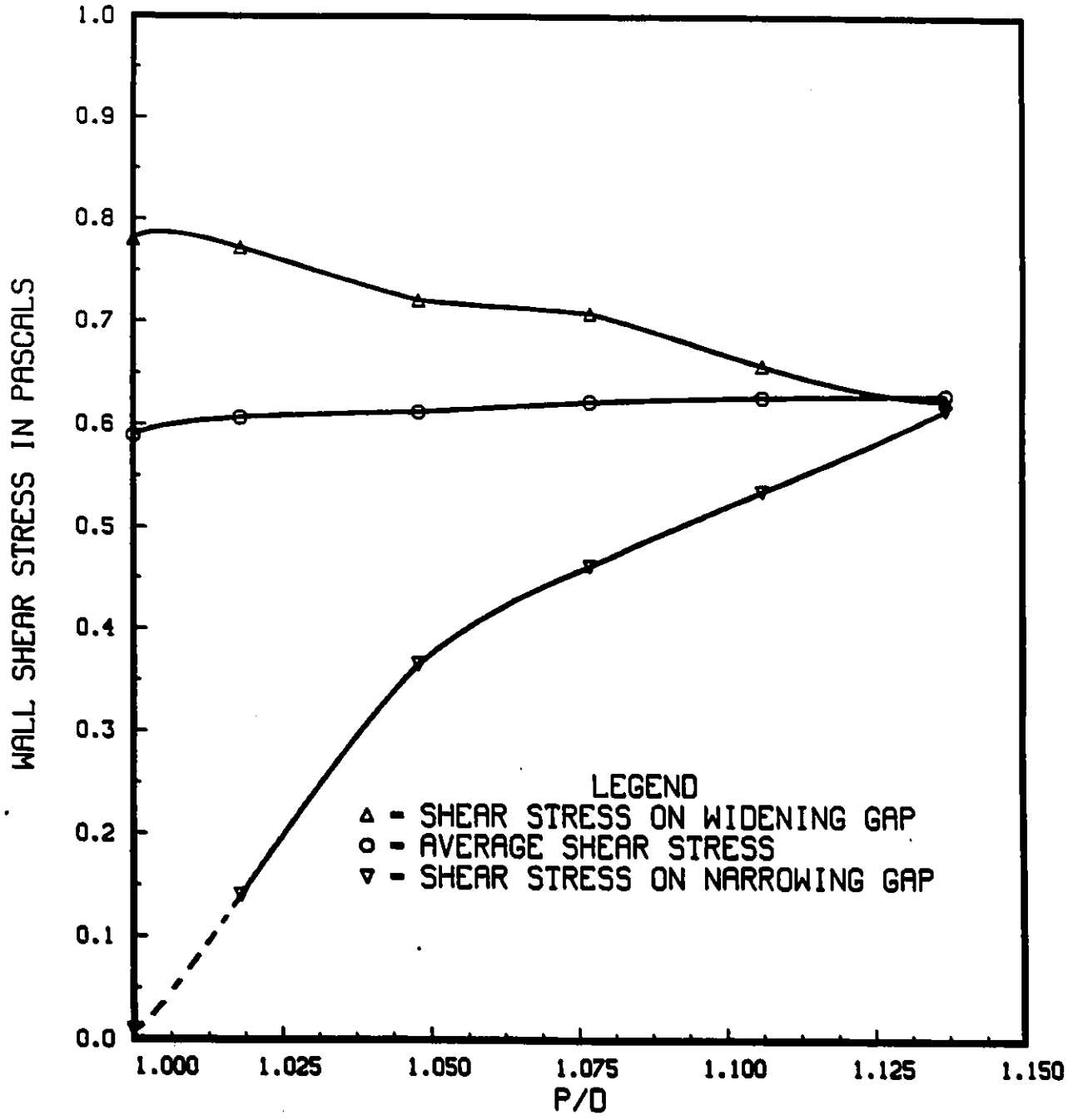

Figure 33. Variation of average wall shear stress and wall shear stresses on rod surfaces facing rod gaps with P/D

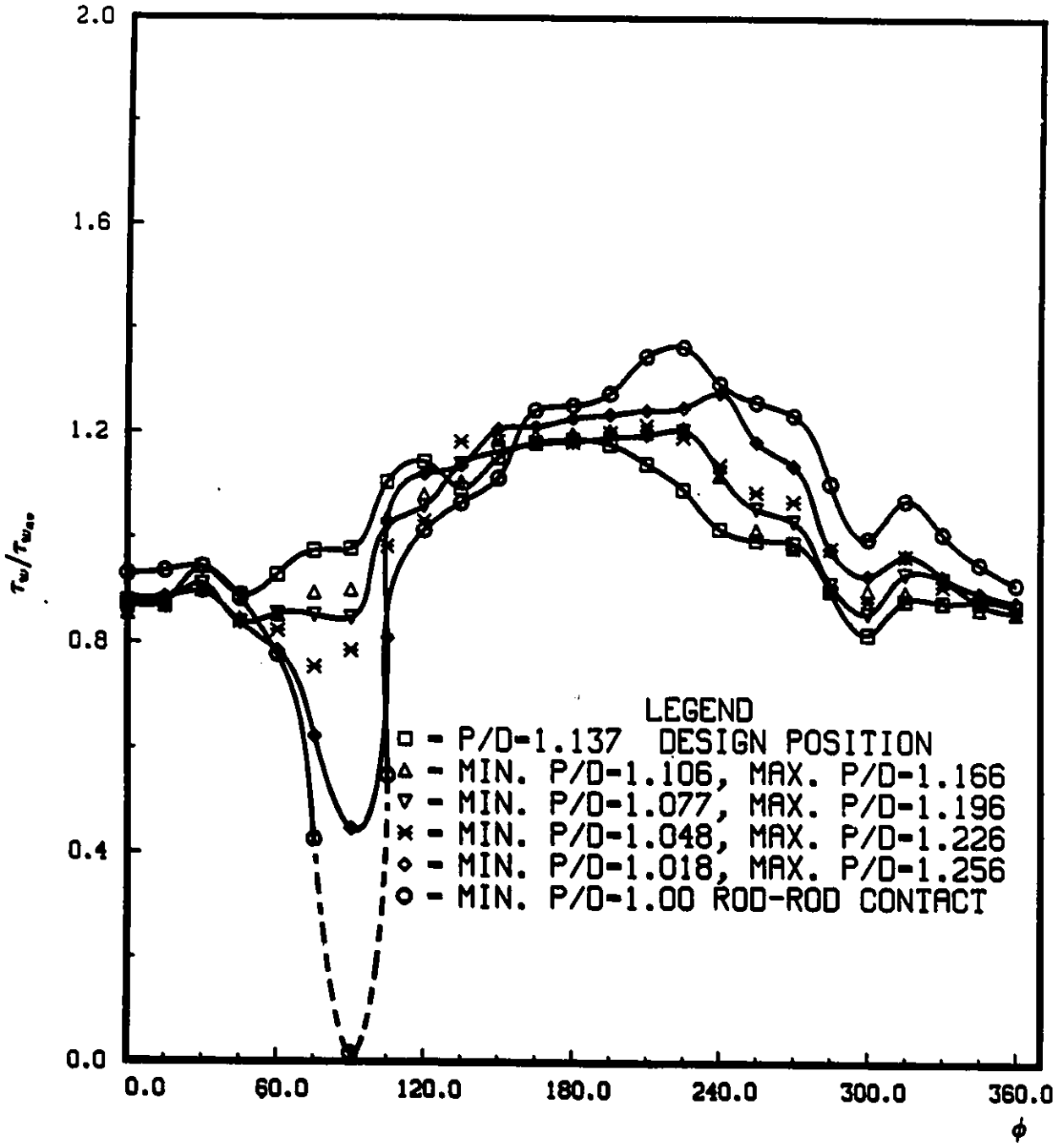

Figure 34. Distribution of wall shear stress around the central rod slanting towards a neighboring one

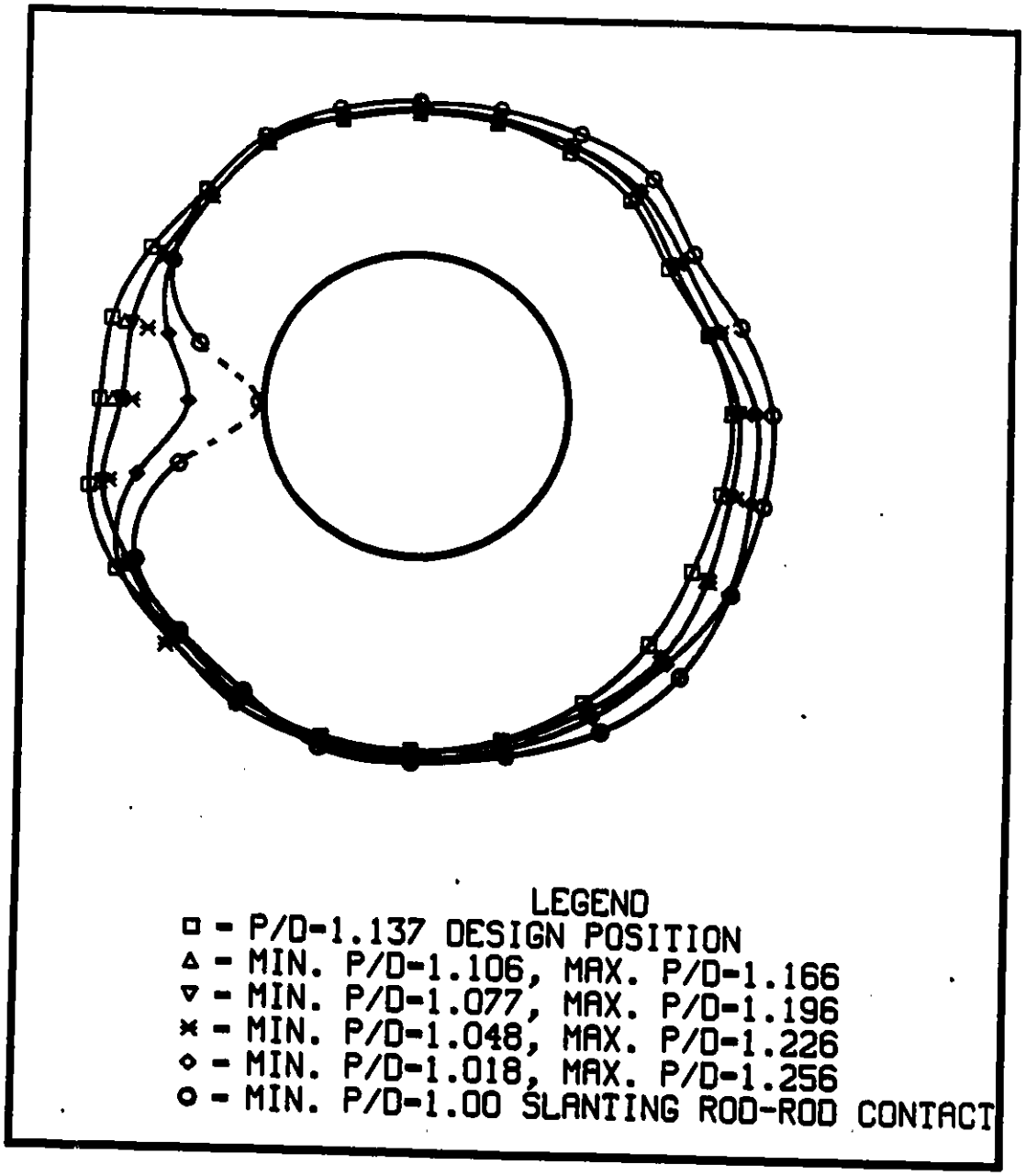

Figure 35. Distribution of wall shear stress around the central rod slanting towards a neighboring one

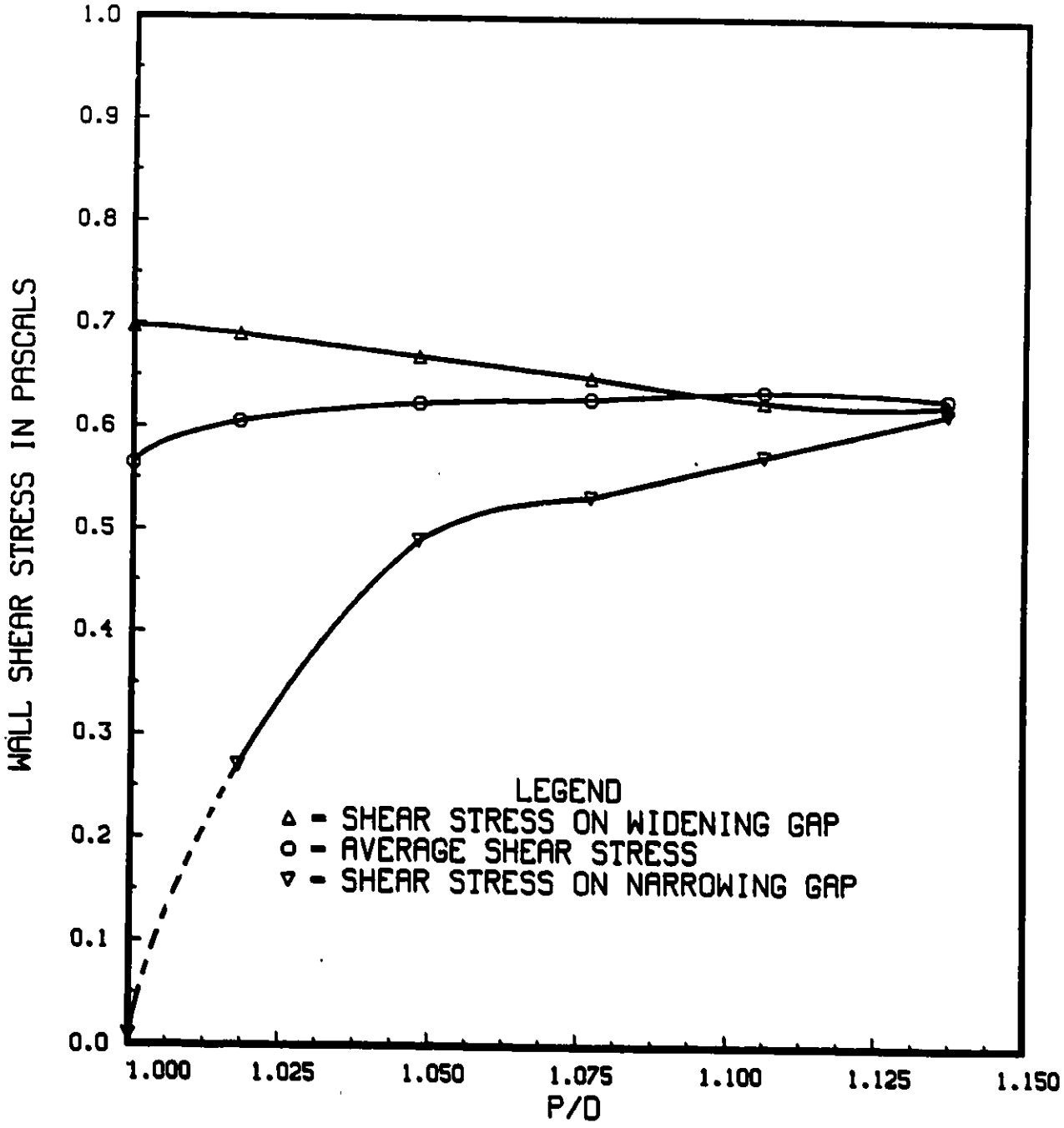

Figure 36. Variation of average wall shear stress and wall shear stresses on slanting rod surfaces facing rod gaps with P/D

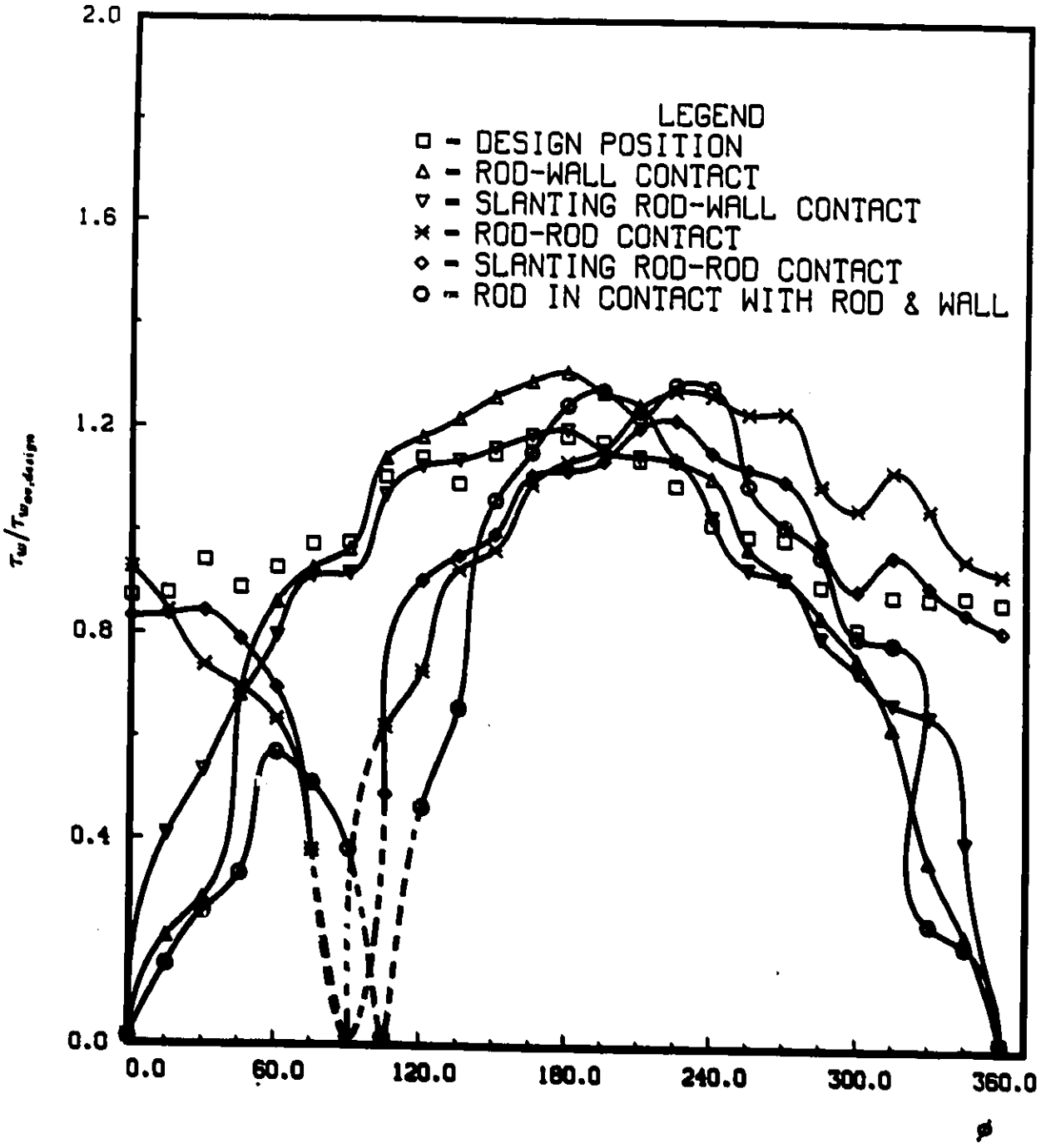

Figure 37. Distribution of wall shear stress around central rod at various positions

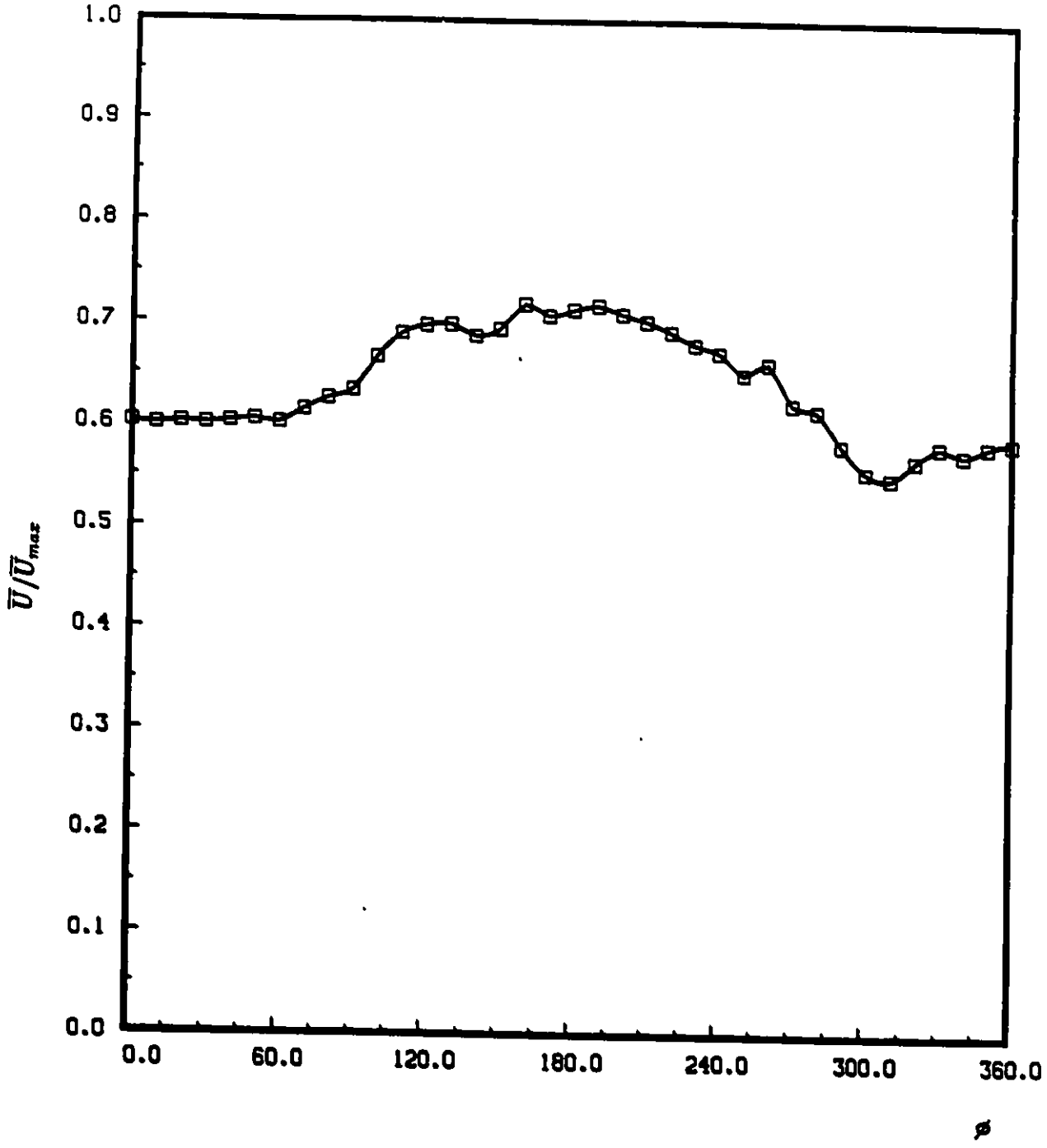

Figure 38. Peripheral variation of axial mean velocity at 2 mm from the rod surface (design geometry)

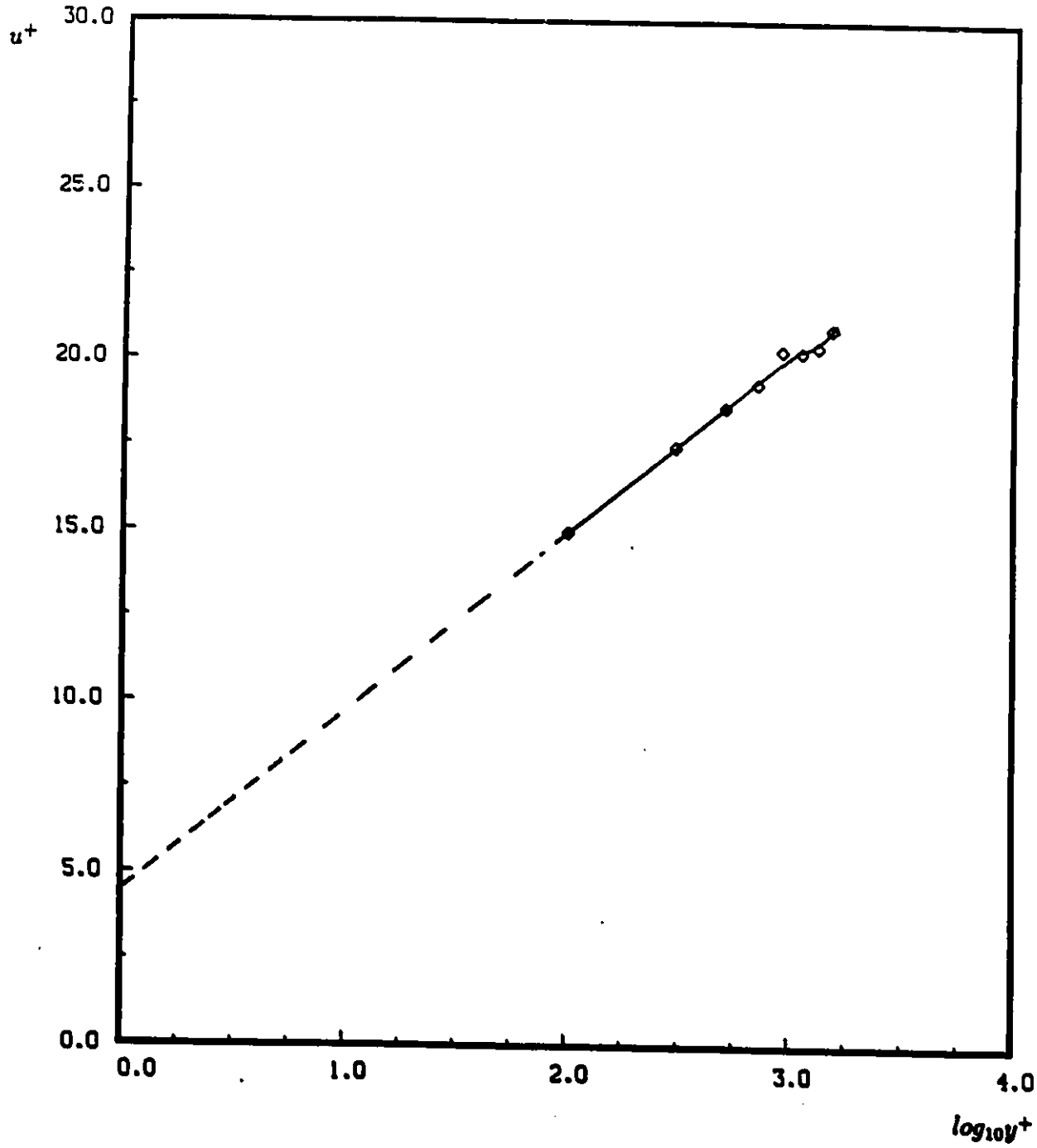

Figure 39. Axial velocity distribution at $\phi = 180^0$ obtained by single hot wire

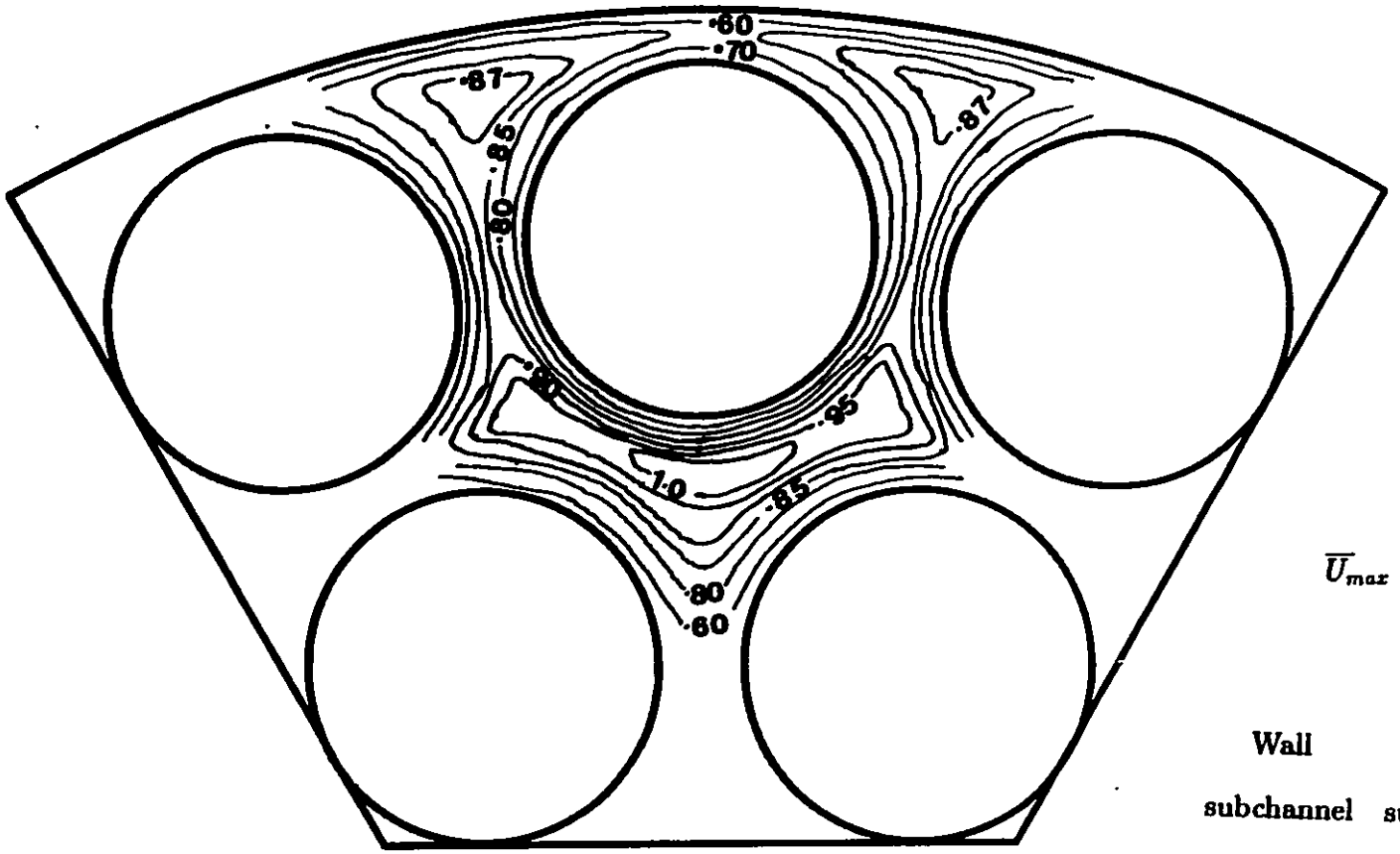

$\overline{U}_{max} = 16.80 m/s$

	Wall subchannel	Inner subchannel 1	Inner subchannel 2
U_b	12.63	13.10	13.95

Figure 40. Isovel contours at design condition

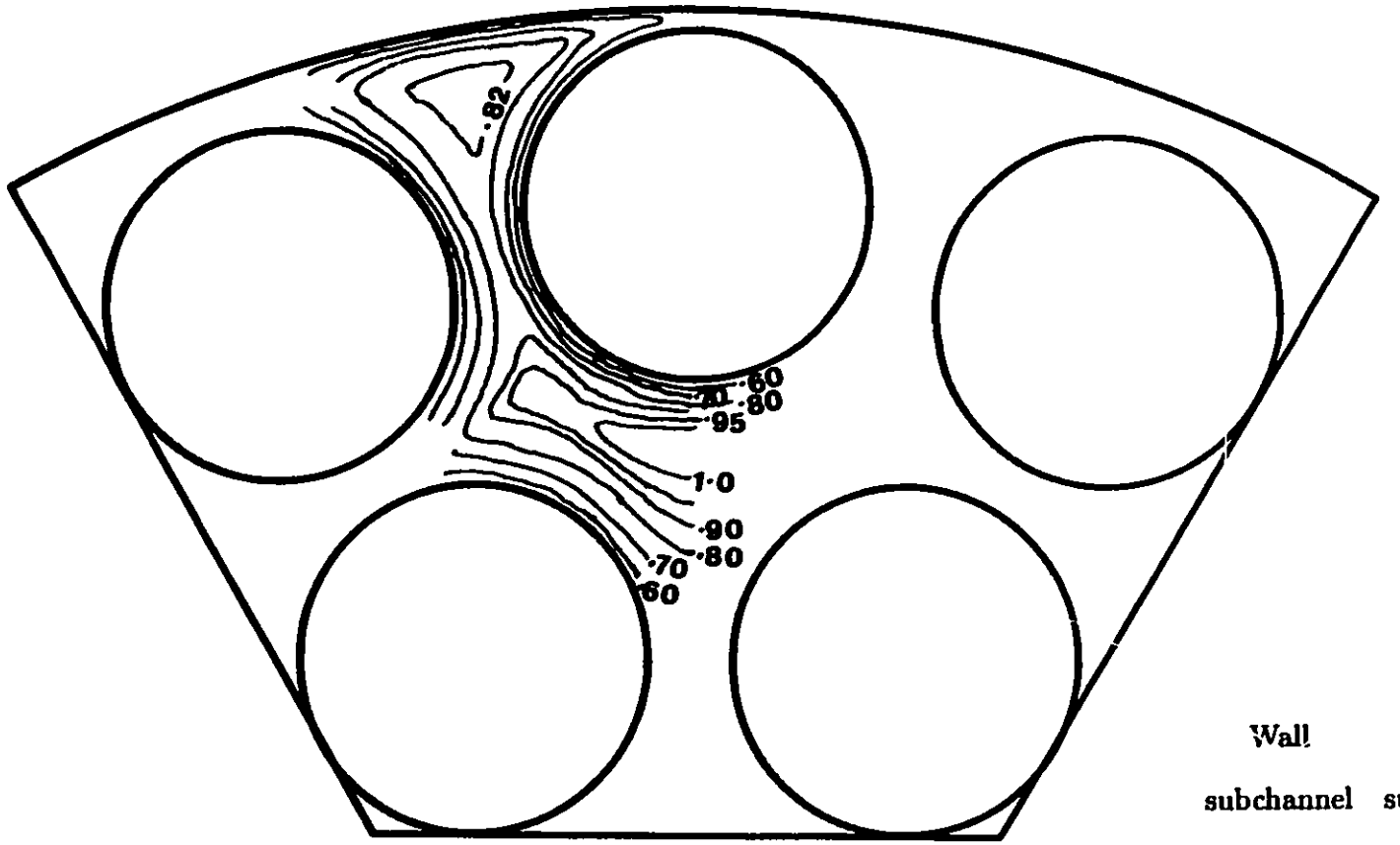

$\overline{U}_{max} = 16.66 m/s$

	Wall subchannel	Inner subchannel 1	Inner subchannel 2
U_b	12.26	13.18	13.99

Figure 41. Isovel contours at W/D=1.059

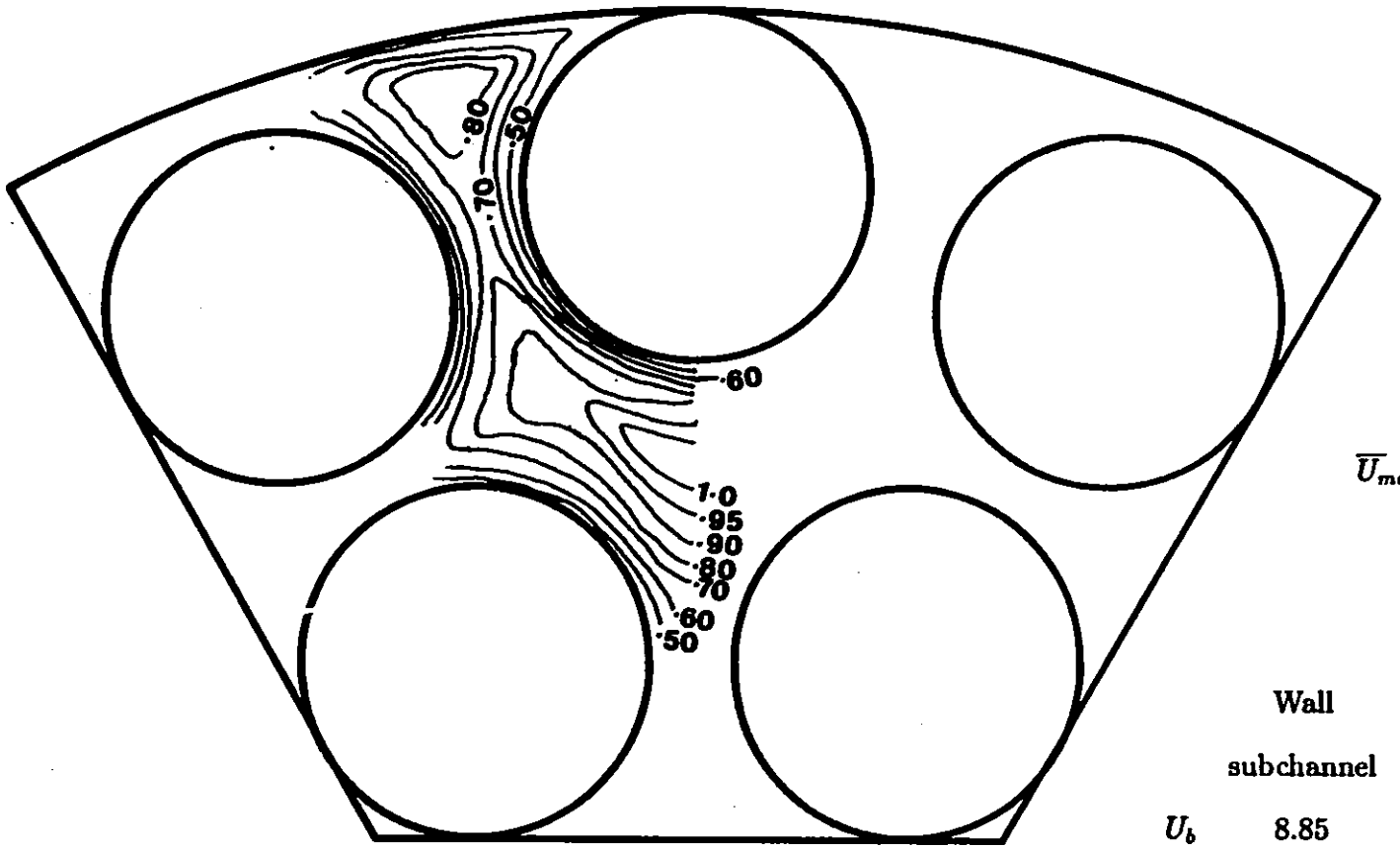

$\overline{U}_{max} = 15.24 m/s$

	Wall subchannel	Inner subchannel 1	Inner subchannel 2
U_b	8.85	12.22	12.47

Figure 42. Isovel contours at rod-wall contact

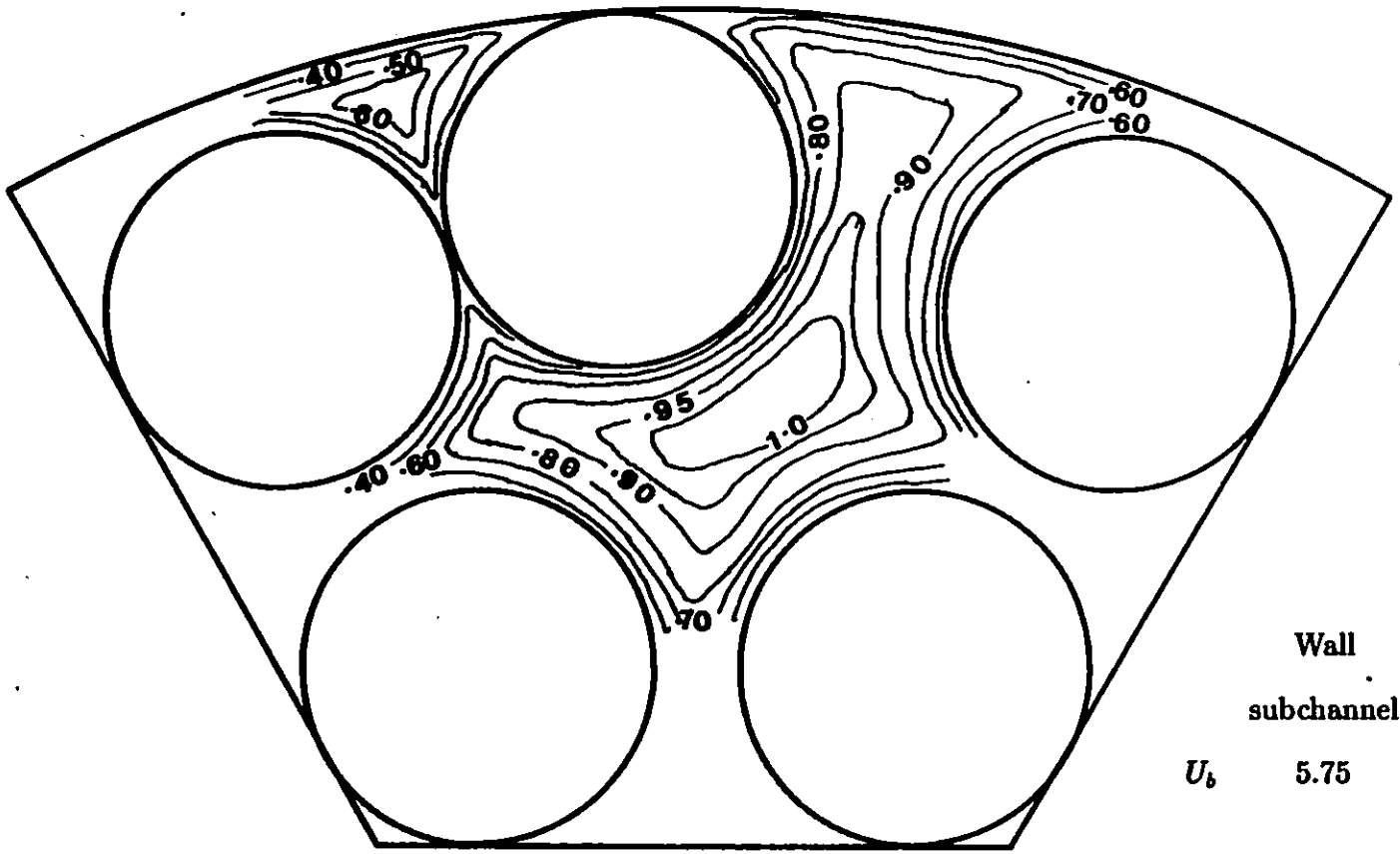

$\overline{U}_{max} = 14.28 m/s$

	Wall subchannel	Inner subchannel 1	Inner subchannel 2
U_b	5.75	8.69	11.65

Figure 43. Isovel contours at rod-rod-wall contact

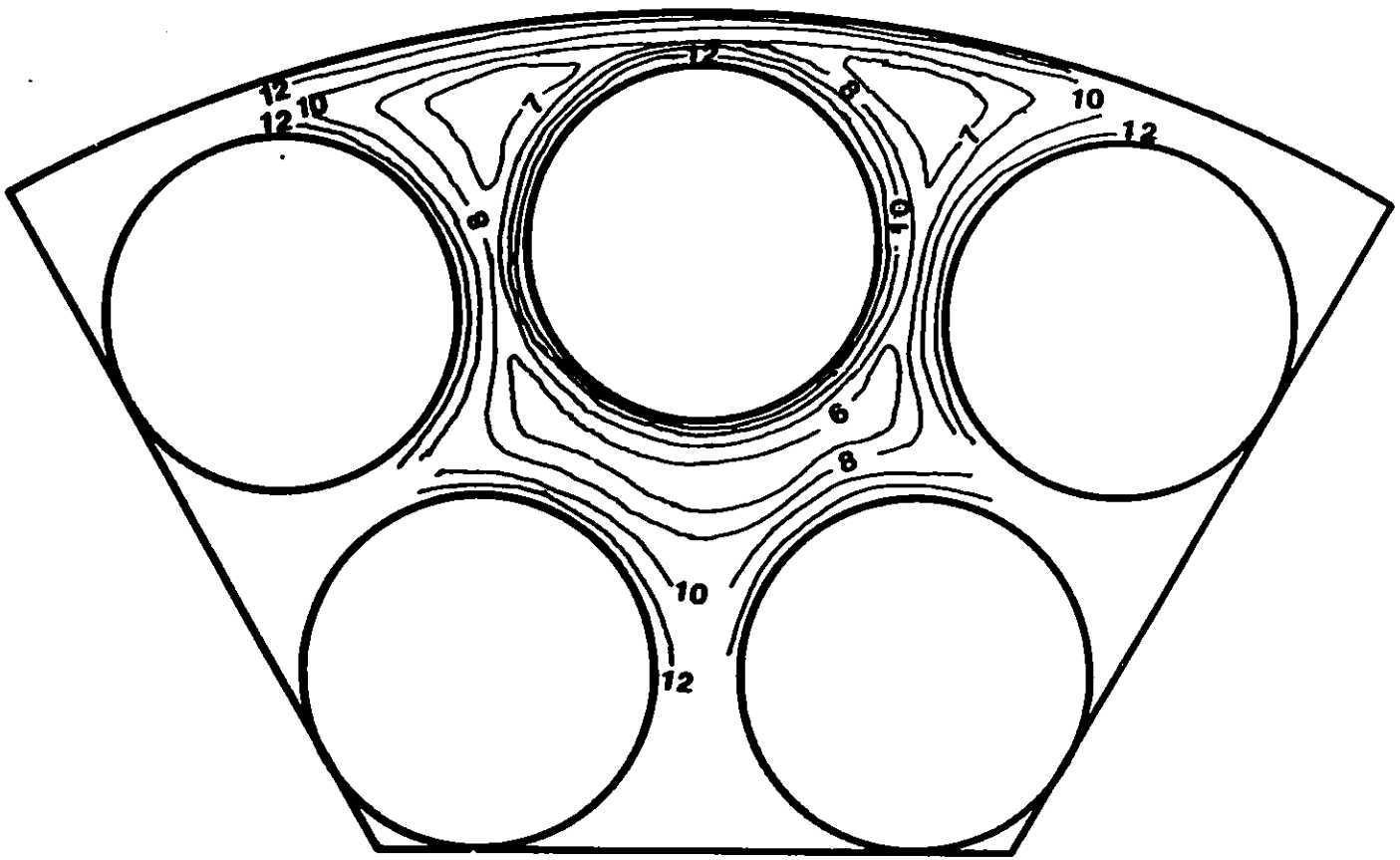

Figure 44. Axial turbulence intensity contours at design condition

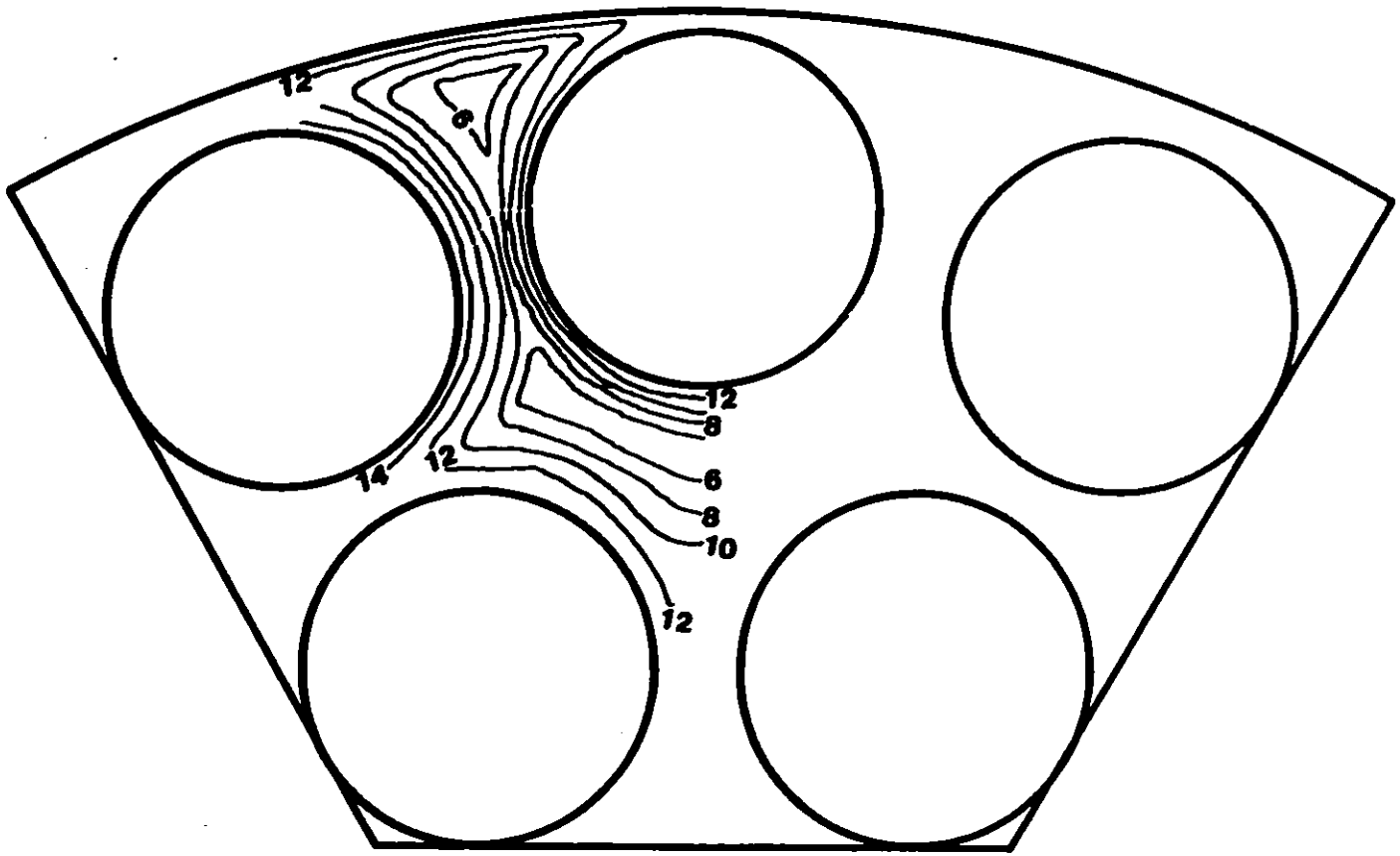

Figure 45. Axial turbulence intensity contours at W/D=1.059

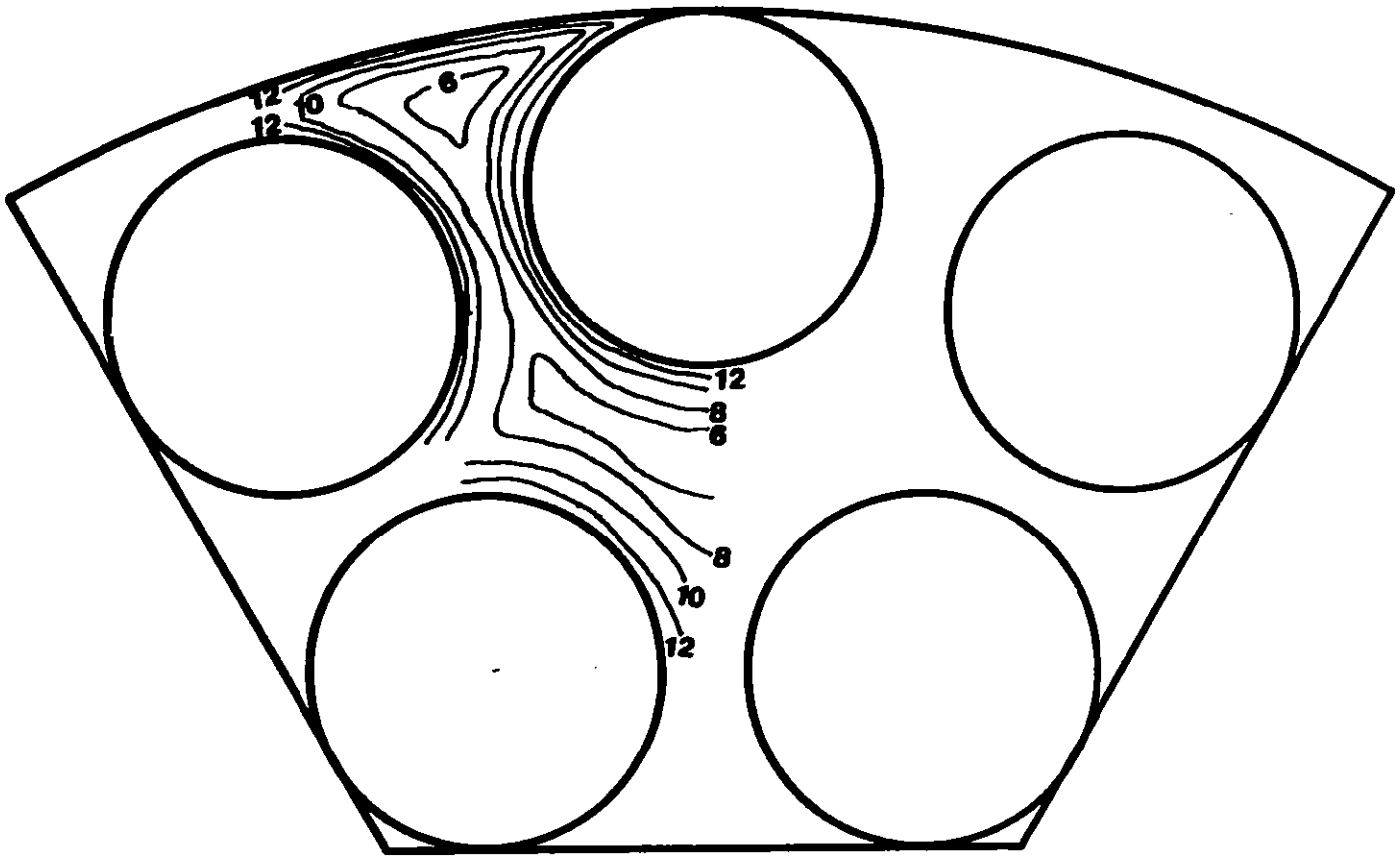

Figure 46. Axial turbulence intensity contours at rod-wall contact

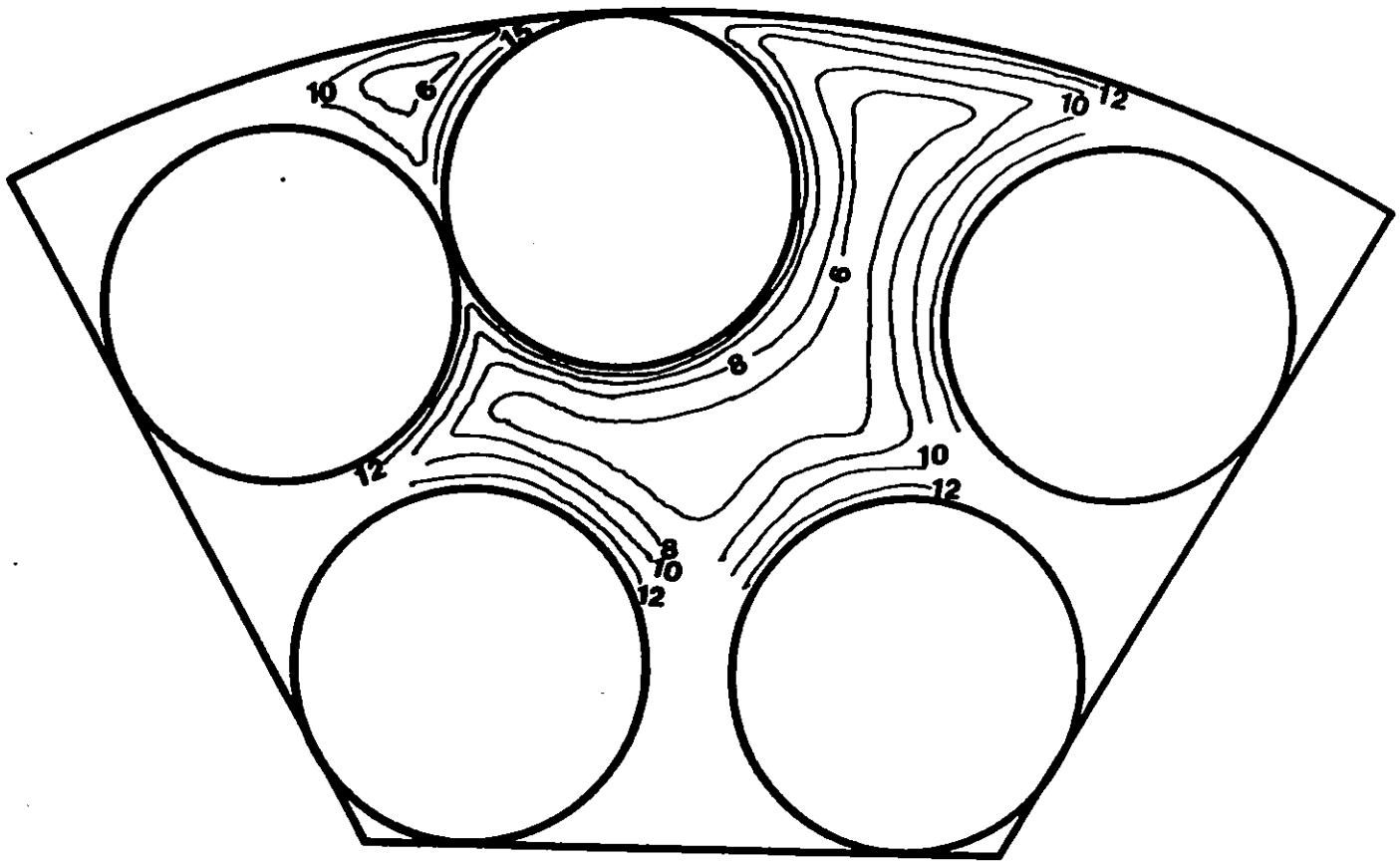

Figure 47. Axial turbulence intensity contours at rod-rod-wall contact

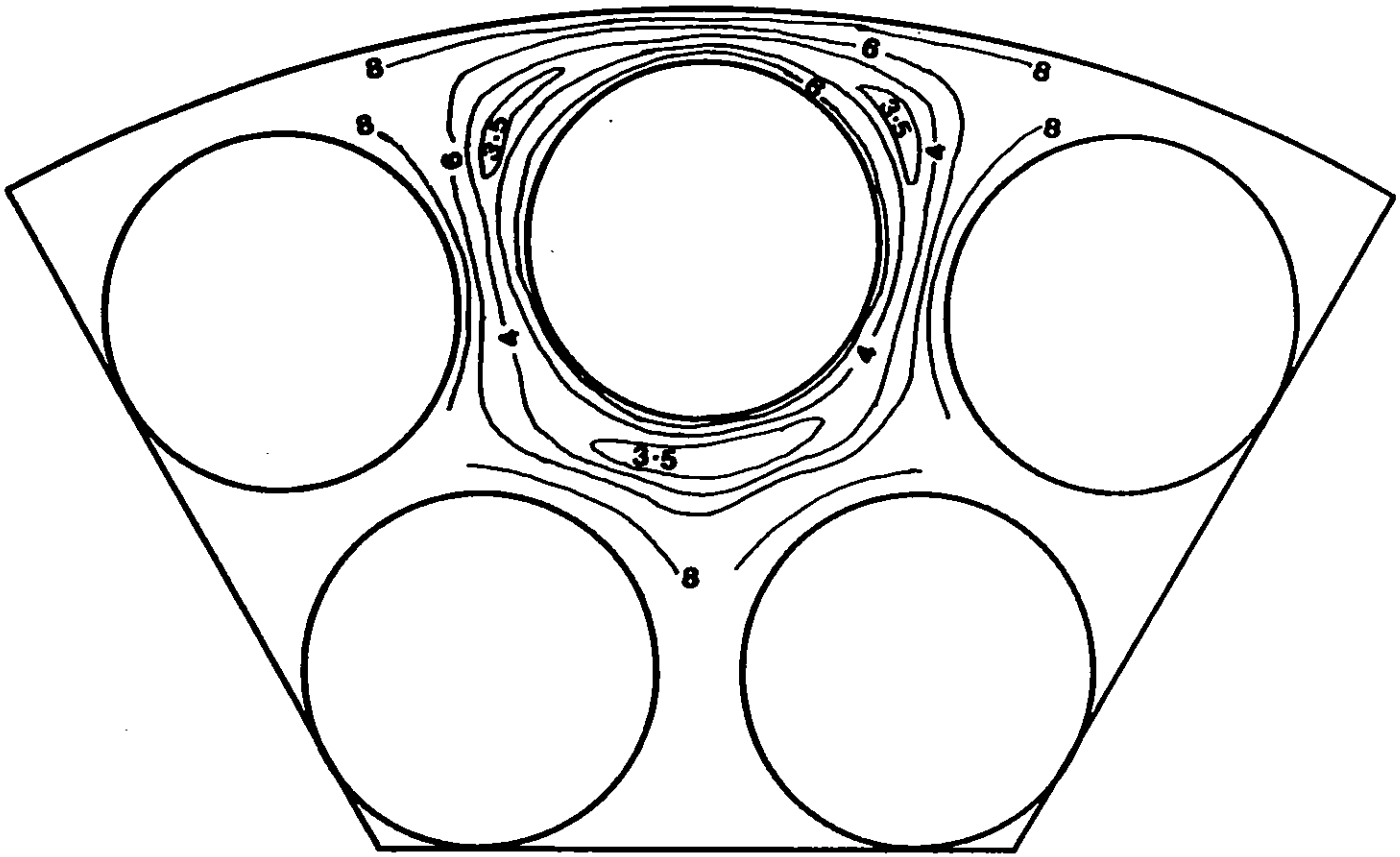

Figure 48. Radial turbulence intensity contours at design condition

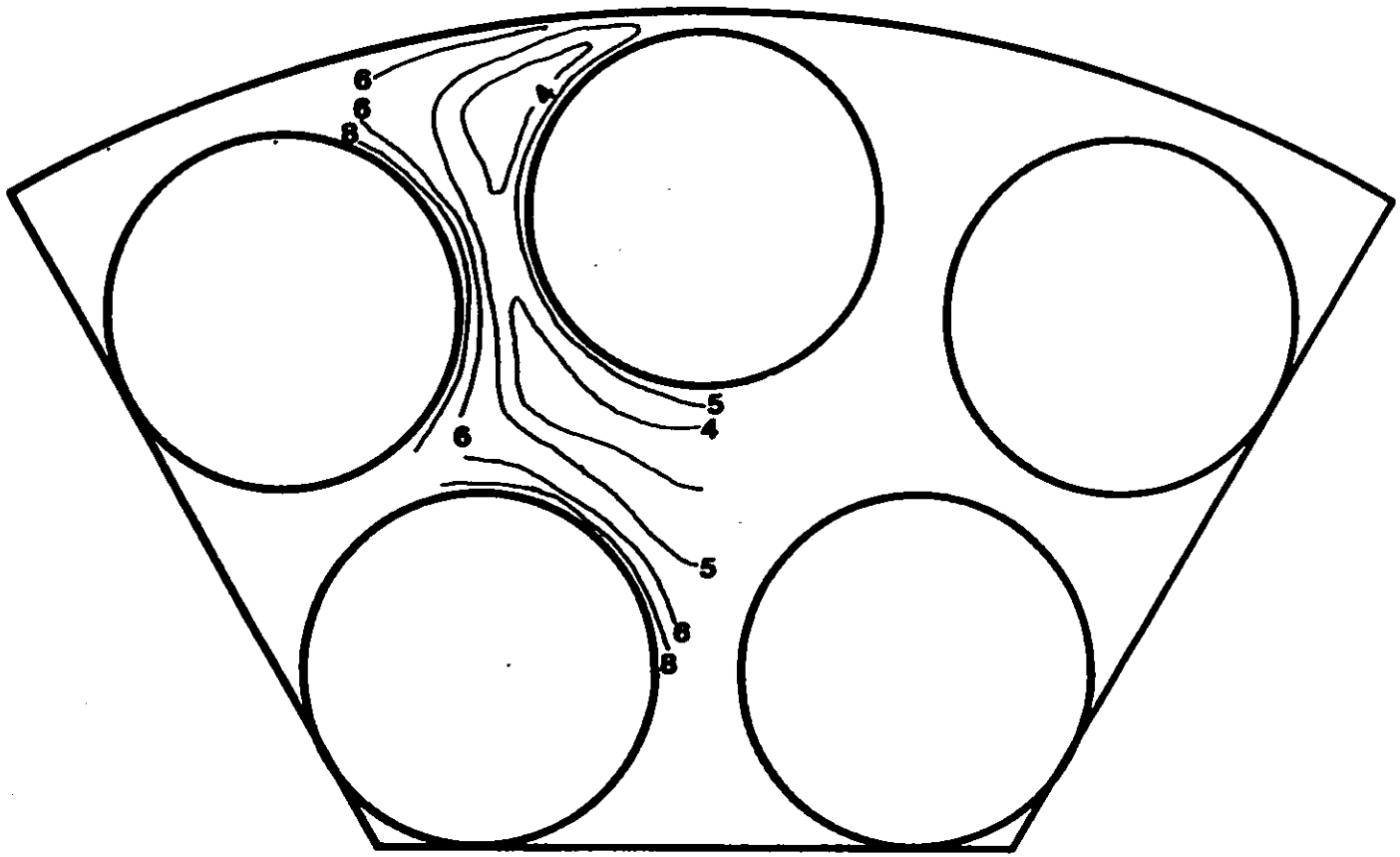

Figure 49. Radial turbulence intensity contours at W/D=1.059

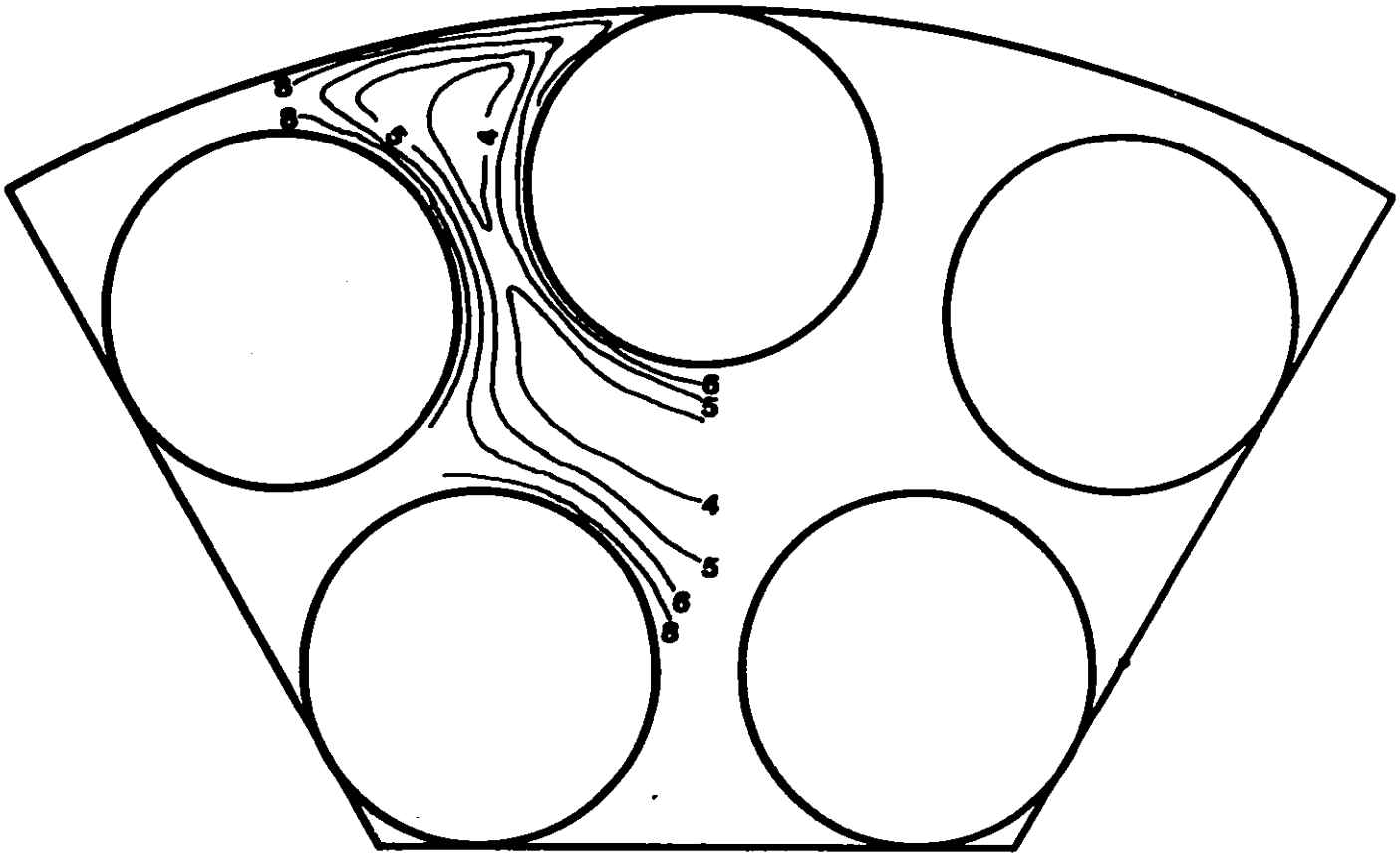

Figure 50. Radial turbulence intensity contours at rod-wall contact

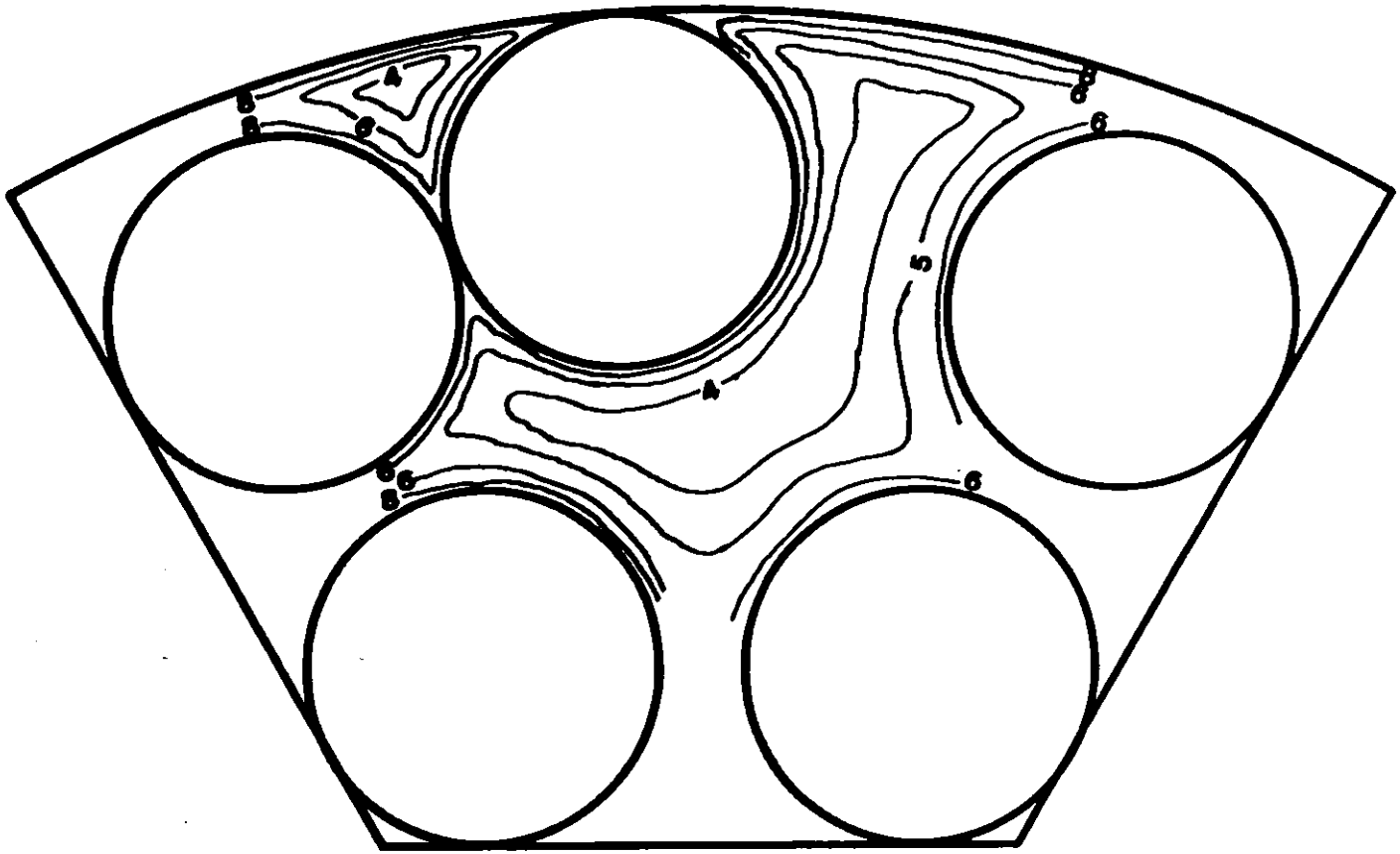

Figure 51. Radial turbulence intensity contours at rod-rod-wall contact

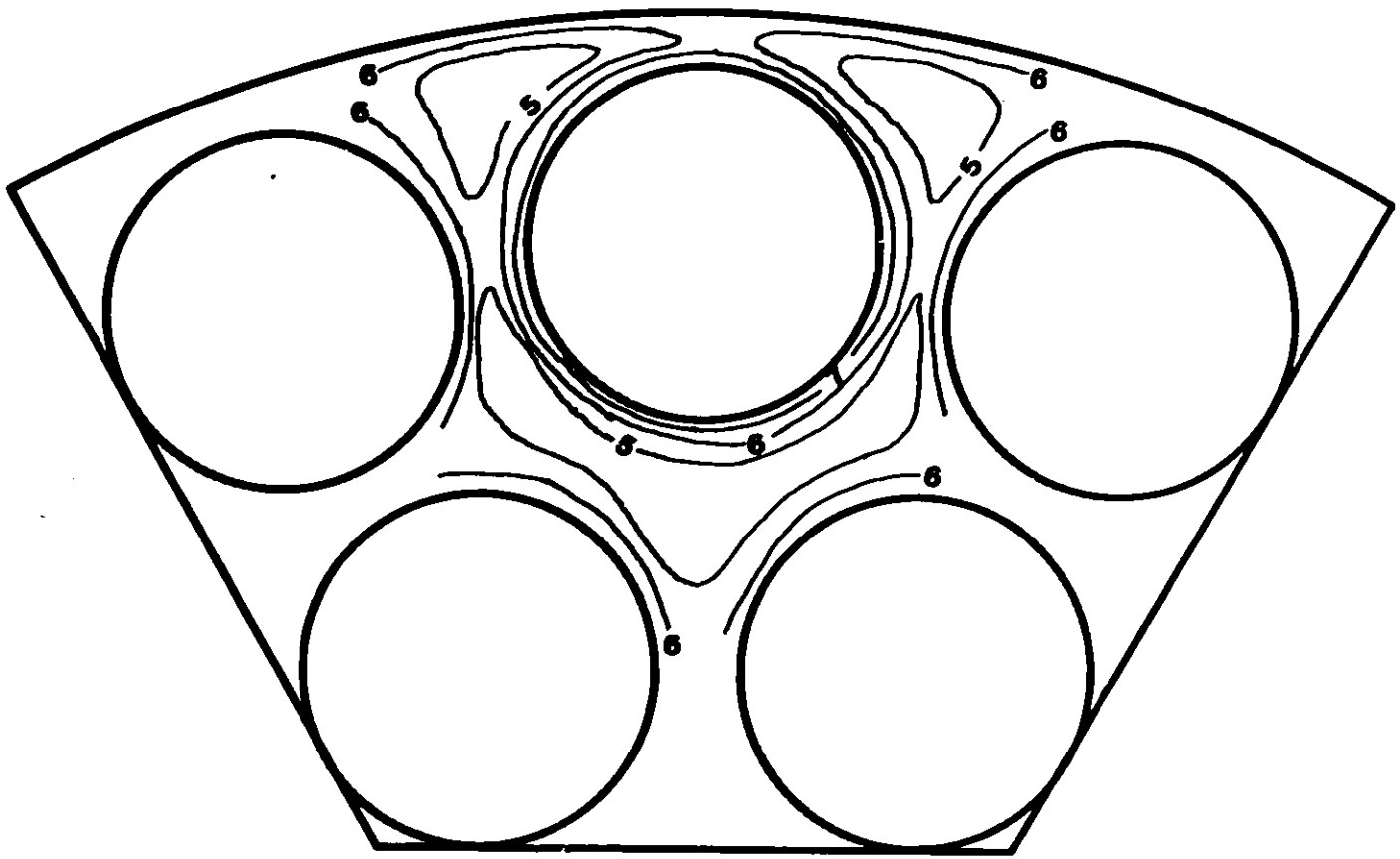

Figure 52. Azimuthal turbulence intensity contours at design condition

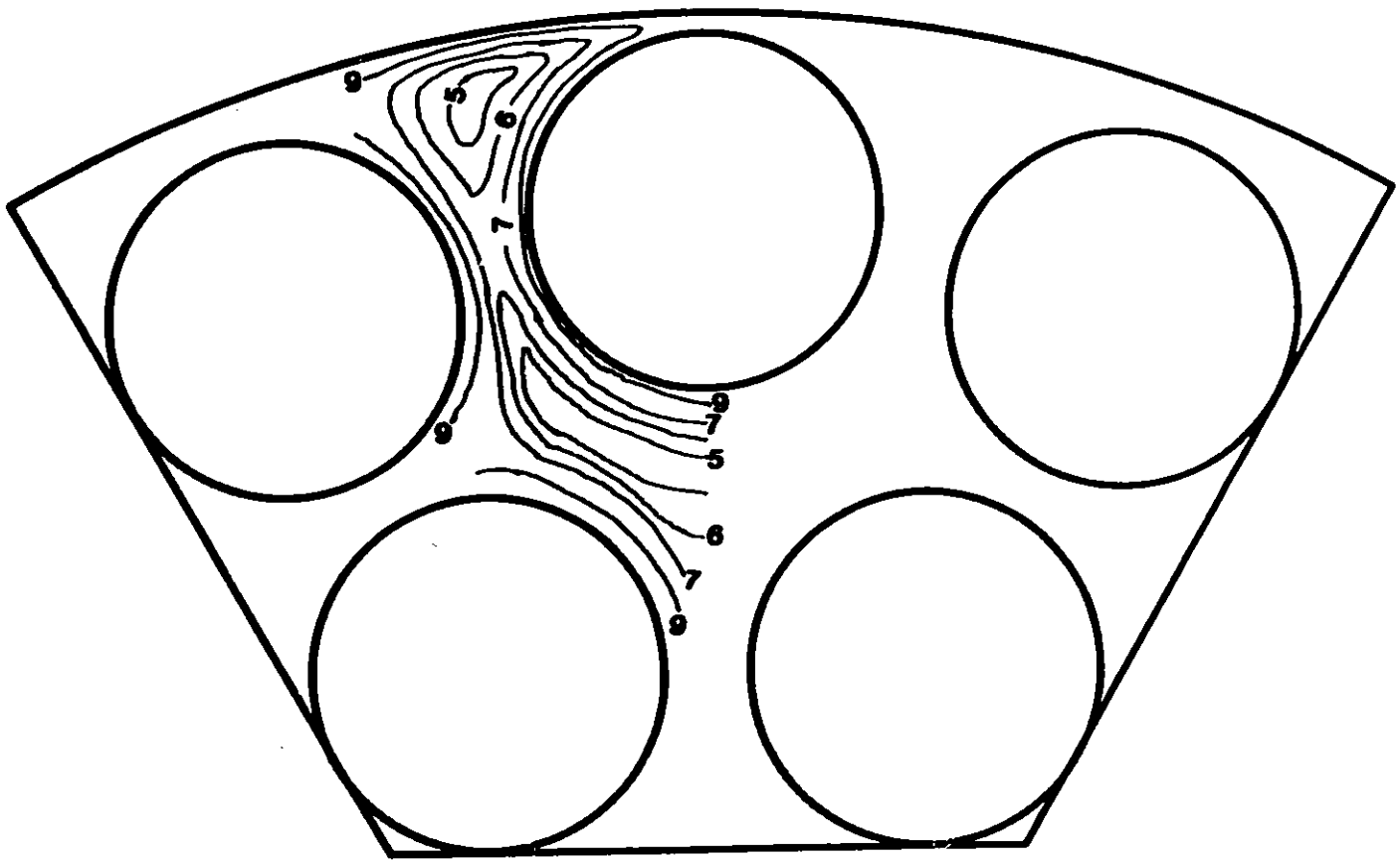

Figure 53. Azimuthal turbulence intensity contours at W/D = 1.059

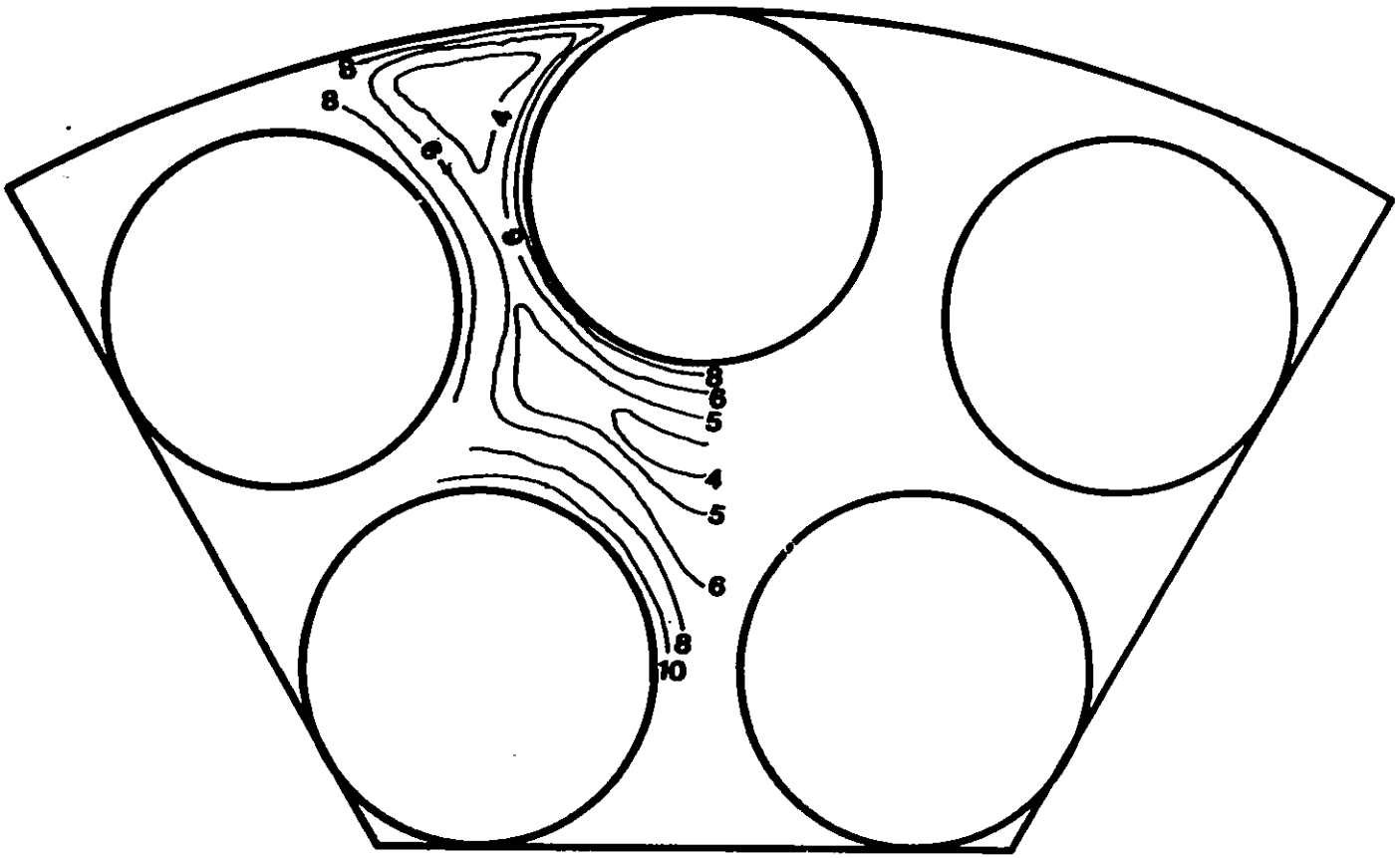

Figure 54. Azimuthal turbulence intensity contours at rod-wall contact

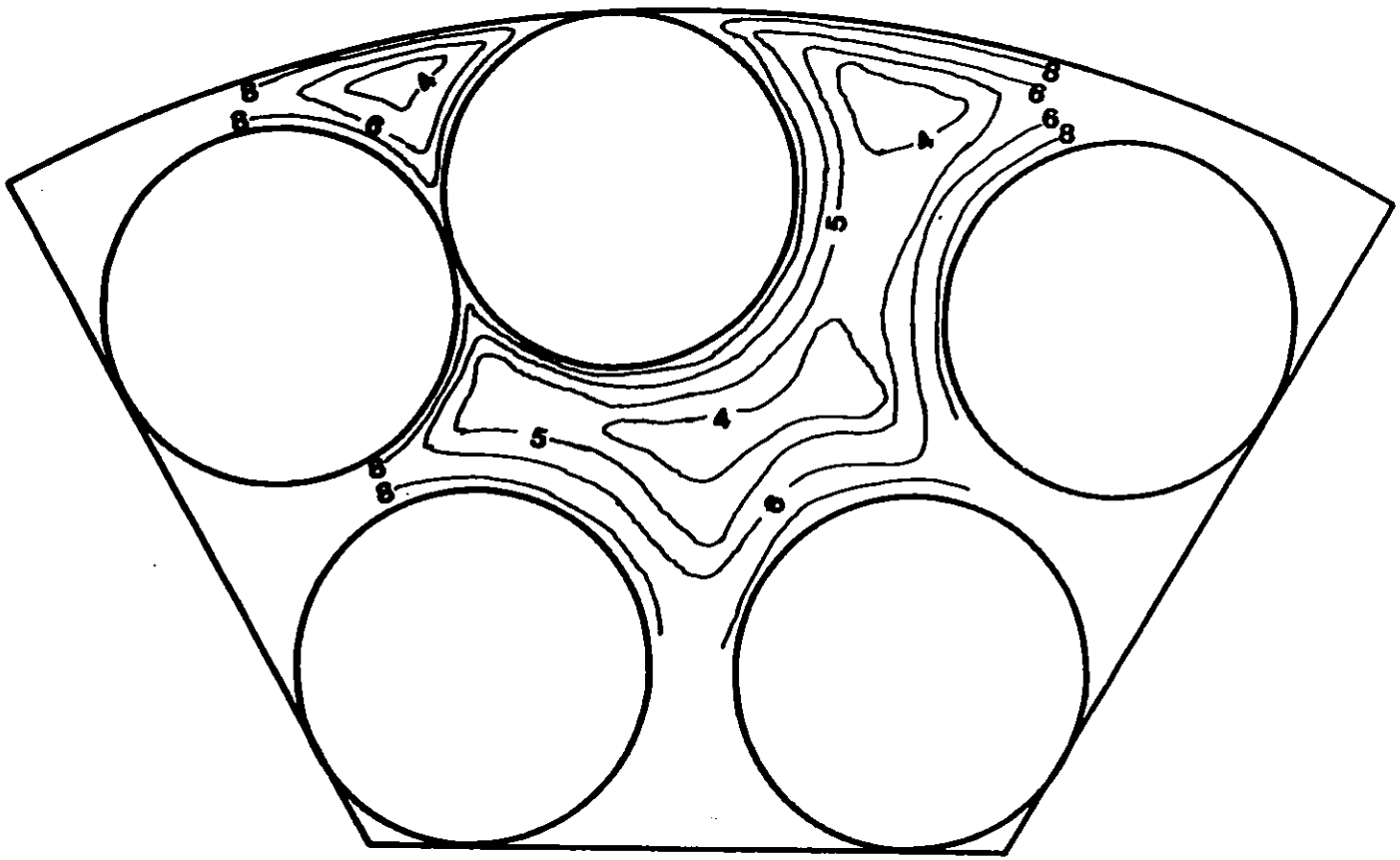

Figure 55. Azimuthal turbulence intensity contours at rod-rod-wall contact

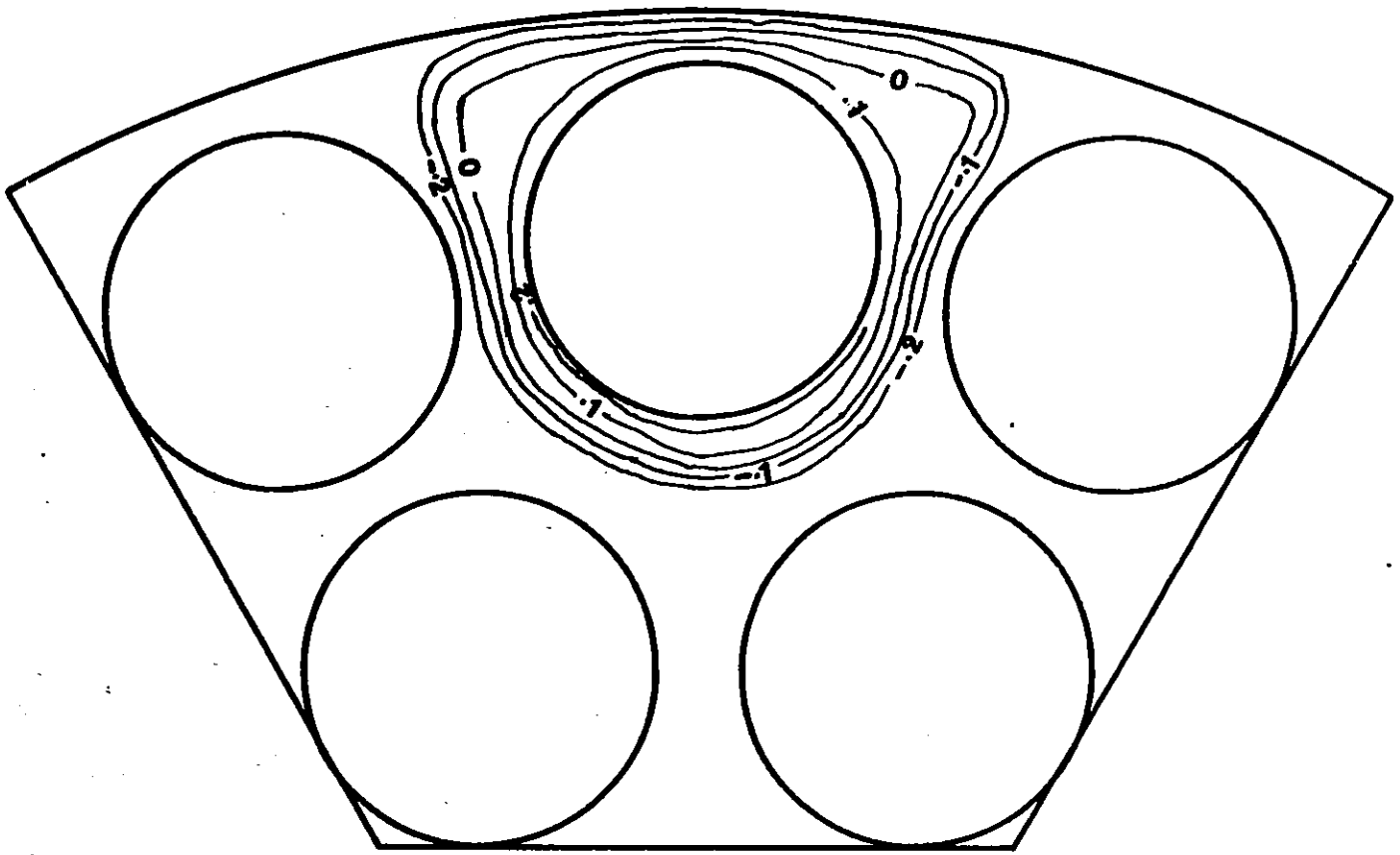

Figure 56. Reynolds shear stress contours at design condition (N/m^2)

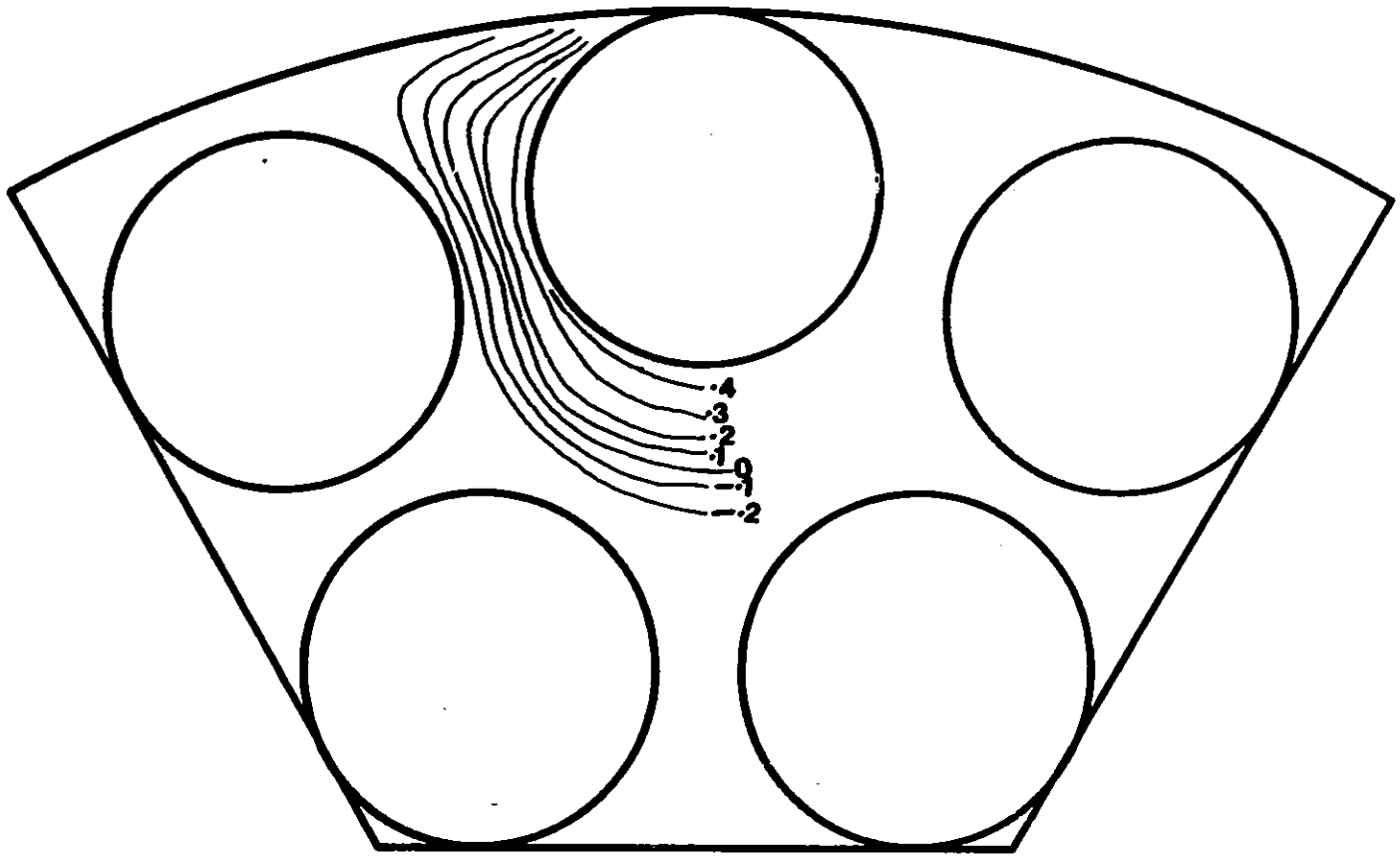

Figure 57. Reynolds shear stress contours at rod-wall contact (N/m^2)

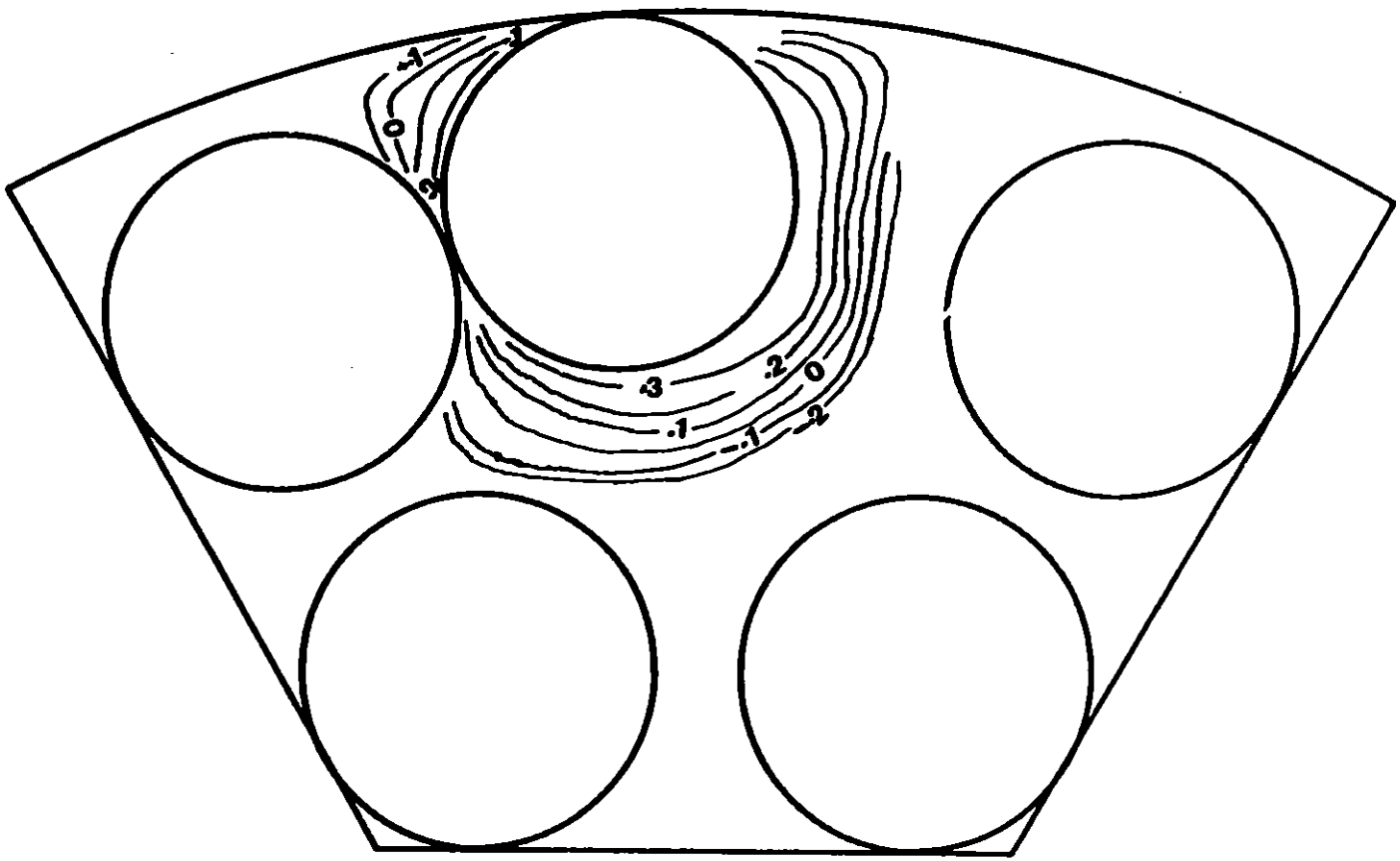

Figure 58. Reynolds shear stress contours at rod-rod-wall contact (N/m^2)

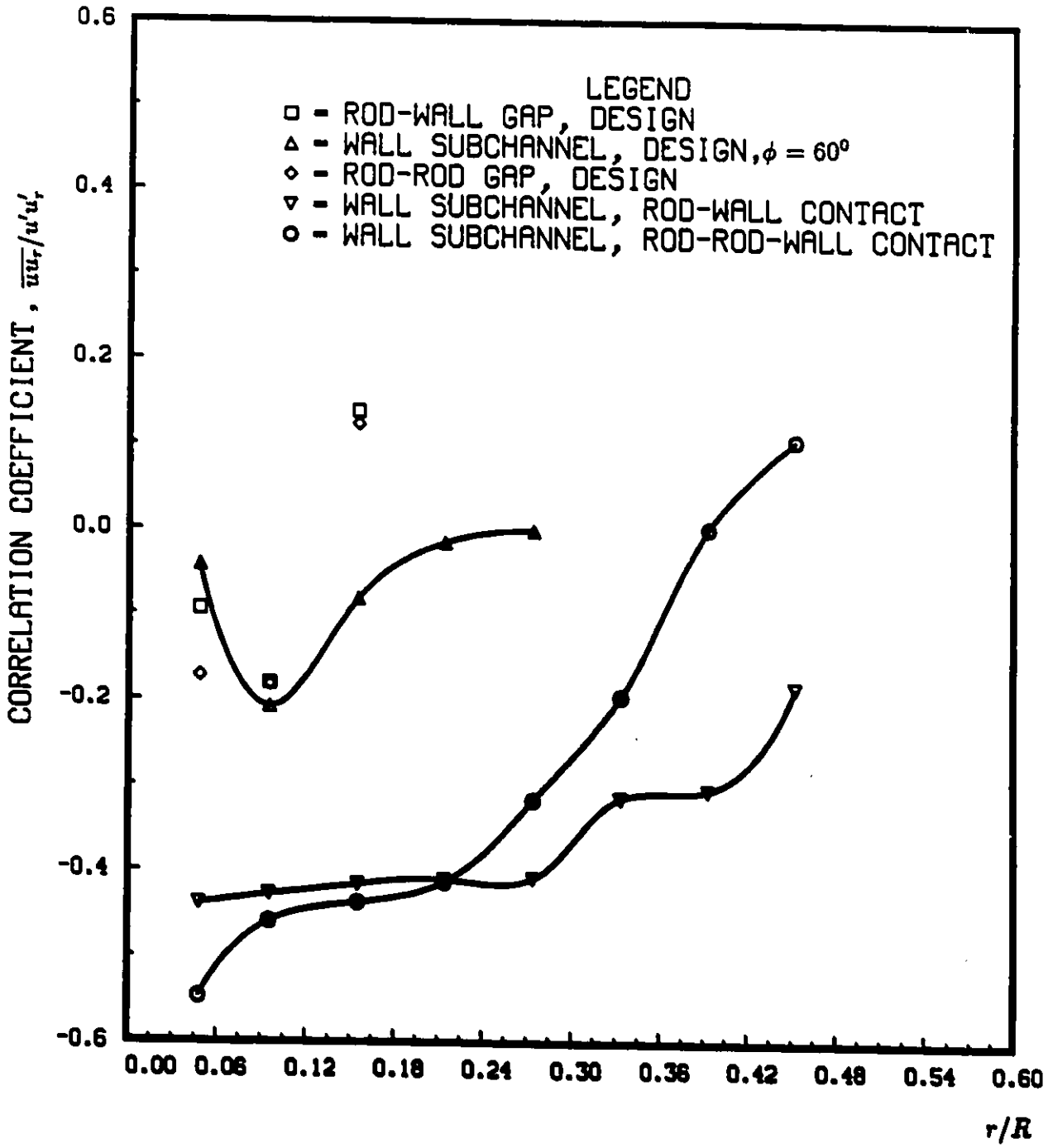

Figure 59. Variation of correlation coefficients

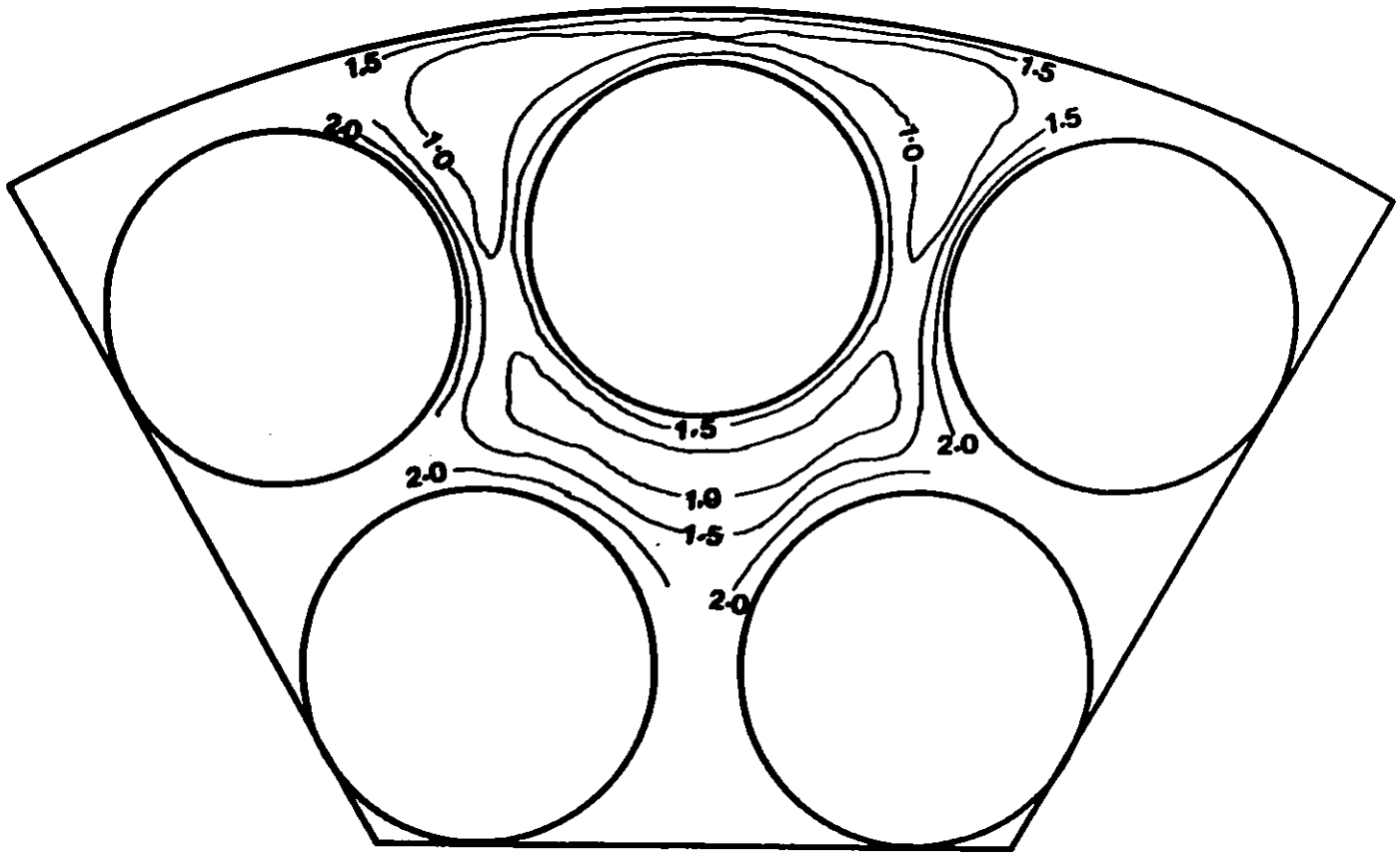

Figure 60. Turbulent kinetic energy (in m^2/s^2) contours at design condition

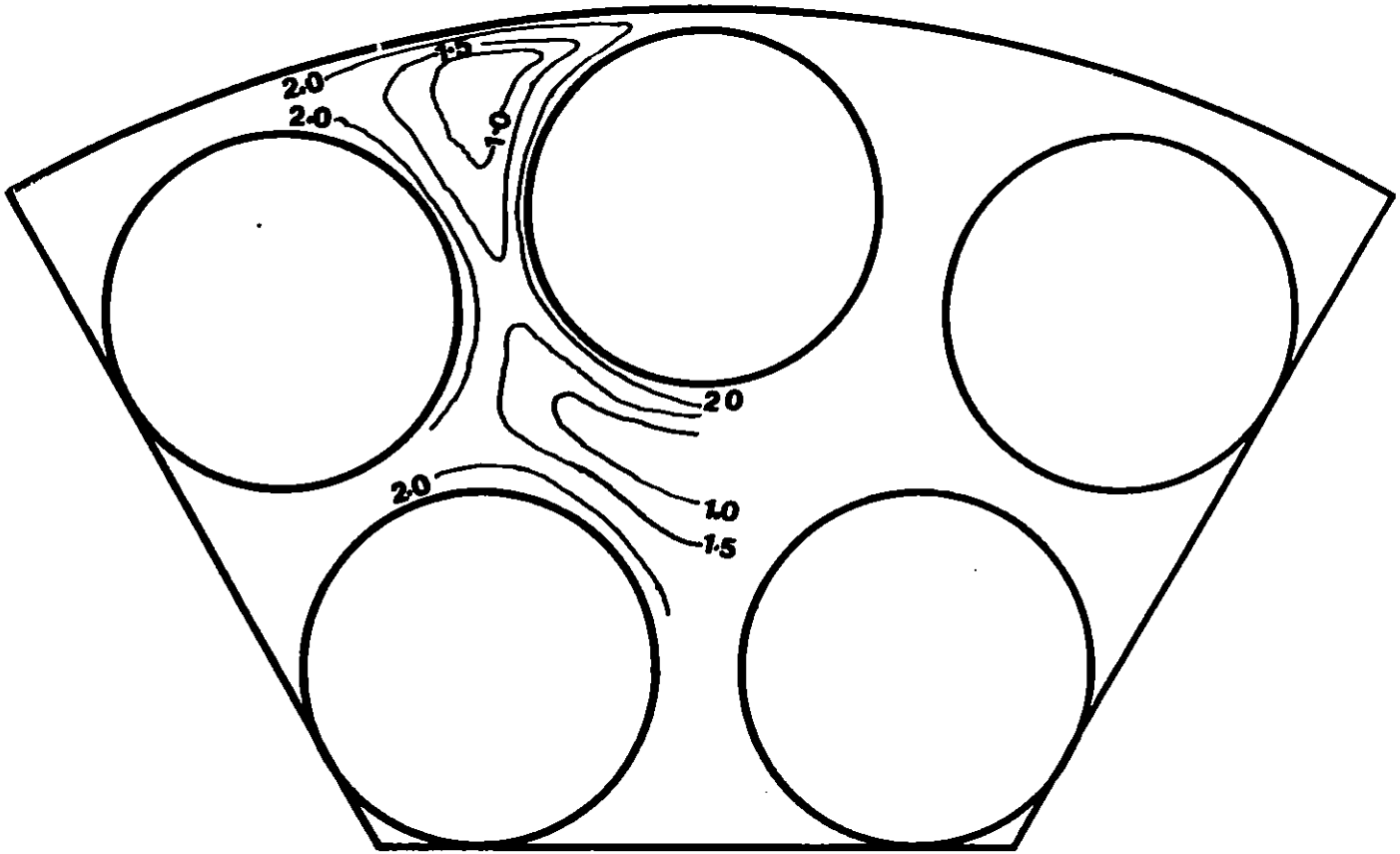

Figure 61. Turbulent kinetic energy (in m^2/s^2) contours at W/D=1.059

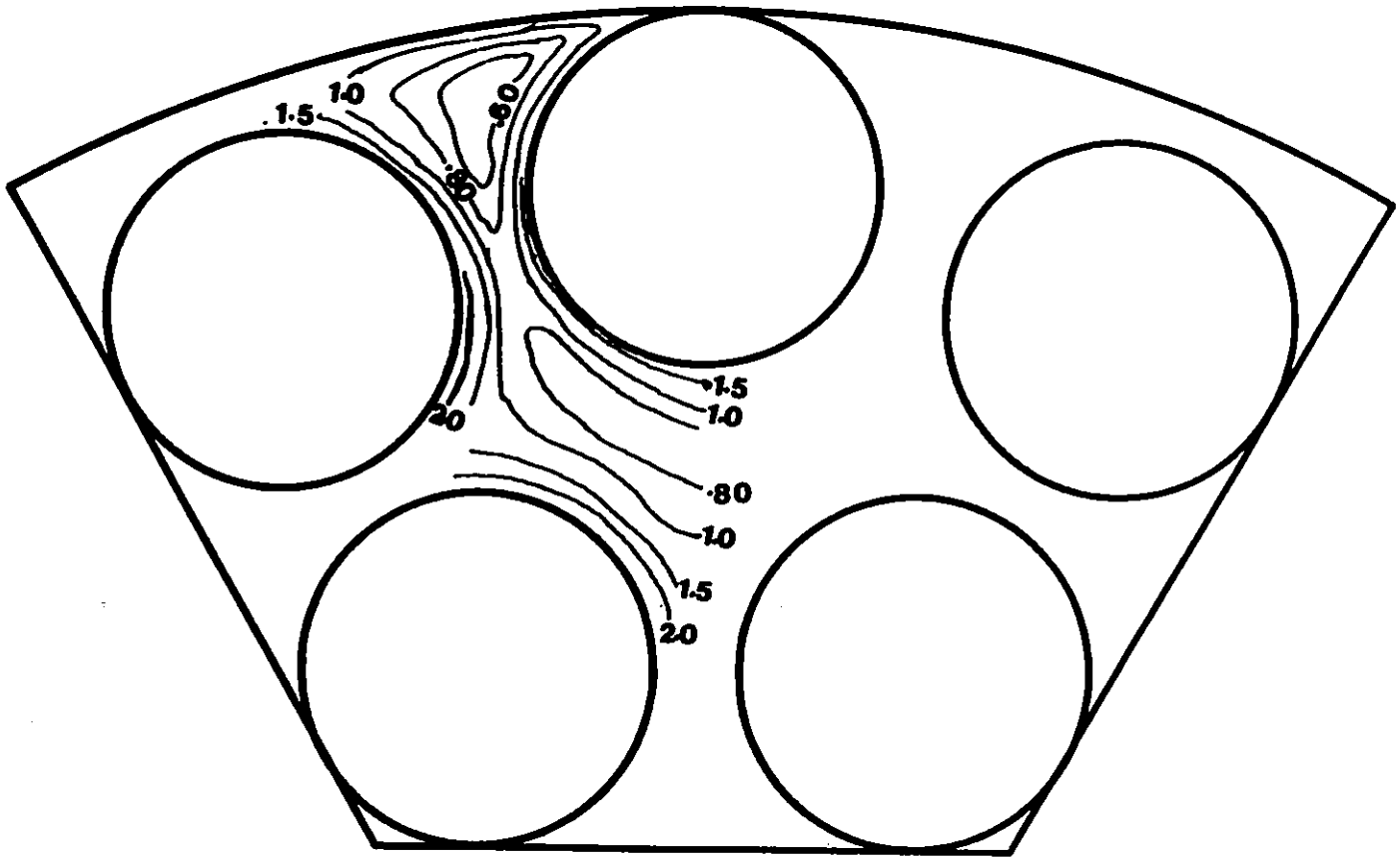

Figure 62. Turbulent kinetic energy (in m^2/s^2) contours at rod-wall contact

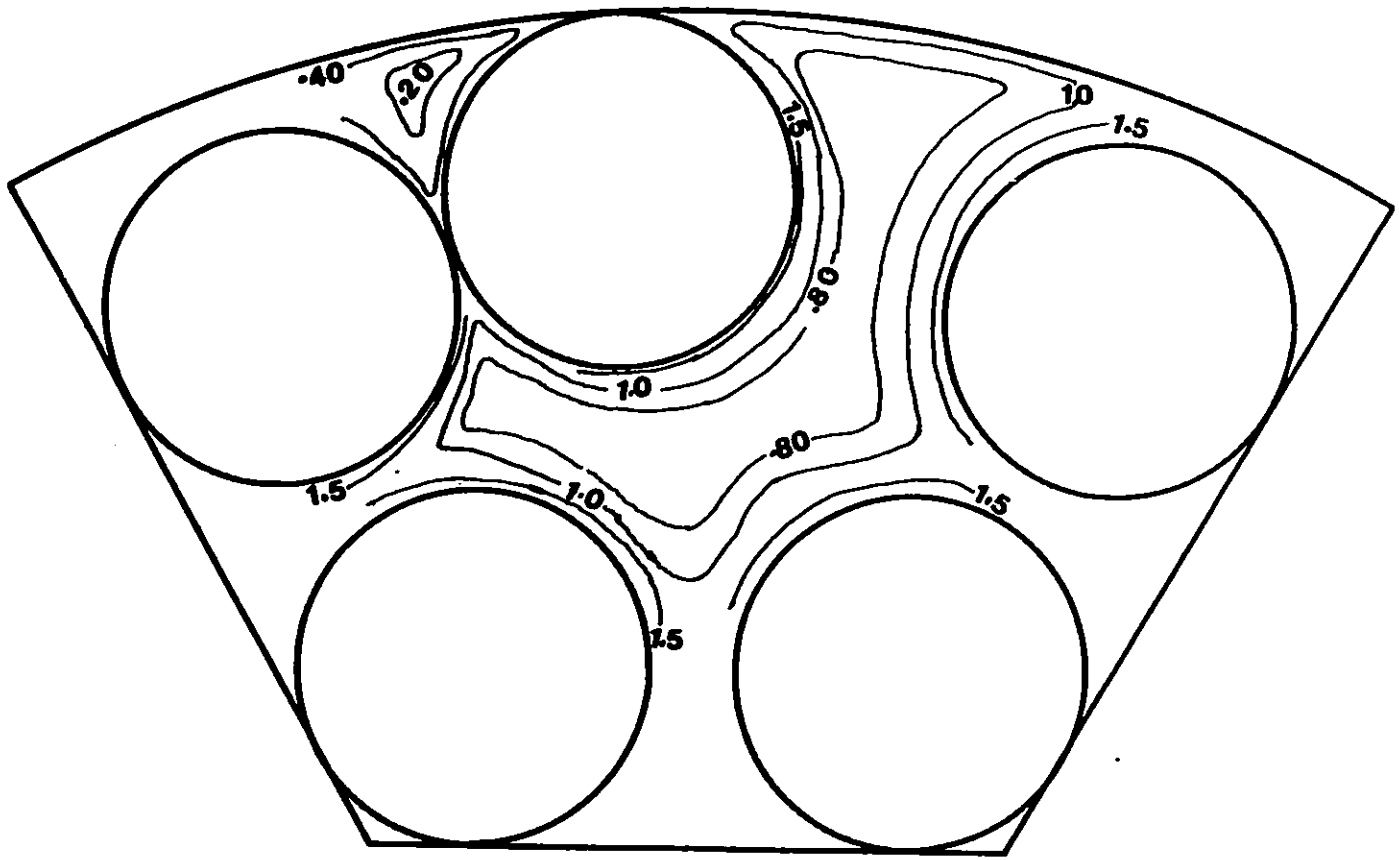

Figure 63. Turbulent kinetic energy (in m^2/s^2) contours at rod-rod-wall contact

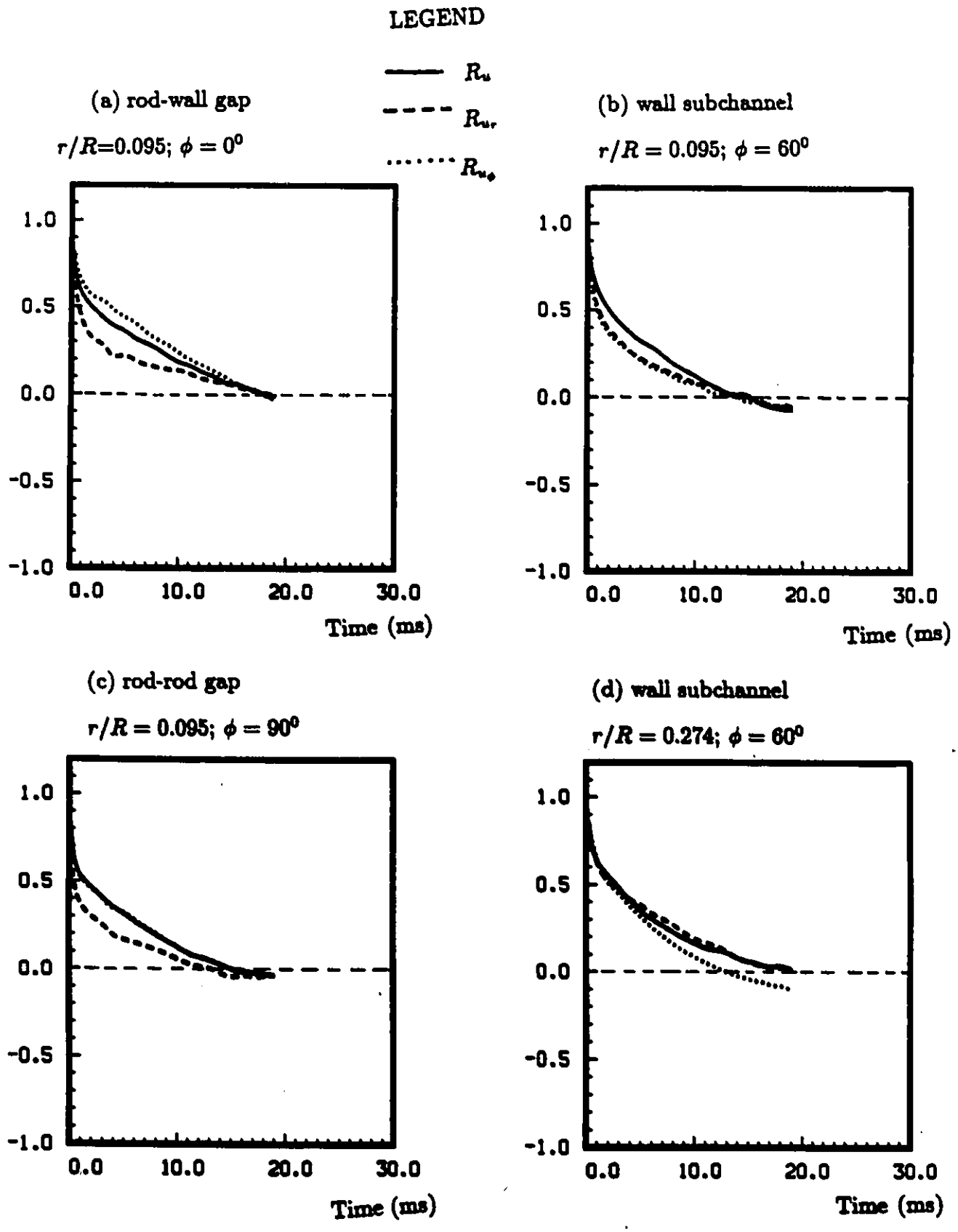

Figure 64. Autocorrelation coefficients at selected positions for the design condition

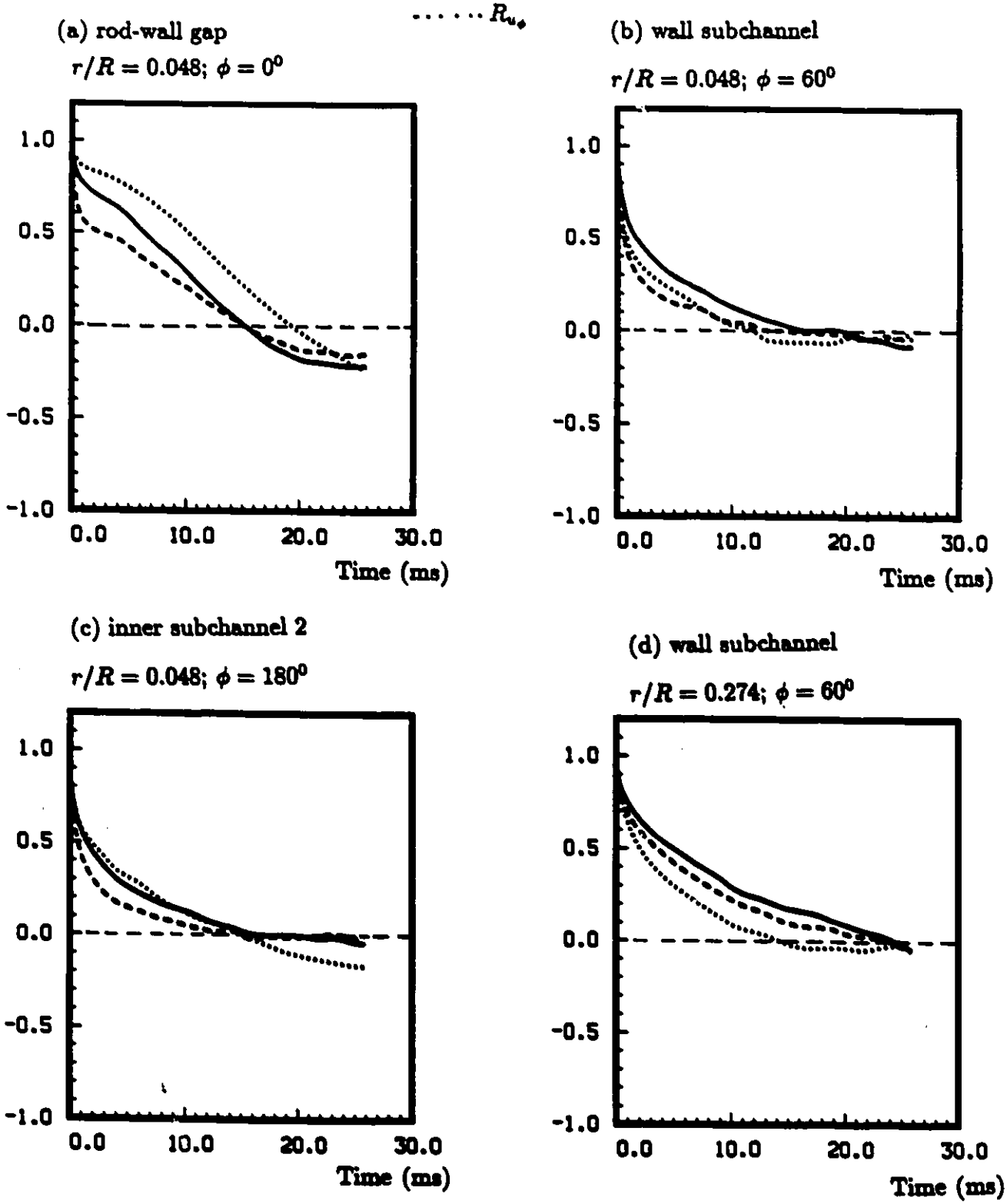

Figure 65. Autocorrelation coefficients at selected positions for W/D= 1.059

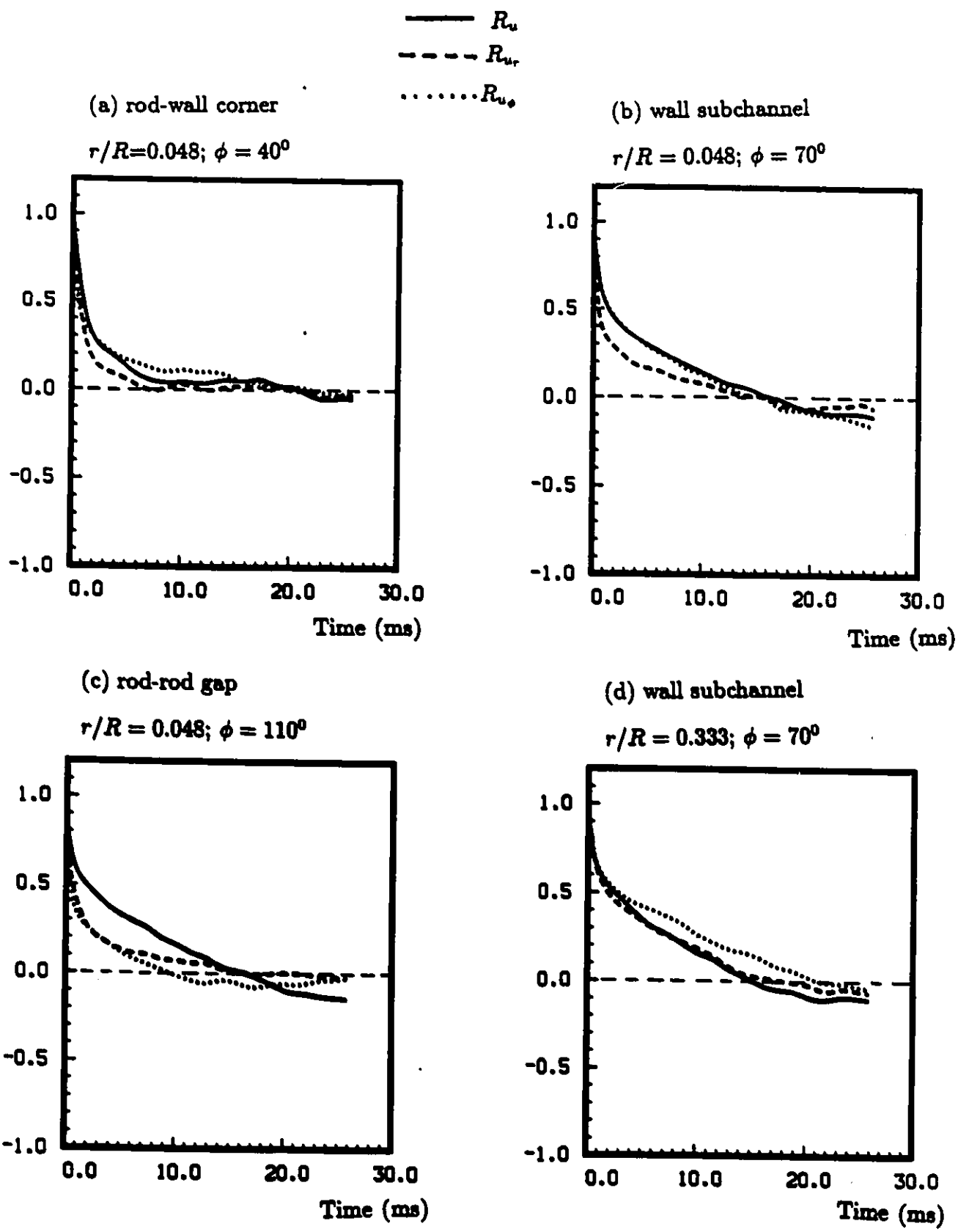

Figure 66. Autocorrelation coefficients at selected positions for rod-wall contact

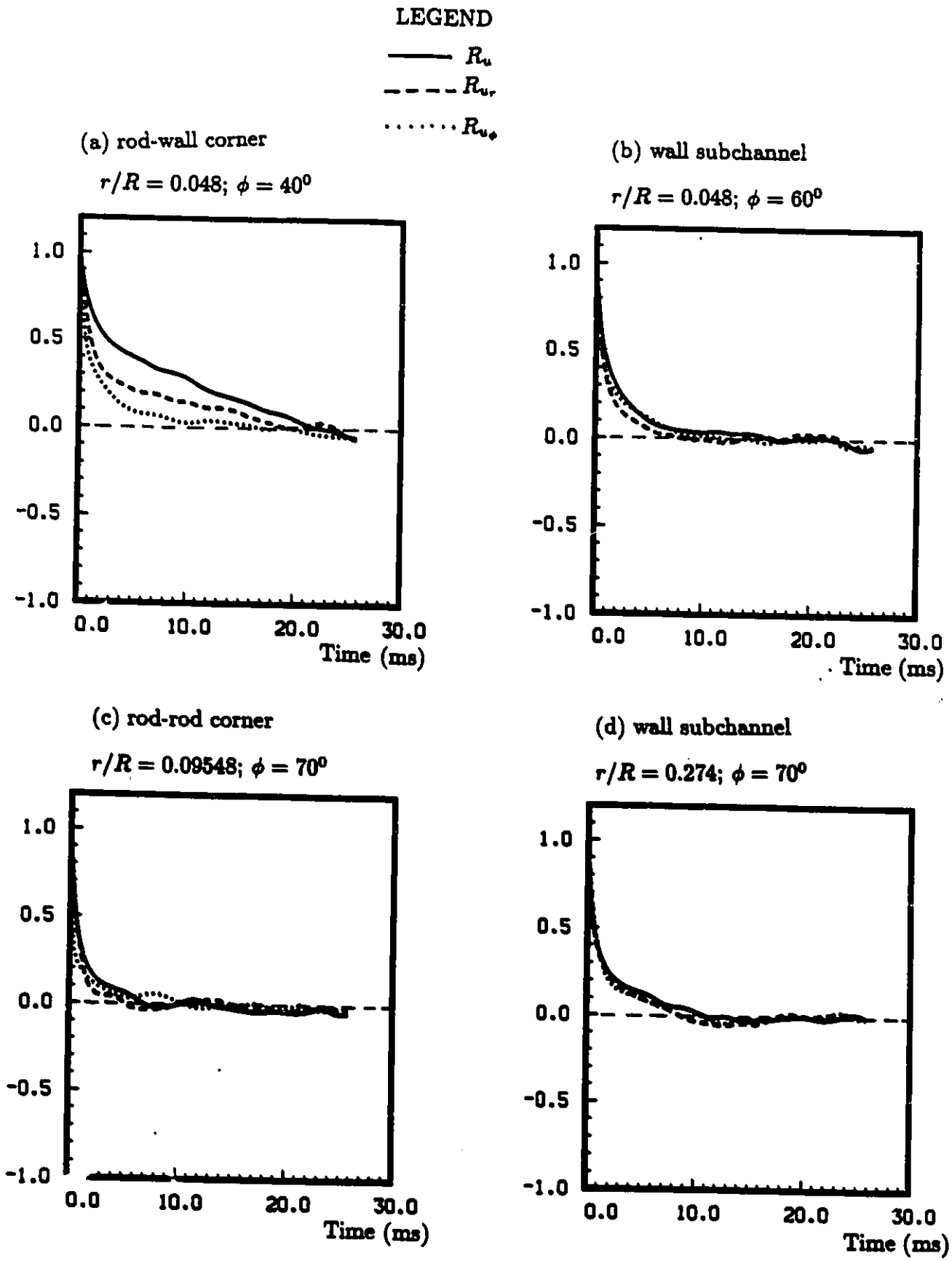

Figure 67. Autocorrelation coefficients at selected positions for rod-rod-wall contact

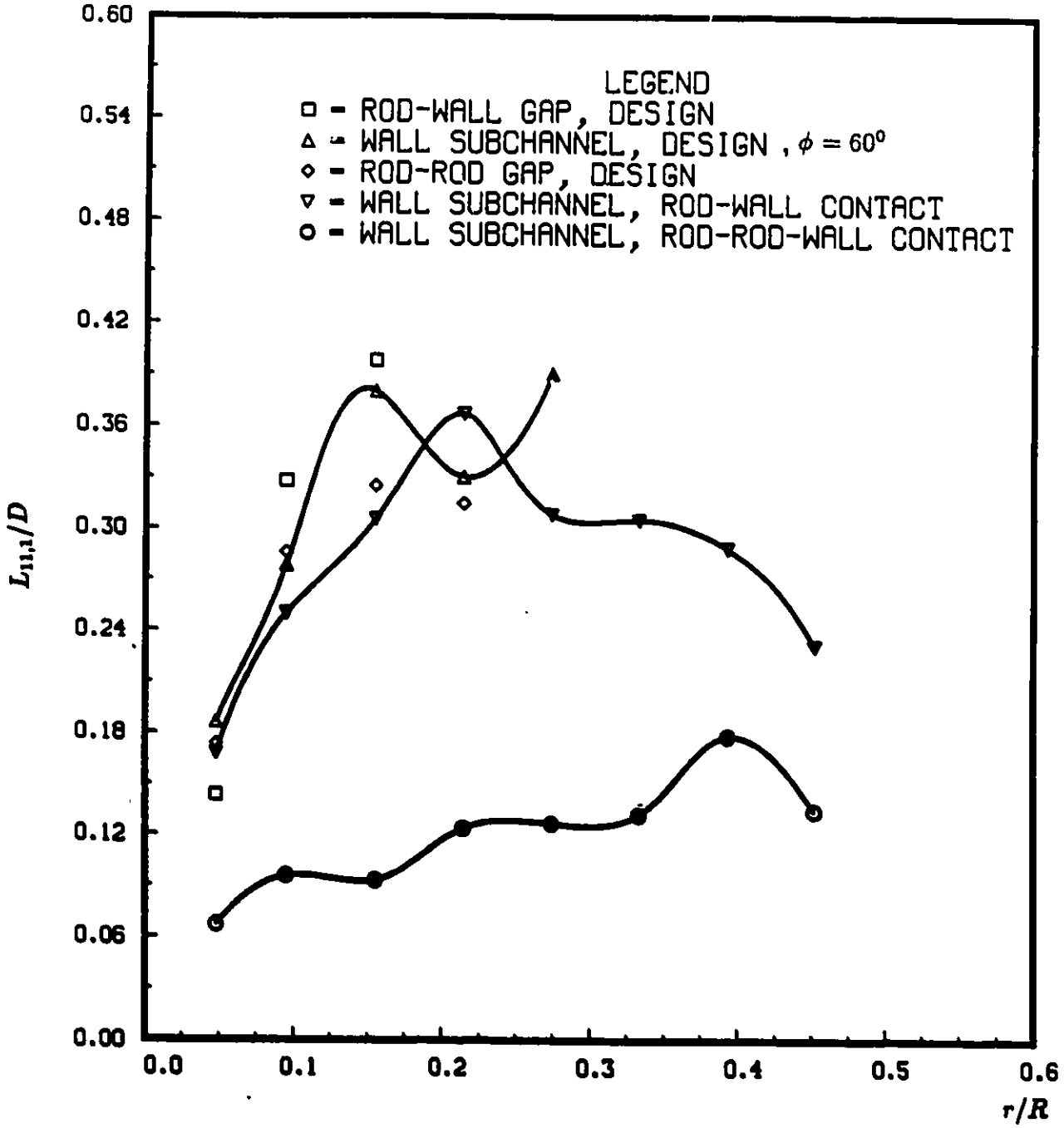

Figure 68. Variation of streamwise Eulerian integral length scale of the axial velocity fluctuation

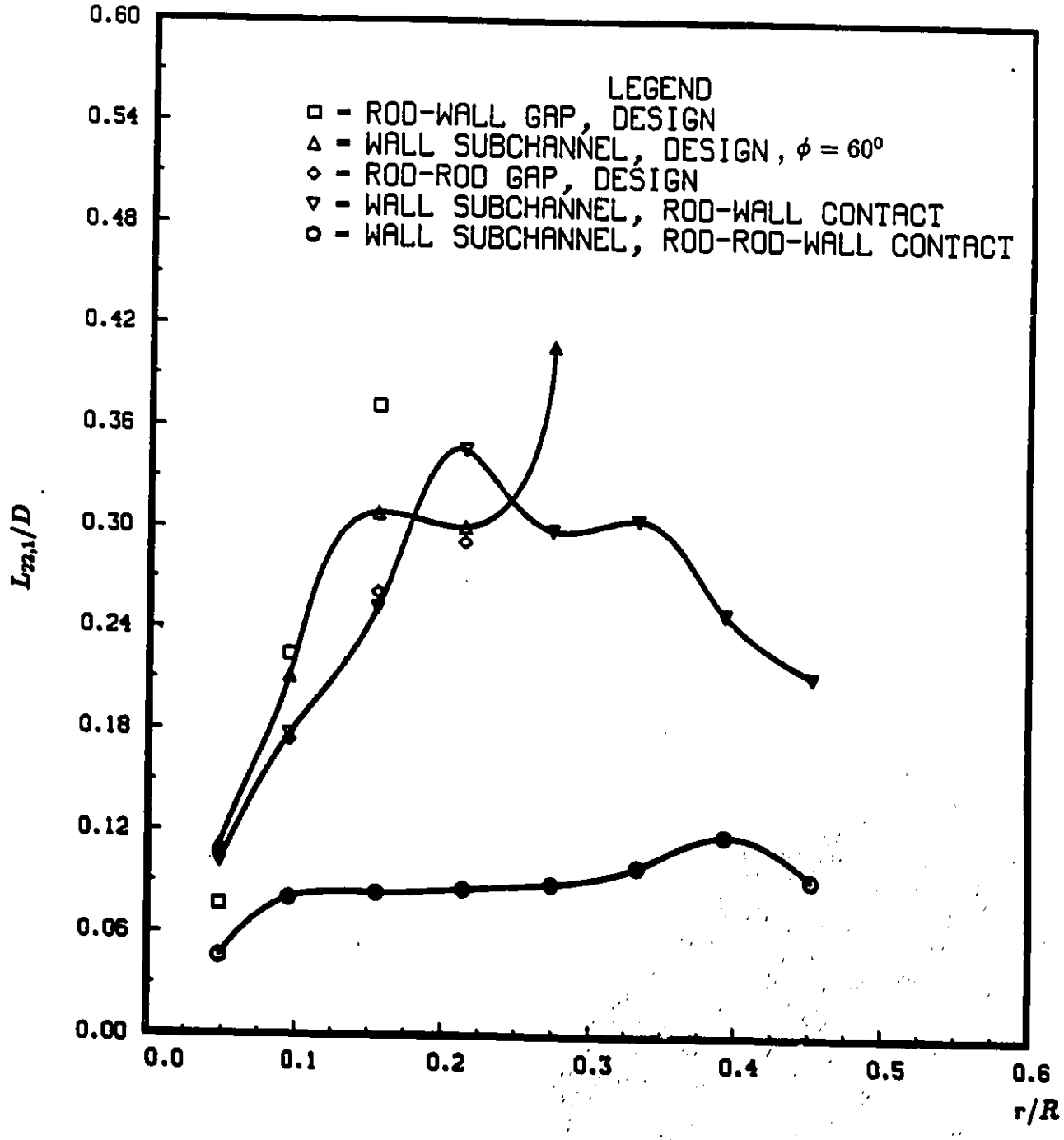

Figure 69. Variation of streamwise Eulerian integral length scale of the radial velocity fluctuation

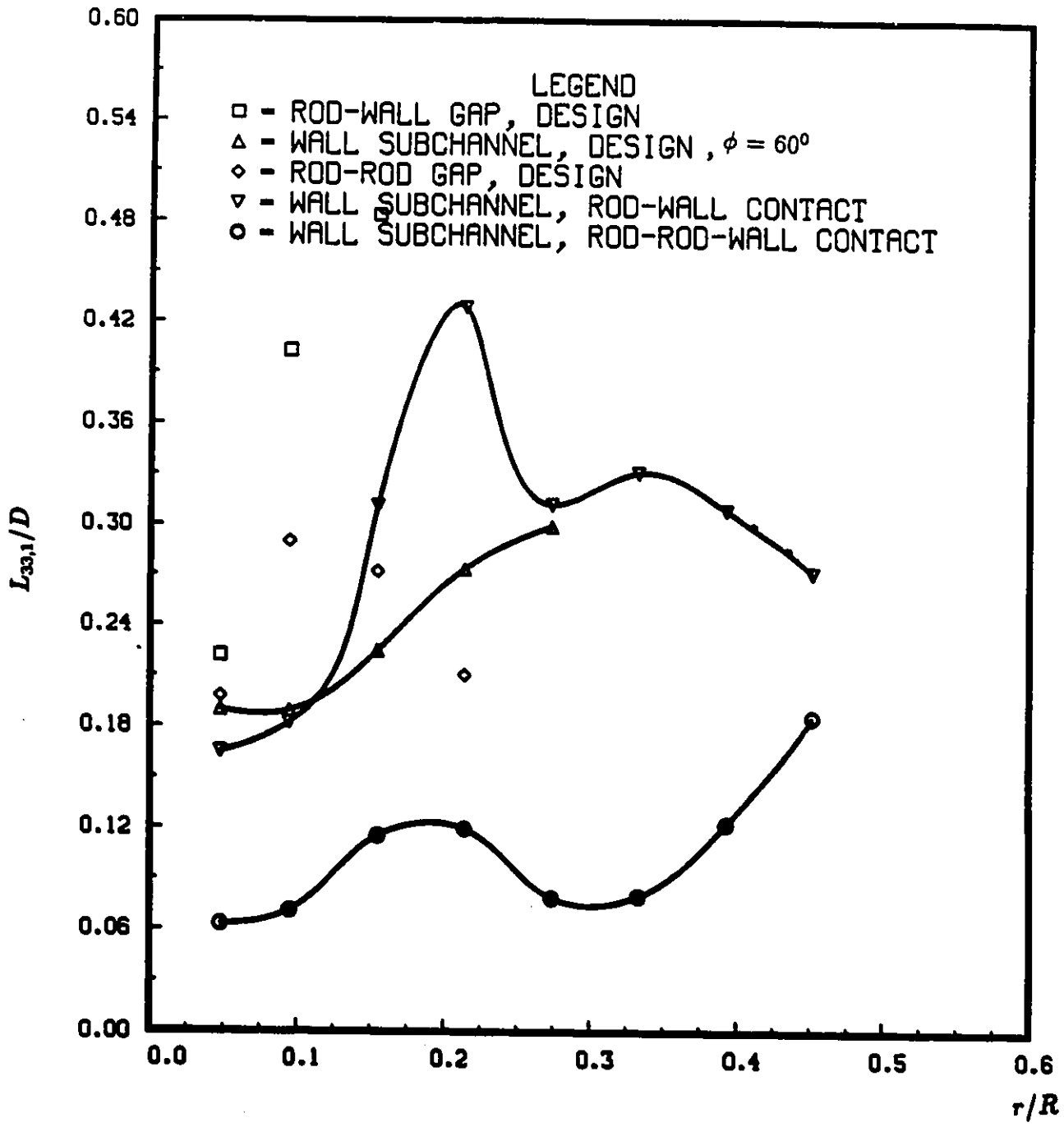

Figure 70. Variation of streamwise Eulerian integral length scale of the azimuthal velocity fluctuation

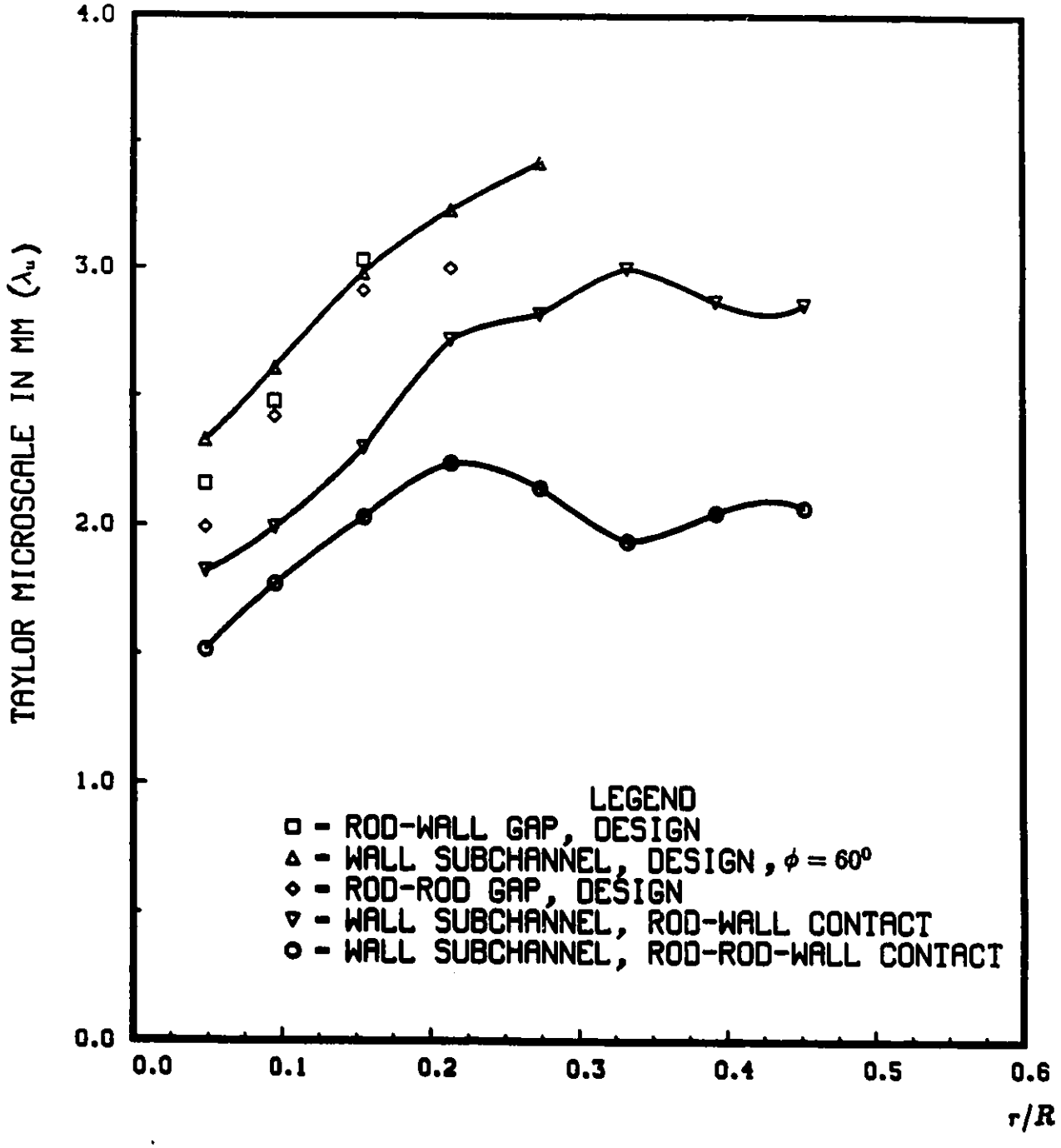

Figure 71. Variation of streamwise Taylor microscale

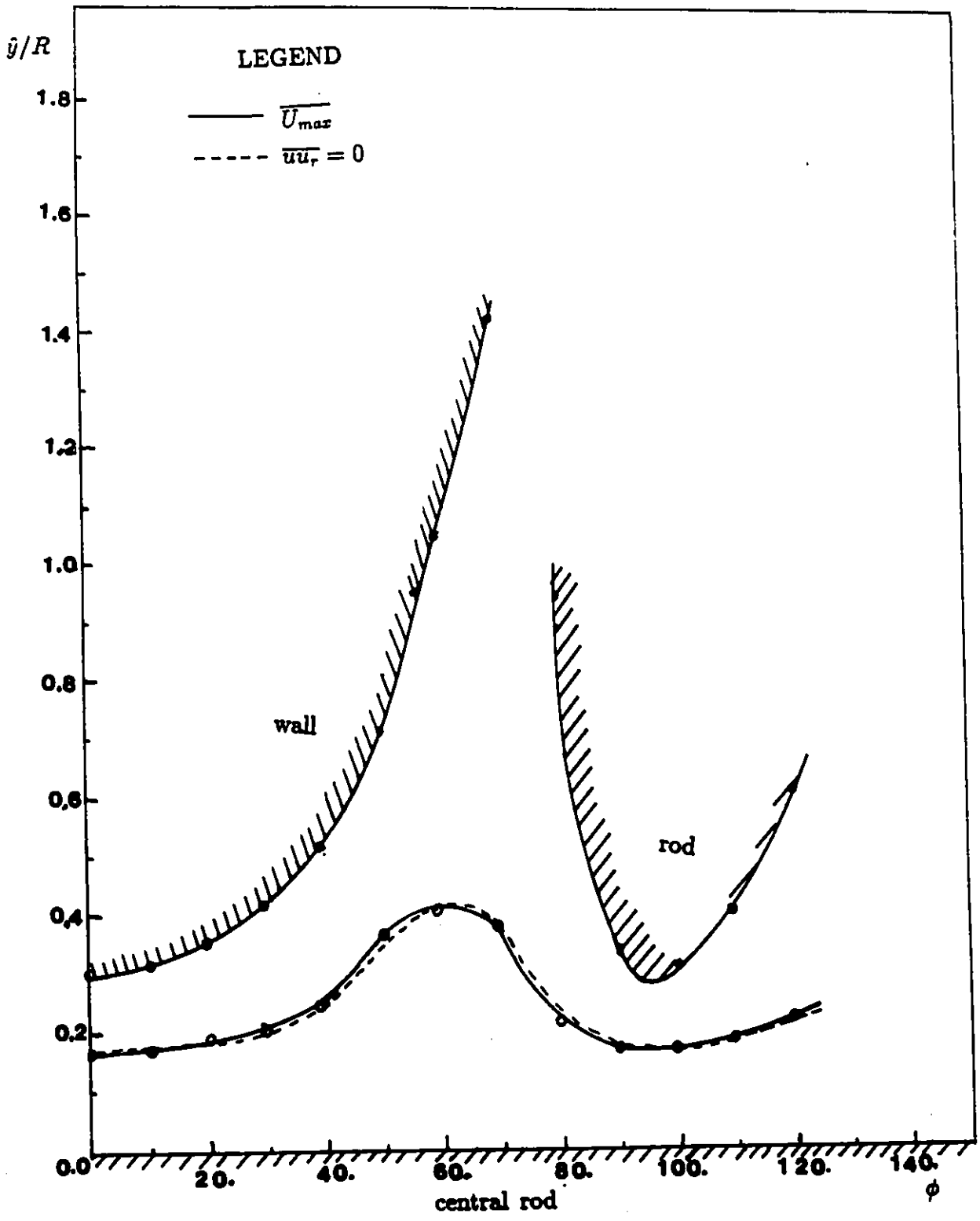

Figure 72. Local characteristic flow width at design conditions

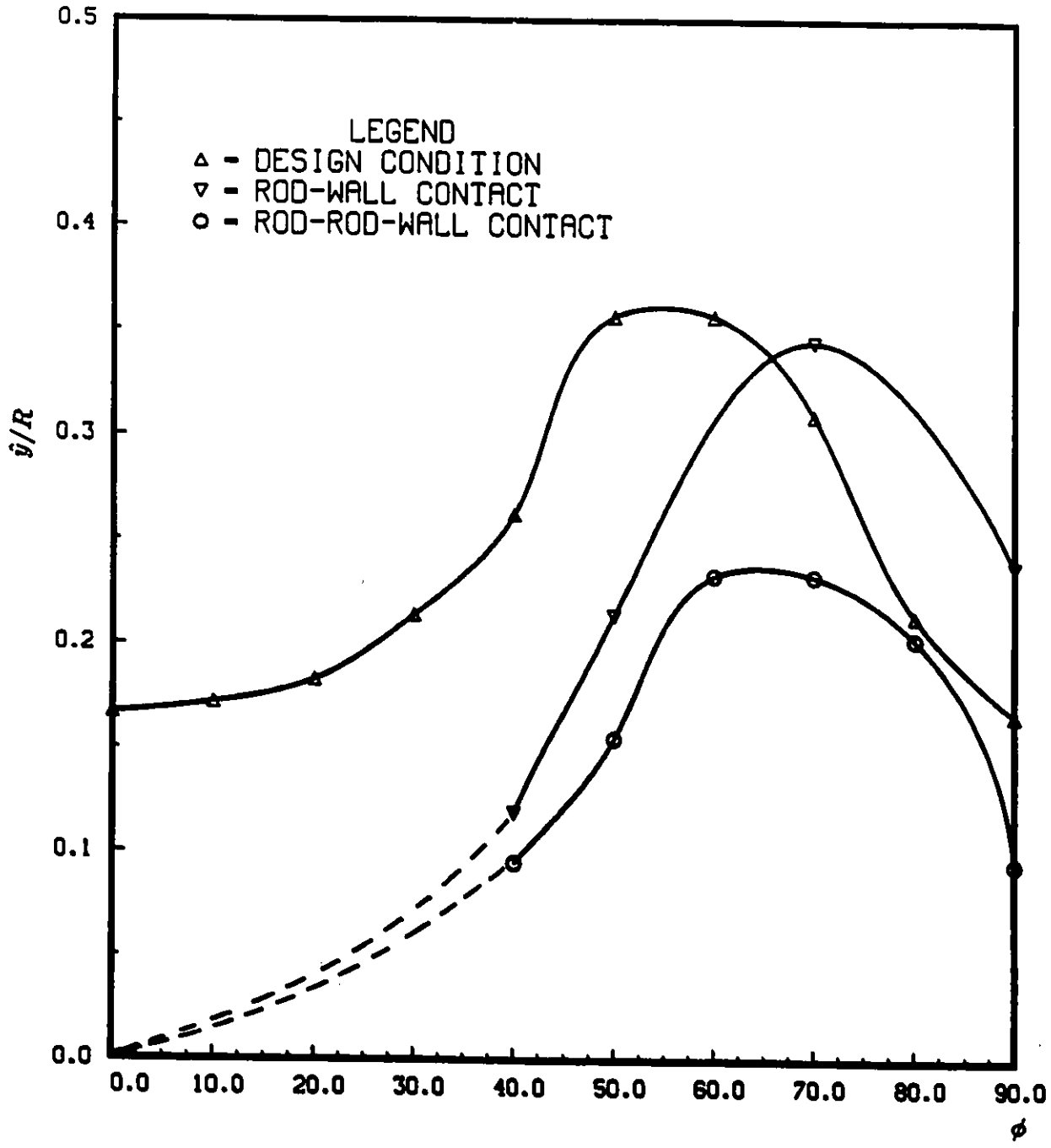

Figure 73. Local characteristic flow width at three different central rod positions

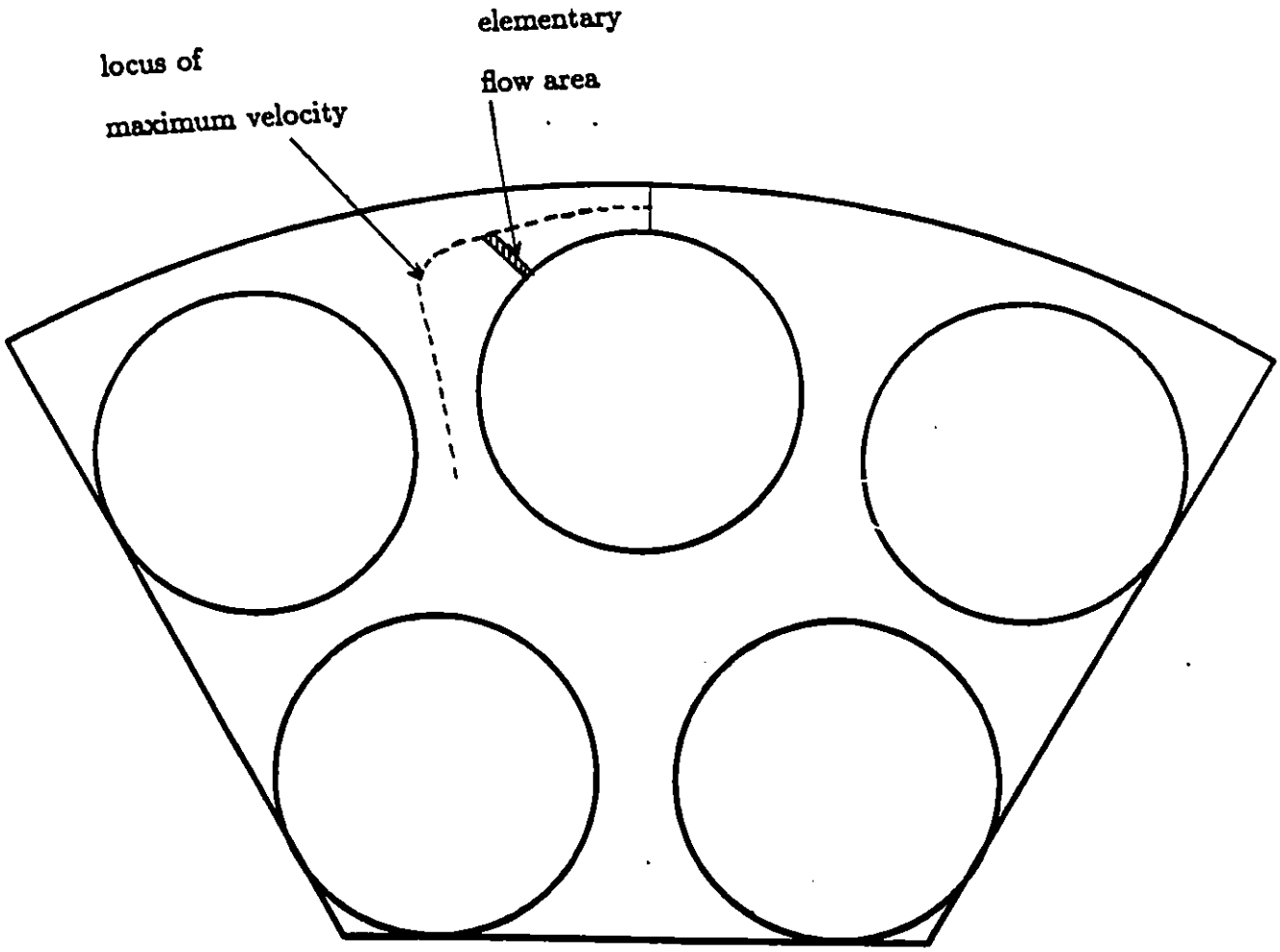

Figure 74. Definition of elementary area used in the determination of the local friction factor

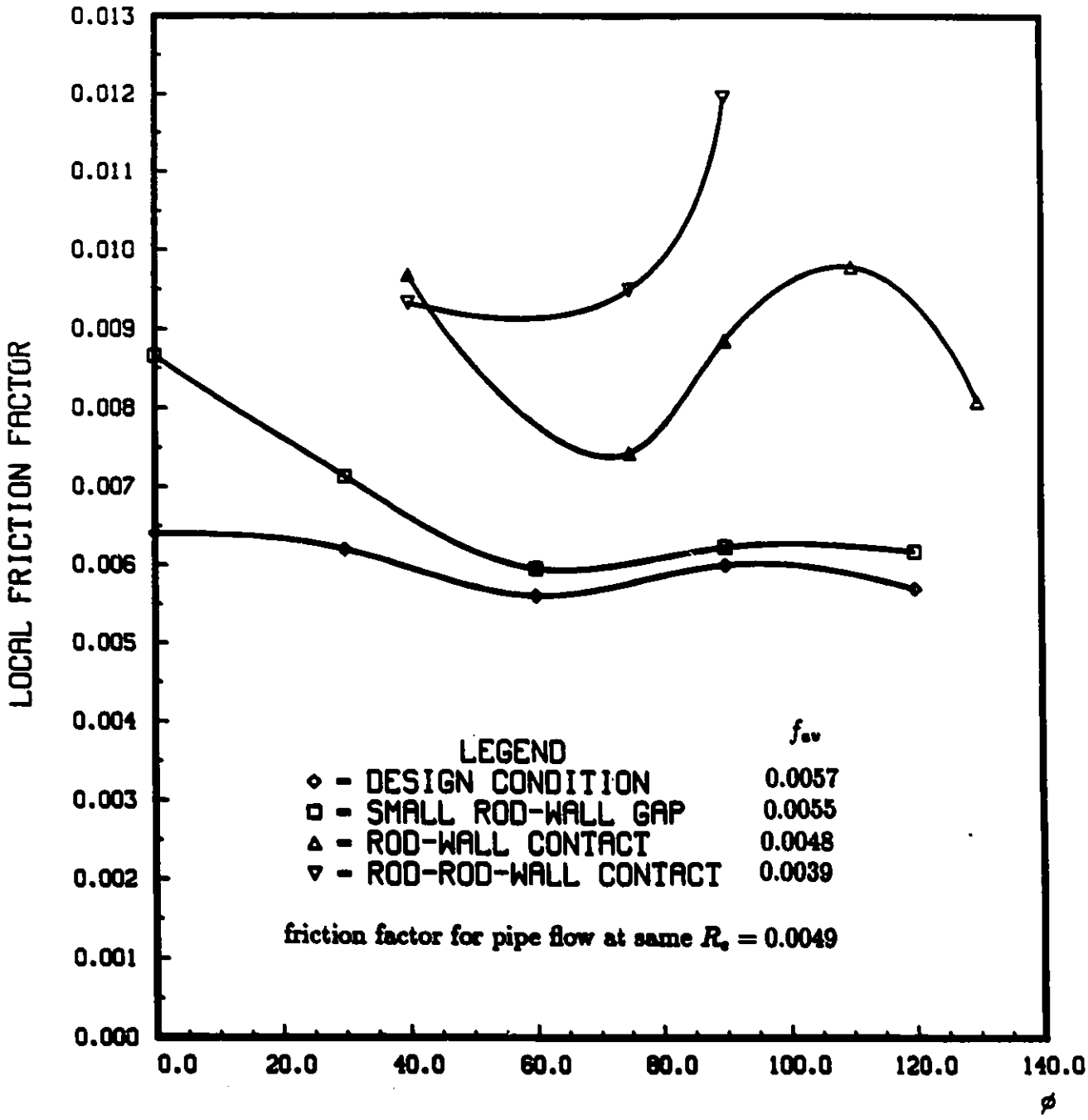

Figure 75. Distribution of local friction factor in the wall subchannel

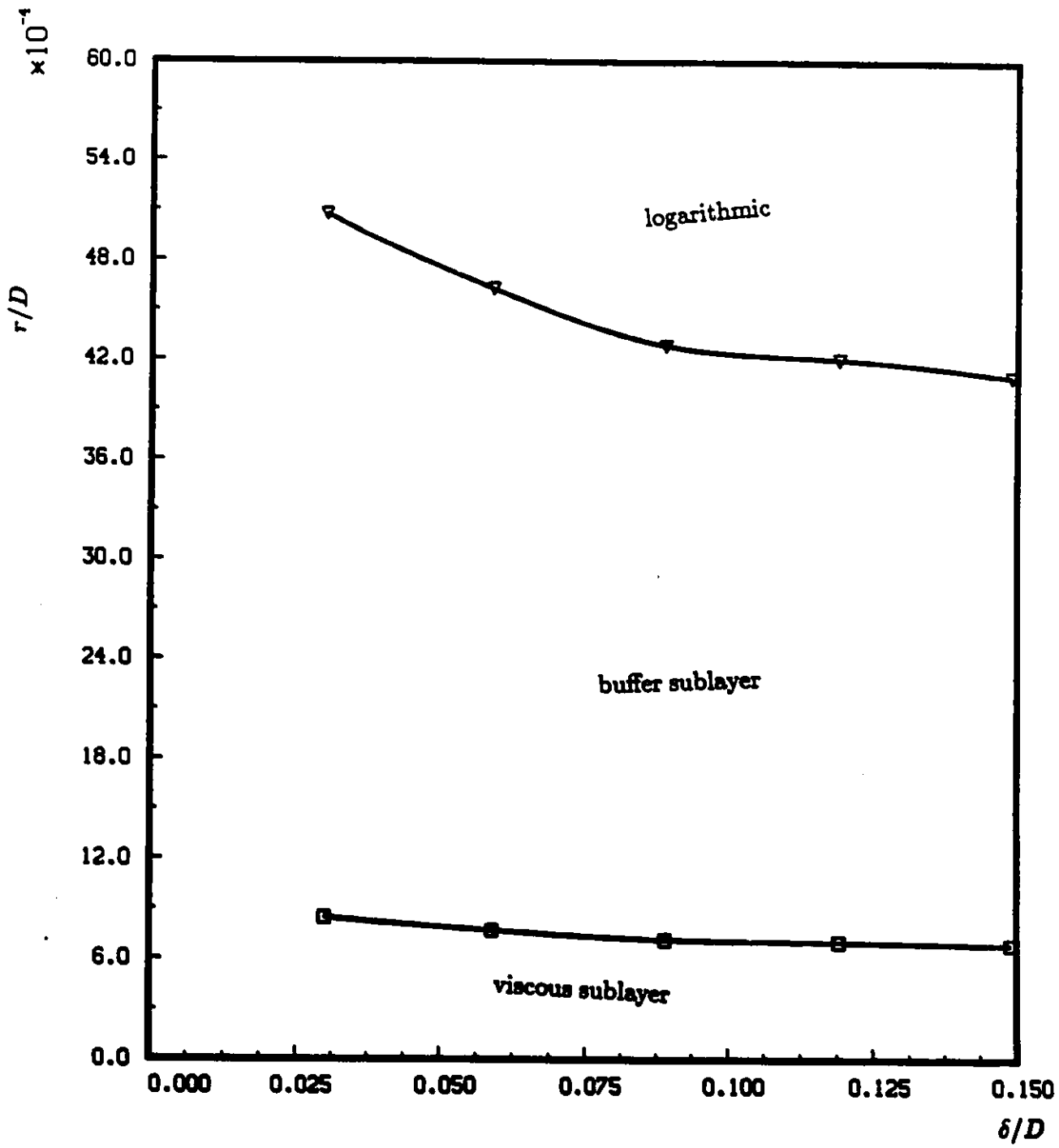

Figure 76a. Variation of inner boundary layer thickness in the rod-wall gap

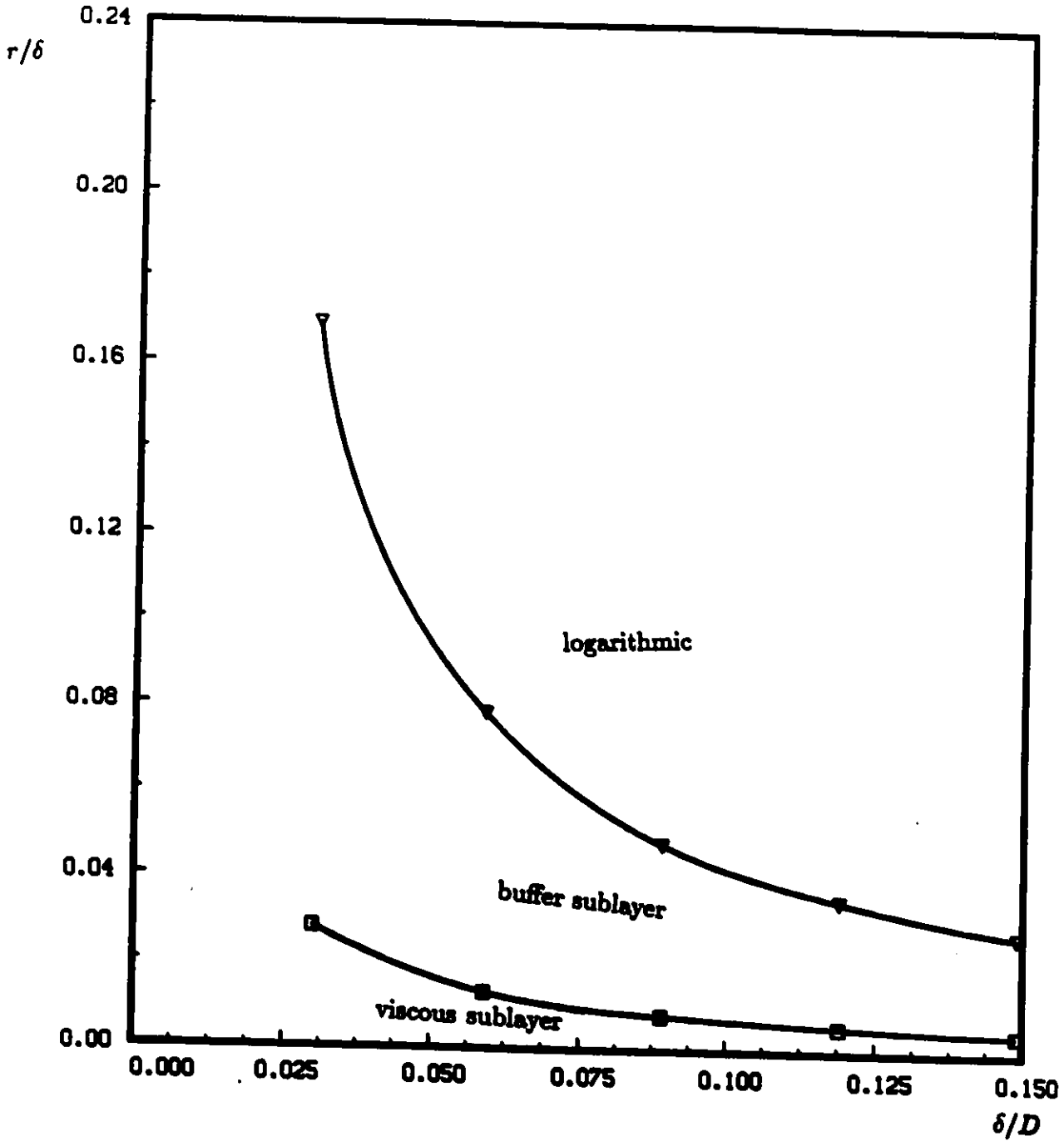

Figure 76b. Variation of inner boundary layer thickness in the rod-wall gap

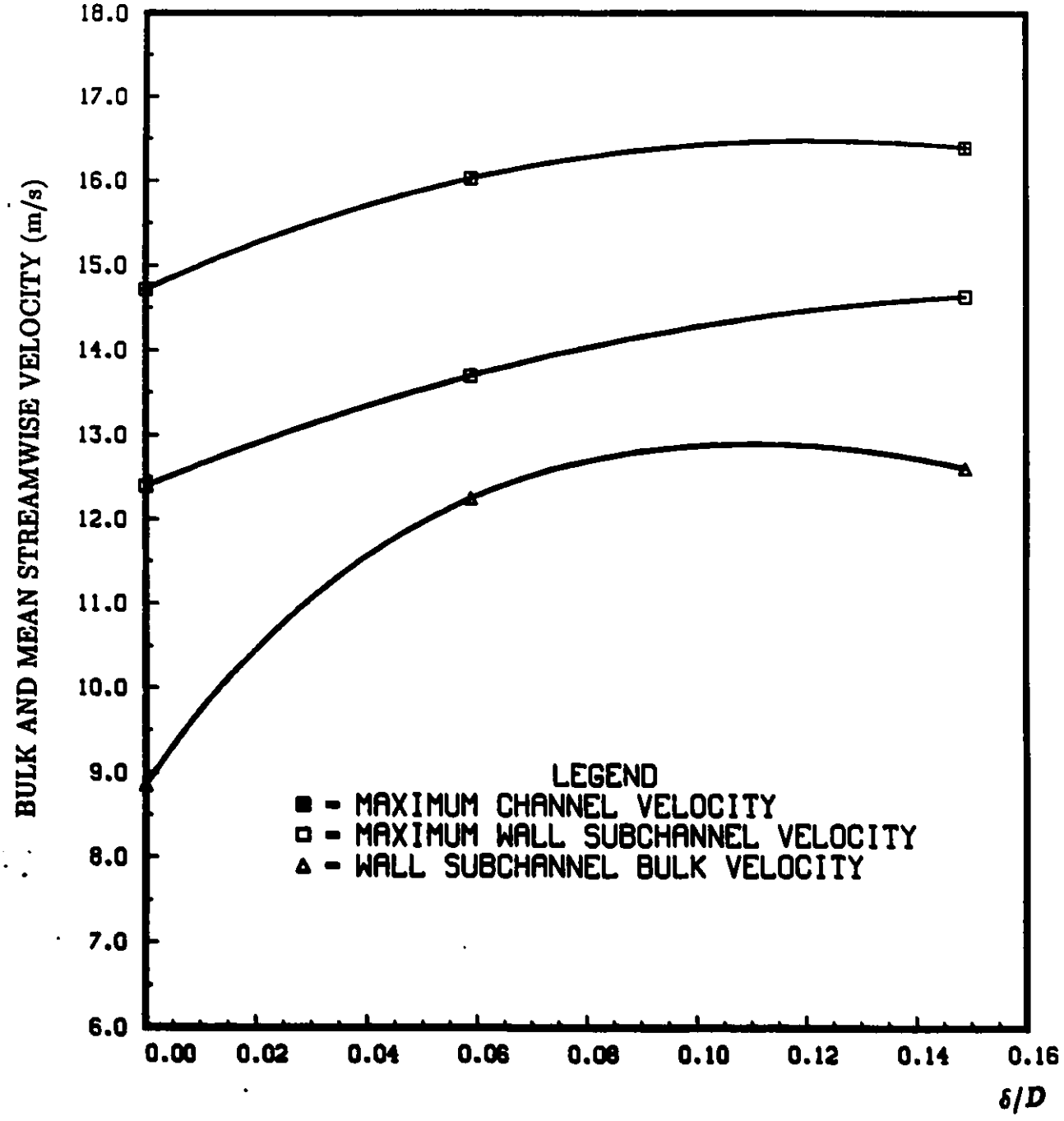

Figure 77. Variation of velocities in the wall subchannel and entire duct with rod-wall gap δ

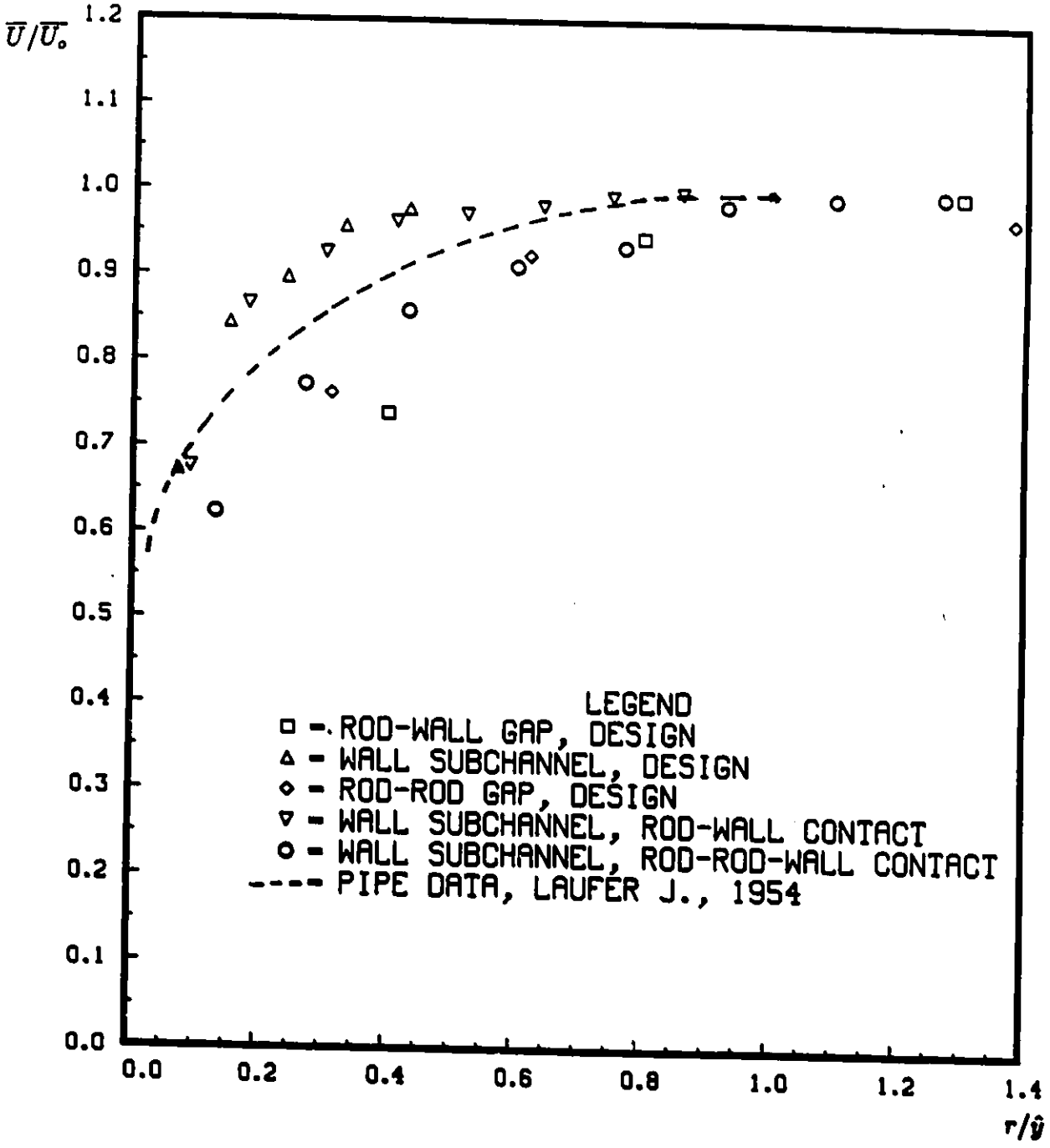

Figure 78. Velocity distribution in the wall subchannel

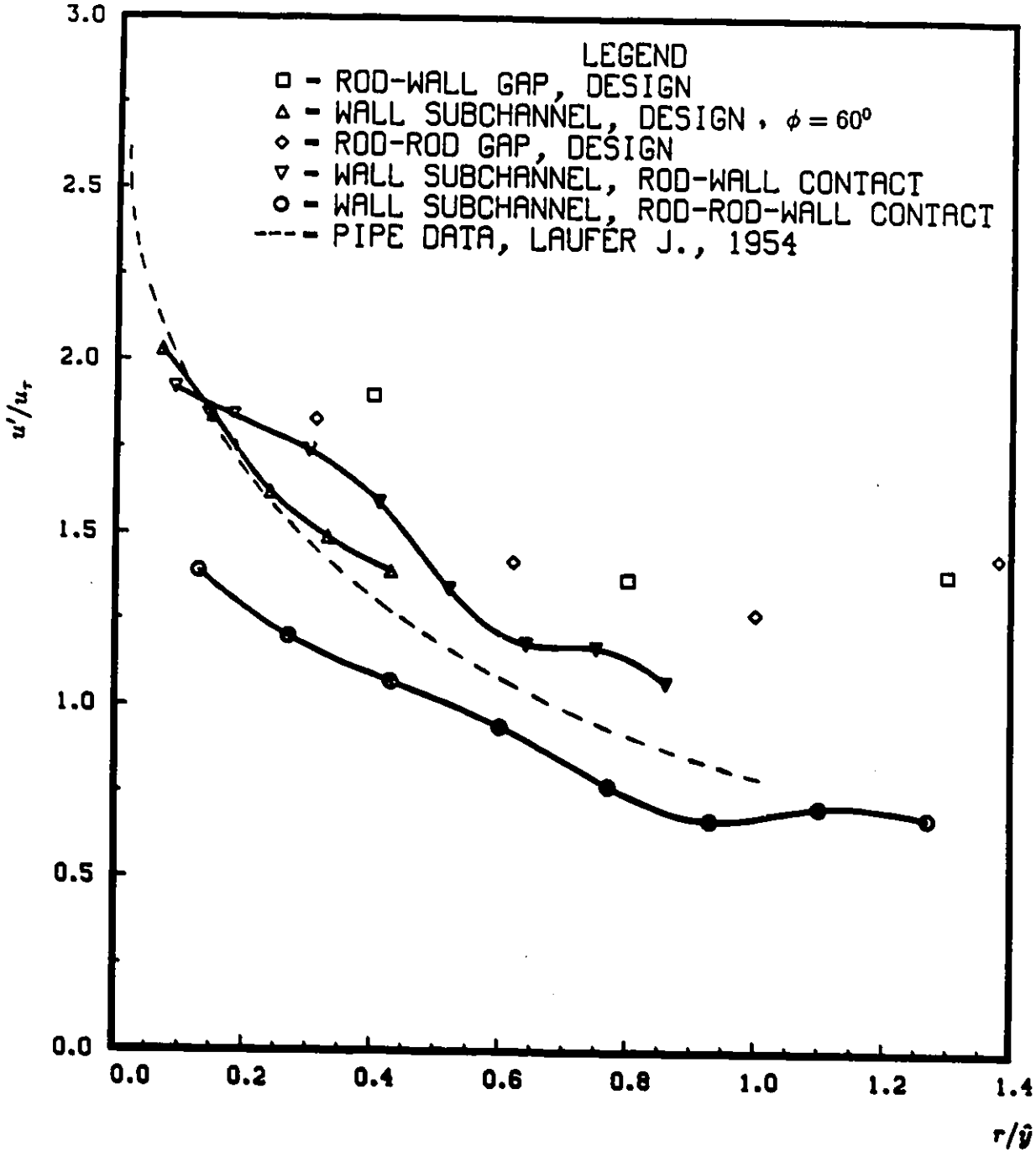

Figure 79. Distribution of the axial rms velocity fluctuation

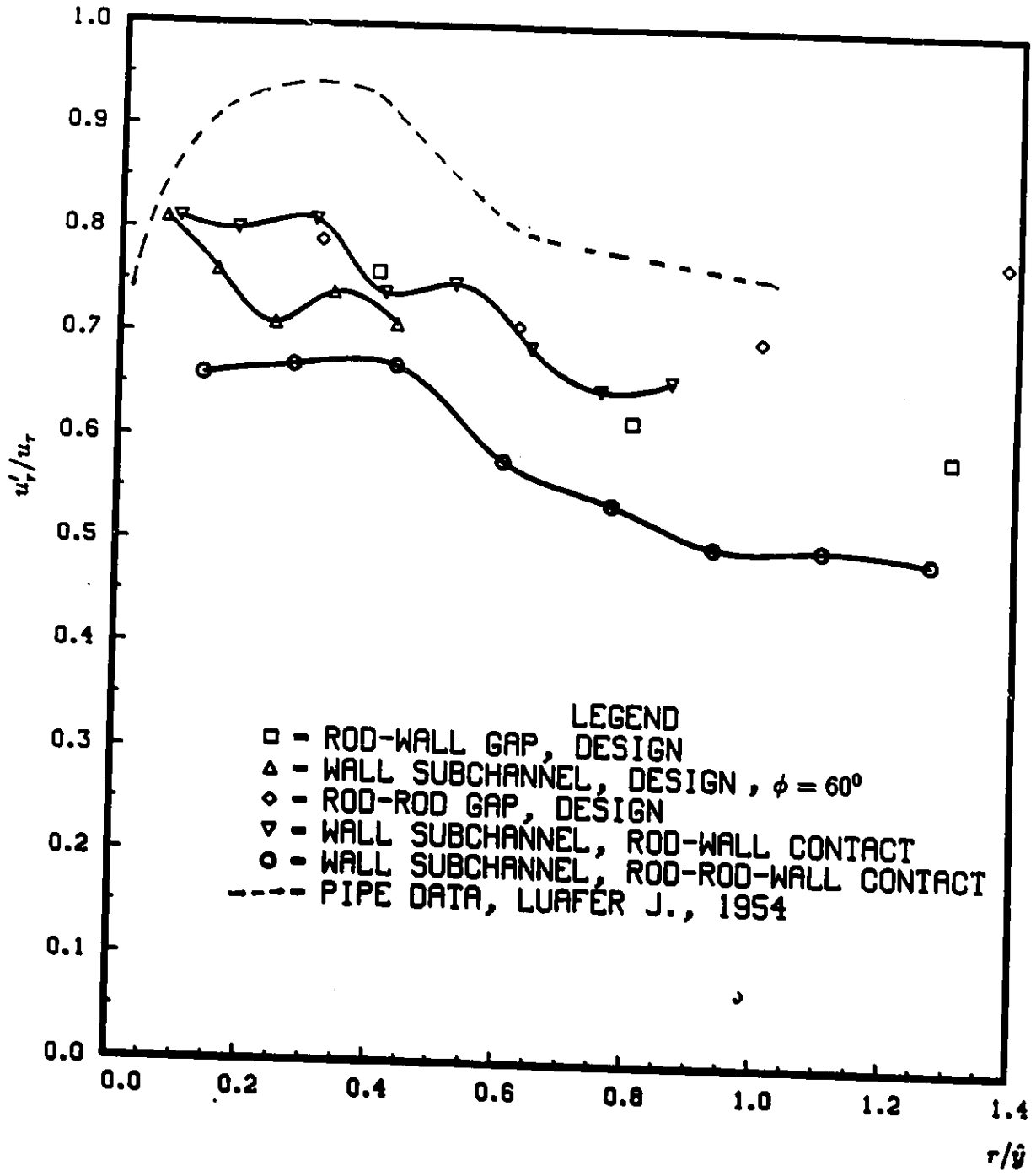

Figure 80. Distribution of the radial rms velocity fluctuation

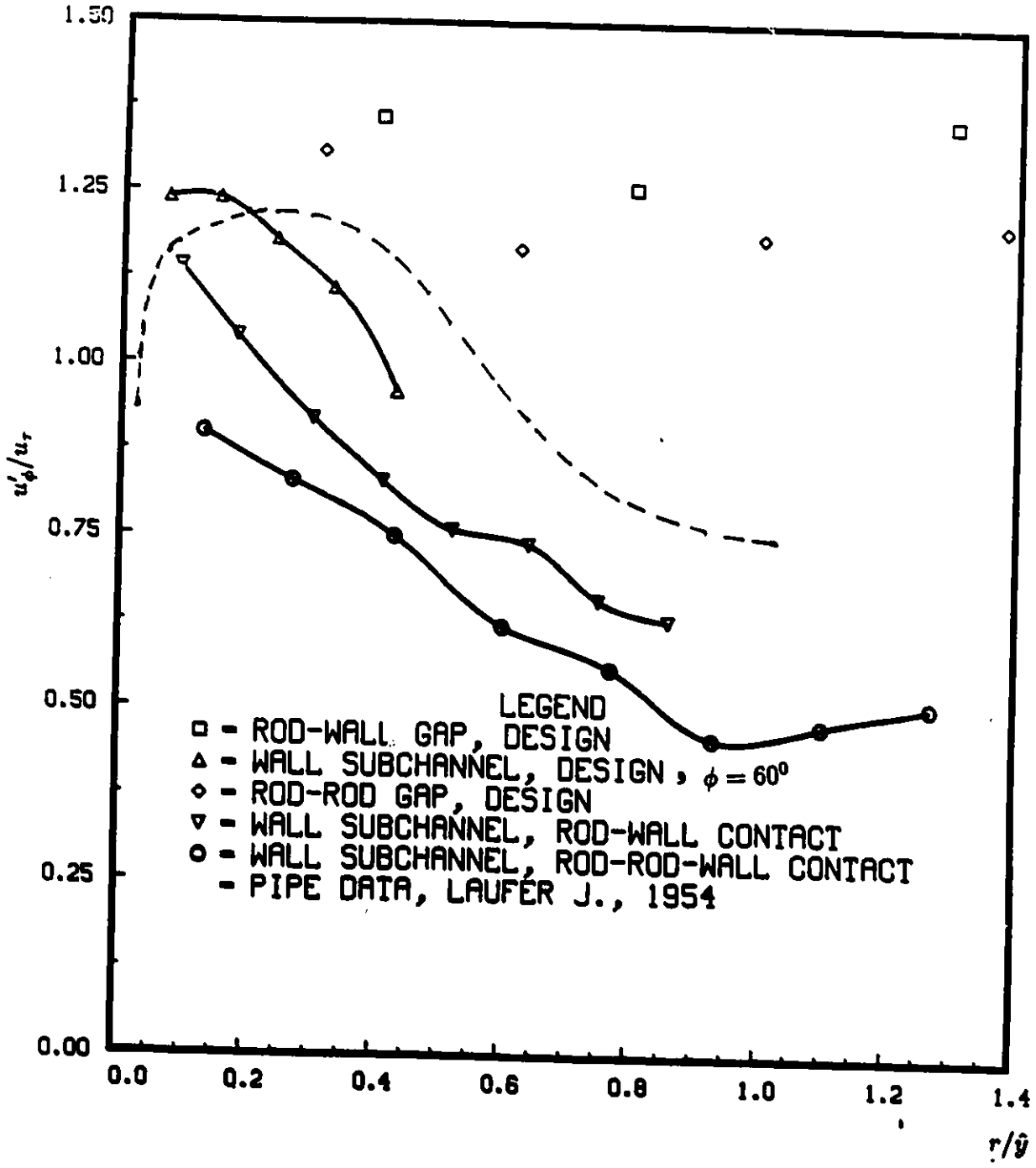

Figure 81. Distribution of the azimuthal rms velocity fluctuation

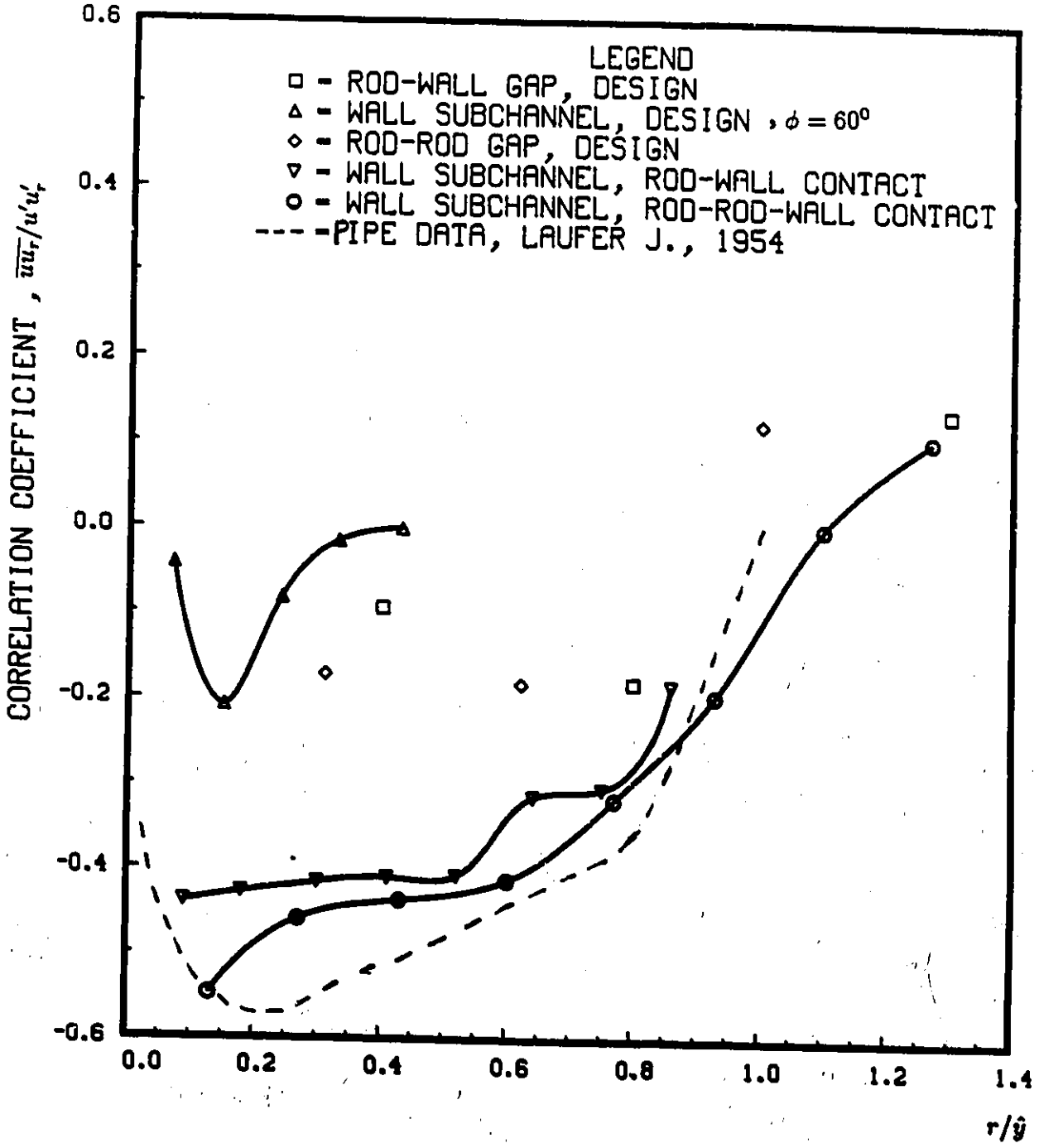

Figure 82. Distribution of correlation coefficient

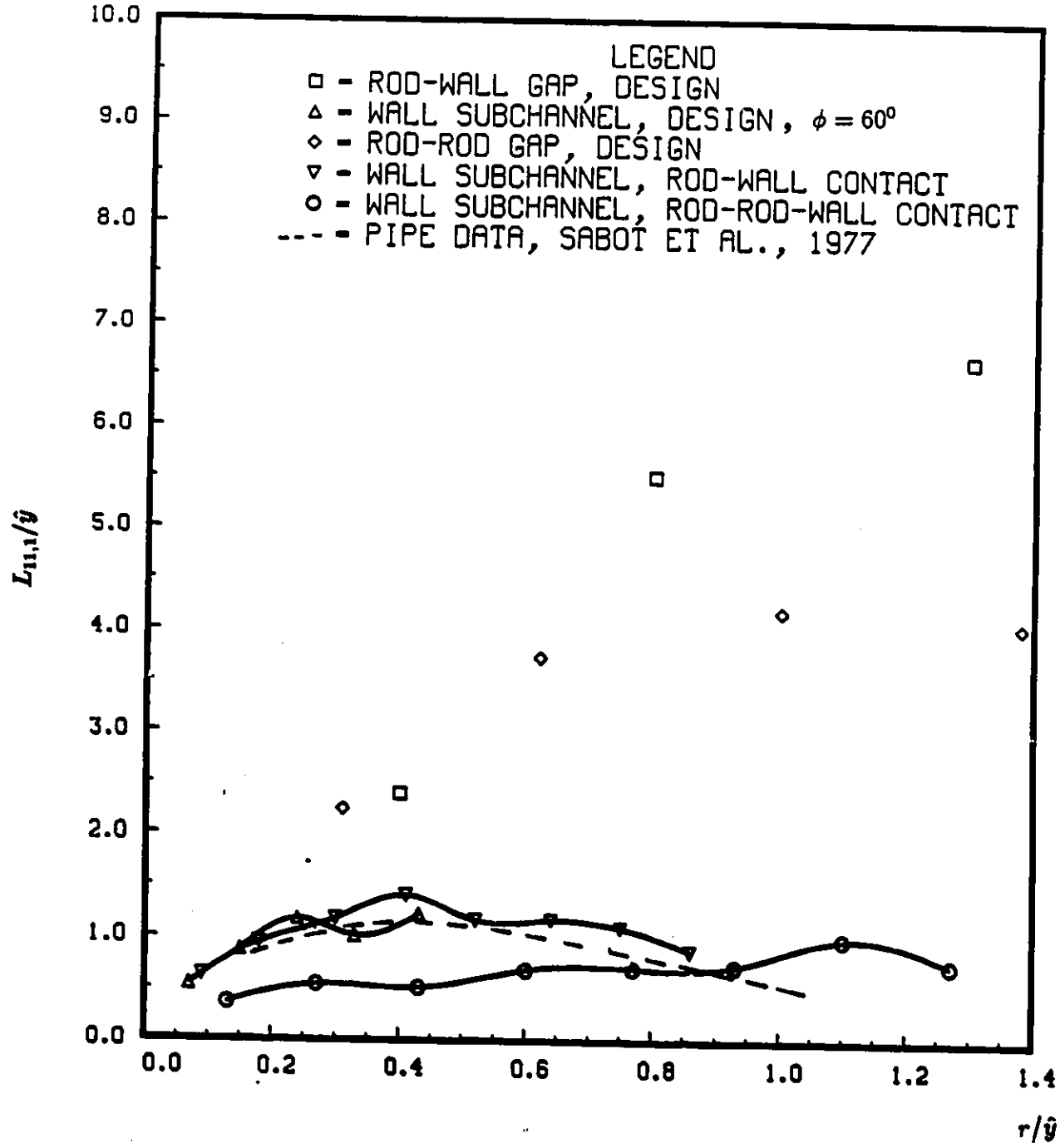

Figure 83. Distribution of streamwise Eulerian integral length scale of the axial fluctuations

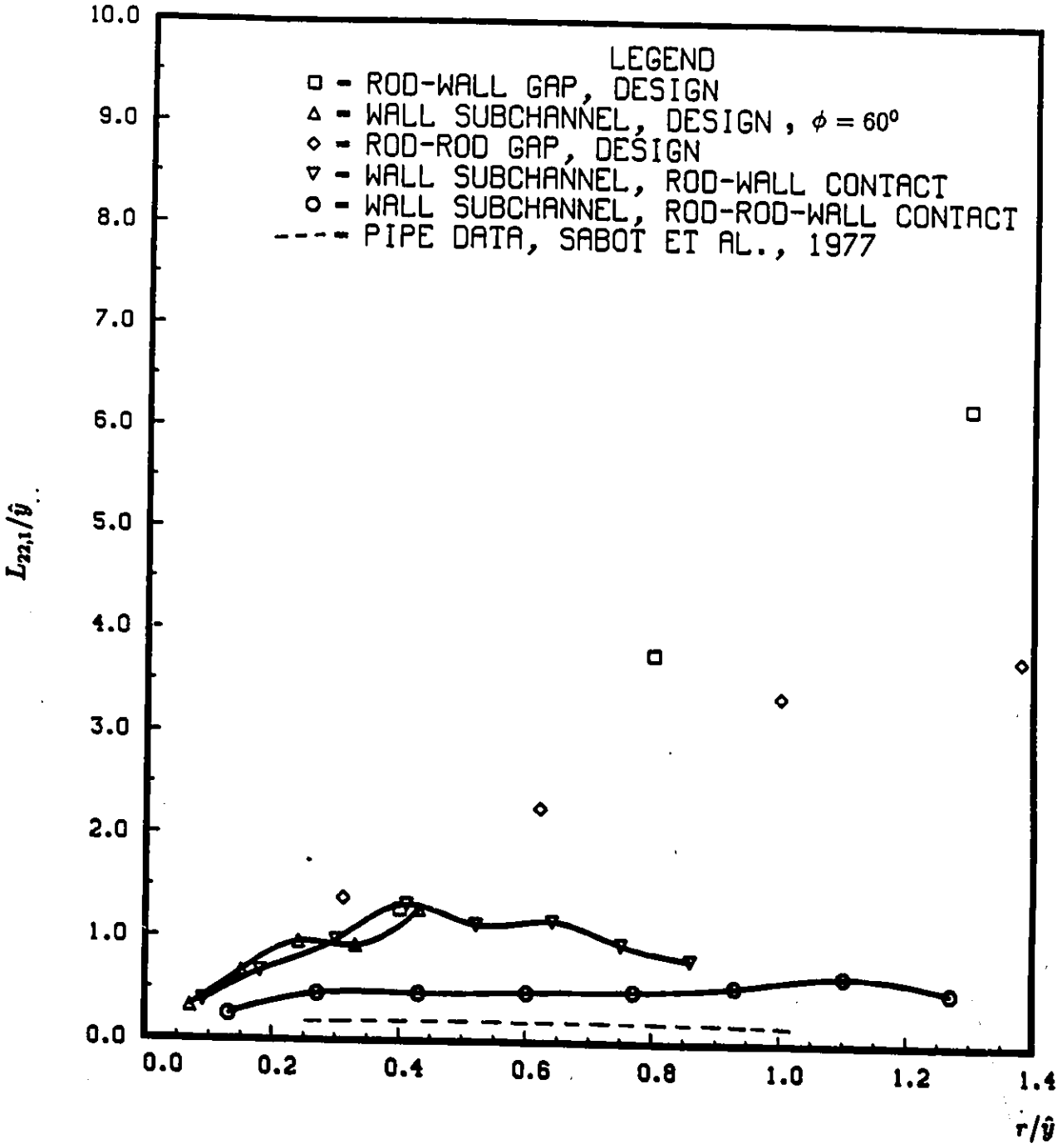

Figure 84. Distribution of streamwise Eulerian integral length scale of the radial fluctuations

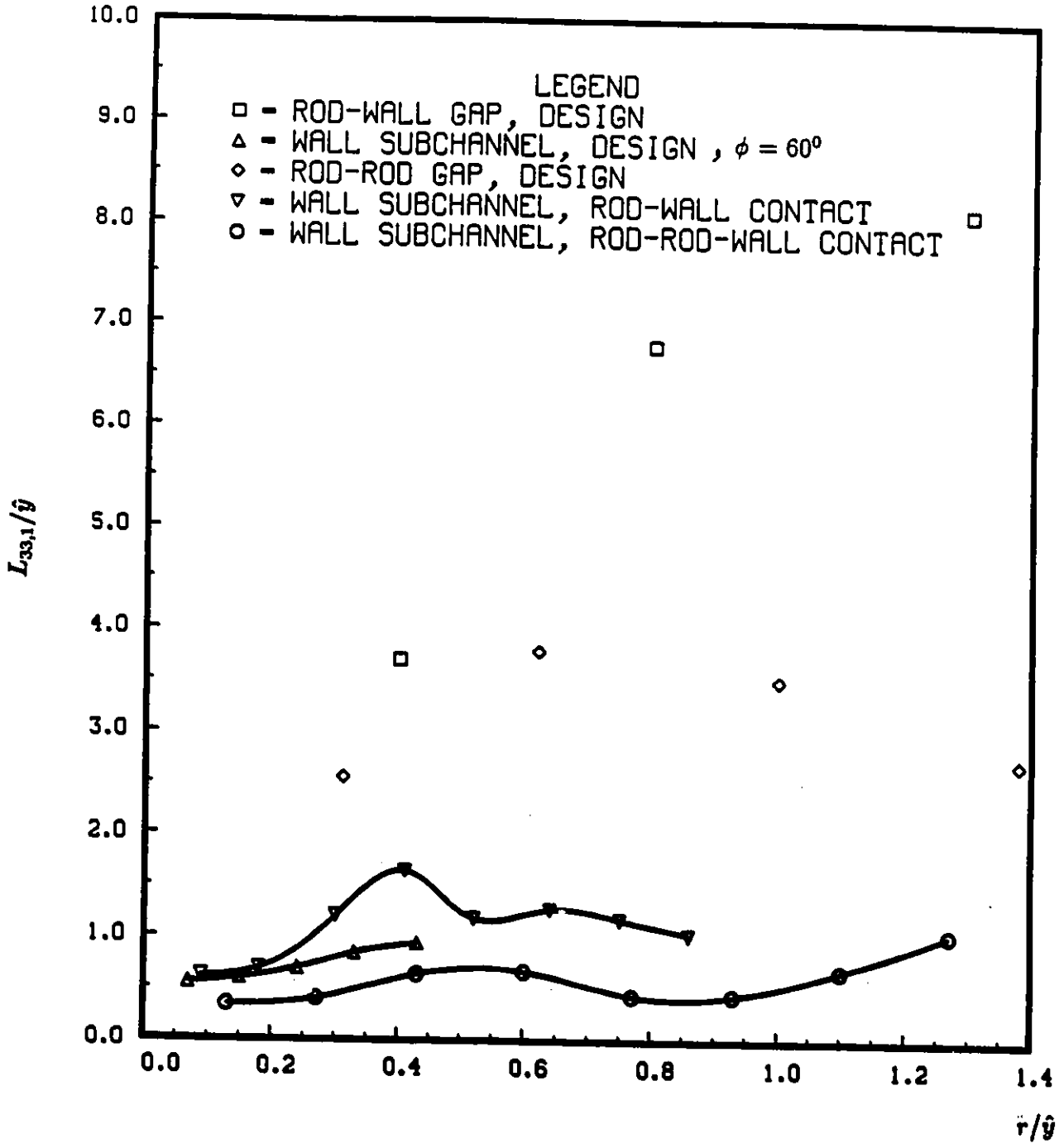

Figure 85. Distribution of streamwise Eulerian integral length scale of the azimuthal fluctuations

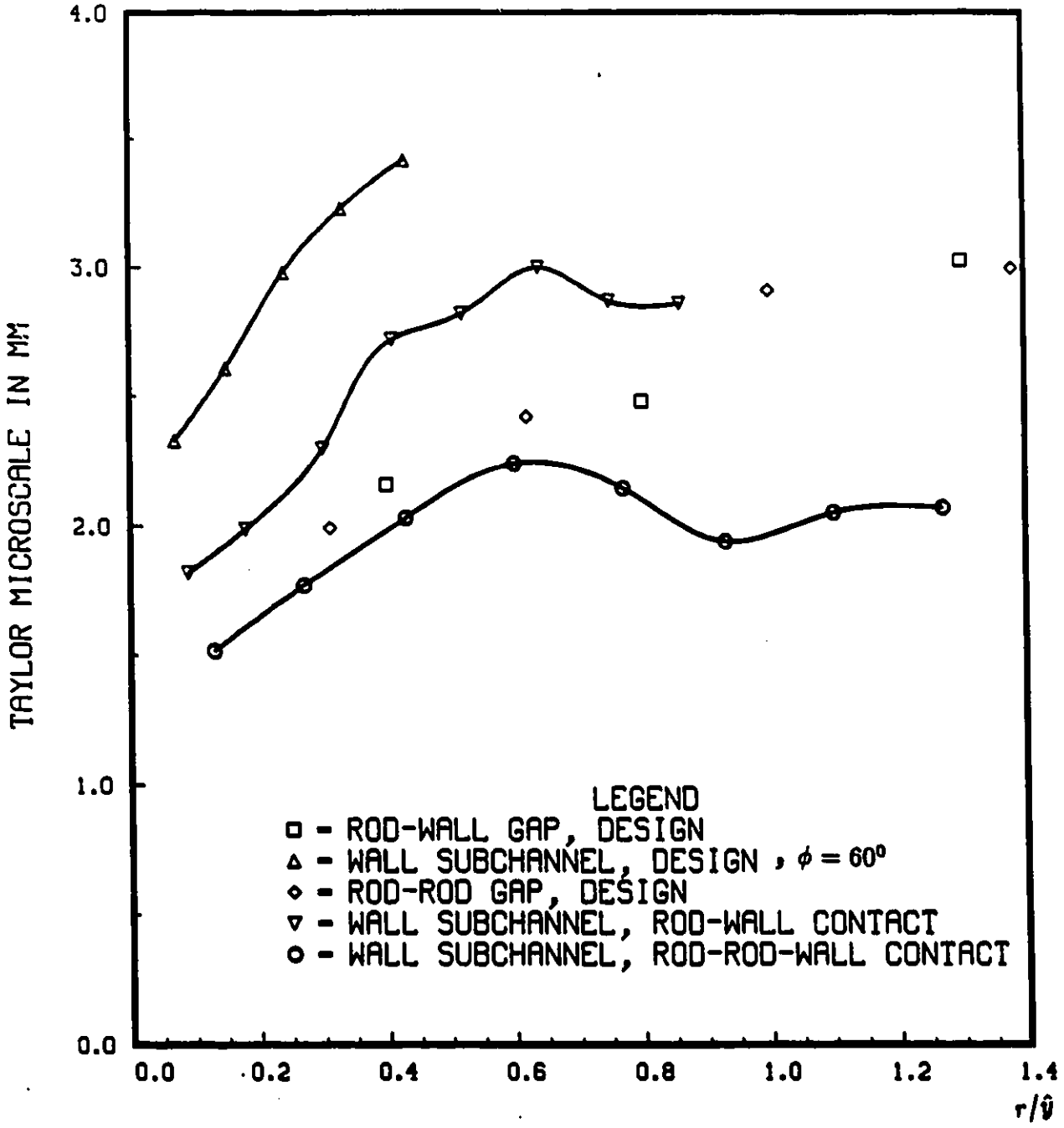

Figure 86. Distribution of streamwise Taylor microscale

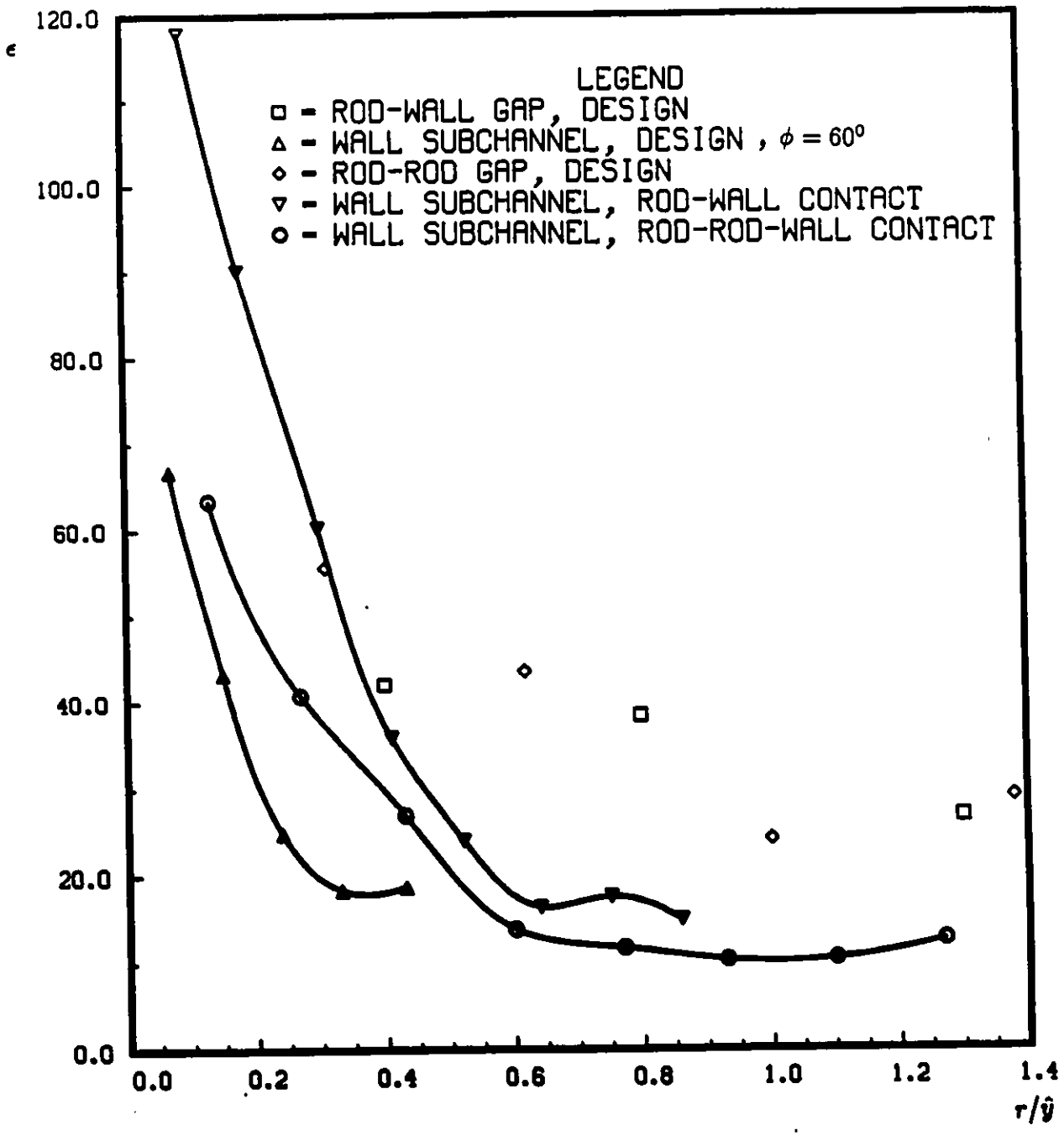

Figure 87. Distribution of turbulent energy dissipation rate

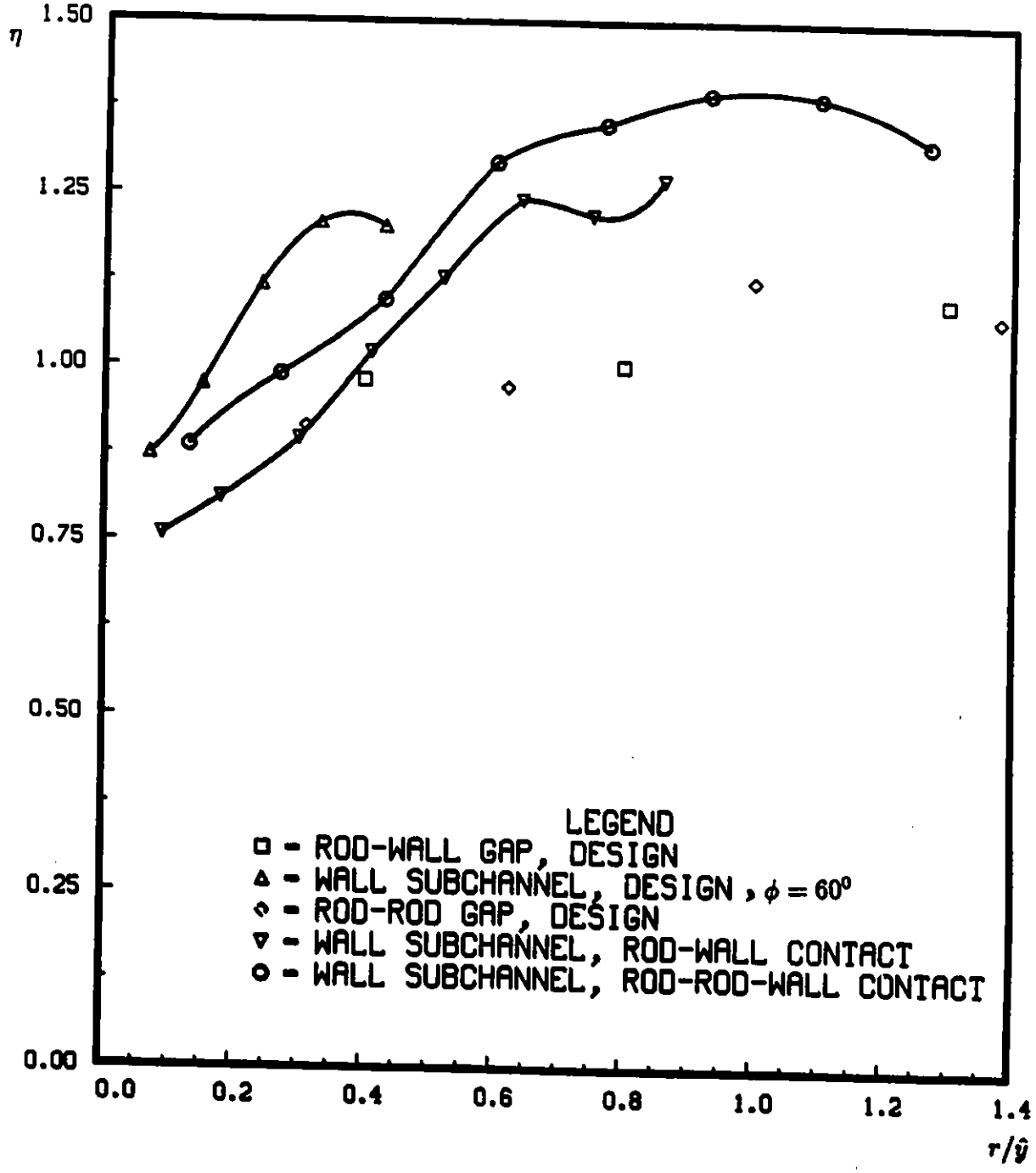

Figure 88. Distribution of Kolmogoroff's microscale